Aspects of Dark Matter Phenomenology and Connection to Neutrino mass

Dibyendu Nanda

A thesis submitted for the degree of

Doctor of Philosophy

Supervisor

Dr. Debasish Borah

Department of Physics
Indian Institute of Technology Guwahati
Guwahati - 781039, Assam, India

Aspects of Dark Matter Phenomenology and Connection to Neutrino mass

A thesis submitted by

Dibyendu Nanda

to

Indian Institute of Technology Guwahati
in partial fulfillment of the requirements
for the award of the degree of
Doctor of Philosophy in Physics

Supervisor

Dr. Debasish Borah

Department of Physics
Indian Institute of Technology Guwahati
Guwahati - 781039, Assam, India

To my Mother

Declaration

Dibyendu Nanda,
Roll No. 166121013
Department of Physics
Indian Institute of Technology Guwahati
Guwahati, India

I hereby declare that works presented in the thesis entitled "**Aspects of Dark Matter Phenomenology and Connection to Neutrino mass**" have been carried out by me under the supervision of **Dr. Debasish Borah** at the Department of Physics, Indian Institute of Technology Guwahati, India. The thesis has not been submitted anywhere else for any degree. Works presented in the thesis are all my own unless referenced to the contrary in the thesis.

Date: 10.02.2021

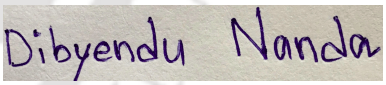

Signature

भारतीय प्रौद्योगिकी संस्थान गुवाहाटी
Indian Institute of Technology Guwahati

Certificate

Dr. Debasish Borah,
Assistant Professor
Department of Physics
Indian Institute of Technology Guwahati
Guwahati, India
email: dborah@iitg.ac.in

It is certified that the work contained in the thesis entitled "**Aspects of Dark Matter Phenomenology and Connection to Neutrino mass**" by Mr. Dibyendu Nanda (Roll No - 166121013), a Ph.D. student in the Department of Physics, Indian Institute of Technology Guwahati is carried out under my supervision and has not been submitted elsewhere for the award of any other degree.

Date: 10.02.2021

Signature

भारतीय प्रौद्योगिकी संस्थान गुवाहाटी
Indian Institute of Technology Guwahati

Thesis consists of :

1. **"Common Origin of Neutrino Mass and Dark Matter from Anomaly Cancellation Requirements of a $U(1)_{B-L}$ Model"**
   Dibyendu Nanda, Debasish Borah.
   *e*print: arXiv: 1709.08417 (hep-ph)
   Published in **Phys.Rev. D96 (2017) no.11, 115014**

2. **"Type III Seesaw for Neutrino Masses in $U(1)_{B-L}$ Model with Multi-component Dark Matter"**
   Anirban Biswas, Debasish Borah, **Dibyendu Nanda**
   *e*print: arXiv: 1908.04308 (hep-ph)
   Published in **JHEP 1912 (2019) 109**

3. **"Connecting Light Dirac Neutrinos to a Multi-component Dark Matter Scenario in Gauged $B-L$ Model"**
   Dibyendu Nanda, Debasish Borah.
   *e*print: arXiv: 1911.04703 (hep-ph)
   Published in **Eur.Phys.J.C 80 (2020) 6, 557**

4. **"Observing Left-Right Symmetry in the Cosmic Microwave Background"**
   Debasish Borah, Arnab Dasgupta, Chayan Majumdar, **Dibyendu Nanda**
   *e*print: arXiv: 2005.02343 (hep-ph)
   Published in **Phys.Rev.D 102 (2020) 3, 035025**

5. **"When Freeze-out Precedes Freeze-in: Sub-TeV Fermion Triplet Dark Matter with Radiative Neutrino Mass"**
   Anirban Biswas, Debasish Borah, **Dibyendu Nanda**
   *e*print: arXiv: 1806.01876 (hep-ph)
   Published in **JCAP 1809 (2018) no.09, 014**

6. **"Common Origin of Dirac Neutrino Mass and Freeze-in Massive Particle Dark Matter"**
   Debasish Borah, Biswajit Karmakar, **Dibyendu Nanda**
   *e*print: arXiv: 1805.11115 (hep-ph)
   Published in **JCAP 1807 (2018) no.07, 039**

Other publications :

1. **"keV Neutrino Dark Matter in a Fast Expanding Universe"**
   Anirban Biswas, Debasish Borah, **Dibyendu Nanda**
   *e*print: arXiv: 1809.03519 (hep-ph)
   Published in **Phys.Lett. B786 (2018) 364372**

2. **"Right-handed Neutrino Dark Matter with Radiative Neutrino Mass in Gauged $B-L$ Model"**
   Debasish Borah, **Dibyendu Nanda**, Nimmala Narendra, Narendra Sahu
   *e*print: arXiv: 1810.12920 (hep-ph)
   Published in **Nucl.Phys. B950 (2020) 114841**

3. **"Common origin of modified chaotic inflation, non thermal dark matter and Dirac neutrino mass"**
   Debasish Borah, **Dibyendu Nanda**, Abhijit Kumar Saha
   *e*print: arXiv: 1904.04840 (hep-ph)
   Published in **Phys.Rev.D101 (2020) no.7, 075006**

4. **"Planck scale origin of nonzero θ_{13} and super-WIMP dark matter"**
   Debasish Borah, Biswajit Karmakar, **Dibyendu Nanda**
   *e*print: arXiv: 1906.02756 (hep-ph)
   Published in **Phys.Rev.D100 (2019) no.5, 055014**

5. **"Inelastic Fermion Dark Matter Origin of XENON1T Excess with Muon (g−2) and Light Neutrino Mass"**
   Debasish Borah, Satyabrata Mahapatra, **Dibyendu Nanda**, Narendra Sahu
   *e*print: arXiv: 2007.10754 (hep-ph)
   Published in **Phys.Lett. B811 (2020) 135933**

भारतीय प्रौद्योगिकी संस्थान गुवाहाटी
Indian Institute of Technology Guwahati

Acknowledgements

I would like to thank everyone who has helped me and inspired me throughout this journey of my life. Above all, it gives me immense pleasure to express my respect to my mother for the struggle she did throughout her life for raising us.

I would like to take this opportunity to express my sincere gratitude to my thesis advisor Dr. Debasish Borah who have introduced me to this amazing research field and sharing his knowledge and ideas with me. Without his encouragement, valuable advice, and constant supports, this journey would have been difficult. I have learned a great deal from him, not just about how to be researcher or an eloquent speaker but also to be honest, and patient.

I would like to thank my doctoral committee members, Dr. Arunansu Sil, Dr. Soumitra Nandi, Dr. Sovan Chakraborty, for their insightful comments and suggestions whenever needed. I also want to thank Dr. Subhaditya Bhattacharya, Dr. Sayan Chakrabarti, and Dr. Debaprasad Maity for many useful discussions and suggestions. I must acknowledge Hemanta Da and Basab Da for their cooperation with computational issues.

I thank all my collaborators and co-authors: Prof. Narendra Sahu, Dr. Anirban Biswas, Dr. Biswajit Karmakar, Dr. Arnab Dasgupta, Dr. Abhijit Kumar Saha, Dr. Nimmala Narendra, Chayan Majumdar, Satyabrata Mahapatra. Because of them, I got the opportunity to work on various problems and, in the process, acquired a great extent of knowledge and experience. I cannot express how grateful I am to Dr. Anirban Biswas for those long and fruitful discussions we had on many different topics. I owe a lot to Dr. Sunando Kumar Patra for helping me improve my computational skill. I am indebted to my first teacher, Shasi Kanta Kumar, who made me fall in love with physics. I would also take this opportunity to thank Dr. Bhupati Chakrabarti, Dr. Samapti Pal, and Prof. Nilakshi Das, who encouraged me to pursue my career as a physicist.

I gratefully acknowledge the support from our group members, Devabrat, Suruj. I have spent many evenings by discussing with them on different topics. I am grateful to have friends like Kajal, Lopamudra, Sayandeep, Suman, Abhisek, and Deepshikha. We have spent so much time and exchanged many valuable thoughts on physics and non-physics topics. I am also very much fortunate to have some of the wonderful human beings as my friend from my school days to this date. This list includes Emon, Kakima, Abir, Chayan, Surajit, Avijit, Tufan, Dibyendu, Sunny Da, Abhishek Da, Souvik, Rishav Da, Basabendu Da, Arghya, Madhurima, Ipsita, Sahabub, and Prantik and many more.

Last but not least, I would like to convey a very special thanks to my sisters (Bordi, Mesdi, Milu di, Bulu Di, Tulu di, Nilu Di) and brothers (Borda, Shuvo Da, Pintu Da, Rintu Da, Mintu) for their unconditional support throughout my academic career.

भारतीय प्रौद्योगिकी संस्थान गुवाहाटी
Indian Institute of Technology Guwahati

Abstract

After the remarkable discovery of the Higgs boson at the Large Hadron Collider (LHC) in 2012, the standard model (SM) of particle physics has been established as the most successful theory of elementary particles and their fundamental interactions except gravity. However, there are convincing reasons to believe that there is new physics beyond the standard model (BSM) as several observed phenomena as well as theoretical questions remain unanswered in the SM. Among such observed phenomena, the presence of dark matter (DM) giving rise to around 26% of the present Universe is very appealing. Although the first evidence for DM appeared in the 1930s, it was only in the early 1980s that astronomers were convinced of the fact that most of the mass holding galaxies and clusters of galaxies together is non-luminous. Since the nature of particle DM and its interactions with the SM particles, except gravitational interactions, are not yet known, there exist two broad scenarios: one in which DM couples to SM with couplings of the order of electroweak interactions and one in which DM-SM couplings are very feeble. The first scenario, popularly known as the weakly interacting massive particle (WIMP) paradigm, is the most studied particle DM candidate in the literature. WIMP can be defined as a new elementary particle whose interaction strength is as weak as or weaker than the weak nuclear force. The typical mass range for WIMPs can vary from a few GeV to a few TeV. WIMPs can be thermally produced in the early Universe through their interaction with the bath particles. Their relic abundance can be found from the very well known "freeze-out" mechanism. WIMPs can also leave observable signatures at several direct, indirect search experiments by virtue of their sizeable interactions. While no such observations have been made yet, the other scenario, known as the feebly interacting massive particle (FIMP) scenario, has also gained attention in the last few years. In this paradigm, DM will have very feeble interaction with SM particles, which prevents them from getting produced thermally in the early Universe. However, it is extremely difficult to produce or detect such particles directly in our ongoing experiments.

Another observed phenomena is the existence of tiny but non-zero neutrino mass and large mixing, which have been confirmed by several neutrino experiments for more than two decades till now. Specially, the more recent experimental results have not only confirmed the results from earlier experiments but also discovered the non-zero reactor mixing angle θ_{13}. The two most important unknowns at present in the neutrino sector are the mass hierarchy: whether it is normal ($m_3 > m_2 > m_1$) or inverted ($m_2 > m_1 > m_3$), and the leptonic Dirac CP phase δ. Apart from neutrino oscillation experiments, the neutrino sector is constrained by the data from cosmology and rare decay experiments. For example, the combined data from the Planck 2018 and BAO experiments constrains the sum of absolute neutrino masses $\sum_i |m_i| < 0.12$ eV at 95% CL. If there are no right-handed neutrinos, the Higgs field, which

lies at the origin of all massive particles in the SM, can not have any Dirac Yukawa coupling with the neutrinos. If we include right-handed neutrinos by hand without a Majorana mass for the right-handed neutrinos, the required Yukawa couplings are extremely small, around 10^{-12} or smaller, usually considered as unnatural. Additionally, a bare mass term of the right-handed neutrinos is allowed by gauge symmetries, introducing a new scale outside the purview of the SM.

The purpose of this thesis is to study minimal models of scalar or fermion DM, where light neutrino mass can also arise naturally with a non-trivial connection to the DM sector. To do that, we have extended the particle content as well as the symmetry of the SM either by gauge or global symmetries and studied their phenomenological consequences. We have shown that such symmetries not only stabilize DM but also play a crucial role in generating neutrino mass and mixing. We elaborate upon direct and collider search prospects of the models both in the context of WIMP, and in some specific scenarios, we have also discussed the possibilities of constraining the model from the cosmological observations like effective relativistic degrees of freedom (DOF) in cosmic microwave background (CMB). We have also discussed the interplay of thermal and non-thermal contribution to DM relic density. The thesis has been divided into five chapters. We have started with a brief introduction of the DM physics and the neutrino mass generation mechanism in chapter 1. In chapter 2, we have studied a class of a very well motivated BSM framework based on the gauged $B - L$ extension of the SM with B, L being baryon and lepton numbers, respectively. This minimal and economical model generating nonzero neutrino mass has been studied for a long time. The most interesting feature of the minimal version of this framework is that the inclusion of three right-handed neutrinos, as it is done in the type I seesaw mechanism of generating light neutrino masses, is no longer a choice but a necessity due to the requirement of the new $U(1)_{B-L}$ gauge symmetry to be anomaly free. We have discussed three different versions of the model where neutrino mass (either Majorana or Dirac) and DM physics, namely the stability, type and number of DM candidates are dictated by the anomaly cancellation requirements. In chapter 3, we consider the possibility of probing the left-right symmetric model (LRSM) via the CMB. LRSM has been one of the most popular BSM frameworks studied in the literature. Here the gauge symmetry of the SM is extended to $SU(3)_c \times SU(2)_L \times SU(2)_R \times U(1)_{B-L}$ so that the right-handed fermions (which are singlets in SM) can form doublets under the new $SU(2)_R$. This not only makes the inclusion of right-handed neutrino automatic, but also puts the left and right-handed fermions on equal footing. Due to the presence of gauge interactions of the right-handed neutrinos, they can be thermally produced in the early Universe and contribute to the total effective relativistic DOF and can be significantly constrained. The chapter 4 discusses the role of discrete symmetries in physics of DM and neutrinos. It is based on two different scenarios where the relic abundance of DM is generated either from a hybrid of thermal and non-thermal mechanisms or from purely non-thermal mechanism. While in the first scenario, $\mathbb{Z}_2$ symmetry plays the role of stabilizing DM and generating radiative neutrino mass, in the latter scenario, the non-abelian discrete symmetry group A_4 is implemented to generate light neutrino mass and mixing. In the first case, we have shown that a thermally under-abundant DM candidate can get non-thermal contribution to satisfy relic density bounds. The second section is dedicated to providing a common framework explaining the origin of tiny couplings required for light Dirac neutrinos and non-thermal DM. In chapter 5, we have summarized our discussion and mentioned the future directions.

भारतीय प्रौद्योगिकी संस्थान गुवाहाटी
Indian Institute of Technology Guwahati

Permissions and Attributions

- The content of Chapter 2 is based on the following works,
  (a) **Phys.Rev.D 96 (2017) no.11, 115014** in collaboration with Debasish Borah.
  (b) **JHEP 1912 (2019) 109** in collaboration with Anirban Biswas and Debasish Borah.
  (c) **Eur.Phys.J.C 80 (2020) 6, 557** in collaboration with Debasish Borah.
- The content of Chapter 3 is based on the following work,
  (a) **Phys.Rev.D 102 (2020) 3, 035025** in collaboration with Debasish Borah, Arnab Dasgupta, Chayan Majumdar
- The content of chapter 4 is based on the following works
  (a) **JCAP 1809 (2018) no.09, 014** in collaboration with Anirban Biswas, Debasish Borah
  (b) **JCAP 1807 (2018) no.07, 039** in collaboration with Debasish Borah, Biswajit Karmakar.

भारतीय प्रौद्योगिकी संस्थान गुवाहाटी
Indian Institute of Technology Guwahati

Contents

List of Figures

List of Tables

CHAPTER 1

Introduction

One of the most astonishing revelations of the last century in terms of the understanding of our Universe is that ordinary luminous and baryonic matter, that is, the matter made up of neutrons and protons, is not the dominant form of matter in the present Universe. Rather, different astrophysical and cosmological observations indicate that a large amount of the Universe's energy density, roughly five times more than the ordinary matter, consists of some non-luminous and non-baryonic form of matter, known as dark matter (DM). Recent data from WMAP [15], PLANCK [16], which probe anisotropies in Cosmic Microwave Background Radiation (CMBR), state that the present Universe contains nearly 27% DM, 68% in the form of an unknown energy, known as Dark Energy. Only the remaining 5% of the total energy content is made up of luminous baryonic matter from which all the known objects such as stars, galaxies, galaxy clusters, etc., are formed. It all started in 1933, when Fritz Zwicky, a Swiss astronomer, wanted to estimate how much matter is there in a galaxy cluster, namely Coma cluster [17, 18], situated at 99 Mpc away from Earth. He used the observed Doppler shifts in the galactic spectra to calculate the velocity dispersion of the galaxies and then employed the virial theorem to calculate the total mass of the Coma cluster. He observed around 1000 nebula in the cluster and found that the average mass of each nebula was $\mathrm{M_{nebula}} = 4.5 \times 10^{10}\,\mathrm{M}_\odot$ with $M_\odot$ being the solar mass. On the other hand, by using the standard M/L ratio for nebula, where M is the total mass of the cluster and L is the luminosity, the total mass of the cluster was found to be approximately 2% of this value, indicating that the vast majority of the mass of the Coma cluster was either missing or non-luminous. Zwicky named this non-luminous matter as 'Dark Matter (or dunkel materie)'.

The idea of DM was largely ignored until the 1970s when American astronomer Vera Rubin and her collaborators had found the similar behavior in their study [1] of the velocity of stars moving around the center of a galaxy. Several groundbreaking studies of the flat rotation curves of galaxies came up in the early 1980s [19,20] with similar conclusions. In this first chapter of the thesis, we will discuss some basic aspects of DM and its phenomenological consequences. This chapter is organized as follows. In section 1.1, we have discussed some astounding evidences that point to a large abundance of this unknown form of matter in our Universe. In section 1.2, we have discussed about the possibilities of thermal and non-thermal DM candidates and their experimental prospects as well as current status. In the last section of this chapter 1.3, we briefly discuss about the evidences suggesting the existence of small neutrino mass and mixing, another observed phenomena which the SM fails to address.

1.1 Evidences of dark matter

1.1.1 Dark matter in galaxies and clusters

The most robust and well-known evidence for the presence of DM in the galaxy comes from the observations of the rotation curves of spiral galaxies [21–23]. A spiral galaxy consists of a flat rotating disk that contains stars, intergalactic gas, and dust, and the star's motion is controlled by gravitational interactions. There is a central bulge in the galaxy where most of its mass is concentrated while the spiral arms are spread out, forming an overall disk-like shape for such galaxies. By using the standard Newtonian gravity, we can write the circular velocity v_c of a star as,

$$v_c(r) = \sqrt{\frac{GM(r)}{r}}, \tag{1.1}$$

where G is the gravitational constant, and $M(r)$ is the mass enclosed inside a galactic disk of radius r. Using Gauss' law in equation (1.1), one can conclude that the circular velocity should increase up to some radius $r_{\max}$ (typically a few kpc) which contains most of the luminous matter and then should fall as $1/\sqrt{r}$. However, the observations indicate that after rising from $r = 0$ to $r_{\max}$ the circular velocity remains flat, implying that $M(r) \propto r$. This suggests that in addition to the observed luminous disc and central bulge, there exists an additional "dark" component of matter whose mass increases linearly with the distance from the galactic centre. Figure 1.1 illustrates the 21 Sc rotation curves of spiral galaxies observed by Rubin *et al* [1], which show that the circular velocity becomes almost constant at large radial distance from the center of the galaxy. Since then, there have been many studies and evidences supporting these conclusions [19–23].

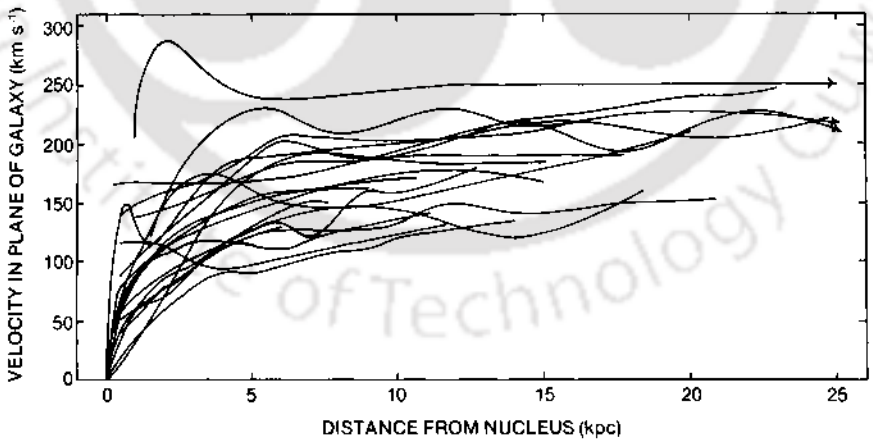

Figure 1.1: Rotation curves of spiral galaxies as observed by Rubin *et al* [1].

Similarly, there have also been evidences of the existence of DM on the scales of galaxy clusters. According to general relativity, the gravitational field of a massive object can bend the path of light travelling around it. The mass of this object, which acts as a lens, can be ascertained by this bending effect. This method, known as gravitational lensing, completely

relies on the gravitational interaction and includes both luminous as well as non-luminous matter. If one is fortunate enough, she can observe multiple images, arcs, or even rings, known as Einstein ring, through lensing (also referred to as strong gravitational lensing). Unfortunately, in many cases the lensing is not so strong. In such cases, instead of producing the multiple images and arcs associated with strong lensing, one can still manage to get a weakly distorted image of the source, appearing more elliptical in shape. By observing a large ensemble of such sources, this 'shape noise' can be averaged out, so that we can obtain the information of the intermediate matter distribution. By using this method, known as weak lensing, people have spectacularly mapped the mass distribution of the two colliding clusters, "Bullet Cluster (1E0657-558)" [24, 25]. In fact, it is one of the most convincing pieces of evidence supporting the existence of DM. It was an cosmic event, around 4 billion light years from our solar system, where two giant galaxy clusters collided with each other. After the collision, the distribution of the hot gas, which makes up most of the luminous matter in the clusters, has been mapped by the Chandra X-ray observatory. It is shown in figure 1.2 which reveals that the baryonic matter or the hot gas (the yellow and red patches), has been held up in the middle due to electromagnetic interactions while the DM (blue patch) has passed straight through. So, it not only provides an observational evidence for the existence of DM but also dictates that DM interacts very weakly with baryonic matter, suggesting its collisionless nature. Observations of clusters like MACS J0025.4-1222 [26], Abel cluster [27] have also reported similar results.

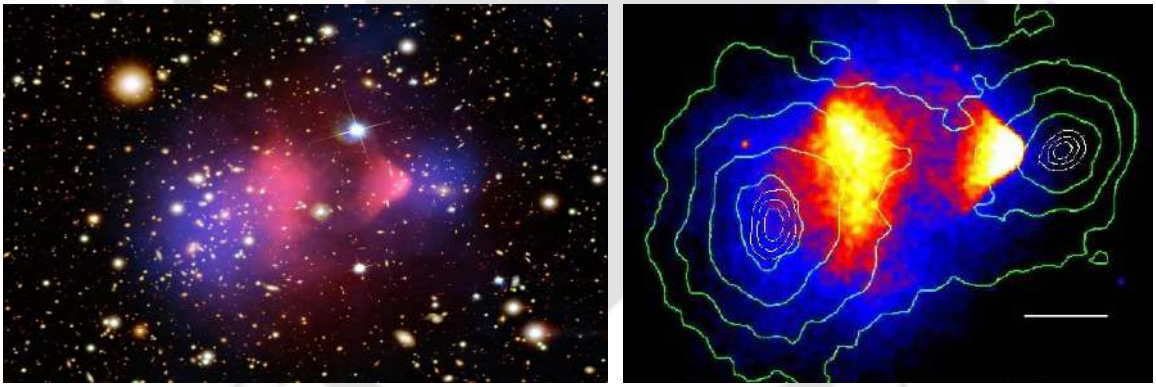

Figure 1.2: Representation of the collision of two galaxy clusters. Red region are showing the electromagnetic interaction within the visible sector matter by the Chandra X-ray observatory. The Blue region is the region where most of the DM is present after the collision mapped by the gravitational lensing. Figure has been taken from [2].

1.1.2 Dark matter in the Milky Way: The standard halo model

Perhaps the most appropriate place to look for DM in the Universe is our own galaxy, the Milky Way. Scientists are searching for DM through direct detection and indirect detection experiments, as discussed later in this chapter. These experiments depend on two crucial parameters: the local DM velocity distribution and density profile. Therefore it is imperative to know how DM is distributed in the galaxy. The 'Standard Halo Model (SHM)' [28, 29],

the simplest model describing the DM distribution, assumes that the DM is distributed spherically, isotropically and smoothly.

In this model, the DM density ρ and the velocity distribution f can be written as

$$\rho(x) = \int d^3v\, \mathcal{F}(x,v),\;\; f(v) = \int d^3x\, \mathcal{F}(x,v), \tag{1.2}$$

where $\mathcal{F}(x,v)$ is the distribution function, defined in such a way that $\mathcal{F}d^3xd^3v/M_H$ is the probability of having a DM particle with velocity v and position x in the given range. It is assumed that the halo has already achieved a steady state, so it no longer depends on time. M_H is the total mass of the DM halo used to normalize $\mathcal{F}$ as following,

$$\int d^3xd^3v\mathcal{F}(x,v) = M_H. \tag{1.3}$$

In SHM, the distribution function $\mathcal{F}$ is given as,

$$\mathcal{F}_{\rm SHM}(x,v) = \frac{\rho_0}{(2\pi\sigma^2)^{3/2}}\exp\left(\frac{\psi - \frac{1}{2}v^2}{\sigma^2}\right), \tag{1.4}$$

where σ and ρ_0 are constants and ψ is the relative potential defined by the sum of the gravitational potential $(-\Phi)$ and an appropriately chosen constant Φ_0, i.e $\psi \equiv -\Phi + \Phi_0$. Poisson's equation related to ψ can be written as

$$\nabla^2\psi = -4\pi G\rho. \tag{1.5}$$

The above assumption of DM being distributed spherically, isotropically and smoothly, implies that ψ depends only on r. Substituting equation (1.4) in equation (1.2) and integrating over all velocities, the Poisson's equation can be written as following

$$\frac{d}{dr}\left(r^2\frac{d\ln\rho}{dr}\right) = -\frac{4\,\pi\,G}{\sigma^2}r^2\rho. \tag{1.6}$$

Solving this, one will get

$$\rho(r) = \frac{\sigma^2}{2\,\pi\,G\,r^2}. \tag{1.7}$$

Similarly for velocity distribution, we will get

$$f(v) \propto \exp\left(\frac{-v^2}{2\sigma^2}\right), \tag{1.8}$$

which is very well-known Maxwell-Boltzmann distribution, with a velocity dispersion $\overline{v^2} = 3\sigma^2$. Interestingly, if we start from the equation of hydrostatic equilibrium for an isothermal gas we will get an equation similar to equation (1.6)

$$\frac{dp}{dr} = \frac{k_BT}{m}\frac{d\rho}{dr} = -\rho\frac{d\Phi}{dr} = -\rho\frac{GM(r)}{r^2}, \tag{1.9}$$

where p and T are the pressure and temperature of the gas, k_B is the Boltzmann constant, m is the particle mass and $M(r)$ is the galaxy mass interior to radius r. Multiplying both

side by $r^2 m/(\rho k_B T)$ and then differentiating with respect to r, we get an equation similar to (1.6) which further implies

$$\sigma^2 \equiv \frac{k_B T}{m}. \tag{1.10}$$

Thus the velocity and density distributions of the SHM are analogous to an isothermal self-gravitating sphere of gas. The circular velocity v_0 and galactic mass interior to radius r are obtained to be

$$v_0(r) = \sqrt{2}\sigma, \;\; M(r) = \frac{2\sigma^2 r}{G}. \tag{1.11}$$

Hence, the SHM predicts that circular velocity is independent of radius r, which agrees pretty well with the observations of a flat rotational curve discussed in the previous section. Though this simple model can explain the flatness of the circular speed, it has many limitations. The halo's infinite size and the divergence of mass, as $r \to \infty$, are among the most severe problems of this model, which directly contradicts the real galaxies, which are finite in size and mass. N-body simulations of DM [30–32] have shown that the density profile of a typical halo departs from the above assumptions. Simulations have also shown the DM velocity distribution to be significantly different from the Maxwell-Boltzmann distribution [33–36].

Halo Profile	α	β	γ	δ	r_s (kpc)	ρ_s (GeV/cm^3)
NFW [37, 38]	1	3	1	0	20.0	0.259
Isothermal [39]	2	2	0	0	3.5	2.069
Moore [40]	1	3	1.16	0	30.28	0.108
Kravtsov [41]	2	3	0.4	0	10.0	0.570
Burkert [42]	2	3	1	1	12.67	0.727
Einasto [43, 44]	0.17	–	–	–	20.0	0.061

Table 1.1: List of relevant parameters and their numerical values for different DM halo profiles.

So far, no unique profile for DM density exists in the literature to explain the above-mentioned properties. There exist different parametrizations for the halo density profile of DM, and the one which has been used by many groups is given by

$$\rho(r) = \frac{\rho_s}{\left(\delta + \left(\frac{r}{r_s}\right)^{\gamma}\right)\left(1 + \left(\frac{r}{r_s}\right)^{\alpha}\right)^{\frac{\beta-\gamma}{\alpha}}}, \tag{1.12}$$

where ρ_s is the normalization factor, r_s is the scale radius and, α, β, γ, δ are arbitrary constants. The values of the parameters for different density profiles have been given in table 1.1. The normalization factor ρ_s is obtained by claiming that at the distance of the solar location from galactic center ($\mathrm{r} = \mathrm{r}_\odot = 8.5\,\mathrm{kpc}$) the DM density is $\rho(\mathrm{r}) = \rho_\odot = 0.3\,\mathrm{GeV/cm^3}$. Another commonly used DM density profile is, the Einasto profile, given by

$$\rho(r)_{\text{Einasto}} = \rho_s \exp\left[-\frac{2}{\alpha}\left\{\left(\frac{r}{r_s}\right)^{\alpha} - 1\right\}\right]. \tag{1.13}$$

The variation of different DM halo density profiles has been shown in figure 1.3 with respect to the radial distance r from the galactic centre. One interesting point to note here is that the profiles like Moore, NFW, Einasto, and Kravtsov indicate that DM density increases towards the galaxy's inner parts (known as the "cuspy" nature) and the cosmological N body simulations support this predictions. On the other hand, profiles like Isothermal and Burkert, show more or less constant DM density around the galactic centre, known as "core" like structures. The astrophysical observations such as rotation curves of galaxies and others seem to indicate similar nature. So there is contradiction between these two different density profiles known as the "core/cusp problem" (see [45] for review).

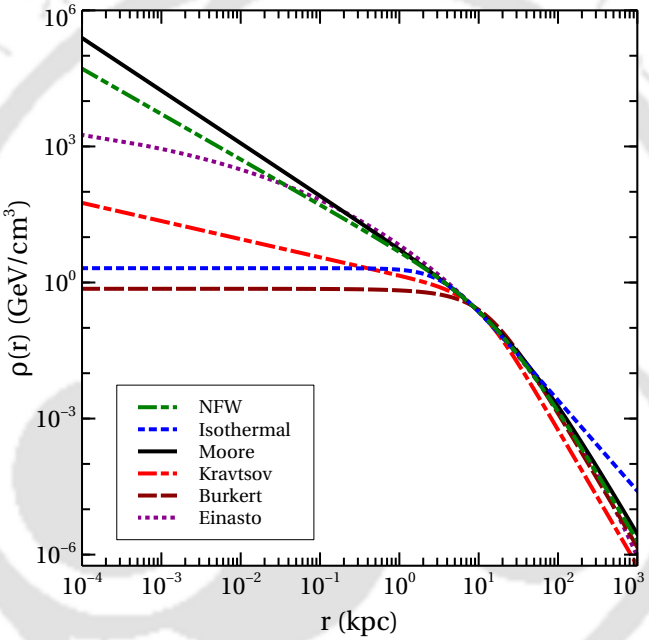

Figure 1.3: Variation of the energy densities of different halo profiles with the radial distance r (in kpc)from the centre of our Milky way galaxy.

1.1.3 Dark matter and ΛCDM cosmology

Standard cosmological model, also known as the ΛCDM model, is the most successful cosmological model so far and this model consists of six independent parameters namely, baryon density ($\Omega_b h^2$), the DM density ($\Omega_{\text{DM}} h^2$), scalar spectral index (n_s), age of the Universe (t_0), curvature fluctuation amplitude (Δ_r^2), and reionization optical depth (τ). All the other parameters of interest can be derived from these. Most importantly, the measurements of the anisotropies of CMB [16] are in great agreement with the ΛCDM model. Assuming the spatial isotropy and homogeneity, the Universe can be well described by the Friedmann-Lemaitre-Robertson-Walker (FLRW) metric:

$$ds^2 = dt^2 - a^2(t)\left(\frac{dr^2}{1-k\,r^2} + r^2\left(d\theta^2 + sin^2\theta\; d\phi^2\right)\right), \tag{1.14}$$

where, $r\,,\theta\,,\phi\,,t$ are comoving coordinates, $a(t)$ is the cosmic scale factor. The parameter k, which determines the spatial curvature, can take values +1, -1, 0 corresponding to positive, negative and flat Universe respectively. The dynamical equations of motion, famously known as the Friedmann equations, can be derived by using the metric given in equation (1.14) in Einstein's equation,

$$\mathcal{R}_{\mu\nu} - \frac{1}{2}\mathcal{R}g_{\mu\nu} = 8\pi\,G\,T_{\mu\nu} + \Lambda\,g_{\mu\nu}, \tag{1.15}$$

where $\mathcal{R}_{\mu\nu}$ and $\mathcal{R}$ are the Ricci tensor and the Ricci scalar respectively, $T_{\mu\nu}$ is the energy-momentum tensor, and Λ is the cosmological constant. Considering the Universe to be composed of a perfect fluid, the energy-momentum tensor can be written as

$$T_{\mu\nu} = -p\,g_{\mu\nu} + (p+\rho)\,u_\mu u_\nu, \tag{1.16}$$

where, ρ and p are the energy density and the pressure of the perfect fluid respectively while u_μ is the velocity vector in the comoving coordinates. The equation of state which relates the pressure and the energy density is written as $p = \omega\rho$. ω takes different values for radiation, matter and vacuum energy. The dynamics of the scale factor can be related to the energy density and the pressure by the Friedmann equations as

$$H^2 \equiv \frac{\dot{a}^2}{a^2} = \frac{8\pi\,G\,\rho}{3} - \frac{k}{a^2} + \frac{\Lambda}{3}, \tag{1.17}$$

$$\frac{\ddot{a}}{a} = \frac{\Lambda}{3} - \frac{4\pi\,G}{3}\left(\rho + 3p\right), \tag{1.18}$$

where H is known as the Hubble expansion rate and one can derive a very important equation from the above two equations,

$$\dot{\rho} = -3H\left(\rho + p\right), \tag{1.19}$$

which dictates the evolution of energy density in the Universe. Let us now define the energy densities of radiation, matter and dark energy as $\Omega_{\rm rad} = \rho_{\rm rad}/\rho_c$, $\Omega_m = \rho_m/\rho_c$, and $\Omega_\Lambda = \Lambda/\rho_c$, where ρ_c is known as the critical density defined as $\rho_c \equiv \frac{3H^2}{8\pi\,G}$. Using the above parameters, the equation (1.17) can be rewritten as,

$$\frac{k}{a^2} = H^2\left(\Omega_{\rm rad} + \Omega_m + \Omega_\Lambda - 1\right). \tag{1.20}$$

Observations made by the Planck satellite have led to the precise measurements of different parameters defined above while being in excellent agreement with similar estimates obtained from large scale structure (LSS) and big bang nucleosynthesis (BBN) measurements. From Planck measurements, it was revealed that the present abundance of baryon and DM can be quantified as $\Omega_b \sim 0.0486$, $\Omega_{\rm DM} \sim 0.2589$ [16] respectively. Figure 1.4 shows an incredible agreement between the measurements from LSS, supernova, BBN, and CMB observations.

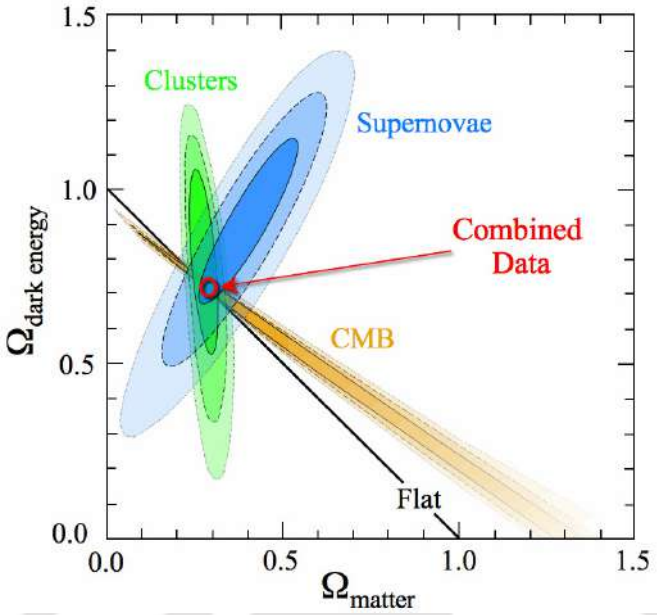

Figure 1.4: This figure shows an incredible agreement between the measurements from LSS, supernova, BBN, and CMB. It also suggests that our Universe is almost flat. Figure has been taken from [3].

1.2 Dark matter candidates

Based on numerous evidences discussed above, the existence of the non-luminous matter in the Universe has become a well-established fact now. However, the particle nature of DM is still an open question. While it is challenging to settle this question, it is relatively easier to rule out certain types of particles from being DM candidates. This is because any particle DM candidate must satisfy certain criteria. Firstly, DM must be stable on cosmological time scales to be present with sizeable abundance today. At the same time, DM has to be electrically neutral as it does not have any electromagnetic interactions. Secondly, data from different cosmological observations like BBN and CMB reveal its non-baryonic nature. In fact, the observation of the Bullet Cluster indicate that DM must be very weakly interacting, and if has any interactions at all apart from gravity, it must be weaker compared to that of baryonic matter. Lastly, N-body simulations show that DM must be cold to explain the structures we see in the Universe today. None of the SM particles can satisfy all the above-mentioned properties of DM. Neutrino would have come closest to satisfying these criteria as it is electrically neutral, stable, and very weakly interacting. However, the last criteria rules out that possibility as being relativistic, neutrino will have a very large free-streaming length significantly limiting the LSS formation. Additionally, neutrinos can give rise to only a tiny fraction of total DM abundance in the present Universe.

The scarcity of an appropriate candidate for DM within the SM is one of the most important reason to look for the physics beyond SM. In this section, we will discuss about such popular BSM frameworks for realizing particle DM and their phenomenological conse-

quences.

1.2.1 Thermal dark matter

Perhaps the most widely studied particle DM candidate in literature is the Weakly Interacting Massive Particles or WIMPs, which can be defined as a new elementary particle whose interaction strength is as weak as or weaker than the electroweak force. Such weak interaction strength of WIMPs with the SM particles is, however, sufficient to ensure its thermal production in the early Universe. The typical mass range for WIMPs can vary from a few GeV to a few TeV, and being massive, it would become non-relativistic at very early epochs thereby satisfying the requirement of being cold. In this thesis, WIMPs are the one which will be mostly discussed. One crucial aspect of WIMPs is that they can be thermally produced in the early Universe through their interaction with the bath particles. Their relic abundance can be found from the very well known "freeze-out" mechanism [46–48]. Let us consider a particle χ with mass m_χ to be in chemical and thermal equilibrium with the other particles present in the thermal bath in the early Universe. The necessary condition for this is that the production rate of χ from the thermal bath have to be equal to the annihilation rate Γ, which keeps the particle in chemical equilibrium. This equilibrium will be maintained until the expansion rate (H) of the Universe becomes greater than Γ. In the non-relativistic limit ($i.e. m_\chi >> T$), the equilibrium number density of χ can be written a as

$$n_\chi^{\rm eq} = g_\chi \left(\frac{m_\chi T}{2\,\pi}\right)^{3/2} \exp(-m_\chi/T), \tag{1.21}$$

where T is the temperature of the thermal bath and g_χ is the number of internal degrees freedom of χ. We have assumed that there is no asymmetry between the particle and anti-particle of DM and hence set the chemical potential to be zero when they are in equilibrium. From the above equation, it is clear that for low temperatures, the number density will be extremely small due to the exponential suppression. However, the particle will not follow the equilibrium distribution forever. It will decouple from the thermal bath if Γ falls below the expansion rate H, which is known as the "freeze-out" from the thermal bath. To follow the dynamics of the thermal freeze-out and know the relic abundance of χ we have to solve the Boltzmann equation, which can be written as

$$L\left[f_\chi\left(p_\chi^\mu, x^\mu\right)\right] = C\left[f_\chi\left(p_\chi^\mu, x^\mu\right)\right], \tag{1.22}$$

where f_χ is phase space distribution function of χ with four momentum p^μ at any space-time point x^μ. $L\left[f_\chi\left(p_\chi^\mu, x^\mu\right)\right]$ is the Liouville operator, which determines the net rate of change in time of the particle phase space distribution function f_χ, and collision operator $C\left[f_\chi\left(p_\chi^\mu, x^\mu\right)\right]$ represents the number of particles per phase space volume per unit time which are being lost or gained due to collision with other particles. In a spatially homogeneous and isotropic Universe, as described by the FLRW cosmological model, the phase space distribution function f_χ depends only on its energy E_χ and t. Therefore, the Liouville operator can be written as

$$L\left[f_\chi\left(E_\chi,\, t\right)\right] = E_\chi \frac{\partial f_\chi}{\partial t} - H\,|\overrightarrow{p}_\chi|^2\,\frac{\partial f_\chi}{\partial E_\chi}. \tag{1.23}$$

From the phase space distribution function f_χ, we can also find out the number densities of the species χ as

$$n_\chi = \frac{g_\chi}{(2\pi)^3}\int f_\chi\left(E_\chi,\, t\right) d^3p_\chi. \tag{1.24}$$

The evolution of the number density can be followed by using the Liouville operator defined in equation (1.23) as

$$\begin{aligned}\frac{g_\chi}{2\pi^3}\int \frac{L\left[f_\chi\left(E_\chi,t\right)\right]}{E_\chi} d^3p_\chi &= \frac{\partial}{\partial t}\left(\frac{g_\chi}{2\pi^3}\int f_\chi\left(E_\chi, x^\mu\right) d^3p_\chi\right) \\ &\quad -\frac{g_\chi}{2\pi^3}4\pi H\int \frac{|\overrightarrow{p_\chi}|^4}{E_\chi}\frac{\partial f_\chi}{\partial E_\chi} dp_\chi.\end{aligned} \tag{1.25}$$

Using the definition of number density given in equation (1.24), one can simplify the above equation as

$$\begin{aligned}\frac{g_\chi}{2\pi^3}\int \frac{L\left[f_\chi\left(E_\chi,t\right)\right]}{E_\chi} d^3p_\chi &= \frac{\partial n_\chi}{\partial t} - \frac{g_\chi}{2\pi^3}4\pi H\int |\overrightarrow{p_\chi}|^3\frac{\partial f_\chi}{E_\chi} dE_\chi \\ &= \frac{\partial n_\chi}{\partial t} - \frac{g_\chi}{2\pi^3}4\pi H\left[\left(|\overrightarrow{p_\chi}|^3\right)_0^\infty - 3\int |\overrightarrow{p_\chi}|^2\frac{\partial\,|\overrightarrow{p_\chi}|}{\partial E_\chi} f_\chi dE_\chi\right] \\ &= \frac{\partial n_\chi}{\partial t} + \frac{g_\chi}{2\pi^3}4\pi H\int 3\,|\overrightarrow{p_\chi}|^2\frac{E_\chi}{|\overrightarrow{p_\chi}|} f_\chi dE_\chi \\ &= \frac{\partial n_\chi}{\partial t} + 3\,H\,\frac{g_\chi}{2\pi^3}\int f_\chi d^3p_\chi \\ &= \frac{\partial n_\chi}{\partial t} + 3\,H\,n_\chi.\end{aligned} \tag{1.26}$$

The first term on the right hand side (RHS) in the above equation is the time evolution of the number density whereas the second term is the dilution factor due to the expansion of the Universe. Therefore, the Boltzmann equation, defined in equation (1.22) can be rewritten as

$$\frac{\partial n_\chi}{\partial t} + 3\,H\,n_\chi = \frac{g_\chi}{2\pi^3}\int \frac{C\left[f_\chi\left(E_\chi,t\right)\right]}{E_\chi} d^3p_\chi. \tag{1.27}$$

Now, let us try to simplify the RHS of the above equation for the collision process $\chi + a \to y + z$. The collision term for this process can be written as,

$$\begin{aligned}\frac{g_\chi}{2\pi^3}\int \frac{C\left[f_\chi\left(E_\chi,t\right)\right]}{E_\chi} d^3p_\chi &= -\sum_{\text{spin}}\int d\Pi_\chi d\Pi_a d\Pi_y d\Pi_z\,(2\pi)^4\,\delta^4\left(p_\chi + p_a - p_y - p_z\right)\times \\ &\quad \Big[\,|M|^2_{\chi+a\to y+z}\, f_\chi f_a(1\pm f_y)(1\pm f_z) - \\ &\quad |M|^2_{y+z\to\chi+a}\, f_y f_z(1\pm f_\chi)(1\pm f_a)\Big],\end{aligned} \tag{1.28}$$

where, f_i is the phase space distribution function of the individual species (χ, a, y, z) and

$$d\Pi_i = g_i \frac{d^3 p_i}{2E_i \left(2\pi\right)^3}. \tag{1.29}$$

The energy momentum conservation is ensured by the four dimensional Dirac delta function and the $|M|^2$ is the matrix element squared of the process $\chi + a \to y + z$. The first term inside the square bracket represents the loss of the number of χ whereas the second term shows the gain of the same species. The phenomena of Bose enhancement and Pauli blocking are also coming into the picture through the $(1 \pm f_i)$ term where the plus is for bosons and the minus is for fermions. For further simplification, we have used the following well motivated assumptions.

- Firstly, we have assumed that the final state particles y and z are in thermal equilibrium with the other particles present in the cosmic plasma and follows the Maxwell-Boltzmann (MB) distribution. So,

$$f_y\, f_z = e^{-\frac{E_y}{T}} \times e^{-\frac{E_z}{T}} = e^{-\frac{E_y + E_z}{T}} = e^{-\frac{E_\chi + E_a}{T}} = f_\chi^{\rm eq}\, f_a^{\rm eq}. \tag{1.30}$$

- Secondly, by using the T (or CP) invariance in the above-mentioned collision process, we can write the following condition

$$|M|^2_{y+z\to\chi+a} = |M|^2_{\chi+a\to y+z} \equiv |M|^2 .$$

- Another important assumption is that, for all species, we use Maxwell-Boltzmann statistics instead of Fermi-Dirac or Bose-Einstein statistics. This is a valid assumption, as the systems we are interested in, have temperature smaller than $E - \mu$ where E is the energy and μ is the chemical potential of the species. Under this assumption, $(1 \pm f_i)$ factors can be ignored, as $(1 \pm f_i) \approx 1$.

Hence the equation (1.28), under all the above-mentioned assumptions, can be written as

$$\begin{aligned} \frac{g_\chi}{2\pi^3} \int \frac{C\left[f_\chi\left(E_\chi, t\right)\right]}{E_\chi} d^3 p_\chi \;=\; & -\sum_{\rm spin} \int d\Pi_\chi d\Pi_a d\Pi_y d\Pi_z \left(2\pi\right)^4 \delta^4\left(p_\chi + p_a - p_y - p_z\right) \\ & \times |M|^2 \left[f_\chi f_a - f_\chi^{\rm eq} f_a^{\rm eq}\right]. \end{aligned} \tag{1.31}$$

Another important quantity is the annihilation cross-section which, by definition, can be written as

$$\sigma_{\chi+a\to y+z} = \frac{1}{4E_\chi E_a g_\chi g_a\, v} \sum_{spin} \int d\Pi_y d\Pi_z (2\pi)^4 \delta^4\left(p_\chi + p_a - p_y - p_z\right) |M|^2_{\chi+a\to y+z}\,, \tag{1.32}$$

where, the energies of the initial particles χ and a are E_χ and E_a respectively and g_χ, g_a are their respective internal degrees of freedoms. The relative velocity between the initial particles, defined as v, is expressed by

$$v = \frac{\sqrt{(\vec{p_\chi} \cdot \vec{p_a})^2 - m_\chi^2 m_a^2}}{E_\chi E_a}, \tag{1.33}$$

and finally, the collision term given in equation (1.31) can be expressed as

$$\begin{aligned} \frac{g_\chi}{2\pi^3} \int \frac{C\left[f_\chi\left(E_\chi, t\right)\right]}{E_\chi} d^3 p_\chi &= -\int \sigma_{\chi+a\to y+z} v \left(dn_\chi dn_a - dn_\chi^{\rm eq} dn_a^{\rm eq}\right) \\ &= -\left\langle \sigma_{\chi+a\to y+z} v \right\rangle \left(n_\chi n_a - n_\chi^{\rm eq} n_a^{\rm eq}\right), \end{aligned} \tag{1.34}$$

where $\langle \sigma_{\chi+a\to y+z} v \rangle$ is known as the thermally averaged annihilation cross-section and defined as

$$\left\langle \sigma_{\chi+a\to y+z} v \right\rangle = \frac{\int \sigma_{\chi+a\to y+z}\, v\, dn_\chi^{\rm eq}\, dn_a^{\rm eq}}{\int dn_\chi^{\rm eq}\, dn_a^{\rm eq}}. \tag{1.35}$$

For two identical particle initial state (a is same as χ), which is the most common scenario in the literature, the thermally averaged cross-section, defined is equation (1.35), can be derived as [49]

$$\left\langle \sigma_{\chi+a\to y+z} v \right\rangle = \frac{1}{8 m_\chi^4 T K_2^2\left(m_\chi/T\right)} \int_{4m\chi^2}^{\infty} \sigma_{\chi+a\to y+z} \sqrt{s} \left(s - 4m_\chi^2\right) K_1\left(\sqrt{s}/T\right) ds, \tag{1.36}$$

where, K_i is the modified Bessel functions of order i and s is the square of the center of mass energy of the system. One important point to note here is that to derive the expression given in equation (1.36) one has to take a crucial assumption that the particle χ was present in the thermal bath at some point of time and can be described by a Maxwell-Boltzmann phase space distribution function. If in addition to the process $\chi + a \to y + z$, other annihilation processes also exist, then their contribution also have to added together and the $\sigma_{\chi+a\to y+z}$ would be replaced by $\sigma_{\rm eff}$. So the final form of the Boltzmann equation can be written as

$$\frac{\partial n_\chi}{\partial t} + 3H\, n_\chi = -\left\langle \sigma_{\rm eff} v \right\rangle \left(n_\chi^2 - \left(n_\chi^{\rm eq}\right)^2\right). \tag{1.37}$$

Let us now define a very useful dimensionless quantity, namely the comoving number density, $Y = \frac{n}{s}$ defined as the ratio of number density n of a species to the entropy density s of the Universe. By using the fact that the total entropy of the Universe per comoving volume (sa^3) is conserved, the Boltzmann equation can be rewritten as

$$\begin{aligned} \frac{\partial n_\chi}{\partial t} + 3H\, n_\chi = s\dot{Y}_\chi &= -\left\langle \sigma v \right\rangle \left(n_\chi^2 - \left(n_\chi^{eq}\right)^2\right), \\ \frac{dY_\chi}{dt} &= -s\left\langle \sigma v \right\rangle \left(Y_\chi^2 - \left(Y_\chi^{eq}\right)^2\right). \end{aligned}$$

The entropy density can be written as

$$s = \frac{2\pi^2}{45} g_{*s} T^3, \tag{1.38}$$

where g_{*s} is the total relativistic degrees of freedom contributing to the entropy density of the Universe at temperature T and can be defined as

$$g_{*s} = \sum_{i=\text{bosons}} g_i \frac{T_i^3}{T^3} + \frac{7}{8} \sum_{i=\text{fermion}} g_i \frac{T_i^3}{T^3}. \tag{1.39}$$

Here g_i and T_i are the internal degrees of freedom and the temperature of the species i respectively. By using the Friedmann's equations discussed earlier, the Hubble parameter can be written as

$$H\left(T\right) = \sqrt{\frac{8\pi\, G}{3} \rho\left(T\right)}, \tag{1.40}$$

where $\rho(T)$ is the total energy density of the Universe at a certain epoch when the temperature of the thermal plasma is T. For an usual WIMP, it decouples from the thermal bath in the radiation dominated era and the the radiation energy density can be written as

$$\rho_{\text{rad}} = g_* \frac{\pi^2}{30} T^4, \tag{1.41}$$

where g_* is the the total relativistic degrees of freedom contributing to the radiation energy density at temperature T and can be defined as

$$g_* = \sum_{i=\text{bosons}} g_i \frac{T_i^4}{T^4} + \frac{7}{8} \sum_{i=\text{fermion}} g_i \frac{T_i^4}{T^4}. \tag{1.42}$$

Hence, in the radiation dominated Universe, H(T) $\approx \frac{T^2}{M_{\text{Pl}}}$ where M_{Pl} is the reduced Planck mass defined as $M_{\text{pl}} = 1/\sqrt{8\pi\, G}$. Let us now define another dimensionless parameter $x = m_\chi/T$ where T is temperature of the thermal bath and m_χ is the mass of the species χ and then the time variable t can be related to the x as

$$t = 0.301 \frac{1}{\sqrt{g_*}} \frac{M_{\text{Pl}}}{m_\chi^2} x^2. \tag{1.43}$$

By using all these re-definitions of the variables, the Hubble parameter now can be written as

$$H(x) = \frac{H(m_\chi)}{x^2}, \tag{1.44}$$

where $H(m_\chi) = 1.67\sqrt{g_*}\frac{m_\chi^2}{M_{\text{Pl}}}$. Figure 1.5 shows the evolution of g_* and g_{*s} for the SM with the temperature of the bath. Hence, we can now write a convenient form of the Boltzmann equation in terms of the comoving number density Y_χ as

$$\frac{dY_\chi}{dx} = -\frac{x \left\langle \sigma_{\text{eff}} v \right\rangle s}{H\left(m_\chi\right)} \left(Y_\chi^2 - \left(Y_\chi^{\text{eq}}\right)^2\right). \tag{1.45}$$

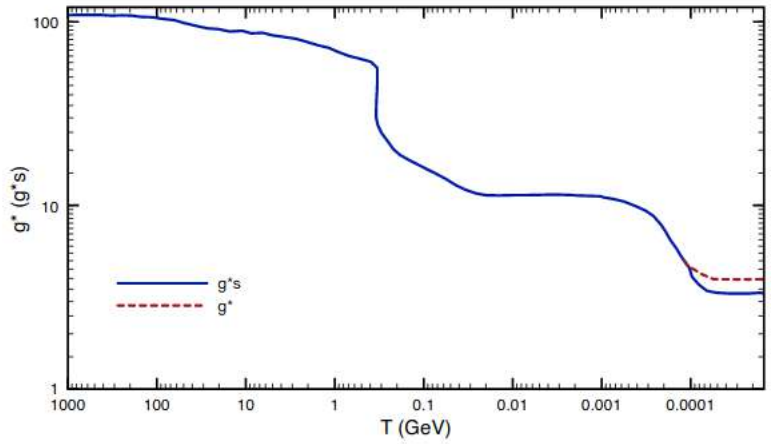

Figure 1.5: Variation of the relativistic degrees of freedom as a function the bath temperature T. A small difference is noted between g_* and g_{*s} due to neutrino decoupling and annihilation of the electron positron to photon. Figure has been taken from [4].

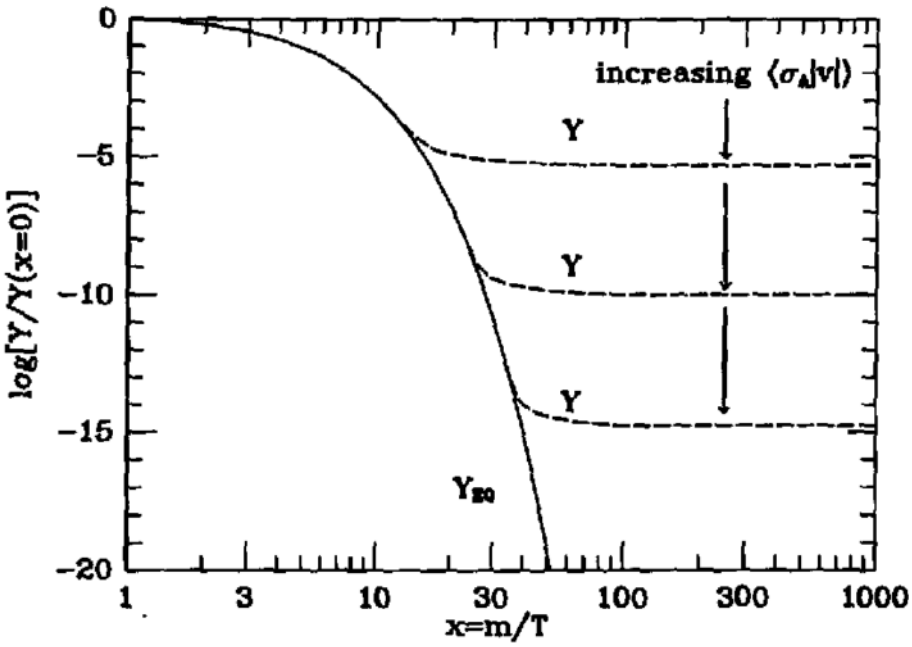

Figure 1.6: Variation of the comoving number density (Y_χ) of χ as a function of $x = m_\chi/T$ from three different values of the thermally averaged cross-section $\langle\sigma v\rangle$. The solid line represents the equilibrium comoving number density. Figure has been taken from [5].

We solve equation (1.45) to find the final comoving number density of the species χ after they decouple from the thermal bath. For example, figure 1.6 shows the variation of the comoving number density as a function of x. One important point to note here is that increasing the interaction cross-section ensures the late decoupling of the species. As a result

the final abundance will also decrease accordingly. Finally, knowing the value of the present comoving number density of the species χ, it is easy to calculate to the relic abundance as

$$\Omega_\chi h^2 \left(x = \infty\right) = 2.755 \times 10^8 \left(\frac{m_\chi}{\text{GeV}}\right) Y_\chi \left(x = \infty\right), \tag{1.46}$$

where h = (Hubble Parameter/(100 Km s^{-1} Mpc^{-1})). The latest data from the Planck mission suggest that the present dark matter abundance is quantified as [50]

$$\Omega_{\text{DM}} h^2 = 0.120 \pm 0.001$$

.

Direct searches for dark matter

After discussing the historical introduction and the formalism for calculating the relic density of thermal DM, we now discuss the general features of the direct detection of DM. Detecting a new fundamental particle whose interactions and exact mass are completely unknown is not an easy task. However, motivated from the success of thermal DM or "WIMP" paradigm in generating correct relic abundance sizeable interactions of DM, several attempts have been made in this direction. If we are surrounded by the DM particles and they interact weakly, as suggested by the WIMP paradigm, one can expect a collision with the nucleons kept in laboratories. The measurement of recoil energy of the nucleon due to such collisions will have the potential to reveal the properties of DM particles. This idea was first proposed by Goodman and Witten in 1985 [51]. Depending on the type of interaction we can define two types of DM-nucleon scattering cross-section ($\sigma_{\chi n}$). DM can interact coherently with nucleus of mass number A and in that case the total cross-section will vary as

$$\sigma_{\chi N} \approx \sigma_{\chi n} A^2.$$

This is known as the spin-independent direct detection cross section. On the other hand, if DM couples to the nucleon spin and as spins add incoherently inside nuclei, the DM-nucleus cross section behaves as

$$\sigma_{\chi N} \approx \sigma_{\chi n},$$

which is known as spin-dependent direct detection cross section. However, let us first understand whether detecting a weakly interacting particle like WIMP is at all achievable or not. For that, one has to estimate the recoil rate for DM scattering off nuclei by starting with some simple kinematics. One can estimate the recoil energy of the nucleus after scattering with a DM particle of mass m_χ as

$$E_R = \frac{\mu_{\chi T}^2}{m_T} v_\chi^2 \left(1 - \cos\theta\right), \tag{1.47}$$

where m_T is the mass of the target nucleus, $\mu_{\chi T}$ is the reduced mass of DM-target system, θ is the scattering angle in the center of mass frame, and v_χ is the velocity of DM. As any such rate (R) in particle physics depends on the number of target nuclei (N_T) , the average flux of DM particles (Φ_χ) and the differential cross-section $d\sigma/dE_R$, we can write

$$\frac{dR}{dE_R} = N_T \, \phi_\chi \, \frac{d\sigma_{\chi N}}{dE_R}. \tag{1.48}$$

By using equation (1.47) in equation (1.48) and replacing the flux in terms of the velocity distribution function $f(v)$ of DM particles in the DM halo, one can write the more general form as [52]

$$\frac{dR}{dE_R} = N_T \frac{\rho_\chi m_T}{m_\chi \mu_{\chi T}^2} \int_{v_{min}}^{esc} \frac{f(v)}{v} \frac{d\sigma}{d\cos\theta} d^3v. \tag{1.49}$$

At this point, the particle physics model of DM has come into play in terms of the differential scattering cross-section $d\sigma/d\cos\theta$. Let us have a rough estimate of the recoil events by putting some realistic numbers. Consider a DM particle with GeV order mass and a detector whose energy threshold is of the order of keV. We can replace the incoming DM flux by the ratio ρ_χ/m_χ and can estimate event rate per day per kg detector as [52]

$$R = \frac{0.06 \text{ events}}{\text{kg day}} \left(\frac{100}{A}\right) \left(\frac{\sigma}{10^{-38}\,\text{cm}^2}\right) \left(\frac{\rho_\chi}{0.3 \text{ GeV/cm}^3}\right) \left(\frac{v}{200 \text{ km/s}}\right). \tag{1.50}$$

The above numbers looks quite realistic and achievable provided the cross-section σ is of the order of $10^{-38}\,\text{cm}^2$, which is the typical order of scattering cross-section for electroweak interactions. There are dedicated experiments, namely LUX [53], XENON100 [54], XENON1T [6,55], PANDA [56,57] looking for such events triggered by DM-nucleon scattering. However, none of these experiments have observed any positive signal so far and null results from all such experiments have put very stringent upper limits on the DM-nucleon cross-section as a function of its mass as shown in figure 1.7. One can see that the bound is stronger for the spin-independent cross-section compared to the spin-dependent case and the strongest bound comes from XENON1T [6] experiment. However the above-mentioned experiments are not sensitive for low mass WIMPs, i.e below few GeV. Theoretical aspects of low mass DM detection and some recent experimental searches can be found in [58–61] and references therein.

Indirect searches for dark matter

Besides the direct searches of DM discussed above, there is another class of DM searches where DM can be looked for in an indirect manner, known as indirect detection of DM. Without detecting the DM itself, these experiments try to detect the products of DM annihilation or decay in our galaxy, or beyond. While the annihilation is highly suppressed after the thermal freeze-out of DM, it can still happen at observable rates in a region where the DM density is sufficiently high. Depending upon the particle physics model of DM, it can directly annihilate into photons or some other SM particles which can subsequently produce photons as secondary products. We can also look for other final state particles such as protons, anti-protons, electrons, positrons (via satellite borne experiments like PAMELA [62], AMS [63]), neutrinos (via experiments like ICECUBE [64], ANTARES [65]). However, the cleanest signature will be the photon final states as they propagate mostly unperturbed and

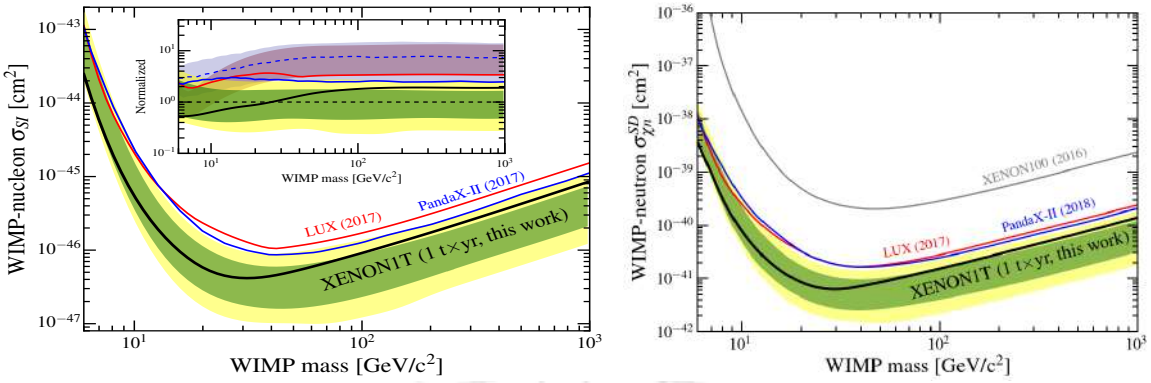

Figure 1.7: Upper limits on WIMP-nucleon scattering cross-section as a function of WIMP mass for spin-independent (left panel) and spin-dependent (right panel) interactions. Figure has been taken from [6, 7].

(optimistically) be detected by some of the ground-based telescopes, like H.E.S.S [66], VARITUS [67], or a satellite based experiment like Fermi-LAT [8, 68]. The most crucial quantity in all such experiments is the photon flux coming from the annihilation or decay of DM. Assuming the presence of multiple annihilation channels for DM, the annihilation rate per particle can be written as

$$\sum_i \frac{\rho\left[r\left(\ell,\psi\right)\right]}{m_\chi} \times \langle \sigma_i v \rangle \,, \tag{1.51}$$

where $\langle \sigma_i v \rangle$ is the velocity averaged cross-section, r is the radial distance between the galactic center and annihilation event. r depends on two parameters namely, the distance of the line-of-sight (l.o.s), ℓ, and the angle, ψ it obtains from the galactic plane. The total annihilation within a given volume dV can be found by multiplying equation (1.51) with the total number of DM particles in the volume as

$$\left(\sum_i \frac{\rho\left[r\left(\ell,\psi\right)\right]}{m_\chi} \times \langle \sigma_i v \rangle\right) \times \left(\frac{\rho\left[r\left(\ell,\psi\right)\right]}{2m_\chi}\, dV\right), \tag{1.52}$$

where dV can be defined as $dV = \ell^2 d\ell d\Omega$, and the extra $1/2$ factor in the above expression arises due to the fact that there are two DM particle involved in every annihilation. The photon flux in the direction ψ can be written as

$$\frac{d\Phi}{dE_\gamma}\left(E_\gamma,\psi\right) = \frac{1}{4\pi}\int_{\Delta\Omega} d\Omega \int_{\text{l.o.s}} d\ell\ \rho\left[r\left(\ell,\psi\right)\right]^2 \sum_i \frac{\langle \sigma_i v \rangle}{2m_\chi^2}\frac{dN_i}{dE_\gamma}. \tag{1.53}$$

One additional $1/2$ factor will come in case if DM is not its own anti-particle. However, the most challenging aspect of indirect detection is to overcome the astrophysical uncertainties which will affect the determination of the photon flux. All such uncertainties can be absorbed in the J-factor [69]

$$J = \frac{1}{\Delta\Omega}\int d\Omega \int_{\text{l.o.s}} d\ell\ \rho\left[r\left(\ell,\psi\right)\right]^2 . \tag{1.54}$$

The astrophysical objects with larger J-factors are more interesting targets to look for DM annihilation. The J-factor for our own galaxy is roughly $J \sim 10^{22-25}\,\text{GeV}^2/\text{cm}^5$ within 0.1°and it is a few order smaller for our neighbouring galaxy, the Adromeda galaxy, $J \sim 10^{20}\,\text{GeV}^2/\text{cm}^5$. However, the most interesting astrophysical objects for indirect detection are the dwarf galaxies with $J \sim 10^{19-20}\,\text{GeV}^2/\text{cm}^5$ as they are mostly DM dominated and contain very less number of stars. Figure 1.8 shows the current limit on DM annihilations into $b\bar{b}$, W^+W^-, $\tau\overline{\tau}$, and $\mu\overline{\mu}$ final states [8]. Let us now briefly mention some of the interesting excess events observed in different experiments which may have emerged from DM.

One of the very promising electromagnetic signal is the 3.55 keV monochromatic X-ray line observed by the several groups [70, 71] from the Perseus cluster and also supported by similar kind of observations from many different galaxies including Andromeda [72–78]. In 2003, another anomalous signal of an emmision line at an energy of 511 keV was observed from the galactic bulge by the spectrometer SPI on the INTEGRAL gamma-ray observatory [79–81]. The presence of this signal was also confirmed, in 2015, by the detection of the the 511 keV line with the measured flux $\Phi_{511}^{\text{exp}} = (0.96 \pm 0.07) \times 10^{-3}\,\text{ph}\,\text{cm}^{-2}\,\text{s}^{-1}$ with 56σ significance level [82]. The Fermi-LAT, a satellite borne γ-ray telescope, has reported an excess[1] of gamma ray events around energy of $\sim$ 1-3 GeV in their photon spectra from the galactic center [83–91]. From the analysis of Fermi-LAT publicly available data [91, 92], existence of a monochromatic gamma-ray line from the direction of galactic centre of energy $\sim$ 130 GeV has been claimed in [93, 94] with 4.6σ confidence level. Similar results has also been observed from other independent analysis [95, 96]. All such anomalies, however, can be explained from several astrophysical scenarios [97–103]. Instead of these astrophysical explanations, there also exist DM interpretations of these gamma ray excess [104–110]. For example, the DM interpretations of the 3.5 keV X-ray line are mostly based on the decaying DM scenarios where a DM particle with mass 7 keV which can have different decay modes. Such as a scalar DM can decay into two photons [107, 108, 111], or a fermion DM can decay into a neutrino and photon [73, 111]. It is also possible that a heavy DM can decay to a lighter one along with a photon of energy 3.55 keV [109, 110, 112, 113] (see [114] for a brief review). Using the latest cosmological data, the authors in [115] showed that the 511 keV excess can not be explained by the annihilation of light thermally-produced WIMP and this strongly suggests a more exotic DM explanation [116, 117] or an unknown astrophysical source [118, 119] of the signal.

So far all the above-mentioned signatures have been in the excess of photons in different energy ranges starting from keV to GeV energies. Let us now discuss an excess recently found in the proton and anti-proton fluxes as observed by AMS collaboration [120, 121]. Prior to this excess, the PAMELA satellite had also reported an excess in their data for the positron fraction $e^+/\left(e^+ - e^-\right)$ in the energy range 10-100 GeV [62], later confirmed by the Fermi-LAT collaboration in [122–125] with an extension of the energy range up to 200 GeV. Besides several astrophysical explanations [126–131], the annihilation of DM is also a plausible explanation these excess [130, 132–135].

[1]The observational data is available in https://fermi.gsfc.nasa.gov/ssc/data/access/

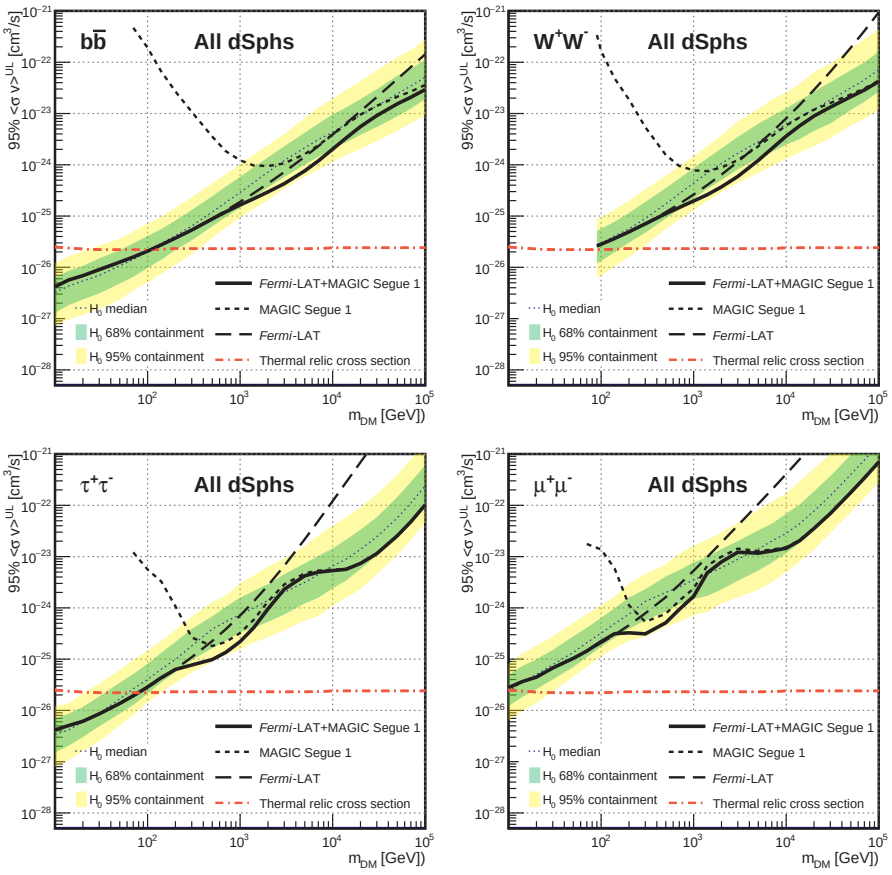

Figure 1.8: Upper bounds on the thermally-averaged cross-section for DM particles annihilating into $b\bar{b}$ (top-left), W^+W^- (top-right), $\tau\overline{\tau}$ (bottom-left), and $\mu^+\mu^-$ (bottom-right) at 95% CL. Figure has been taken from [8].

Dark matter at particle colliders

Let us now discuss the possible ways to search for DM at particle colliders or more specifically at the large hadron collider or LHC which is the largest particle collider we have, located near Geneva, Switzerland. The most important question to ask here is whether one can at all expect to study the properties of DM particles with colliders in the same way we have studied the SM particles. Unfortunately the answer is no as, even for the theoretical frameworks predicting WIMPs, we will not be able to produce huge number of DM at colliders given the current luminosity of the LHC. Now, with such low fluxes and the given direct detection limits, it is almost impossible to directly detect it. Secondly, whatever particle gets produced at collider, it will be unclear to know whether it has anything to do with galactic DM or if it is long lived over the cosmological scales to be the DM candidate with the right cosmic abundance. Also, due to their weak interactions strength (if it interacts at al in addition to gravitational interactions) to SM particles, they will not produce any visible signal at the collider. The transverse momentum conservation is the only way through which DM particles can be inferred as shown in figure 1.9.

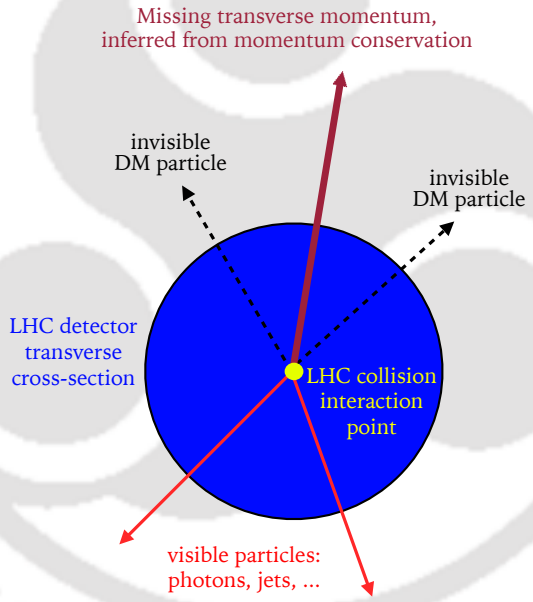

Figure 1.9: Schematic diagram for searching of DM production via missing transverse momentum in a general LHC detector. Figure has been taken from [9].

There are two different search strategies adopted to search for DM at collider. They are summarised as follows.

- One can start with a "complete" given theory and look for specific and distinct signals at colliders and one such example is "supersymmetry" (SUSY) models. In these models, all the SM particles have their own supersymmetric partners, with a half-integral spin difference. The presence of the R-parity ensures the stability of the lightest SUSY particle and can be a viable WIMP DM candidate. However, in such complete theories, they have a large number of parameters, as in supersymmetric theories we have to

specify the mass and interactions of all the superpartners. Instead of searching for specific complete theories, most of the time, experimentalists at the LHC look for some simplified models [136–141]. Unfortunately, no experimental evidences have been found so far (for experimental constraints on SUSY particles please see [142]).

- In recent years, another probing strategy have been motivated by a model independent effective field theory (EFT) approach [141, 143–147]. In this case, we have to assume that the particle responsible for mediating the interaction between SM and DM is very heavy and can be integrated out to produce an effective interaction. The standard process collider will look for is the pair production of DM along with one or more SM particles radiated by initial state quarks or gluons in combination with significant missing transverse energy ($E_T^{\rm miss}$). This kind of search is known as mono-X search and has been discussed by several authors [148–155]. The EFT approach is a very useful tool to encapsulate the phenomenology of WIMP interaction. However, one crucial point of EFT is the energy scale we are trying to probe and this theory breaks down as energies approaches to the scale of the mediating particle.

- The simplified DM models, besides a stable DM particle contain at least one mediator which couples the DM to the other SM particles. There are different simplified DM models can be found in the literature. For example, the simplest interaction between a fermionic DM particle χ with the SM particles (q) by the effective operator $(\overline{\chi}\Gamma^m\chi)\,(\overline{q}\Gamma_m q)$ can be mediated by a scalar (or pseudo scalar) mediator, or a vector (or axial vector) mediators. The DM particles can be produced in collider through these mediators and can be constrained from the reconstruction of the transverse missing energy.

1.2.2 Non-thermal dark matter

As discussed above, many experiments have been searching for thermal DM or WIMPs for a few decades now and failed to produce any positive signal. Null results in these experiments motivate people to pursue beyond the simplest thermal WIMP paradigm where the interaction scale of DM with SM can be much lower than the scale of weak interaction. Such small interactions will forbid the production of DM particle in the thermal bath, rather they will be produced non-thermally through the annihilation or decay of the bath particle. Due to its feeble interaction with the thermal plasma, these kinds of DM candidates are known as Feebly Interacting Massive Particle (FIMP) [10, 11]. In contrast with popular WIMP scenarios , FIMPs have almost negligible abundance to begin with in the early Universe and slowly freezes in as the Universe evolves. One peculiar feature of the thermal freeze-out mechanism is that the yield is dominant at low temperatures and will decouple from the bath typically at a temperature a factor of 20 - 25 below the DM mass. Practically, this behaviour is independent of the uncertain thermal history of the early Universe and possible new interactions at high scales. However, the final abundance will be highly dependent on the interaction strength. As shown in the right panel of figure 1.6, the freeze-out abundance will decrease with increasing cross-section. The exactly opposite will happen for freeze-in DM scenario, as shown in the left panel of figure 1.6, as we discuss below.

Let us now consider that we have a set of bath particles which have already established a thermal equilibrium among them at some temperature T and introduce some other long-lived particle χ which have very tiny interaction with the bath particles. This tiny interaction will always keep the interaction rate (Γ) to be smaller than the expansion rate of the Universe (H) by maintaining the following condition

$$\frac{\Gamma_{DM}\,(T)}{H(T)} << 1 \;\; (\forall\; T)\,. \tag{1.55}$$

χ particles will be produced from collisions or decays of bath particles with the evolution of the Universe. Let us consider the decay of a heavier bath particle (B) to give the dominant contribution to the production of DM particle χ ($\mathrm{B} \to \chi\chi$). One important point to note here is that if both decay and annihilation are producing DM with similar couplings involved in both the processes, then decay will always have the dominant contribution. However, if the mother particle itself is also out of equilibrium then the calculation will be different and the details can be found in [156]. By following the [10, 11], the Boltzmann equation can be written as

$$\frac{dn_\chi}{dt} + 3\,H\,n_\chi = 2\frac{K_1\,(M_B/T)}{K_2\,(M_B/T)}\,\Gamma_B\,n_B^{\mathrm{eq}}, \tag{1.56}$$

where $\mathrm{M_B}$, and $\mathrm{n_B^{eq}}$ are the mass, and the equilibrium density of the decaying particle B, and Γ_B is the decay width of the process $\mathrm{B} \to \chi\chi$. The above equation can also be written in terms of the previously mentioned dimensionless parameters $\mathrm{Y_\chi} \equiv \mathrm{n_\chi/s}$ and $\mathrm{x} \equiv \mathrm{M_B/T}$, as

$$\frac{dY_\chi}{dx} = 2\frac{K_1\,(M_B/T)}{K_2\,(M_B/T)}\,\frac{\Gamma_B}{H\,x}Y_B^{\mathrm{eq}}. \tag{1.57}$$

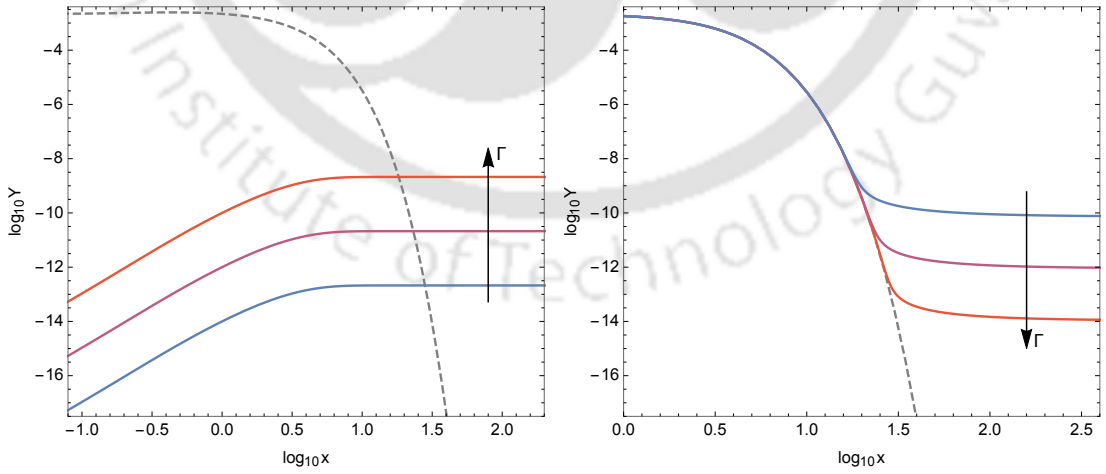

Figure 1.10: Contrasting behaviour between freeze-in and freeze-out scenarios. The final yield decrease with increasing interaction strength in case of freeze-in case (as shown by the upward arrow) whereas the opposite is happening for the freeze-out case. Figure has been taken from [10].

By assuming the Maxwell-Boltzmann distribution for the bath particles, we can approximately solve the above equation (1.57) and find the relic abundance of χ as

$$\Omega_{\chi,0}h^2 = 4.48 \times 10^8 \frac{g_B}{g_{*s}\sqrt{g_*}} \left(\frac{M_\chi}{\text{GeV}}\right) \frac{M_{\text{Pl}}\Gamma_B}{M_B^2}, \tag{1.58}$$

where g_B is the internal degrees of freedom of B, and M_χ is the mass of the DM χ. Note that the relic density is proportional to the decay width of the mother particle and the abundance will increase with the increasing interaction strength. This is the exactly opposite behaviour in comparison with the freeze-out scenarios as shown in the figure 1.10. However, we can not keep on increasing the interaction strength as at some point those interactions will thermalise the DM particles. Figure 1.11 shows the schematic representation the comparison between the coupling constant (λ) required for freeze-in and freeze-out mechanism.

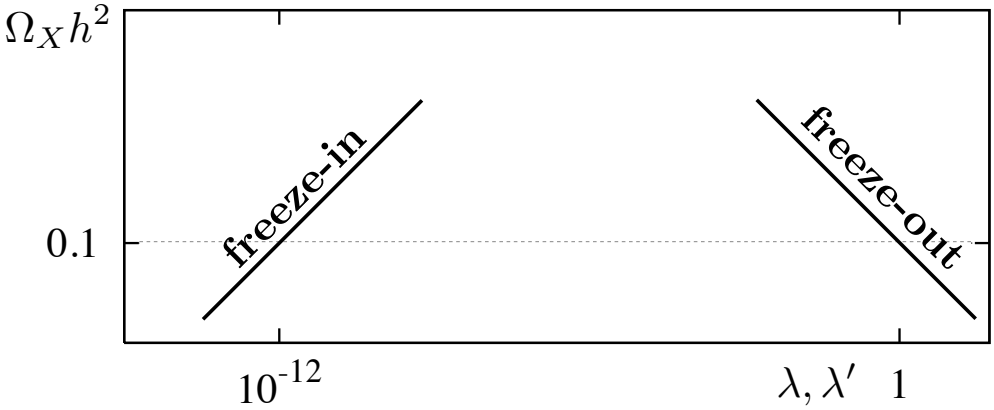

Figure 1.11: Schematic illustration representing the approximate orders of magnitude of coupling constants (λ, λ') required for thermal and non-thermal DM production. Figure has been taken from [11].

In case of thermal DM scenarios, once the DM particles get thermalised, their production history becomes irrelevant and they will follow the usual thermal freeze-out mechanism. However, freeze-in DM is highly sensitive to its initial production history (see [11, 157] for detail review). The mechanism we have discussed so far is known as IR (infra-red) freeze-in [108, 158–162]. Another type of non-thermal production mechanism also exists literature, known as UV (ultra-violet) [163–168] freeze-in where the non-renormalisable operators for DM-SM interactions play the role and yield depends crucially upon the reheating temperature (T_R) [164]. Unlike IR freeze-in which typically dominates at low temperatures close to DM mass, UV freeze-in dominates at high temperatures close to T_R.

Due to such small interaction strength, the freeze-in models are difficult to search for in direct detection or particle collider experiments. However, the authors in [169] has shown that

is possible to test a class of freeze-in models, where the SM and DM are coupled through a light mediator particle, through direct detection experiments. Freeze-in mechanism typically requires a lightest observable sector particle (LOSP) along with FIMP. This LOSP can have sizable interaction with SM sector particles and can be produced abundantly at collider experiments. Late time decay of these particles leading to displaced vertex or charged track signatures can be probed at colliders [170, 171]. To summarise, detection aspects of FIMP type DM crucially depends upon the particular model implementation.

1.3 Existence of neutrino mass

One of the overwhelming achievements in experimental high-energy physics in the last few decades is the discovery of neutrino oscillations, a quantum mechanical phenomenon driven by the mixing of the different neutrino flavors. The clue to this oscillation effect came from an anomaly known as "solar neutrino problem", a deficiency in the number of electron type neutrino from the Sun, discovered at the Homestake experiment [172–175]. The observation of the neutrino oscillation phenomena at the SuperKamiokande followed by confirmations at different long baseline and reactor neutrino experiments have strongly established the existence of non-zero neutrino mass [176–187]. Apart from the fact that neutrinos have mass, the neutrino oscillation have also revealed that the interaction eigenstates or the weak eigenstates (ν_e, ν_μ, ν_τ) are not same as the mass eigenstates (ν_1, ν_2, ν_3) for neutrinos, rather they are the coherent superposition of the mass eigenstates with masses (m_1, m_2, m_3). Additionally, neutrino oscillation experiments have also revealed the large mixing angles in lepton sector, in sharp contrast with the quark sector where mixing angles are tiny. The weak eigenstates and the mass eigenstates can be related by using the unitary Pontecorvo-Maki-Nakagawa-Sakata (PMNS) matrix ($U_{\lambda k}$) [188, 189] as

$$\nu_\lambda = \sum_i U_{\lambda k}\, \nu_i, \tag{1.59}$$

where $\lambda = e,\, \mu,\, \tau$ and $k = 1,\, 2,\, 3$. The PMNS matrix can be parameterized by three mixing angles θ_{12}, θ_{23}, and θ_{13}, a CP-violating Dirac phase δ, and two Majorana phases α, β and can be written as

$$U = \begin{pmatrix} c_{12}\, c_{13} & s_{12}\, c_{13} & s_{13}\, e^{-i\delta} \\ -s_{12}\, c_{23} - c_{12}\, s_{23}\, s_{13}\, e^{i\delta} & c_{12}\, c_{23} - s_{12}\, s_{23}\, s_{13} e^{i\delta} & s_{23}\, c_{13} \\ s_{12}\, s_{23} - c_{12}\, c_{23} s_{13} e^{i\delta} & -c_{12}\, s_{23} - s_{12}\, c_{23}\, s_{13}\, e^{i\delta} & c_{23}\, c_{13} \end{pmatrix} \begin{pmatrix} 1 & 0 & 0 \\ 0 & e^{i\frac{\alpha}{2}} & 0 \\ 0 & 0 & e^{i\frac{\beta}{2}} \end{pmatrix} \tag{1.60}$$

where $c_{ij} \equiv \cos\theta_{ij}$ and $s_{ij} \equiv \sin\theta_{ij}$. α and β will vanish if neutrinos are Dirac particle and then we will be left with only one physical phase δ. The neutrino oscillation experiments have measured the two mass squared differences defined as

$$\Delta m^2_{21} \equiv m^2_2 - m^2_1,\;\; \Delta m^2_{32} \equiv m^2_3 - m^2_2 \sim \Delta m^2_{31} \equiv m^2_3 - m^2_1, \tag{1.61}$$

and three mixing angles θ_{12}, θ_{23}, θ_{13}. The two mass squared differences are also known as solar $\Delta m^2_{\rm sol}$ and atmospheric $\Delta m^2_{\rm atm}$ respectively. By following the recent global fit [14], the status of these measurements is shown in table 1.2.

		Normal Ordering (best fit)		Inverted Ordering ($\Delta\chi^2 = 2.7$)	
		bfp $\pm 1\sigma$	3σ range	bfp $\pm 1\sigma$	3σ range
without SK atmospheric data	$\sin^2\theta_{12}$	$0.304^{+0.013}_{-0.012}$	$0.269 \to 0.343$	$0.304^{+0.013}_{-0.012}$	$0.269 \to 0.343$
	$\theta_{12}/^\circ$	$33.44^{+0.78}_{-0.75}$	$31.27 \to 35.86$	$33.45^{+0.78}_{-0.75}$	$31.27 \to 35.87$
	$\sin^2\theta_{23}$	$0.570^{+0.018}_{-0.024}$	$0.407 \to 0.618$	$0.575^{+0.017}_{-0.021}$	$0.411 \to 0.621$
	$\theta_{23}/^\circ$	$49.0^{+1.1}_{-1.4}$	$39.6 \to 51.8$	$49.3^{+1.0}_{-1.2}$	$39.9 \to 52.0$
	$\sin^2\theta_{13}$	$0.02221^{+0.00068}_{-0.00062}$	$0.02034 \to 0.02430$	$0.02240^{+0.00062}_{-0.00062}$	$0.02053 \to 0.02436$
	$\theta_{13}/^\circ$	$8.57^{+0.13}_{-0.12}$	$8.20 \to 8.97$	$8.61^{+0.12}_{-0.12}$	$8.24 \to 8.98$
	$\delta_{\rm CP}/^\circ$	195^{+51}_{-25}	$107 \to 403$	286^{+27}_{-32}	$192 \to 360$
	$\frac{\Delta m^2_{21}}{10^{-5}\ {\rm eV}^2}$	$7.42^{+0.21}_{-0.20}$	$6.82 \to 8.04$	$7.42^{+0.21}_{-0.20}$	$6.82 \to 8.04$
	$\frac{\Delta m^2_{3\ell}}{10^{-3}\ {\rm eV}^2}$	$+2.514^{+0.028}_{-0.027}$	$+2.431 \to +2.598$	$-2.497^{+0.028}_{-0.028}$	$-2.583 \to -2.412$
		Normal Ordering (best fit)		Inverted Ordering ($\Delta\chi^2 = 7.1$)	
		bfp $\pm 1\sigma$	3σ range	bfp $\pm 1\sigma$	3σ range
with SK atmospheric data	$\sin^2\theta_{12}$	$0.304^{+0.012}_{-0.012}$	$0.269 \to 0.343$	$0.304^{+0.013}_{-0.012}$	$0.269 \to 0.343$
	$\theta_{12}/^\circ$	$33.44^{+0.77}_{-0.74}$	$31.27 \to 35.86$	$33.45^{+0.78}_{-0.75}$	$31.27 \to 35.87$
	$\sin^2\theta_{23}$	$0.573^{+0.016}_{-0.020}$	$0.415 \to 0.616$	$0.575^{+0.016}_{-0.019}$	$0.419 \to 0.617$
	$\theta_{23}/^\circ$	$49.2^{+0.9}_{-1.2}$	$40.1 \to 51.7$	$49.3^{+0.9}_{-1.1}$	$40.3 \to 51.8$
	$\sin^2\theta_{13}$	$0.02219^{+0.00062}_{-0.00063}$	$0.02032 \to 0.02410$	$0.02238^{+0.00063}_{-0.00062}$	$0.02052 \to 0.02428$
	$\theta_{13}/^\circ$	$8.57^{+0.12}_{-0.12}$	$8.20 \to 8.93$	$8.60^{+0.12}_{-0.12}$	$8.24 \to 8.96$
	$\delta_{\rm CP}/^\circ$	197^{+27}_{-24}	$120 \to 369$	282^{+26}_{-30}	$193 \to 352$
	$\frac{\Delta m^2_{21}}{10^{-5}\ {\rm eV}^2}$	$7.42^{+0.21}_{-0.20}$	$6.82 \to 8.04$	$7.42^{+0.21}_{-0.20}$	$6.82 \to 8.04$
	$\frac{\Delta m^2_{3\ell}}{10^{-3}\ {\rm eV}^2}$	$+2.517^{+0.026}_{-0.028}$	$+2.435 \to +2.598$	$-2.498^{+0.028}_{-0.028}$	$-2.581 \to -2.414$

Table 1.2: Three-flavor oscillation parameters by following the global data in [14].

In table 1.2, $\ell = 1, 2$ depending upon the neutrino mass ordering. The sign of Δm^2_{21} is already known as the Mikheyev-Smirnov-Wolfenstien or MSW effect [190, 191] in the Sun depends on it. However, the sign of the other mass squared difference namely, the atmospheric $\Delta m^2_{\rm atm}$, is still unknown due two possible ways of neutrino mass ordering: $m_1 < m_2 < m_3$, known as normal ordering (NO) and $m_3 < m_1 < m_2$, known as inverted ordering (IO). Another important parameter which comes to the picture of neutrino oscillation is the CP-violating phase δ. Recent global fits hint at $\delta \approx -\pi/2$ [14]. Along with the ordering of the neutrino masses, the measurement of δ is also a prime target for the future oscillation experiments.

Neutrino oscillation experiments are not sensitive to the absolute mass scale of neutrinos. However, we can get a lower limit of 0.05 eV from the square root of the magnitude of the atmospheric $\Delta m^2_{\rm atm}$. The lightest neutrino mass namely, m_1 with NO or m_3 with

IO can be either vanishing or as large as approximately the square root of mass squared differences. Apart from the different neutrino oscillation experiments, the neutrino sector is also constrained by the data from cosmology and rare decay experiments. For example, laboratory based experiment KATRIN [192–194] is sensitive to the absolute mass scale of neutrinos from the measurement of the beta decay end-point spectrum of tritium. The current sensitivity of the KATRIN experiment is expected to be around 0.2 eV [195]. Very recently, KATRIN has obtained an upper bound of 1.1 eV on absolute mass of neutrinos at 90% CL [196]. On the other hand, the combined data from the Planck 2018 and baryon acoustic oscillation (BAO) experiments put a stringent constraint on the sum of absolute neutrino masses $\sum_i |m_i| < 0.12$ eV [50] at 95% CL. Thus, even though neutrino oscillation experiments reveal only the mass squared differences, rare decay and cosmology experiments give some ideas about their absolute masses. Additionally, no experiments have been able to reveal the nature of neutrinos: whether it is a Dirac fermion or a Majorana fermion. Since Majorana nature of light neutrinos imply violation of lepton number by two units, a promising arena to probe this nature is neutrinoless double beta decay $(0\nu\beta\beta)$[2]. While a positive signal at such experiments is still awaited, a future signal of this type will validate the Majorana nature of light neutrinos [198].

Let us briefly discuss about the general ways that neutrinos can gain mass. All the fermions in the SM except neutrinos acquire their masses through the usual Higgs mechanism after the electroweak symmetry breaking. As, all the left-handed fields (ψ_L) form doublet and the right handed fields(ψ_R) form singlet under the $SU(2)_L$ gauge symmetry of the SM, we can write the yukawa interactions of leptons and quarks as

$$Y_\ell \, \overline{L} \, H \, e_R \; + \; Y_{q_L}^{(d)} \, \overline{Q_L} \, H \, d_R \; + \; Y_{q_R}^{(d)} \, \overline{Q_L} \, \tilde{H} \, u_R \; + \; h.c. \,, \tag{1.62}$$

where, H is the higgs boson and $\tilde{H}$ is defined as $\tilde{H} = i\,\sigma_2\, H^*$. All the SM particles and their charges under the SM gauge symmetry, *i.e.* $SU(3)_c \times SU(2)_L \times U(1)_Y$, is shown below.

$$H = \begin{pmatrix} 0 \\ \frac{v+h}{\sqrt{2}} \end{pmatrix} \sim \left(1, 2, \frac{1}{2}\right), \tag{1.63}$$

$$L = \begin{pmatrix} \nu_L \\ e_L \end{pmatrix} \sim \left(1, 2, -\frac{1}{2}\right), \; e_R \sim (1, 1, -1)\,, \tag{1.64}$$

$$Q_L = \begin{pmatrix} u_L \\ d_L \end{pmatrix} \sim \left(3, 2, \frac{1}{6}\right), \; u_R \sim \left(3, 1, \frac{2}{3}\right), \; d_R \sim \left(3, 1, -\frac{1}{3}\right), \tag{1.65}$$

When, H gets a vacuum expectation value, the fermions will acquire their masses. However, there is no right-handed neutrino component present in the SM which forbids the generation of neutrino mass from Higgs mechanism at renormalisable level. One can generate a tiny Majorana mass for the neutrinos from the same Higgs field of the SM, at the non-renormalisable level, through the dimension five operator $\frac{\ell\ell HH}{\Lambda}$, known as Weinberg operator [199]. However, the unknown cutoff scale Λ in such operators points towards the existence of new physics at some high energy scale.

There have been many BSM proposals where the effects of such higher-dimensional operators can be realized within a renormalisable theory by incorporating the existence of

[2]See [197] for a review.

additional fields. They are popularly known as the seesaw mechanism [200–209]. The simplest possibility is to include the right-handed neutrinos ($N_R \sim (1,1,0)$) by hand with the particle content of the SM and write the new interaction as,

$$-\mathcal{L}_{\rm new} = Y_\nu\,\overline{L}\,\tilde{H}\,N_R \;+\; \frac{1}{2}\overline{N_R^c}\,M_R\,N_R \;+\; h.c. \tag{1.66}$$

where the second term, the bare mass term of the right-handed neutrinos allowed by gauge symmetries, introducing a new scale outside the purview of the SM. This leads us to a mass matrix for neutrinos, left and right handed neutrinos together, as

$$M = \begin{pmatrix} 0 & M_D \\ M_D^T & M_R \end{pmatrix}. \tag{1.67}$$

Diagonalizing this mass matrix, one gets the mass matrix for the light neutrino masses to be as follows,

$$M_\nu = -\frac{1}{2}\,Y_\nu\,\frac{v^2}{M_R}\,Y_\nu^T \tag{1.68}$$

It becomes evident from the above equation that the smallness of neutrino mass can be ascribed to the largeness of M_R. These kind of mechanism is known as the type-I seesaw mechanism [200–203]. Apart from the conventional type-I seesaw mechanism, there exists other kinds of seesaw mechanism as well. Instead of adding three right-handed neutrinos the neutrino mass can be generated by adding one heavy Higgs triplet (Δ) and the new interactions can be written as

$$-\mathcal{L}_{\rm new} = \frac{1}{2}\,Y_\Delta\,\overline{\ell_\Delta}\,\Delta\,i\,\sigma_2\,\ell_L^c \;-\; \lambda_\Delta\,M_\Delta H^T\,i\,\sigma_2\,\Delta\,H \;+\; h.c.\,, \tag{1.69}$$

where

$$\Delta \equiv \begin{pmatrix} \Delta^- & -\sqrt{2}\Delta^0 \\ \sqrt{2}\Delta^0 & -\Delta^- \end{pmatrix}.$$

After the electroweak symmetry breaking the light neutrino masses can be written as

$$\lambda_\Delta\,Y_\Delta\,\frac{v^2}{M_\Delta}, \tag{1.70}$$

where the heaviness of M_Δ will ensure the lightness of neutrinos and this mechanism is known as the type-II seesaw mechanism [204–208]. Another interesting variant also exists in the literature known as type-III seesaw mechanism [209] where the light neutrino mass was generated by introducing three heavy fermion triplets (Σ). The new interaction in this case will be

$$-\mathcal{L}_{\rm new} = \sqrt{2}Y_\Sigma\,\overline{\ell}_L\,\Sigma^c\,\tilde{H} \;+\; \frac{1}{2}Tr\left(\overline{\Sigma}\,M_\Sigma\,\Sigma^c\right) \;+\; h.c., \tag{1.71}$$

where

$$\Sigma \equiv \begin{pmatrix} \Sigma^0/\sqrt{2} & \Sigma^+ \\ \Sigma^- & -\Sigma^0/\sqrt{2} \end{pmatrix}.$$

After the electroweak symmetry breaking the light neutrino masses can be written as

$$-\,Y_\Sigma\,\frac{v^2}{M_\Sigma}\,Y_\Sigma^T, \tag{1.72}$$

again the heaviness of M_Σ will ensure the lightness of neutrinos. However, it is difficult to search for the new heavy degrees of freedoms in all such seesaw mechanisms, as the sensitivity of our current experiments have not reached to that level. One interesting alternative was proposed in 2005 by the authors in [12] where the neutrino mass can be realized in one loop level, shown in figure 1.12, instead of tree level seesaw mechanisms. However, we have to sacrifice the minimality in terms of the particle content and have to add one new doublet scalar $\left(\eta \sim \left(1, 2, \frac{1}{2}\right)\right)$ along with three right-handed neutrinos. We also have to impose as $\mathbb{Z}_2$ symmetry to all these new fields to forbid the interaction with SM higgs.The new interactions can be written as

$$-\,\mathcal{L}_{\rm new} = \left(h_{ij}\bar{\ell}_i\,\tilde{\eta}\,N_{Rj}\;+\;\frac{1}{2}\overline{N_R^c}\,M_R\,N_R\;+\;h.c.\right)\;+\;V\left(H,\eta\right), \tag{1.73}$$

where

$$\begin{aligned} V\left(H,\eta\right) \;=\; & m_H^2 H^\dagger H + m_\eta^2 \eta^\dagger\eta + \frac{1}{2}\lambda_1\left(H^\dagger H\right)^2 + \frac{1}{2}\lambda_2\left(\eta^\dagger\eta\right)^2 + \lambda_3\left(H^\dagger H\right)\left(\eta^\dagger\eta\right) \\ & \lambda_4\left(H^\dagger\eta\right)\left(\eta^\dagger H\right) + \frac{1}{2}\lambda_5\left[\left(H^\dagger\eta\right)^2 + h.c.\right]. \end{aligned}$$

By calculating the one loop contribution one can find out the mass matrix for the light

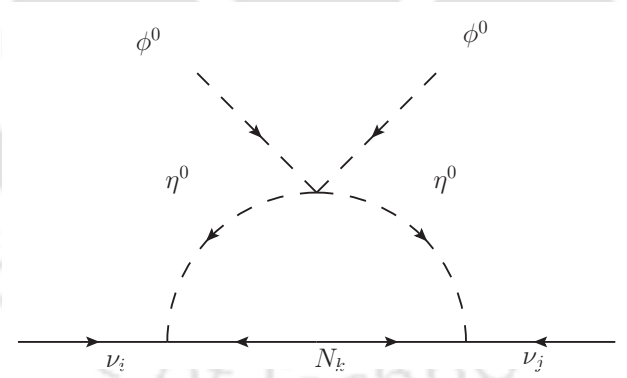

Figure 1.12: Mechanism generating neutrino mass at one-loop as considered by Ernest Ma [12].

neutrinos as

$$\mathcal{M}_{ij}^\nu = \frac{h_{ik}h_{jk}}{16\pi^2}M_k^2\left(\frac{m_R^2}{m_R^2 - M_k^2}\ln\frac{m_R^2}{M_k^2} - \frac{m_I^2}{m_I^2 - M_k^2}\ln\frac{m_I^2}{M_k^2}\right), \tag{1.74}$$

where M_R and M_I are the masses of the real scalar and the pseudo scalar part of the new scalar doublet η, and M_k are the masses of the right-handed neutrinos. One notable difference here is that due to the loop suppression the light neutrino mass can be realized at TeV scale physics which was absent in the tree level seesaw mechanisms. Another interesting

point to note here is that the lightest $\mathbb{Z}_2$ odd particle be will be completely stable and can play the role of dark matter and because of this nature it is also known as scotogenic. The word scotogenic comes from the greek words 'skotos' and 'genein' and can be translated as produced by darkness ie dark matter may be the origin of a radiative neutrino mass.

All such above mentioned mechanisms predict the Majorana nature of the neutrinos. However, experiments looking for $0\nu\beta\beta$, a promising signature of Majorana neutrinos mentioned above, have not yet found any positive results. Though this does not necessarily exclude the Majorana nature, yet it is motivating to study the possibility of light Dirac neutrinos. With this motivation, several works [210–245] have discussed different ways of generating light Dirac neutrino masses by suitable extension of the SM with new particles and symmetries. Some possibilities of light Dirac neutrino mass and connection to thermal as well as non-thermal DM will also be discussed in this thesis.

In the following three chapters we will discuss in detail a few minimal models of scalar or fermion DM, where light neutrino mass can also arise naturally. To do that, we have extended the particle content as well as the symmetry of the SM either by gauge or global discrete symmetries and studied their phenomenological consequences. We have shown that such symmetries not only stabilize DM but also play a crucial role in generating neutrino mass and mixing. We elaborate upon direct and collider search prospects of the models both in the context of WIMP, and in some specific scenarios, we have also discussed the possibilities of constraining the model from the cosmological observations like effective relativistic degrees of freedom in CMB. We have also discussed the interplay of thermal and non-thermal contribution to DM and possible connection to neutrino mass. Due to predictive nature of these minimal scenarios which connects neutrino, dark matter with several signatures at experiments operational at cosmic, intensity and energy frontiers, near future data will be able to validate or rule out some of these scenarios.

CHAPTER 2

Dark matter and neutrino mass in gauged B – L Model

2.1 Introduction

In this chapter, some aspects of dark matter and neutrino mass mechanisms will be discussed based on a very well motivated BSM framework known as the gauged $U(1)_{B-L}$ symmetry, where B and L correspond to baryon and lepton numbers, respectively. This minimal framework from the point of view of generating non-zero neutrino mass has been studied for a long time [206, 246–250]. The most interesting feature of this model is that the inclusion of three right handed neutrinos, as it is done in type I seesaw mechanism for generating light neutrino masses, is no longer a choice but a necessity due to the requirement of the new $U(1)_{B-L}$ gauge symmetry to be anomaly free. The model has also been studied in the context of DM by several groups, see [251–255] for example. DM in scale invariant versions of this model was also studied by several authors [256, 257]. The interesting feature of such a model from DM point of view is the issue of DM stability that can be ensured in this model if the $U(1)_{B-L}$ gauge symmetry gets spontaneously broken down to a remnant discrete symmetry like $\mathbb{Z}_2$, so that the lightest $\mathbb{Z}_2$ odd particle can be stable. However, many $U(1)_{B-L}$ models also considered additional discrete symmetries to ensure DM stability, for example [258,259]. Although experimental limits from LEP II data constrain such new gauge sector by giving a lower bound on the ratio of new gauge boson mass to the corresponding gauge coupling $M_{Z_{BL}}/g_{BL} \geq 7$ TeV [260, 261], there can be several interesting consequences of such extended gauge symmetry that can be probed at several ongoing experiments like the LHC. In a recent work [262], two-component fermion DM was also proposed as a new anomaly free gauged $B - L$ model[1]. The neutrino mass in this model originate from just two right handed neutrinos, often referred to as the littlest seesaw (LS) model [265], leading to a vanishing lightest neutrino mass. Motivated by these interesting features of the gauged $U(1)_{B-L}$ model, here we study three different versions of it where the extra fermion fields responsible for anomaly cancellations can not only be viable DM candidates, but also take part in generating tiny neutrino masses either via tree level or radiative seesaw mechanisms.

This chapter is organized as follows. In section 2.2, we give an overview of gauged $B - L$ model and different solutions to anomaly conditions which already exist in the literature. The

[1]Please see [263, 264] and references therein for general approach to build anomaly free Abelian gauge extensions of SM with inclusion of DM.

next three sections are dedicated to three different versions of the gauged $B-L$ extensions and there phenomenological consequences.

2.2 Gauged B − L model

As mentioned above, gauged $B-L$ symmetric extension of the SM [246–250, 266] is one of the most popular and very well motivated BSM frameworks that has been studied quite well for a long time. Since the SM already has an accidental and global $B-L$ symmetry at renormalisable level, it is very straightforward as well as motivating to uplift it to a gauge symmetry and study the consequences. Compared to an arbitrary Abelian gauge extension of the SM, gauged $B-L$ symmetry emerges as a very natural and minimal possibility as the corresponding charges of all the SM fields under this new symmetry are well known. However, a $U(1)_{B-L}$ gauge symmetry with only the SM fermions is not anomaly free. This is because the triangle anomalies for both $U(1)^3_{B-L}$ and the mixed $U(1)_{B-L}-(\text{gravity})^2$ diagrams are non vanishing. These triangle anomalies for the SM fermion content are given as

$$\begin{aligned}\mathcal{A}_1\left[U(1)^3_{B-L}\right] &= \mathcal{A}_1^{\rm SM}\left[U(1)^3_{B-L}\right] = -3\,,\\ \mathcal{A}_2\left[(\text{gravity})^2\times U(1)_{B-L}\right] &= \mathcal{A}_2^{\rm SM}\left[(\text{gravity})^2\times U(1)_{B-L}\right] = -3\,.\end{aligned} \tag{2.1}$$

The A's are known as the anomaly-coefficient and can be defined as

$$A_{Abc} \equiv \text{Tr}\left(T_A\left[T_b,T_c\right]_+\right)_R - Tr\left(T_A\left[T_b,T_c\right]_+\right)_L\,,$$

where T_i are the different generators of the gauge groups involved and '+' represents the anti-commutation between the two generators. One can easily derive the equation (2.1) by using the $B-L$ charges of the SM particles from the above expression. Remarkably, if three right handed neutrinos are added to the model, they contribute

$$\mathcal{A}_1^{\rm New}\left[U(1)^3_{B-L}\right] = 3, \mathcal{A}_2^{\rm New}\left[(\text{gravity})^2\times U(1)_{B-L}\right] = 3$$

leading to vanishing total of triangle anomalies. This is the most natural and economical $U(1)_{B-L}$ model where the fermion sector has three right handed neutrinos apart from the usual SM fermions and it has been known for a long time.

However, there exist non-minimal ways of constructing anomaly free versions of $U(1)_{B-L}$ model. For example, it has been known for a few years that three right handed neutrinos with exotic $B-L$ charges $5,-4,-4$ can also give rise to vanishing triangle anomalies [267]. It is clear to see how the anomaly cancels, as follows

$$\mathcal{A}_1\left[U(1)^3_{B-L}\right] = \mathcal{A}_1^{\rm SM}\left[U(1)^3_{B-L}\right] + \mathcal{A}_1^{\rm New}\left[U(1)^3_{B-L}\right] = -3+\left[-5^3-(-4)^3-(-4)^3\right] = 0\,,$$

$$\begin{aligned}\mathcal{A}_2\left[(\text{gravity})^2\times U(1)_{B-L}\right] &= \mathcal{A}_2^{\rm SM}\left[(\text{gravity})^2\times U(1)_{B-L}\right] + \mathcal{A}_2^{\rm New}\left[(\text{gravity})^2\times U(1)_{B-L}\right]\,,\\ &= -3+\left[-5-(-4)-(-4)\right] = 0\,.\end{aligned} \tag{2.2}$$

This model was also discussed recently in the context of neutrino mass [215, 268] and DM [269–273] by several groups. Another solution to the anomaly cancellation conditions with irrational $B-L$ charges of new fermions was proposed by the authors of [274] where both DM and neutrino mass can have a common origin through radiative linear seesaw. Very recently, another anomaly free $U(1)_{B-L}$ framework was proposed where the additional right handed fermions possess more exotic $B-L$ charges namely, $-4/3, -1/3, -2/3, -2/3$ [275]. The triangle anomalies get canceled as follows.

$$\begin{aligned}\mathcal{A}_1\left[U(1)_{B-L}^3\right] &= \mathcal{A}_1^{\rm SM}\left[U(1)_{B-L}^3\right] + \mathcal{A}_1^{\rm New}\left[U(1)_{B-L}^3\right] \\ &= -3 + \left[-(-4/3)^3 - (-1/3)^3 - (-2/3)^3 - (-2/3)^3\right] = 0\end{aligned}$$

$$\begin{aligned}\mathcal{A}_2\left[(\text{gravity})^2 \times U(1)_{B-L}\right] &= \mathcal{A}_2^{\rm SM}\left[(\text{gravity})^2 \times U(1)_{B-L}\right] + \mathcal{A}_2^{\rm New}\left[(\text{gravity})^2 \times U(1)_{B-L}\right] \\ &= -3 + \left[-(-4/3) - (-1/3) - (-2/3) - (-2/3)\right] = 0 \qquad (2.3)\end{aligned}$$

These four chiral fermions constitute two Dirac fermion mass eigenstates, the lighter of which becomes the DM candidate having either thermal [275] or non-thermal origins [156]. One can have even more exotic right handed fermions with $B-L$ charges $-17/3, 6, -10/3$ so that the triangle anomalies cancel as

$$\begin{aligned}\mathcal{A}_1\left[U(1)_{B-L}^3\right] &= \mathcal{A}_1^{\rm SM}\left[U(1)_{B-L}^3\right] + \mathcal{A}_1^{\rm New}\left[U(1)_{B-L}^3\right] \,, \\ &= -3 + \left[-(-17/3)^3 - (6)^3 - (-10/3)^3\right] = 0 \,,\end{aligned}$$

$$\begin{aligned}\mathcal{A}_2\left[(\text{gravity})^2 \times U(1)_{B-L}\right] &= \mathcal{A}_2^{\rm SM}\left[(\text{gravity})^2 \times U(1)_{B-L}\right] + \mathcal{A}_2^{\rm New}\left[(\text{gravity})^2 \times U(1)_{B-L}\right] \,, \\ &= -3 + \left[-(-17/3) - (6) - (-10/3)\right] = 0 \,. \qquad (2.4)\end{aligned}$$

In the recent work on $U(1)_{B-L}$ gauge symmetry with two-component DM [262], the authors considered two right handed neutrinos with $B-L$ number -1 each so that the model still remains anomalous. The remaining anomalies were cancelled by four chiral fermions with fractional $B-L$ charges leading to two Dirac fermion mass eigenstates both of which are stable and hence DM candidates. Motivated by these new anomaly cancellation conditions with interesting phenomenological consequences, in this chapter we have studied three different versions of such a model [276–278]. While the first version [276] discusses single component fermion or scalar DM with radiative neutrino masses, the second version [277] studies the implementation of type III seesaw with two-component Dirac fermion DM being responsible for anomaly cancellation. The third version [278] is a variant of the second while keeping light neutrinos as Dirac with interesting cosmological consequences due to the possibility of additional thermalised relativistic degrees of freedom.

Particles	$SU(3)_c \times SU(2)_L \times U(1)_Y \times U(1)_{B-L}$
$q_L = \begin{pmatrix} u_L \\ d_L \end{pmatrix}$	$(3, 2, \frac{1}{6}, \frac{1}{3})$
u_R	$(3, 1, \frac{2}{3}, \frac{1}{3})$
d_R	$(3, 1, -\frac{1}{3}, \frac{1}{3})$
$\ell_L = \begin{pmatrix} \nu_L \\ e_L \end{pmatrix}$	$(1, 2, -\frac{1}{2}, -1)$
e_R	$(1, 1, -1, -1)$
N_1	$(1, 1, 0, -\frac{1}{3})$
N_2	$(1, 1, 0, -\frac{2}{3})$
N_3	$(1, 1, 0, -\frac{2}{3})$
N_4	$(1, 1, 0, -\frac{4}{3})$

Table 2.1: Fermion Content of the Model

2.3 Dark matter and radiative neutrino mass in $\mathrm{U(1)_{B-L}}$ model

In this section, we stick to the choice with four right handed neutrinos having $B-L$ charges -4/3, -1/3, -2/3, -2/3 and propose a common framework for the origin of neutrino mass and DM. In the original reference where this possibility was proposed [275], the origin of neutrino mass was considered to be through type II seesaw mechanism, which remains decoupled from the DM sector composed of the singlet fermions having exotic $B-L$ charges. The authors in fact constructed two Dirac fermions from the four singlet fermions by appropriately choosing the chirality and studied the corresponding DM phenomenology. Here instead of adding scalar triplet for type II seesaw, we consider the addition of scalar doublets having appropriate $B-L$ charges so that light neutrino mass can arise at one loop level, allowing the possibility of both scalar doublet and fermion singlet DM scenario.

2.3.1 The Minimal Model

In this section, we propose a $U(1)_{B-L}$ model based on the newly suggested anomaly cancellation solution with four right handed neutrinos having $B-L$ charges $-4/3, -1/3, -2/3, -2/3$, but with a minimal scalar content to realise one-loop neutrino mass. The fermion and scalar content of the model are shown in table 2.1 and 2.2 respectively.

The Yukawa Lagrangian for leptons can be written as

$$\begin{aligned}\mathcal{L}_Y = {} & Y_e \overline{\ell_L} H e_R + Y_{i4} (\overline{\ell_L})_i i\tau_2 \eta_1^* N_4 + Y_{i2} (\overline{\ell_L})_i i\tau_2 \eta_2^* N_2 + Y_{i3} (\overline{\ell_L})_i i\tau_2 \eta_2^* N_3 \\ & + f_1 \phi_1 N_1 N_2 + f_2 \phi_1 N_1 N_3 + f_3 \phi_2 N_2 N_4 + f_4 \phi_2 N_3 N_4 + \text{h.c.} \end{aligned} \tag{2.5}$$

The scalar potential of the model can be written as

Particles	$SU(3)_c \times SU(2)_L \times U(1)_Y \times U(1)_{B-L}$
$H = \begin{pmatrix} H^+ \\ H^0 \end{pmatrix}$	$(1, 2, \frac{1}{2}, 0)$
$\eta_1 = \begin{pmatrix} \eta_1^+ \\ \eta_1^0 \end{pmatrix}$	$(1, 2, \frac{1}{2}, -\frac{1}{3})$
$\eta_2 = \begin{pmatrix} \eta_2^+ \\ \eta_2^0 \end{pmatrix}$	$(1, 2, \frac{1}{2}, \frac{1}{3})$
ϕ_1	$(1, 1, 0, 1)$
ϕ_2	$(1, 1, 0, 2)$

Table 2.2: Scalar content of the Minimal Model

$$
\begin{aligned}
V = & -\mu_H^2|H|^2 + \lambda_H|H|^4 + \sum_{i=1,2}\left(\mu_{\eta_i}^2|\eta_i|^2 + \lambda_{\eta_i}|\eta_i|^4\right) + \sum_{i=1,2}\left(-\mu_{\phi_i}^2|\phi_i|^2 + \lambda_{\phi_i}|\phi_i|^4\right) \\
& + \sum_{i=1,2}\lambda_{H\eta_i}(\eta_i^\dagger\eta_i)(H^\dagger H) + \sum_{i=1,2}\lambda'_{H\eta_i}(\eta_i^\dagger H)(H^\dagger\eta_i) + \sum_{i=1,2}\lambda_{H\phi_i}(\phi_i^\dagger\phi_i)(H^\dagger H) \\
& + \lambda_{H\eta}\left((\eta_1^T H^\dagger)(\eta_2^T H^\dagger) + \text{h.c.}\right) + \sum_{i,j=1,2}\lambda_{\eta_i\phi_j}(\eta_i^\dagger\eta_i)(\phi_j^\dagger\phi_j) + \lambda_\phi(\phi_1^\dagger\phi_1)(\phi_2^\dagger\phi_2) \\
& + \mu_\phi\left(\phi_1\phi_1\phi_2^\dagger + \text{h.c.}\right) \qquad (2.6)
\end{aligned}
$$

We choose the mass squared terms of $\eta_{1,2}$ to be positive so that the neutral components of only H, ϕ_1, ϕ_2 acquire non-zero vacuum expectation value (vev). We denote these vev's as

$$\langle H\rangle = \frac{v}{\sqrt{2}}\begin{pmatrix}0\\1\end{pmatrix}, \quad \langle\phi_1\rangle = \frac{u_1}{\sqrt{2}}, \quad \langle\phi_2\rangle = \frac{u_2}{\sqrt{2}}$$

The minimisation conditions of the above scalar potential corresponds to

$$\mu_H^2 = \lambda_H v^2 + \lambda_{H\phi_1}\frac{u_1^2}{2} + \lambda_{H\phi_2}\frac{u_2^2}{2}$$

$$\mu_{\phi_1}^2 = \lambda_{\phi_1}u_1^2 + \lambda_\phi\frac{u_2^2}{2} + \lambda_{H\phi_1}\frac{v^2}{2} + \sqrt{2}\mu_\phi u_2$$

$$\mu_{\phi_2}^2 = \lambda_{\phi_2}u_2^2 + \lambda_\phi\frac{u_1^2}{2} + \lambda_{H\phi_2}\frac{v^2}{2} + \frac{1}{\sqrt{2}}\mu_\phi\frac{u_1^2}{u_2}$$

Writing down the kinetic terms of the relevant scalar fields as

$$
\begin{aligned}
\mathcal{L}_{\text{kinetic}} \supset & |(\partial_\mu + ig\vec{T}\cdot\vec{W} + ig'YB_\mu)H|^2 + |(\partial_\mu + ig_{BL}Z'_\mu)\phi_1|^2 \\
& + |(\partial_\mu + i2g_{BL}Z'_\mu)\phi_2|^2 \qquad (2.7)
\end{aligned}
$$

where $T_i = \sigma_i/2$, we can find out the masses of gauge bosons as

$$M_W = \frac{1}{2}gv, \quad M_Z = \frac{1}{2}gv\sqrt{1+\left(\frac{g'}{g}\right)^2}, \quad M_{Z_{BL}} = g_{BL}\sqrt{u_1^2+4u_2^2}$$

The neutral scalar mass matrix constructed from the singlet Higgs fields is given by

$$M^2_{\phi_r} = \begin{pmatrix} 2\lambda_{\phi_1}u_1^2 & u_1(\lambda_\phi u_2 + \sqrt{2}\mu_\phi) \\ u_1(\lambda_\phi u_2 + \sqrt{2}\mu_\phi) & 2\lambda_{\phi_2}u_2^2 - \frac{\mu_\phi u_1^2}{\sqrt{2}u_2} \end{pmatrix} \tag{2.8}$$

The neutral pseudoscalar mass matrix constructed from the singlet Higgs fields is given by

$$M^2_{\phi_i} = \begin{pmatrix} -2\sqrt{2}u_2\mu_\phi & \sqrt{2}u_1\mu_\phi \\ \sqrt{2}u_1\mu_\phi & -\frac{u_1^2\mu_\phi}{\sqrt{2}u_2} \end{pmatrix} \tag{2.9}$$

which clearly gives rise to a vanishing eigenvalue, corresponding to the Goldstone boson that gets converted into the longitudinal mode of the $U(1)_{B-L}$ gauge boson. After the electroweak symmetry breaking, these mass matrices become 3×3 due to mixing with the components of the Higgs doublet H. The neutral scalar mass matrix becomes

$$M^2_{(H\phi)_r} = \begin{pmatrix} 2\lambda_H v^2 & \lambda_{H\phi_1}u_1 v & \lambda_{H\phi_2}u_2 v \\ \lambda_{H\phi_1}u_1 v & 2\lambda_{\phi_1}u_1^2 & u_1(\lambda_\phi u_2 + \sqrt{2}\mu_\phi) \\ \lambda_{H\phi_2}u_2 v & u_1(\lambda_\phi u_2 + \sqrt{2}\mu_\phi) & 2\lambda_{\phi_2}u_2^2 - \frac{\mu_\phi u_1^2}{\sqrt{2}u_2} \end{pmatrix}. \tag{2.10}$$

Assuming the third neutral Higgs to be very heavy and decoupled, we can find the mixing between the light and next to lightest neutral Higgs (in the small mixing limit) as

$$\tan 2\theta_1 \approx 2\sin\theta_1 \approx 2\xi = \frac{2\lambda_{H\phi_1}u_1 v}{2\lambda_{\phi_1}u_1^2 - 2\lambda_H v^2}. \tag{2.11}$$

The mixing parameter ξ plays a non-trivial role in DM phenomenology as we discuss later. Such a mixing can be tightly constrained by LEP as well as LHC Higgs exclusion searches as shown recently by [279]. These constraints are more strong for low mass scalar and the upper bound on the mixing angle can be as low as $\sin\theta < 0.1$ [279]. We consider a conservative upper limit on the mixing parameter $\xi \leq 0.1$ for our analysis. This can be easily satisfied by suitable tuning of the parameters involved in the expression for mixing given in (2.11).

The neutral scalar mass matrix constructed from the doublets $\eta_{1,2}$ is given by

$$M^2_{\eta_r} = \begin{pmatrix} M^2_{r11} & M^2_{r12} \\ M^2_{r21} & M^2_{r22} \end{pmatrix} \tag{2.12}$$

where

$$M^2_{r11} = \mu^2_{\eta_1} + (\lambda_{H\eta_1} + \lambda'_{H\eta_1})\frac{v^2}{2} + \frac{1}{2}(\lambda_{\eta_1\phi_1}u_1^2 + \lambda_{\eta_1\phi_2}u_2^2)$$

$$M^2_{r12} = M^2_{r21} = \lambda_{H\eta}\frac{v^2}{2}$$

$$M^2_{r22} = \mu^2_{\eta_2} + (\lambda_{H\eta_2} + \lambda'_{H\eta_2})\frac{v^2}{2} + \frac{1}{2}(\lambda_{\eta_2\phi_1}u_1^2 + \lambda_{\eta_2\phi_2}u_2^2)$$

The pseudoscalar mass matrix constructed from the doublets $\eta_{1,2}$ is given by

$$M^2_{\eta_i} = \begin{pmatrix} M^2_{i11} & M^2_{i12} \\ M^2_{i21} & M^2_{i22} \end{pmatrix} \tag{2.13}$$

where

$$M^2_{i11} = \mu^2_{\eta_1} + (\lambda_{H\eta_1} + \lambda'_{H\eta_1})\frac{v^2}{2} + \frac{1}{2}(\lambda_{\eta_1\phi_1}u_1^2 + \lambda_{\eta_1\phi_2}u_2^2)$$

$$M^2_{i12} = M^2_{i21} = -\lambda_{H\eta}\frac{v^2}{2}$$

$$M^2_{i22} = \mu^2_{\eta_2} + (\lambda_{H\eta_2} + \lambda'_{H\eta_2})\frac{v^2}{2} + \frac{1}{2}(\lambda_{\eta_2\phi_1}u_1^2 + \lambda_{\eta_2\phi_2}u_2^2)$$

One can find the mass eigenstates of scalars and pseudoscalars using orthogonal rotations. For example, the scalar mass eigenstates are

$$\eta'_{1r} = \eta_{1r}\cos\theta - \eta_{2r}\sin\theta,\ \ \eta'_{2r} = \eta_{1r}\sin\theta + \eta_{2r}\cos\theta$$

where

$$\theta = \frac{1}{2}\tan^{-1}\left(\frac{2M^2_{r12}}{M^2_{r22} - M^2_{r11}}\right)$$

Similarly one can find the mass eigenstates of the pseudoscalars with a rotation angle $\theta' = -\theta$. It is straightforward to see that the scalars are degenerate with their pseudoscalar counterparts which can have serious consequences for DM physics as we discuss later.

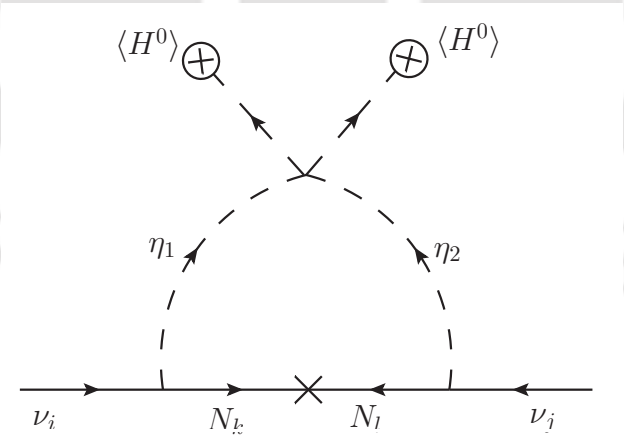

Figure 2.1: One loop neutrino mass for the particle content shown in table 2.1, 2.2

The one loop neutrino mass arising from the diagram in figure 2.1 can be estimated as [12]

$$(m_\nu)_{ij} = \frac{Y_{ik}Y_{jk}M_k}{16\pi^2}\left(\frac{m_R^2}{m_R^2 - M_k^2}\ln\frac{m_R^2}{M_k^2} - \frac{m_I^2}{m_I^2 - M_k^2}\ln\frac{m_I^2}{M_k^2}\right) \tag{2.14}$$

Here $m^2_{R,I} = m^2_{H,A}$ are the masses of scalar and pseudo-scalar part of $\eta^0_{1,2}$ and M_k is the mass of singlet fermion N_k in the internal line. The index $i, j = 1, 2, 3$ runs over the three fermion generations as well as three copies of N_i. For $m^2_H + m^2_A \approx M^2_k$, the above expression can be simply written as

$$(m_\nu)_{ij} \approx \frac{m^2_A - m^2_H}{32\pi^2} \frac{Y_{ik} Y_{jk}}{M_k} \tag{2.15}$$

From the discussion of scalar and pseudoscalar masses above, one can find the mass difference between η'_{1r} and η'_{2i} to be

$$m^2_A - m^2_H = \sqrt{(M^2_{r22} - M^2_{r11})^2 + 4M^4_{r12}}$$

The light neutrino mass matrix, in the simplified approximation above (2.15) has a type I seesaw structure upto a loop suppression factor. The structure of this mass matrix can be obtained as

$$m_\nu = c_1 Y M^{-1}_R Y^T, \quad c_1 = \frac{m^2_A - m^2_H}{32\pi^2}$$

where Y, M_R can be found from the Yukawa Lagrangian (2.5) as

$$Y = \begin{pmatrix} 0 & Y_{12} & Y_{13} & Y_{14} \\ 0 & Y_{22} & Y_{23} & Y_{24} \\ 0 & Y_{32} & Y_{33} & Y_{34} \end{pmatrix}, \quad M_R = \begin{pmatrix} 0 & f_1 u_1 & f_2 u_1 & 0 \\ f_1 u_1 & 0 & 0 & f_3 u_2 \\ f_2 u_1 & 0 & 0 & f_4 u_2 \\ 0 & f_3 u_2 & f_4 u_2 & 0 \end{pmatrix} \tag{2.16}$$

The light neutrino mass matrix constructed from these mass matrices has one vanishing eigenvalue predicting the lightest neutrino mass to be zero. The non-vanishing masses can be kept within experimentally observed limits ($\sim$ 0.1 eV), either by tuning the Yukawa couplings or the scalar-pseudoscalar mass difference while keeping the right handed neutrino mass around the TeV scale. From the right handed neutrino mass matrix written above, it is also clear that there is a two-fold degeneracy in the masses with two pairs of right handed neutrinos having degenerate masses.

2.3.2 Dark Matter

The relic abundance of a DM particle DM, which was in thermal equilibrium at some earlier epoch can be calculated by solving the Boltzmann equation

$$\frac{dn_{\rm DM}}{dt} + 3Hn_{\rm DM} = -\langle\sigma v\rangle (n^2_{\rm DM} - (n^{\rm eq}_{\rm DM})^2) \tag{2.17}$$

where $n_{\rm DM}$ is the number density of the DM particle DM and $n^{\rm eq}_{\rm DM}$ is the number density when DM was in thermal equilibrium. H is the Hubble expansion rate of the Universe and $\langle\sigma v\rangle$ is the thermally averaged annihilation cross section of the DM particle DM. In terms of partial wave expansion $\langle\sigma v\rangle = a + bv^2$. Numerical solution of the Boltzmann equation above gives [5, 280]

$$\Omega_{\rm DM} h^2 \approx \frac{1.04 \times 10^9 x_F}{M_{\rm Pl}\sqrt{g_*}(a + 3b/x_F)} \tag{2.18}$$

where $x_F = M_{\rm DM}/T_F$, T_F is the freeze-out temperature, $M_{\rm DM}$ is the mass of DM, g_* is the number of relativistic degrees of freedom at the time of freeze-out and and $M_{\rm Pl} \approx 2.4 \times 10^{18}$ GeV is the Planck mass. DM particles with electroweak scale mass and couplings freeze out at temperatures approximately in the range $x_F \approx 20 - 30$. More generally, x_F can be calculated from the relation

$$x_F = \ln \frac{0.038 g M_{\rm Pl} M_{\rm DM} < \sigma v >}{g_*^{1/2} x_F^{1/2}} \tag{2.19}$$

which can be derived from the equality condition of DM interaction rate $\Gamma = n_{\rm DM}\langle\sigma v\rangle$ with the rate of expansion of the Universe $H \approx g_*^{1/2}\frac{T^2}{M_{Pl}}$. There also exists a simpler analytical formula for the approximate DM relic abundance [281]

$$\Omega_{\rm DM} h^2 \approx \frac{3 \times 10^{-27} cm^3 s^{-1}}{\langle\sigma v\rangle} \tag{2.20}$$

The thermal averaged annihilation cross section $\langle\sigma v\rangle$ is given by [49]

$$\langle\sigma v\rangle = \frac{1}{8m^4 T K_2^2(m/T)} \int_{4m^2}^{\infty} \sigma(s - 4m^2)\sqrt{s} K_1(\sqrt{s}/T) ds \tag{2.21}$$

where K_i's are modified Bessel functions of order i, m is the mass of DM particle and T is the temperature.

If there exists some additional particles having mass difference close to that of DM, then they can be thermally accessible during the epoch of DM freeze out. This can give rise to additional channels through which DM can coannihilate with such additional particles and produce SM particles in the final states. This type of coannihilation effects on DM relic abundance were studied by several authors in [282–284]. Here we summarise the analysis of [282] for the calculation of the effective annihilation cross section in such a case. The effective cross section can given as

$$\begin{aligned} \sigma_{eff} &= \sum_{i,j}^{N} \langle\sigma_{ij} v\rangle r_i r_j \\ &= \sum_{i,j}^{N} \langle\sigma_{ij} v\rangle \frac{g_i g_j}{g_{eff}^2} (1+\Delta_i)^{3/2} (1+\Delta_j)^{3/2} e^{\left(-x_F(\Delta_i+\Delta_j)\right)} \end{aligned} \tag{2.22}$$

where $x_F = \frac{m_{DM}}{T_F}$ and $\Delta_i = \frac{m_i - M_{\rm DM}}{M_{\rm DM}}$ and

$$g_{eff} = \sum_{i=1}^{N} g_i (1+\Delta_i)^{3/2} e^{-x_F \Delta_i} \tag{2.23}$$

The masses of the heavier components of the inert Higgs doublet are denoted by m_i. The thermally averaged cross section can be written as

$$\langle \sigma_{ij} v \rangle = \frac{x_F}{8 m_i^2 m_j^2 M_{\rm DM} K_2((m_i/M_{\rm DM})x_F) K_2((m_j/M_{\rm DM})x_F)} \times \int_{(m_i+m_j)^2}^{\infty} ds \sigma_{ij}(s - 2(m_i^2 + m_j^2)) \sqrt{s} K_1(\sqrt{s} x_F / M_{\rm DM}) \tag{2.24}$$

2.3.3 Fermion Dark Matter in the Minimal Model

The lightest of the four Majorana fermions in the minimal model is the DM in this scenario if it has mass smaller than the scalar doublets $\eta_{1,2}$. Since the singlet fermion mass matrix is not diagonal, as can be seen from (2.16), we first diagonalise this mass matrix for some benchmark structure. For example, we choose $f_1 = f, f_2 = 2f, f_3 = 2f, f_4 = f, u_1 = u_2$ so that the mass eigenstates of the right handed neutrinos become

$$\chi_1 = \frac{1}{2}(N_1 - N_2 - N_3 + N_4)$$

$$\chi_2 = \frac{1}{2}(N_1 + N_2 + N_3 + N_4)$$

$$\chi_3 = \frac{1}{2}(N_1 - N_2 + N_3 + N_4)$$

$$\chi_4 = \frac{1}{2}(N_1 + N_2 - N_3 + N_4)$$

having masses $-3fu_1, 3fu_1, -fu_1, fu_1$ respectively. Using the known interactions of $N_{1,2,3,4}$ we then find out the possible interactions of the lightest among χ's in order to calculate its relic abundance. Here we show the results for χ_4 fermion DM though the results for χ_3 having same mass is exactly similar.

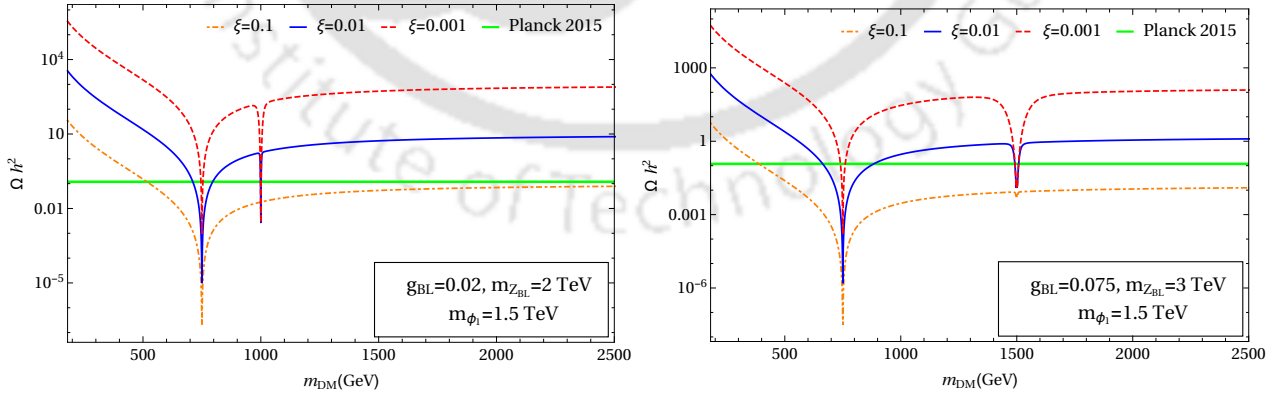

Figure 2.2: Fermion DM relic abundance as a function of DM mass for different benchmark values of free parameters.

Fermion DM can annihilate into SM particles either through Z_{BL} gauge boson or through singlet scalar (denoted by ϕ_1, the lightest of the neutral singlet scalars) by virtue of its mixing

Particles	$SU(3)_c \times SU(2)_L \times U(1)_Y \times U(1)_{B-L}$
$H = \begin{pmatrix} H^+ \\ H^0 \end{pmatrix}$	$(1, 2, \frac{1}{2}, 0)$
$\eta = \begin{pmatrix} \eta^+ \\ \eta^0 \end{pmatrix}$	$(1, 2, \frac{1}{2}, \frac{1}{3})$
$\Delta = \begin{pmatrix} \delta^+/\sqrt{2} & \delta^{++} \\ \delta^0 & -\delta^+/\sqrt{2} \end{pmatrix}$	$(1, 3, 1, \frac{2}{3})$
ϕ_1	$(1, 1, 0, \frac{4}{3})$
ϕ_2	$(1, 1, 0, 2)$

Table 2.3: Scalar content of the non-Minimal Model

with the SM Higgs, parametrised by ξ.We choose benchmark values for $M_{Z_{BL}}, g_{BL}, m_{\phi_1}, \xi$ and show the relic abundance of fermion DM as a function of its mass in figure 2.2. The resonances due to $2M_{DM} = M_{Z_{BL}}, 2M_{DM} = m_{\phi_1}$ are clearly visible in the plots, leading to minimum of the relic abundance as expected. The shallow nature of the $2M_{DM} = M_{Z_{BL}}$ resonance is due to the larger decay width of Z_{BL} compared to the singlet scalar ϕ_1.

2.3.4 Scalar Dark Matter in a non-Minimal Model

We can not have scalar DM in the minimal model discussed above, due to constraints from direct detection experiments. This is because the neutral scalar and pseudoscalars of both the doublets $\eta_{1,2}$ remain degenerate. This will give rise to a large scattering of scalar DM off nuclei through Z boson mediation, which is ruled out by the strong constraints coming from direct detection experiments, which we discuss in details in the next section. Here we consider a slight modification of the previous model so that a mass splitting can be introduced between the neutral scalar and pseudoscalar components of the scalar doublet. To break the degeneracy between scalar and pseudoscalar components of the doublet scalar, required to avoid Z boson mediated direct detection scattering, we simply incorporate the presence of a scalar triplet Δ with hypercharge 1 and $U(1)_{B-L}$ charge $\pm 2/3$. This will allow a term $\mu\eta_1\eta_1\Delta^\dagger$ or $\mu\eta_2\eta_2\Delta^\dagger$ breaking the degeneracy between scalar-pseudoscalar components of η_1, η_2 respectively. However this also allows other terms like $\eta_1 H \Delta \phi_1$ making the scalar DM unstable. Therefore we change the singlet scalar charges of the minimal model apart from incorporating the triplet. Also, it turns out that in this case, the correct neutrino mass can be generated at one loop with just one inert scalar doublet η. The modified scalar content of the model is shown in table 2.3. The Yukawa Lagrangian for leptons in this model can be written as

$$\begin{aligned} \mathcal{L}_Y = Y_e \overline{\ell_L} H e_R + Y_{i2}(\overline{\ell_L})_i i\tau_2 \eta^* N_2 + Y_{i3}(\overline{\ell_L})_i i\tau_2 \eta^* N_3 + f_1 \phi_1 N_2 N_2 \\ + f_2 \phi_1 N_3 N_3 + f_3 \phi_1 N_2 N_3 + f_4 \phi_2 N_2 N_4 + f_5 \phi_2 N_3 N_4 + \text{h.c.} \end{aligned} \tag{2.25}$$

It is clear from this Yukawa Lagrangian that the heavy neutrino N_1 remains massless at renormalisable level. One can however, introduce non-renormalisable operators contributing

to the right handed neutrino masses as

$$f_6\frac{1}{\Lambda}\phi_1^\dagger\phi_2 N_1 N_1 + f_7\frac{1}{\Lambda}\phi_1^2\phi_2 N_4 N_4$$

where Λ is the unknown cut-off scale above the scale of $U(1)_{B-L}$ symmetry. The scalar potential of the model can be written as

$$\begin{aligned}
V = &-\mu_H^2|H|^2 + \lambda_H|H|^4 + \left(\mu_\eta^2|\eta|^2 + \lambda_\eta|\eta|^4\right) + \sum_{i=1,2}\left(-\mu_{\phi_i}^2|\phi_i|^2 + \lambda_{\phi_i}|\phi_i|^4\right) \\
&+ \lambda_{H\eta}(\eta^\dagger\eta)(H^\dagger H) + \lambda'_{H\eta}(\eta^\dagger H)(H^\dagger\eta) + \sum_{i=1,2}\lambda_{H\phi_i}(\phi_i^\dagger\phi_i)(H^\dagger H) \\
&+ \mu_{\Delta\eta}\left((\eta^T\Delta^\dagger\eta) + \text{h.c.}\right) + \sum_{j=1,2}\lambda_{\eta\phi_j}(\eta^\dagger\eta)(\phi_j^\dagger\phi_j) + \lambda_\phi(\phi_1^\dagger\phi_1)(\phi_2^\dagger\phi_2) \\
&+ \mu_\Delta^2\text{Tr}\left[\Delta^\dagger\Delta\right] + \lambda_{\Delta 1}\left[\text{Tr}\left[\Delta^\dagger\Delta\right]\right]^2 + \lambda_{\Delta 2}\text{Tr}\left[\left[\Delta^\dagger\Delta\right]^2\right] + \text{Tr}\left[\Delta^\dagger\Delta\right]\left[\lambda_{\Delta H}(H^\dagger H)\right. \\
&\left.+ \lambda_{\Delta\eta}(\eta^\dagger\eta) + \sum_{i=1,2}\lambda_{\Delta\phi_i}(\phi_i^\dagger\phi_i)\right]
\end{aligned} \tag{2.26}$$

Also, the smallness of the vev of the neutral component of Δ does not arise naturally in the form of an induced vev after electroweak symmetry breaking. This is due to the absence of trilinear coupling of the form $HH\Delta^\dagger$ in the model. However, one needs to keep the vev of left triplet scalar small as the constraints from electroweak ρ parameter restricts it to $v_\delta \leq 2$ GeV [285]. In the SM, the ρ parameter is unity at tree level, given by

$$\rho = \frac{M_W^2}{M_Z^2\cos^2\theta_W}$$

where θ_W is the Weinberg angle. But in the presence of left scalar triplet vev, there arises additional contribution to the electroweak gauge boson masses which results in a departure of the ρ parameter from unity at tree level.

$$\rho = \frac{1+\frac{2v_\delta^2}{v^2}}{1+\frac{4v_\delta^2}{v^2}}$$

Experimental constraints on the ρ parameter $\rho = 1.00040 \pm 0.00024$ [285] forces one to have $v_\delta \leq 2$ GeV. Since, this can not be generated as an induced vev (which can be naturally small), one has to fine tune the quartic couplings and bare mass term of Δ scalar in order to generate such a small vev. However, if we introduce higher dimensional operators, then it is possible to generate an induced vev due to the existence of $\frac{1}{\Lambda}(H^T\Delta^\dagger H)(\phi_2^\dagger\phi_1)$ term. Using the notations for vev as before, we can write down the induced vev as

$$\langle\delta^0\rangle = \frac{v_\delta}{\sqrt{2}} = \frac{v^2u_1u_2}{4M_\Delta^2\Lambda}$$

This gives additional contribution to W boson mass as

$$M_W^2 = \frac{g^2v^2}{4} + \frac{g^2v_\delta^2}{2}$$

The neutral gauge boson mass matrix in the basis $(W_{3\mu}, B_\mu, B'_\mu)$ is given by

$$M_0^2 = \begin{pmatrix} \frac{1}{4}g^2v^2 + g^2v_\delta^2 & -\frac{1}{4}gg'v^2 - gg'v_\delta^2 & \frac{2}{3}gg_{BL}v_\delta^2 \\ -\frac{1}{4}gg'v^2 - gg'v_\delta^2 & \frac{1}{4}g'^2v^2 + g'^2v_\delta^2 & -\frac{2}{3}g'g_{BL}v_\delta^2 \\ \frac{2}{3}gg_{BL}v_\delta^2 & -\frac{2}{3}g'g_{BL}v_\delta^2 & \frac{4}{9}g_{BL}^2v_\delta^2 + g_{BL}^2\left(\frac{16}{9}u_1^2 + 4u_2^2\right) \end{pmatrix} \tag{2.27}$$

In the limit $v_\delta \ll v \ll u_{1,2}$, the non-zero eigenvalues are

$$M_Z^2 \approx \frac{1}{4}(g^2 + g'^2)(v^2 + 4v_\delta^2) + \frac{1}{4}(g^2 + g'^2)\frac{v^2v_\delta^2}{4u_1^2 + 9u_2^2}$$

$$M_{Z_{BL}}^2 \approx \frac{4}{9}g_{BL}^2(4u_1^2 + 9u_2^2 + v_\delta^2)$$

The vanishing eigenvalue corresponds to the massless photon. The other two mixing angles are given by

$$\cos^2\theta_W = \frac{g^2v^2 + 4g^2v_\delta^2}{4M_Z^2}$$

$$\tan\theta_m = \frac{8g_{BL}v_\delta^2}{3g'(v^2 + 4v_\delta^2)}$$

where θ_W corresponds to the usual Weinberg angle whereas θ_m corresponds to the mixing between Z and Z_{BL} gauge bosons. Clearly, this mixing is zero in the limit of $v_\delta \to 0$. The required value of v_δ is obtained from the mass splitting between scalar-pseudoscalar components of η. From the scalar potential given in (2.26), the mass splitting between η^{0r}, η^{0i} where $\eta^0 = (\eta^{0r} + i\eta^{0i})/\sqrt{2}$ is given by

$$M_{\eta^{0i}}^2 - M_{\eta^{0r}}^2 = 2\sqrt{2}\mu_{\Delta\eta}v_\delta$$

Thus, even if the mass splitting is as large as 50 GeV, considered in this work, we can generate a small $v_\delta < 2$ GeV, by tuning the trilinear mass parameter $\mu_{\eta\Delta}$ accordingly. Even for such maximum possible value of v_δ and $g_{BL} \sim g'$, the mixing between $Z - Z_{BL}$ comes out to be

$$\tan\theta_m \approx 1.7 \times 10^{-4}$$

We therefore, ignore the effects due to such gauge mixing in our calculations.

Light neutrino masses can be generated at one loop level through the diagram shown in figure 2.3. Similar to earlier analysis, here also the approximate structure of the light neutrino mass matrix can be obtained as

$$m_\nu = c_1 Y M_R^{-1} Y^T, \quad c_1 = \frac{M_{\eta^{0i}}^2 - M_{\eta^{0r}}^2}{32\pi^2} = \frac{2\sqrt{2}\mu_{\Delta\eta}v_\delta}{32\pi^2}$$

where Y, M_R are can be found from the Yukawa Lagrangian (2.25) in $(\nu_e, \nu_\mu, \nu_\tau), (N_2, N_3, N_4)$ basis as

$$Y = \begin{pmatrix} Y_{12} & Y_{13} & 0 \\ Y_{22} & Y_{23} & 0 \\ Y_{32} & Y_{33} & 0 \end{pmatrix}, \quad M_R = \begin{pmatrix} f_1u_1 & f_3u_1 & f_4u_2 \\ f_3u_1 & f_2u_1 & f_4u_2 \\ f_4u_2 & f_4u_2 & f_7\frac{u_1^2}{\Lambda} \end{pmatrix} \tag{2.28}$$

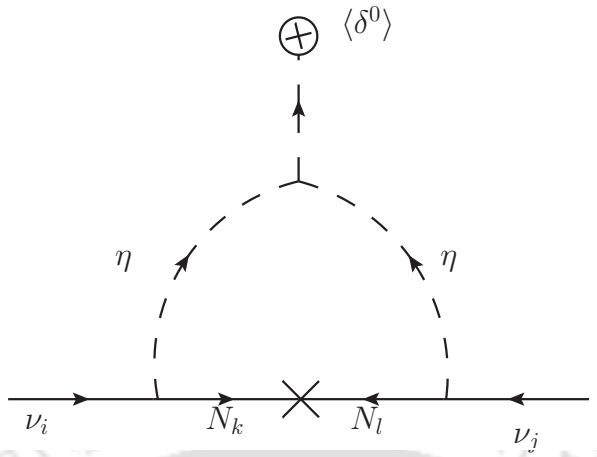

Figure 2.3: One loop neutrino mass for the particle content shown in table 2.1, 2.3

It is clear that the light neutrino mass matrix constructed from these give rise to a vanishing eigenvalue that is, a scenario with vanishing lightest neutrino mass. This is a similar prediction like the minimal model discussed before. On the other hand, one of the right handed neutrinos N_1 can remain light in this scenario, as its mass is generated only by dimension five operators. Such a light right handed neutrino can have interesting cosmological consequences.

The components of dark scalar doublet η acquire masses as

$$M^2_{\eta^\pm} = \mu^2_\eta + \frac{1}{2}\lambda_{H\eta}v^2 + \frac{1}{2}\lambda_{\eta\phi_1}u_1^2 + \frac{1}{2}\lambda_{\eta\phi_2}u_2^2,$$

$$\begin{aligned} M^2_{\eta^{0r}} &= \mu^2_\eta + \frac{1}{2}(\lambda_{H\eta} + \lambda'_{H\eta})v^2 + \sqrt{2}\mu_{\Delta\eta}v_\delta + \frac{1}{2}\lambda_{\eta\phi_1}u_1^2 + \frac{1}{2}\lambda_{\eta\phi_2}u_2^2 \\ &= M^2_{\eta^\pm} + \frac{1}{2}\lambda'_{H\eta}v^2 + \sqrt{2}\mu_{\Delta\eta}v_\delta, \end{aligned}$$

$$\begin{aligned} M^2_{\eta^{0i}} &= \mu^2_\eta + \frac{1}{2}(\lambda_{H\eta} + \lambda'_{H\eta})v^2 - \sqrt{2}\mu_{\Delta\eta}v_\delta + \frac{1}{2}\lambda_{\eta\phi_1}u_1^2 + \frac{1}{2}\lambda_{\eta\phi_2}u_2^2 \\ &= M^2_{\eta^\pm} + \frac{1}{2}\lambda'_{H\eta}v^2 - \sqrt{2}\mu_{\Delta\eta}v_\delta. \end{aligned} \tag{2.29}$$

Without loss of generality, we consider η^{0r} as the DM candidate which implies $\mu_{\Delta\eta} < 0, \frac{1}{2}\lambda'_{H\eta}v^2 + \sqrt{2}\mu_{\Delta\eta}v_\delta < 0$ so that the CP even neutral scalar η^{0r} is the lightest among the components of η and hence a stable DM candidate.

The new scalar fields discussed above can be constrained from the LEP I precision measurement of the Z boson decay width. In order to forbid the decay channel $Z \to \eta^{0r}\eta^{0i}$, one arrives at the constraint $M_{\eta^{0r}} + M_{\eta^{0r}} > M_Z$. In addition to this, the LEP II constraints roughly rule out the triangular region [286]

$$M_{\eta^{0r}} < 80 \ \text{GeV}, \quad M_{\eta^{0i}} < 100 \ \text{GeV}, \quad M_{\eta^{0i}} - M_{\eta^{0r}} > 8 \ \text{GeV}$$

The LEP collider experiment data restrict the charged scalar mass to $m_{\eta^\pm} > 70 - 90$ GeV [287]. The Run 1 ATLAS dilepton limit on such charged component of additional scalar doublets have also been discussed in [288] taking into consideration of specific masses of charged Higgs. Another important restriction on $M_{\eta^\pm}$ comes from the electroweak precision data (EWPD). Since the contribution of the additional scalar doublet η to electroweak S parameter is always small [289], we only consider the contribution to the electroweak T parameter here. The relevant contribution is given by [289]

$$\Delta T = \frac{1}{16\pi^2 \alpha v^2}[F(M_{\eta^\pm}, M_{\eta^{0i}}) + F(M_{\eta^\pm}, M_{\eta^{0r}}) - F(M_{\eta^{0i}}, M_{\eta^{0r}})] \tag{2.30}$$

where

$$F(m_1, m_2) = \frac{m_1^2 + m_2^2}{2} - \frac{m_1^2 m_2^2}{m_1^2 - m_2^2} \ln \frac{m_1^2}{m_2^2} \tag{2.31}$$

The EWPD constraint on ΔT is given as [290]

$$-0.1 < \Delta T + T_h < 0.2 \tag{2.32}$$

where $T_h \approx -\frac{3}{8\pi \cos^2\theta_W} \ln \frac{m_h}{m_Z}$ is the SM Higgs contribution to the T parameter [291].

Another important bound on such additional stable scalars can come from the LHC measurements of the SM Higgs invisible decay width. However, this constraint is applicable only for DM mass $M_{DM} < m_h/2$. The invisible decay width is given by

$$\Gamma(h \to \text{Invisible}) = \frac{\lambda_L^2 v^2}{64\pi m_h} \sqrt{1 - 4\, M_{DM}^2/m_h^2} \tag{2.33}$$

Here, $\lambda_L = (\lambda_{H\eta} + \lambda'_{H\eta})$. The latest constraint on invisible Higgs decay from the ATLAS experiment at the LHC is [292]

$$\text{BR}(h \to \text{Invisible}) = \frac{\Gamma(h \to \text{Invisible})}{\Gamma(h \to \text{Invisible}) + \Gamma(h \to \text{SM})} < 22\%$$

. We incorporate this bound on light scalar DM mass in the next section.

The relic abundance of scalar DM for some benchmark values of mass splitting, DM-Higgs couplings are shown in figure 2.4, 2.5 for low and high mass regimes respectively. The effects of coannihilations between different components of the scalar doublet η are very dominant for small mass splitting $\Delta m_\eta = 5$ GeV, as can be seen from the left panel of the figure 2.4. The multiple resonances shown in the left panel of figure 2.4 corresponds to $W^\pm, Z$ and SM Higgs (h) mediated (co)annihilations. As we increase the mass splitting to 50 GeV, such coannihilation effects disappear and only the DM annihilation through SM Higgs remains, as can be seen from the single resonance shown in the right panel plot of figure 2.4. In fact, for low mass DM such small mass splitting is disfavoured from LEP II data as mentioned above. However, we calculate the relic abundance in this regime to see the interesting differences originating from enhanced coannihilations. In the high mass regime, apart from the usual Higgs portal and electroweak gauge boson portal interactions, we also include the Z_{BL} mediated annihilations for benchmark values of $M_{Z_{BL}}, g_{BL}$. As seen from the figure 2.5, the impact of this Z_{BL} portal on scalar DM relic abundance is very minimal. The relic

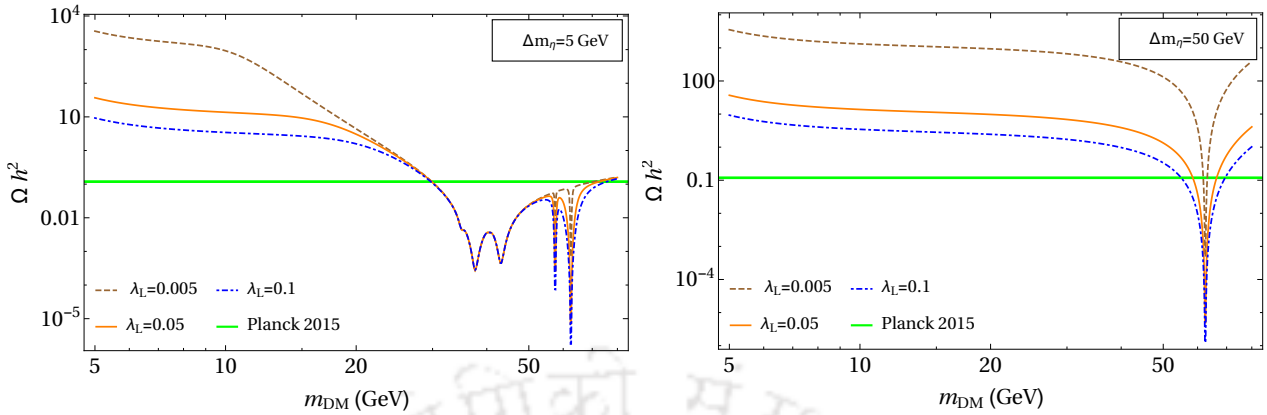

Figure 2.4: Relic abundance of scalar doublet DM η^{0r} as a function of its mass for different benchmark values of DM-Higgs coupling, in the low mass regime. The mass splitting between $\eta^{0i}, \eta^{\pm}$ and η^{0r} is fixed at 5 GeV, 50 GeV in the left and right panel plots respectively.

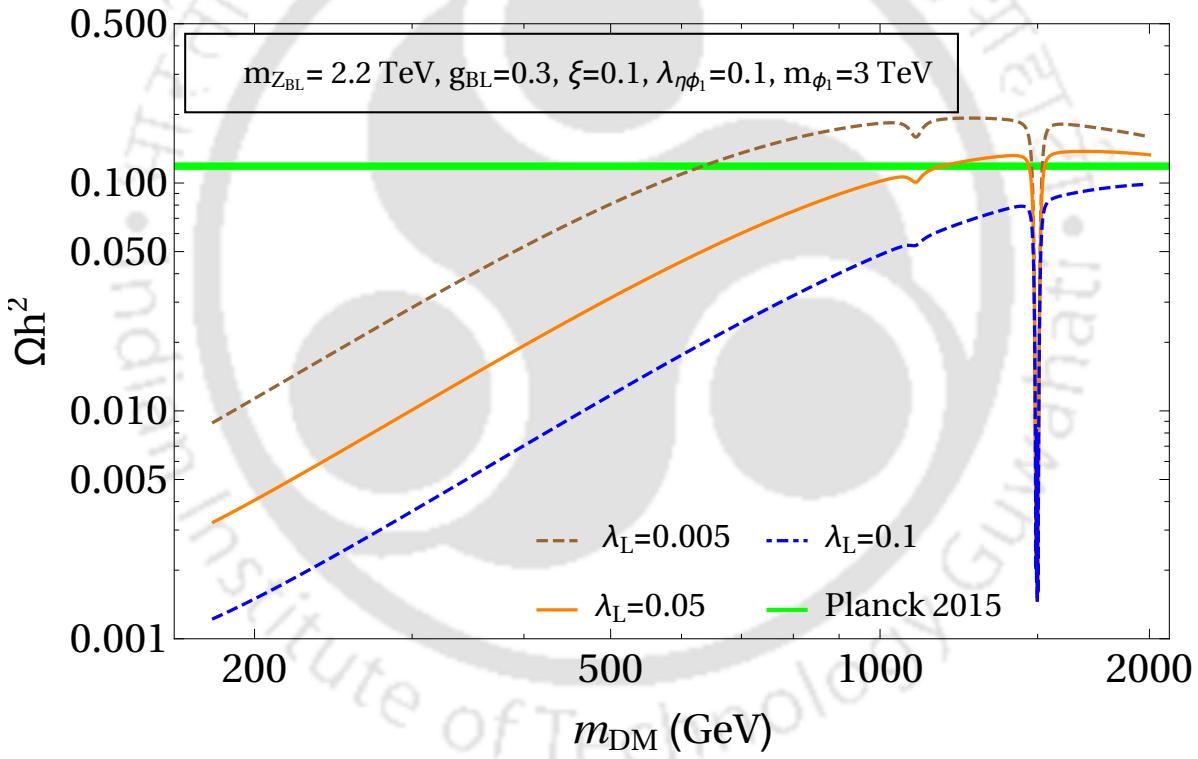

Figure 2.5: Relic abundance of scalar doublet DM η^{0r} as a function of its mass for different benchmark values of DM-Higgs coupling, in the high mass regime. The mass splitting between $\eta^{0i}, \eta^{\pm}$ and η^{0r} is fixed at 5 GeV.

abundance in the high mass regime is mainly dominated by the usual DM-Higgs coupling λ_L and the mass splitting Δm_η. We also take the singlet scalar ϕ_1 mediated annihilations of scalar DM and its contribution to the relic abundance. As can be seen from figure 2.5, this gives rise to a new resonance due to s channel mediation of ϕ_1 resulting in a new allowed

region of scalar doublet DM in the high mass regime. Due to smaller decay width of ϕ_1 compared to Z_{BL}, this resonance is efficient enough to bring the usually overproduced DM in high mass regime to the allowed range.

2.3.5 Direct Detection of Dark Matter

Apart from the relic abundance constraints from Planck experiment, there exists strict bounds on the DM nucleon cross section from direct detection experiments like LUX [53], PandaX-II [56, 57] and Xenon1T [55]. For fermion DM, there are two ways through which it can scatter off nuclei: one is mediated by Z_{BL} and the other mediated by scalars. The scalar mediated interactions occur due to mixing of singlet scalars of the model with the SM Higgs boson. Both these interactions give rise to spin independent DM-nuclei scattering only due to the absence of axial or pseudoscalar type couplings of the mediators with the quarks. Adopting the general formalism given in [293], the Z_{BL} mediated DM-nucleon cross section is found to be

$$\sigma_{SI} = \frac{g_{BL}^4 v^2 m_\chi^2 m_n^4}{2\pi M_{Z_{BL}}^4 (m_n + m_\chi)^4} \tag{2.34}$$

where m_n is the mass of nucleon, m_χ is the DM mass and $v \approx 0.1\%c$ is the typical speed of DM particle. The scalar mediated DM-nucleon scattering cross section is

$$\sigma_{SI} = \frac{\lambda_{\chi\phi}^2 \mu_{\chi n}^2 \xi^2}{\pi m_{\phi_1}^4} f_{n,p}^2 \tag{2.35}$$

where $\mu_{\chi n}$ is the reduced mass of the DM-nucleon system, m_{ϕ_1} is the mass of the mediator and ξ is the mixing parameter between ϕ_1 and the SM Higgs boson. Also, $\lambda_{\chi\phi}$ is the coupling between DM and scalar ϕ_1 and the parameters $f_{n,p}$ correspond to scalar nucleon couplings, taken as input from QCD calculations [294].

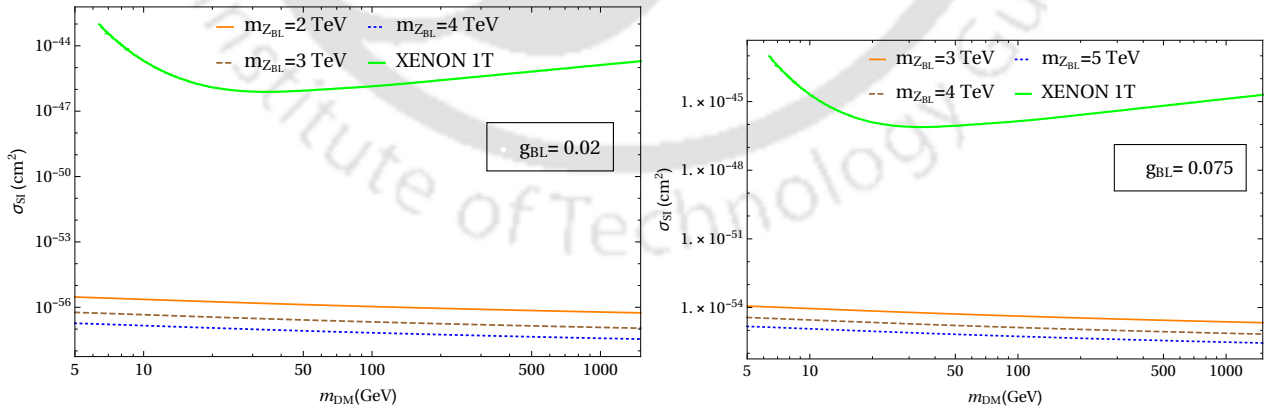

Figure 2.6: Spin independent direct detection cross section for fermion DM mediated by Z_{BL} for different benchmark values of $g_{BL}, M_{Z_{BL}}$.

We first show the direct detection cross section mediated by the Z_{BL} boson for different benchmark values of Z_{BL} masses and couplings g_{BL}. As can be seen from figure 2.6, the

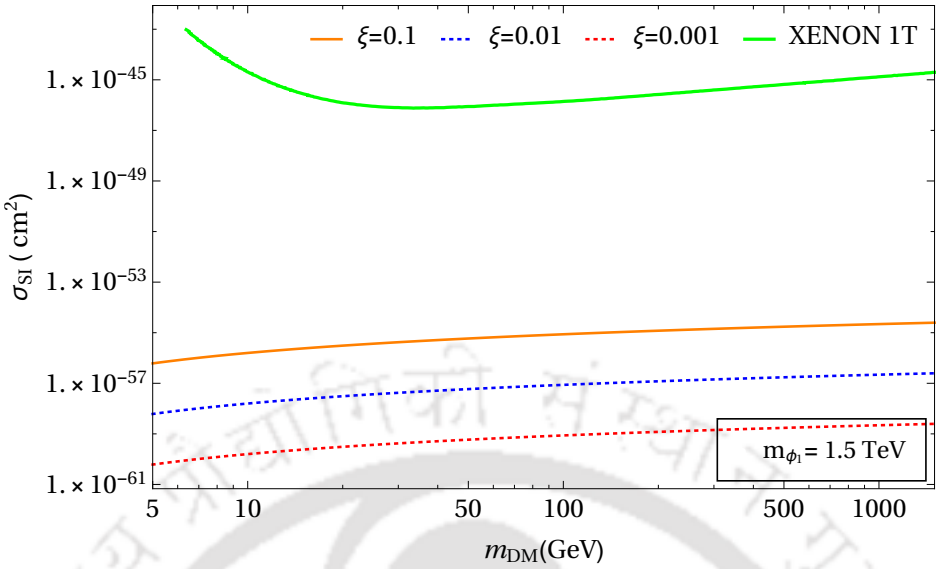

Figure 2.7: Spin independent direct detection cross section for fermion DM mediated by singlet scalar ϕ_1 for different benchmark values of ϕ_1-Higgs mixing ξ.

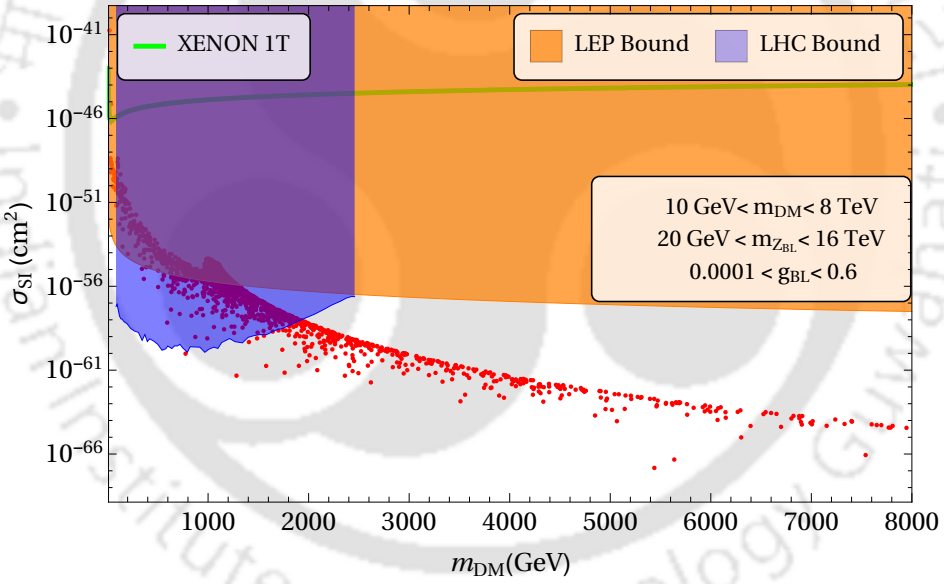

Figure 2.8: Spin independent direct detection cross section for fermion DM mediated by Z_{BL} for randomly varied $M_{DM}, M_{Z_{BL}}, g_{BL}$ in the range denoted by the labels.

model can survive the Xenon1T bound even if the Z_{BL} mass is close to a few TeV and $g_{BL} \sim 0.075, 0.02$. These bounds are in fact weaker than the LEP II bound $M_{Z_{BL}}/g_{BL} \geq 7$ TeV mentioned earlier. This can be realised by taking even smaller values of Z_{BL} mass and larger values of gauge coupling g_{BL} as the spin independent direct detection cross section remains very much suppressed compared to the Xenon1T bound. However, the latest LHC bound can rule out such combinations of $M_{Z_{BL}}, g_{BL}$ as we discuss below. We also show the scalar mediated direct detection cross section for fermion DM, using different benchmark

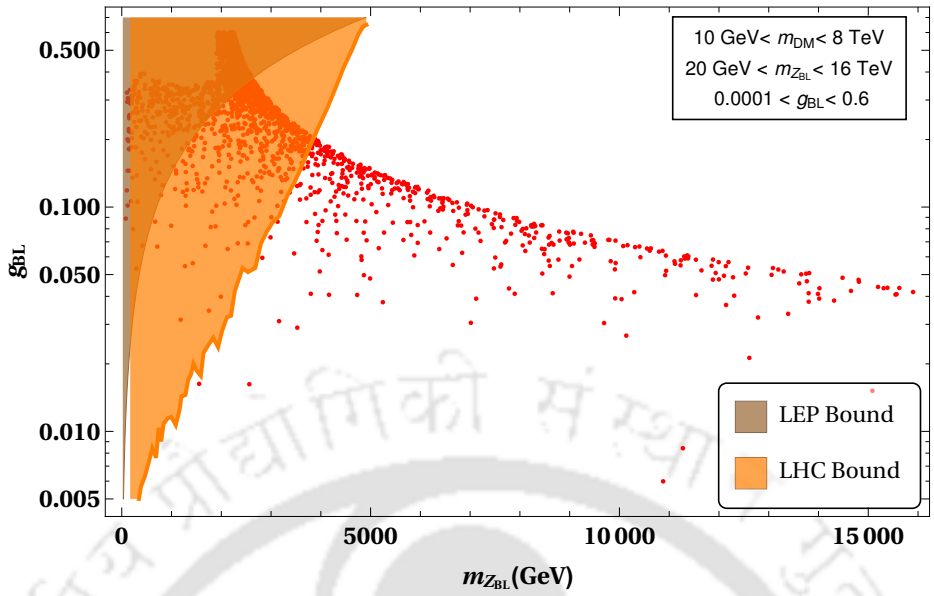

Figure 2.9: Parameter space allowed from relic abundance and direct detection criteria of fermion DM annihilating purely through Z_{BL} portal for randomly varied $M_{DM}, M_{Z_{BL}}, g_{BL}$ in the range denoted by the labels. The excluded parts of parameter space corresponding to LEP, LHC are shown as shaded regions.

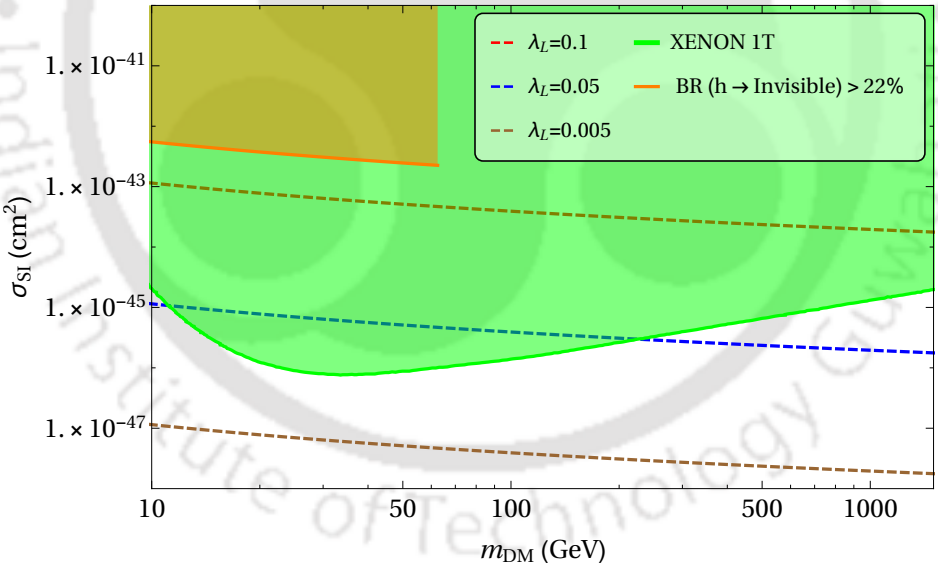

Figure 2.10: Spin independent direct detection cross section for scalar DM for different benchmark values of DM-Higgs couplings. The region ruled out from Xenon1T and LHC results are shown as shaded regions.

values of ϕ_1-Higgs mixing ξ in figure 2.7 and found them to be lying within the Xenon1T upper limit.

To find the allowed parameter space of fermion DM model, we perform a random scan of three parameters $M_{DM}, M_{Z_{BL}}, g_{BL}$ and plot the direct detection cross section for only those

parameters that satisfy the relic abundance criteria. The plot is shown in figure 2.8. The scalar mediated interactions are not taken into account in this scan, so that the strongest constraint on the new gauge sector can be obtained. It shows that DM masses in the entire mass range scanned $M_{DM} \in (10, 8000)$ GeV remain allowed by the Xenon1T constraint for the chosen range of gauge sector parameters $g_{BL} \in (10^{-4}, 0.6), M_{Z_{BL}} \in (20, 16000)$ GeV. We also show the LEP II bound for comparison in figure 2.8. The exclusion line corresponding to this is derived by using $M_{Z_{BL}}/g_{BL} = 7$ TeV in the direct detection formula given by (2.34). It is interesting that the LEP II bound $M_{Z_{BL}}/g_{BL} \geq 7$ TeV remains stronger than the Xenon1T bound and has the potential of ruling few points in the low mass regime of DM. We also include the latest bound from the LHC on the mass of Z_{BL} gauge boson and corresponding coupling g_{BL} given in [295] for Z_{BL} masses all the way upto 5 TeV. Since fermion DM relic is satisfied for $m_{\rm DM} \approx M_{Z_{BL}}/2$, there arises a sharp cut-off at $m_{\rm DM} = 2.5$ TeV, since the LHC bound is available only till $M_{Z_{BL}} = 5$ TeV. Thus, the latest LHC bound is stronger than both Xenon1T and LEP bounds in the low mass regime of DM. We also show the corresponding parameter space in $g_{BL} - M_{Z_{BL}}$ plane in figure 2.9. For simplicity, in the scanned plot of figure 2.9, we apply the most conservative Xenon1T bound, corresponding to DM mass of 35 GeV [55] and minimum of the exclusion line shown before.

For scalar DM considered in this work, the relevant spin independent scattering cross section mediated by the SM Higgs boson is given as [289]

$$\sigma_{\rm SI} = \frac{\lambda_L^2 f^2}{4\pi} \frac{\mu^2 m_n^2}{m_h^4 m_{DM}^2} \tag{2.36}$$

where $\mu = m_n m_{DM}/(m_n + m_{DM})$ is the DM-nucleon reduced mass and λ_L is the quartic coupling involved in DM-Higgs interaction. A recent estimate of the Higgs-nucleon coupling f gives $f = 0.32$ [296] although the full range of allowed values is $f = 0.26 - 0.63$ [297]. We show the Higgs mediated direct detection cross section for scalar doublet DM in figure 2.10 for different benchmark values of λ_L. We find that for large values of quartic coupling $\lambda_L \sim 0.1$, scalar DM mass upto a TeV can be ruled out by the Xenon1T bound. We also show the region ruled out by the LHC limit on the Higgs invisible decay width and found this bound to be much weaker than the latest Xenon1T limits.

2.3.6 Indirect Detection of Dark Matter

Apart from direct detection experiments, DM can also be probed at different indirect detection experiments that are looking for SM particles produced either through DM annihilations or via DM decay in the local Universe. Among these final states, photon and neutrinos, being neutral and stable can reach the indirect detection experiments without getting affected much by intermediate regions of space on the way from source to to the detector. If the DM is of WIMP type, like the one we are discussing in the present work, these photons lie in the gamma ray regime that can be measured at space based telescopes like the Fermi Large Area Telescope (LAT) or ground based telescopes like MAGIC. Here we constrain the DM parameters from the indirect detection bounds arising from the global analysis of the Fermi-LAT and MAGIC observations of dSphs [8].

The observed differential gamma ray flux produced due to DM annihilations is given by

$$\frac{d\Phi}{dE}(\triangle\Omega) = \frac{1}{4\pi}\langle\sigma v\rangle\frac{J(\triangle\Omega)}{2M_{\rm DM}^2}\frac{dN}{dE} \tag{2.37}$$

where $\triangle\Omega$ is the solid angle corresponding to the observed region of the sky, $\langle\sigma v\rangle$ is the thermally averaged DM annihilation cross section, dN/dE is the average gamma ray spectrum per annihilation process and the astrophysical J factor is given by

$$J(\triangle\Omega) = \int_{\triangle\Omega} d\Omega' \int_{LOS} dl\rho^2(l,\Omega'). \tag{2.38}$$

In the above expression, ρ is the DM density and LOS corresponds to line of sight. Thus, measuring the gamma ray flux and using the standard astrophysical inputs, one can constrain the DM annihilation into different final states like $\mu^+\mu^-, \tau^+\tau^-, W^+W^-, b\bar{b}$. Since DM can not couple to photons directly, gamma rays can be produced from such charged final states. Using the bounds on DM annihilation to these final states [8], we show the status of our model for different benchmark values of parameters.

Since the constraint on DM annihilation given in [8] was for 100% annihilations in to a particular final state, we use the appropriate weight factor $w < 1$ while comparing the model prediction with the constraints. For example, to compare the DM annihilation to $\mu^+\mu^-$ final state with the Fermi-LAT constraint, we multiply $\sigma v(\text{DM DM} \to \mu^+\mu^-)$ by the weight factor

$$w = \frac{\sigma v(\text{DM DM} \to \mu^+\mu^-)}{\sigma v(\text{DM DM} \to \text{All})}.$$

This is equivalent to dividing the Fermi-LAT bound by $w < 1$ and comparing with $\sigma v(\text{DM DM} \to \mu^+\mu^-)$. Since there are multiple annihilation channels to different final states, the Fermi-LAT constraints on individual final states are weak for most of the cases. Only in the case of scalar DM annihilations into W^+W^- final states, the constraints can be very severe as scalar DM into W^+W^- is the most dominant annihilation channel for certain mass range of DM.

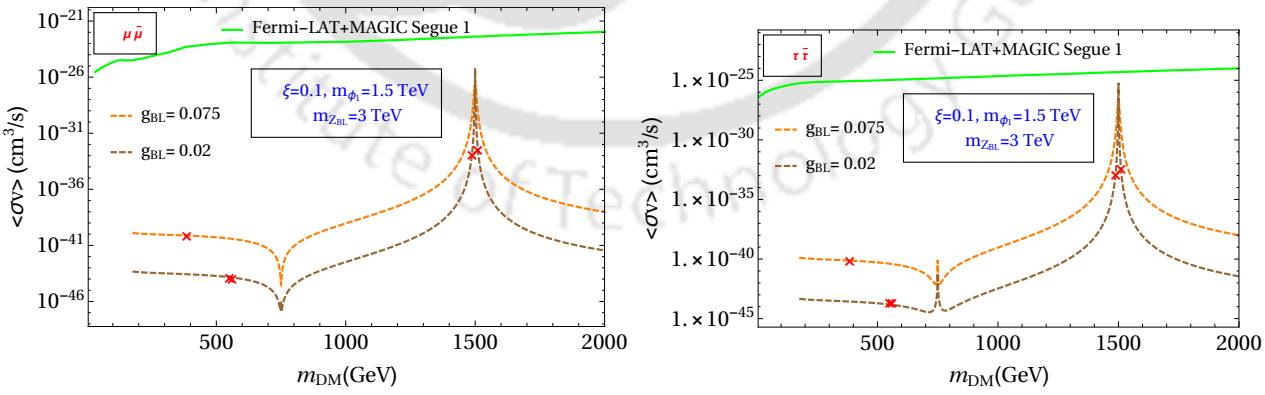

Figure 2.11: Fermion DM annihilations into $\mu^+\mu^-, \tau^+\tau^-$ compared against the indirect detection bounds. The points denoted by $\times$ correspond to the ones satisfying relic abundance criteria.

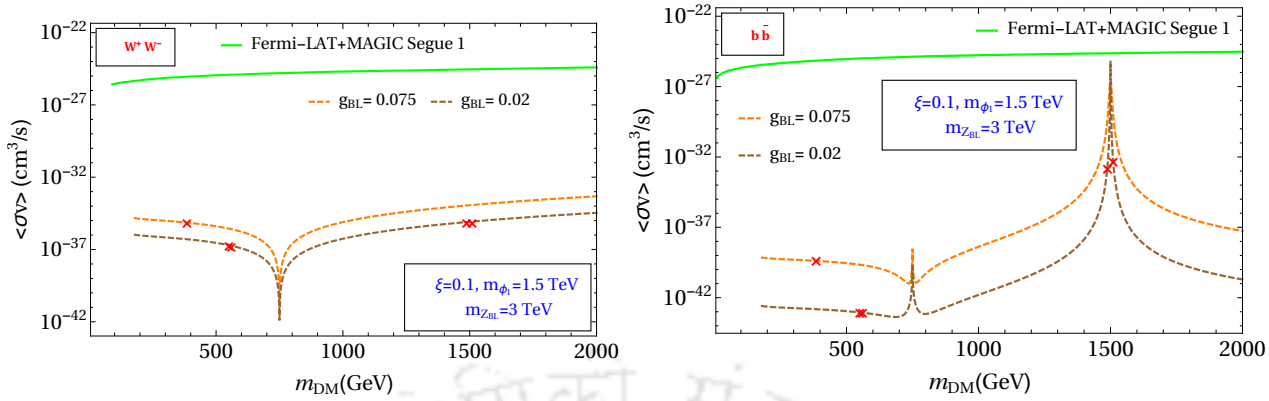

Figure 2.12: Fermion DM annihilations into $W^+W^-, b\bar{b}$ compared against the indirect detection bounds. The points denoted by $\times$ correspond to the ones satisfying relic abundance criteria.

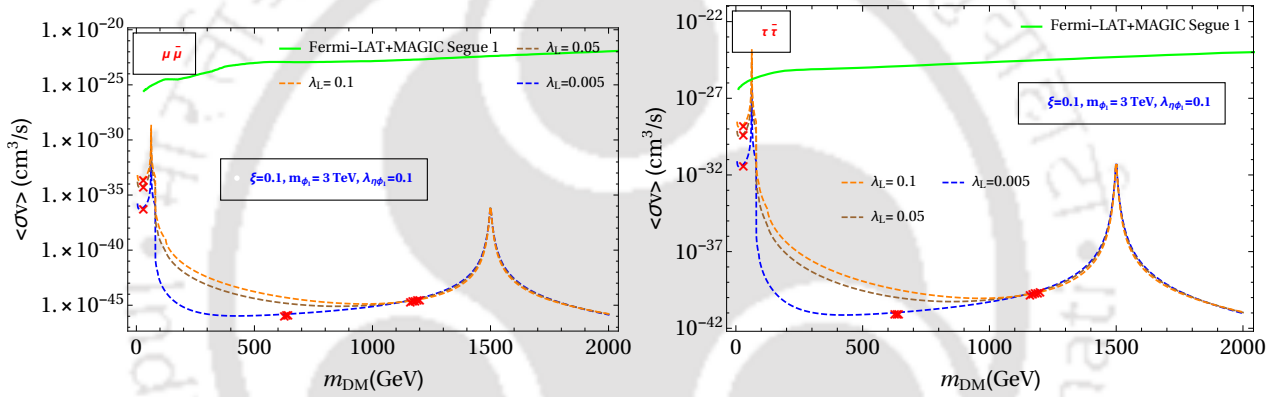

Figure 2.13: Scalar DM annihilations into $\mu^+\mu^-, \tau^+\tau^-$ compared against the indirect detection bounds. The mass splitting between scalar doublet components is $\Delta m_\eta = 5$ GeV. The points denoted by $\times$ correspond to the ones satisfying relic abundance criteria.

We first show the fermion DM annihilation to these final states in figure 2.11 and 2.12 for different benchmark points including the ones used to show the relic abundance as well. We also mark the points by a $\times$ which correspond to the correct relic abundance of fermion DM. It can be seen that, fermion DM having mass near the resonance region $M_{DM} = m_{\phi_1}/2$ for the scalar mediated annihilations, some of the annihilations can almost saturate the Fermi-LAT plus MAGIC bounds. On the other hand, the bounds from W^+W^- final states is weaker even for mixing between singlet scalar and SM Higgs ξ as large 0.1, as can be seen from the left panel of figure 2.12. However, as the relic abundance plots in figure 2.2 shows, the DM remains under-abundant in the resonance region and hence such scenarios are still allowed from indirect detection bounds. We apply the relic bound on the indirect detection plots shown in figure 2.11 and 2.12 by marking those points of $m_{\rm DM}$ which satisfy the correct relic abundance criteria, as can be seen from figure 2.2.

Similar observation is also made for the scalar DM annihilations into these final states as shown in figure 2.13 and 2.14. Although the DM annihilations to $\tau^+\tau^-, b\bar{b}$ saturates the experimental limits only near the Higgs resonance $M_{DM} = m_h/2$, the limit on DM

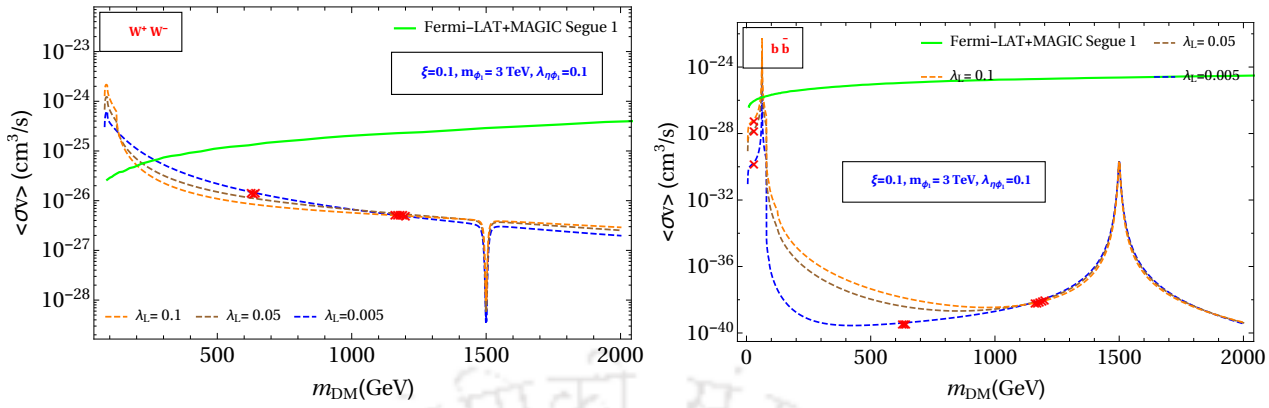

Figure 2.14: Scalar DM annihilations into $W^+W^-, b\bar{b}$ compared against the indirect detection bounds. The mass splitting between scalar doublet components is $\Delta m_\eta = 5$ GeV. The points denoted by $\times$ correspond to the ones satisfying relic abundance criteria.

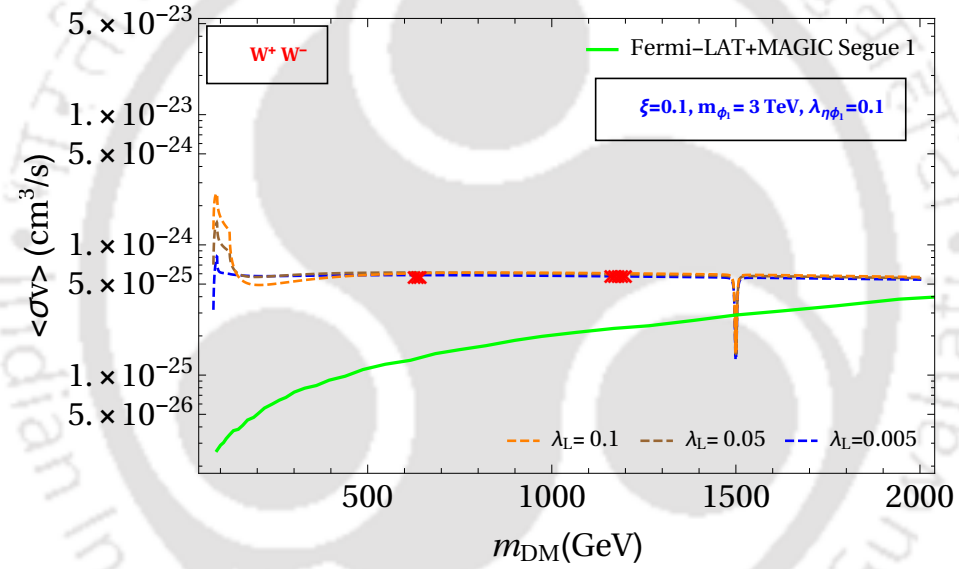

Figure 2.15: Scalar DM annihilations into W^+W^- compared against the indirect detection bounds. The mass splitting between scalar doublet components is $\Delta m_\eta = 50$ GeV. The points denoted by $\times$ correspond to the ones satisfying relic abundance criteria.

annihilations into W^+W^- is more severe and it can rule out DM mass upto a few hundred GeV's depending on the mass splitting between dark scalar doublet components as well as DM-Higgs coupling λ_L. This is because of the large annihilation cross section of scalar DM into W^+W^- pairs for $m_{\rm DM} > M_W$ that can not be suppressed due to its sole dependence on gauge couplings. However, in the high mass region $m_{\rm DM} > M_W$, the relic remains under-abundant as seen from the figure 2.5, specially in the range of DM mass where the constraints from W^+W^- final state are very strong. Beyond a mass of 500 GeV, it is possible to satisfy relic as well as indirect detection constraints simultaneously. But for larger mass splitting say $\Delta m_\eta = 50$ GeV, even the high mass region is ruled out by the strong constraints from indirect detection, as can be seen from figure 2.15. In the low mass region, specially near

the Higgs resonance, the indirect detection bounds can be severe as can be seen clearly by comparing the relic abundance plot in figure 2.4 with the indirect detection ones in figure 2.13. We in fact denote the points which satisfy the relic abundance criteria in the indirect detection plots shown in figure 2.13 and 2.14 and find that all of them remain allowed currently from the Fermi-LAT plus MAGIC bounds. On the other hand, for large splitting, the points satisfying correct relic are disallowed by the indirect detection bounds as seen from figure 2.15.

It should be noted that apart from Fermi-LAT and MAGIC, there are other experiments which put equally strong bounds on DM annihilations to different charged particle final states. For example, there exists strong constraints on DM annihilations from ten years of observations with HESS experiment, as reported recently in [298, 299]. As seen from [299], the HESS constraints on DM annihilations into $\tau^+\tau^-$ final state is very strong and can reach the $\langle\sigma v\rangle$ values expected for DM annihilating at thermal relic cross section. However, since DM in our model remains under-abundant near the resonance regions that can saturate these indirect detection bounds, it does not rule out the allowed parameter space from relic criteria, as discussed above in the context of Fermi-LAT plus MAGIC bounds.

2.3.7 Lepton Flavour Violation

Charged lepton flavour violating decay is a promising process to study from BSM physics point of view. In the SM, such a process occurs at loop level and is suppressed by the smallness of neutrino masses, much beyond the current experimental sensitivity [300]. Therefore, any future observation of such LFV decays like $\mu \to e\gamma$ will definitely be a signature of new physics beyond the SM. In the present model, such new physics contribution can come from the charged component of the additional scalar doublet η going inside a loop along with singlet fermions. Adopting the general prescriptions given in [301], the decay width of $\mu \to e\gamma$ can be calculated as

$$\Gamma(\mu \to e\gamma) = \frac{Y^4 \left(m_\mu^2 - m_e^2\right)^3 \left(m_\mu^2 + m_e^2\right)}{4096\pi^5 m_\mu^3 m_{\eta^-}^4} \left[\frac{\left((t-1)(t(2t+5)-1) + 6t^2 \ln t\right)^2}{144(t-1)^8}\right] \tag{2.39}$$

where $t = m_N^2/m_{\eta^-}^2$. The corresponding branching ratio can be found by

$$\mathrm{BR}(\mu \to e\gamma) \approx \frac{\Gamma(\mu \to e\gamma)}{\Gamma_\mu}$$

where $\Gamma_\mu \approx 2.996 \times 10^{-19}$ GeV denotes the total decay width of muon. The latest bound from the MEG collaboration is $\mathrm{BR}(\mu \to e\gamma) < 4.2 \times 10^{-13}$ at 90% confidence level [300].

We consider a scalar DM scenario so that the singlet neutrinos are heavier than η. By keeping the mass splitting within η to be 5 GeV, we show the new physics contribution to $\mu \to e\gamma$ in figure 2.16 for different benchmark values of Yukawa couplings and mass ratio between singlet fermion and scalar DM. It is seen that even for Yukawa couplings as small as 10^{-2}, this new physics contribution can saturate the experimental upper limit from MEG. We get similar features, even if we consider singlet fermion DM instead of scalar one.

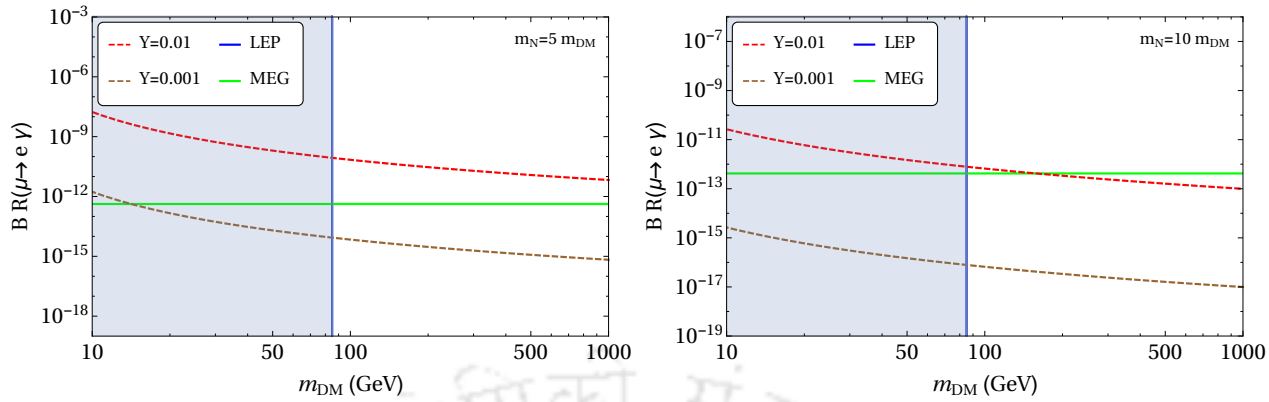

Figure 2.16: BR($\mu \to e\gamma$) as a function of scalar DM mass for different values of Yukawa couplings and singlet fermion mass. The mass splitting between scalar doublet components is $\Delta m_\eta = 5$ GeV.

It should be noted that there are other LFV processes like $\mu^- \to e^+e^-e^-$ or $\mu^- \to e^-$ conversion in nuclei which can get additional contribution at one loop level in this model. For details of such processes, one can refer to [302]. For the chosen benchmark values of heavy singlet neutrinos and DM mass range, the contribution to BR($\mu \to e\gamma$) from new physics remains dominant over others, as shown by the authors of [302]. Also, the constraints on BR($\mu \to e\gamma$) has got updated by MEG experiment recently whereas the bounds on other processes are relatively older [303, 304].

Another interesting flavour observable (a lepton number violating one) is the neutrinoless double beta decay which is tightly constrained from null results at several experiments mentioned earlier [305]. However, the present models do not have any extra contributions to this process at tree level. Therefore, the contribution to this process will be dominated by standard light neutrino mediation which can be kept within limits for hierarchical light neutrino spectrum. Since our models naturally lead to a hierarchical pattern with the lightest neutrino being massless, these bounds can be satisfied naturally.

2.3.8 Collider Signatures

Since all the SM fermions are charged under the $U(1)_{B-L}$ gauge interaction, there can be significant production of the corresponding Z_{BL} gauge boson in proton proton collisions [259, 306]. Such heavy gauge boson, if produced at colliders, can manifest itself as a narrow resonance through its decay into dileptons, say. Since the $U(1)_{B-L}$ charges of the leptons are three times that of quarks, the decay of Z_{BL} into leptons are more in spite of the extra colour factor of quarks. This can be seen from the plot in figure 2.17 showing the branching ratio of Z_{BL} into different final states, along with the total decay width.

Although the branching ratio does not depend upon the value of gauge coupling g_{BL}, the production of this gauge boson in proton proton collisions is sensitive to this. If this coupling is comparable to the electroweak gauge couplings, then such a gauge boson can be produced significantly in colliders. The latest measurement by the ATLAS experiment at 13 TeV LHC constrains such gauge boson mass to be heavier than $3.6 - 4.0$ TeV depending on whether

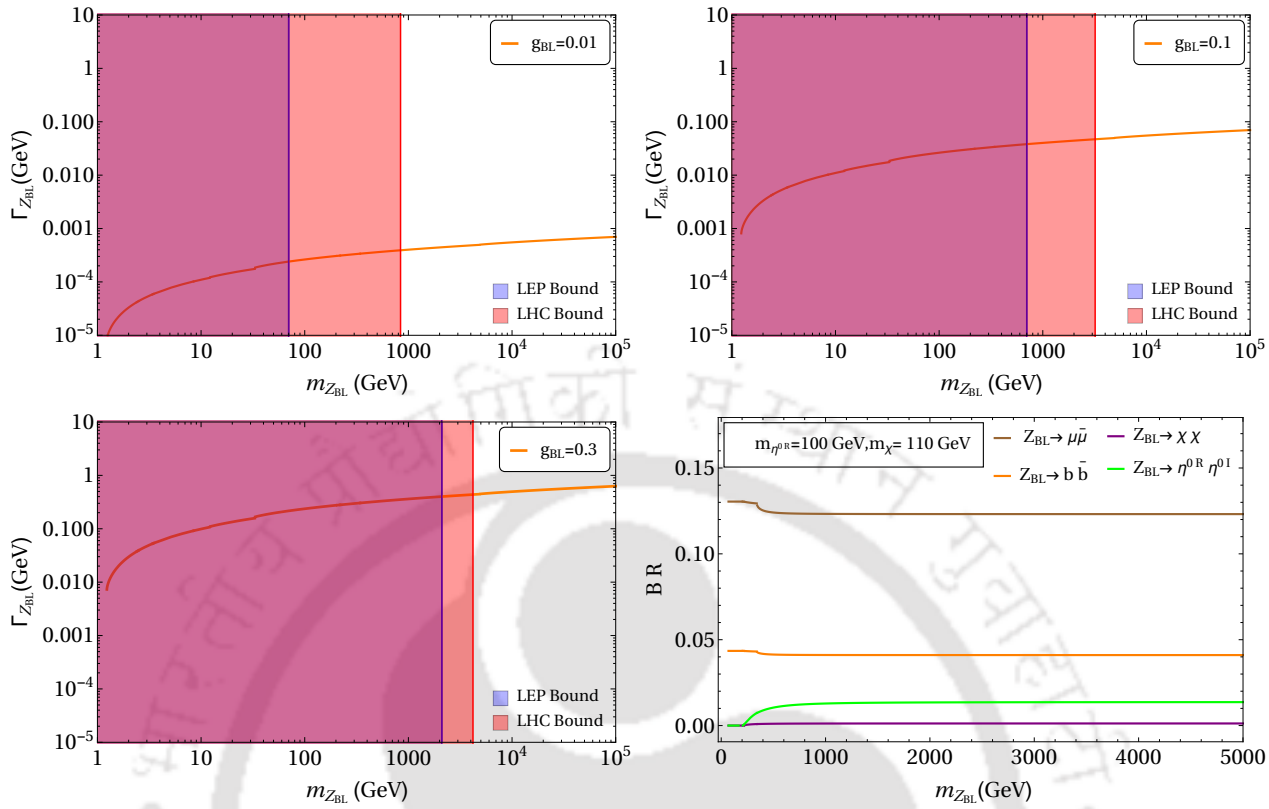

Figure 2.17: Decay width and branching ratio of Z_{BL} into different final states. The shaded regions in the first three plots correspond to the regions ruled out by the LEP and LHC bounds.

the final state leptons are of muon or electron type [295]. The corresponding bound for tau lepton final states measured by the CMS experiment at 13 TeV LHC is slightly weaker, with the lower bound on Z_{BL} mass being 2.1 TeV [307]. In deriving the bounds for $e^+e^-, \mu^+\mu^-$ final states, the corresponding gauge coupling was chosen to be $g_{BL} \approx 0.28$. Therefore, such bounds can get weaker if we consider slightly smaller values of gauge couplings.

Table 2.4: Cross Sections (pb) for $pp \to \mu\bar{\mu}$

$M_{Z_{BL}}(TeV)$	$g_{BL} = 0.01$	$g_{BL} = 0.05$
2	1.44×10^{-5}	3.600×10^{-4}
3	1.29×10^{-6}	3.237×10^{-5}
4	1.52×10^{-7}	3.802×10^{-6}
5	1.91×10^{-8}	4.776×10^{-7}

The differential cross section with respect to the invariant final state dilepton mass M_{ll} is

$$\frac{d\sigma}{dM_{ll}} = \sum_{a,b} \int_{\frac{M_{ll}^2}{E_{CM}^2}}^{1} dx \frac{2M_{ll}}{xE_{CM}^2} f_a(x,Q^2) f_b\left(\frac{M_{ll}^2}{xE_{CM}^2}, Q^2\right) \hat{\sigma}(q\bar{q} \to Z_{BL} \to l^+l^-), \qquad (2.40)$$

Table 2.5: Cross Sections (pb) for $pp \to \chi\chi$

$M_{Z_{BL}}$(TeV)	$g_{BL} = 0.01$	$g_{BL} = 0.05$
2	5.680×10^{-7}	1.420×10^{-5}
3	5.129×10^{-8}	1.283×10^{-6}
4	6.040×10^{-9}	1.510×10^{-7}
5	7.570×10^{-10}	1.898×10^{-8}

Table 2.6: Cross Sections (pb) for $pp \to \eta^{0r}\eta^{0i}$

$M_{Z_{BL}}$(TeV)	$g_{BL} = 0.01$	$g_{BL} = 0.05$
2	1.576×10^{-6}	3.938×10^{-5}
3	1.432×10^{-7}	4.208×10^{-6}
4	1.684×10^{-8}	4.208×10^{-7}
5	2.117×10^{-9}	5.294×10^{-8}

with f_a being the parton distribution function for a parton denoted by 'a' and $E_{CM} = 13$ TeV is the LHC centre of mass energy. The cross section $\hat{\sigma}$ is given by [259]

$$\hat{\sigma} = \frac{1}{81}\frac{g_{BL}^4}{4\pi}\frac{M_{ll}^2}{(M_{ll}^2 - M_{Z_{BL}}^2)^2 + M_{Z_{BL}}^2\Gamma_{Z_{BL}}^2} \tag{2.41}$$

Since the decay width of Z_{BL} boson is narrow, the cross section is almost determined by the integral in the vicinity of the resonance. In the narrow width approximation we can use

$$\sigma(pp \to Z_{BL} \to l^+l^-) = \sigma(pp \to Z_{BL})\text{BR}(Z_{BL} \to l^+l^-) \tag{2.42}$$

We first calculate the production cross section $\sigma(pp \to Z_{BL})$ for benchmark values of $g_{BL}, M_{Z_{BL}}$ at 13 TeV LHC and then multiply by the respective branching ratio to find the final state cross sections. We particularly choose some benchmark values of $g_{BL}, M_{Z_{BL}}$ which are still allowed by the latest LHC constraints [295]. The numerical values of these cross sections for different values of $g_{BL}, M_{Z_{BL}}$ are shown in table 2.4, 2.5, 2.6 for $\mu^+\mu^-, \chi\chi$ and η^{0r}, η^{0i} final states respectively. Although the last two final states just correspond to missing energies depending on fermionic or bosonic nature of DM, the leptonic final states can saturate the ATLAS bounds [295]. In fact, for $g_{BL} = 0.05$, Z_{BL} mass of 2 TeV can saturate the ATLAS upper bounds if we compare the results in table 2.4 with the results of [295]. A more detailed analysis of the model from collider point of view is beyond the scope of the present work and we leave it for future discussions.

2.3.9 Results and Discussion

We have studied a $U(1)_{B-L}$ gauge extension of the SM that can explain the origin of neutrino mass and DM simultaneously. The new fermions that take part in making the $U(1)_{B-L}$ model anomaly free can not only provide a stable DM candidate, but can also give rise to light neutrino masses at one loop level. There also exists additional scalar doublets apart from the SM Higgs, that take part in the radiative generation of neutrino mass. We discuss

two different versions of the model, one with fermion singlet DM and the other with scalar doublet DM. We first calculate the mass spectra for both the models after the spontaneous symmetry breaking. We find that for the minimal scalar content, both the models predict the lightest neutrino mass to be zero.

We first calculate the relic abundance of both fermion and scalar DM and show how it depends on the model parameters, specially the ones related to the $U(1)_{B-L}$ sector. The fermion DM relic abundance crucially depends on the $U(1)_{B-L}$ gauge sector parameters $g_{BL}, M_{Z_{BL}}$, typically satisfying the relic abundance criteria near the resonance region $2M_{DM} = M_{Z_{BL}}$. There can also be Higgs portal interactions due to the existence of additional singlet scalars that not only take part in spontaneous breaking of $U(1)_{B-L}$ gauge symmetry, but can also assist in fermion DM annihilation into SM particles through its mixing with the SM Higgs boson. On the other hand, the scalar DM relic abundance is not very sensitive to the $U(1)_{B-L}$ sector physics and is mostly dictated by the Higgs portal and electroweak gauge sector interactions. The relic abundance criteria can be satisfied in two mass regions namely, the low mass regime $M_{DM} < M_W$ and high mass regime $M_{DM} > 500$ GeV.

We then study the sensitivity of direct detection experiments to both fermion and scalar DM. The spin independent DM-nucleon cross section for fermion DM is found to lie within the latest upper limit given by the Xenon1T experiment. This is observed by taking both gauge and scalar mediated DM-nucleon scatterings. A random scan of fermion DM parameter space consistent with relic abundance criteria also shows the entire DM mass range remains allowed from the direct detection constraints. In fact the Xenon1T constraints remain weaker than the LEP II bound $M_{Z_{BL}}/g_{BL} \geq 7$ TeV as well as LHC bound in fermion DM case, as can be seen from figure 2.8. The direct detection cross section of scalar DM is mostly controlled by the DM-Higgs coupling and is more sensitive to experiments like Xenon1T, primarily due to lighter mediator that is, SM Higgs. We find that for DM-Higgs coupling 0.1, scalar DM masses are ruled out even beyond 1 TeV by the Xenon1T limits. The LHC limit on the Higgs invisible decay width also rules out some region of parameter space for $M_{DM} < m_h/2$ although this constraint remains much weaker than the Xenon1T bounds. We also check the indirect detection bounds on DM annihilations into different SM final states and found that these limits can be saturated only by scalar DM for certain region of parameter space while fermion DM parameter space satisfying correct relic remains allowed. The scalar DM parameter space is more constrained by such indirect detection bounds compared to the fermion counterpart. For example, scalar DM mass can be ruled out far beyond 1 TeV for certain benchmark parameters if we incorporate the indirect detection bounds on DM annihilations into W^+W^- final states.

We then check the sensitivity of rare decay experiments like MEG looking for charged lepton flavour violating decay $\mu \to e\gamma$ to the parameter space of the model. This can arise at one loop level due to similar diagrams that give rise to light neutrino masses. Thus, the same parameters that affect DM phenomenology and light neutrino mass can also give rise to a new contribution to this rare decay process. We find that for some typical values of Yukawa couplings and DM masses, the model can saturate the MEG upper limit on the branching ratio of $\mu \to e\gamma$ and hence can be probed in near future searches.

Finally, we briefly discuss the possibility of probing such a model at energy frontier experiments like the LHC. We calculate the decay width and branching ratio of Z_{BL} into different final states like leptons, DM etc. After calculating the production cross section of

Z_{BL} in proton proton collisions at 13 TeV centre of mass energy of the LHC, we multiply the branching ratio into respective final states to estimate the total cross section into final states. This is possible due to the narrow decay width of the Z_{BL} boson. We find that, the model can be ruled out by the LHC bounds on heavy dilepton resonance searches if Z_{BL} mass is around 2 TeV and the corresponding gauge coupling is 0.05. The model can also predict other final states with missing energy that can be probed at ongoing and near future colliders. We leave a detailed collider study of such final states to future works.

2.4 Two-component dark matter and type-III seesaw in $\mathrm{U(1)_{B-L}}$ model

In this section, we discuss the possibilities of implementing type III seesaw in $U(1)_{B-L}$ model. To do that we consider two copies ($n_\Sigma = 2$) of fermion triplets $\Sigma_{Ri}(i = 1, 2)$ into the model having quantum numbers $(1, 3, 0, -1)$ under $SU(3)_c, SU(2)_L, U(1)_Y$ and $U(1)_{B-L}$ gauge groups respectively. Note that, two copies are enough to satisfy the light neutrino data, as in LS models. The non-vanishing anomalies are

$$[SU(2)_L]^2U(1)_{B-L} = 2n_\Sigma = 4, \;\; [U(1)_{B-L}]^3 = -3 + 3n_\Sigma = 3, \;\; [U(1)_{B-L}] = -3 + 3n_\Sigma = 3. \tag{2.43}$$

Note that the first anomaly is arising only due to the $SU(2)_L$ transformation of newly introduced fermions and was absent in the minimal $B - L$ extension of SM. Obviously, the first anomaly can be cancelled only by introducing an additional field which has non-trivial transformation under both $SU(2)_L$ and $U(1)_{B-L}$. We introduce such additional fields with a goal to keep our setup minimal and connected to the origin of light neutrino mass. Introducing a quintuplet $\Psi(1, 4, 0, n_1)$, the first anomaly becomes

$$[SU(2)_L]^2U(1)_{B-L} = 2n_\Sigma - 5n_1$$

which can vanish if $n_1 = 2n_\Sigma/5 = 4/5$. The other anomalies can be cancelled by introducing additional fields which do not contribute to the first anomaly and hence $SU(2)_L$ singlets. The remaining anomalies are

$$[U(1)_{B-L}]^3 = -3 + 3n_\Sigma - 4n_1^3 = \frac{119}{125}, \;\; [U(1)_{B-L}] = -3 + 3n_\Sigma - 4n_1 = -\frac{1}{5}. \tag{2.44}$$

These remaining anomalies can be cancelled by introducing three $SU(2)_L$ singlet chiral fermions

$$N_{1L}(1, 1, 0, -\frac{7}{5}), N_{2L}(1, 1, 0, \frac{2}{5}), N_{3L}(1, 1, 0, \frac{6}{5}). \tag{2.45}$$

This can be seen as follows

$$[U(1)_{B-L}]^3 = -3 + 3n_\Sigma - 4n_1^3 - \left(\frac{7}{5}\right)^3 + \left(\frac{2}{5}\right)^3 + \left(\frac{6}{5}\right)^3 = \frac{119}{125} - \frac{119}{125} = 0,$$

$$[U(1)_{B-L}] = -3 + 3n_\Sigma - 4n_1 - \frac{7}{5} + \frac{2}{5} + \frac{6}{5} = -\frac{1}{5} + \frac{1}{5} = 0.$$

Since the quintuplet and the other singlet fermions have no role to play in generating light neutrino mass, we do not pursue this possibility further.

We can have three fermion triplets: two of them having $B-L$ charge -1 and the third having exotic charge n_1. We will check if the third fermion can have any possible role in generating light neutrino masses. In such a case, there arises a possibility to get vanishing $[SU(2)_L]^2U(1)_{B-L}$ anomaly. In this case,

$$[SU(2)_L]^2U(1)_{B-L} = 2n_\Sigma - 2n_1$$

which can vanish if $n_1 = n_\Sigma = 2$. The other anomalies can be cancelled by introducing additional fields which do not contribute to the first anomaly and hence $SU(2)_L$ singlets. The remaining anomalies are

$$[U(1)_{B-L}]^3 = -3 + 3n_\Sigma - 3n_1^3 = -21, \;\; [U(1)_{B-L}] = -3 + 3n_\Sigma - 3n_1 = -3. \tag{2.46}$$

We now consider different possible solutions to these anomalies one by one.

Solution 2:

The remaining anomalies mentioned above can be cancelled by introducing four $SU(2)_L$ singlet chiral fermions

$$N_{1R}(1,1,0,2), N_{2R}(1,1,0,-1), N_{3R}(1,1,0,-1), N_{4R}(1,1,0,-3). \tag{2.47}$$

This can be seen as follows

$$[U(1)_{B-L}]^3 = -3 + 3n_\Sigma - 3n_1^3 - (2)^3 - 2\,(-1)^3 - (-3)^3 = -21 + 21 = 0,$$

$$[U(1)_{B-L}] = -3 + 3n_\Sigma - 3n_1 - 2 + 1 + 1 + 3 = -3 + 3 = 0.$$

However, this solution is not very motivating owing to the existence of singlet fermions having $B-L$ charge -1, which will give type I seesaw contribution to light neutrino masses, already discussed by several earlier works.

Solution 3:

The remaining anomalies can also be cancelled by the following fermions with fractional $B-L$ charges:

$$N_{1R}(1,1,0,\frac{2}{3}), N_{2R}(1,1,0,\frac{1}{3}), N_{3R}(1,1,0,-\frac{4}{3}), N_{4R}(1,1,0,-\frac{8}{3}). \tag{2.48}$$

In order to have non-zero masses for all new fermions and sticking to minimal scalar contents having integer $B-L$ charges, we find that there can be one stable DM candidate, in terms of one of the singlet fermions. Since single component DM in such models have already been discussed in several works, we do not pursue this possibility further.

Solution 4:

The most interesting possibility is the solution

$$N_{1R}(1,1,0,\frac{7}{5}), N_{2R}(1,1,0,-\frac{2}{5}), N_{3R}(1,1,0,-\frac{6}{5}), N_{4R}(1,1,0,-\frac{14}{5}). \tag{2.49}$$

which can also be recast as

$$N_{1L}(1,1,0,-\frac{7}{5}), N_{1R}(1,1,0,-\frac{2}{5}), N_{2L}(1,1,0,\frac{6}{5}), N_{2R}(1,1,0,-\frac{14}{5}). \tag{2.50}$$

We can construct two Dirac fermions from these four chiral ones, just by introducing two singlet scalars ϕ_1, ϕ_2 having $B-L$ charges $1, 4$ respectively. The corresponding mass terms will be

$$Y_1\overline{N_{1L}}N_{1R}\phi_1^\dagger + Y_2\overline{N_{2L}}N_{2R}\phi_2 + \text{h.c.}$$

Another scalar singlet having $B-L$ charge 2 is also required in order to give mass to the fermion triplets $\Sigma_{1,2}$. The third fermion triplet acquires mass and also mixes with the other two fermion triplets by virtue of its couplings to the scalars ϕ_1, ϕ_2. Although the third fermion triplet is not stable due to its mixing with the first two, the two Dirac fermions constructed above can be separately stable and hence give rise to multi-component DM. Also, the third fermion triplet, through its mixing with the first two, can contribute to the light neutrino mass matrix as we discuss in details in upcoming sections. Due to these interesting possibilities, we pursue this scenario in our work.

2.4.1 The Model

In this section, we discuss our model elaborately. As mentioned earlier, in this work our prime motivation is to have a multi-component DM scenario where both DM candidates are stable by virtue of a single symmetry group. Additionally, we want to address neutrino mass generation as well. Keeping these two things in our mind, we have extended the SM in all three sectors namely the gauge sector, the fermionic sector and the scalar sector. In the gauge sector, we have demanded an additional local $U(1)_{B-L}$ gauge invariance where B and L are denoting baryon and lepton numbers respectively of a particular field. This introduces anomalies (both axial vector and gauge-gravitational anomalies) in the theory which can only be evaded by the inclusion of additional fermionic degrees of freedom. This has elaborately been discussed in the previous section. We have seen that for the case of three additional $SU(2)_L$ triplet fermions Σ_{iR}, $i = 1$ to 3, two of which with $B-L$ charge -1 are necessary to generate neutrino masses via Type-III seesaw mechanism and the rest having $B-L$ charge 2 is solely required to cancel $[SU(2)_L]^2\, U(1)_{B-L}$ anomaly. We further need four SM gauge singlet chiral fermions with fractional $B-L$ charges to cancel both $U(1)^3_{B-L}$ and $(\text{gravity})^2\, U(1)_{B-L}$ anomalies. Moreover, at least three scalar fields ϕ_i ($i = 1$ to 3) are also necessary to give masses to all new fermions in the broken phase of the $U(1)_{B-L}$ symmetry. We have properly adjusted $B-L$ charges of these ϕ_is such that only the Dirac mass terms among these singlet fermions are possible and more importantly the Dirac mass matrix is diagonal. This results in two physical Dirac fermions out of these four chiral fermions which are simultaneously stable and thus both can be viable DM candidates. In Tables 2.7 and

Particles	$SU(3)_c \times SU(2)_L \times U(1)_Y \times U(1)_{B-L}$
$q_L = \begin{pmatrix} u_L \\ d_L \end{pmatrix}$	$(3, 2, \frac{1}{6}, \frac{1}{3})$
u_R	$(3, 1, \frac{2}{3}, \frac{1}{3})$
d_R	$(3, 1, -\frac{1}{3}, \frac{1}{3})$
$\ell_L = \begin{pmatrix} \nu_L \\ e_L \end{pmatrix}$	$(1, 2, -\frac{1}{2}, -1)$
e_R	$(1, 1, -1, -1)$
Σ_{1R}	$(1, 3, 0, -1)$
Σ_{2R}	$(1, 3, 0, -1)$
Σ_{3R}	$(1, 3, 0, 2)$
N_{1L}	$(1, 1, 0, -\frac{7}{5})$
N_{1R}	$(1, 1, 0, -\frac{2}{5})$
N_{2L}	$(1, 1, 0, \frac{6}{5})$
N_{2R}	$(1, 1, 0, -\frac{14}{5})$

Table 2.7: Fermionic fields of the present Model including the SM fermions.

Particles	$SU(3)_c \times SU(2)_L \times U(1)_Y \times U(1)_{B-L}$
$H = \begin{pmatrix} H^+ \\ H^0 \end{pmatrix}$	$(1, 2, \frac{1}{2}, 0)$
ϕ_1	$(1, 1, 0, 1)$
ϕ_2	$(1, 1, 0, 4)$
ϕ_3	$(1, 1, 0, 2)$

Table 2.8: Scalar fields and their corresponding charges under all the symmetry groups.

2.8, we have listed all fermions as well as scalar fields (including the SM ones) of the present model and their charges under the $SU(3)_c \times SU(2)_L \times U(1)_Y \times U(1)_{B-L}$ symmetry.

The Lagrangian of our present model invariant under the full symmetry group is given by

$$\mathcal{L} \;=\; \mathcal{L}_{SM} - \frac{1}{4} B'_{\alpha\beta}\, B'^{\alpha\beta} + \mathcal{L}_{scalar} + \mathcal{L}_{fermion}\,. \tag{2.51}$$

Here, $\mathcal{L}_{SM}$ denotes the SM Lagrangian involving quarks, gluons, charged leptons, left handed neutrinos and electroweak gauge bosons. The second term is the kinetic term of $B-L$ gauge boson (Z_{BL}) expressed in terms of field strength tensor $B'^{\alpha\beta} = \partial^\alpha Z^\beta_{BL} - \partial^\beta Z^\alpha_{BL}$. From Table 2.8, we have already understood that our model has a very rich scalar sector and the gauge invariant interactions among the scalar fields are described by $\mathcal{L}_{scalar}$ which contains following terms,

$$\begin{aligned}
\mathcal{L}_{scalar} \;=\; & \left(D_{H\mu} H\right)^\dagger \left(D_H{}^\mu H\right) + \sum_{i=1}^{3} \left(D_{\phi_i \mu}\phi_i\right)^\dagger \left(D_{\phi_i}{}^\mu \phi_i\right) - \Bigg[-\mu_H^2 (H^\dagger H) + \lambda_H (H^\dagger H)^2 \\
& + \sum_{i=1}^{3} \left(-\mu^2_{\phi_i} (\phi_i^\dagger \phi_i) + \lambda_{\phi_i} (\phi_i^\dagger \phi_i)^2 \right) + \sum_{i,j=1 (i\neq j)}^{3} \lambda_{\phi_i \phi_j} (\phi_i^\dagger \phi_i)(\phi_j^\dagger \phi_j) \\
& + \sum_{i=1}^{3} \lambda_{H\phi_i} (H^\dagger H)(\phi_i^\dagger \phi_i) + \left(\beta\, \phi_1 \phi_1 \phi_3 \phi_2^\dagger + \delta\, \phi_1 \phi_1 \phi_3^\dagger + \zeta\, \phi_3 \phi_3 \phi_2^\dagger + h.c. \right) \Bigg]
\end{aligned} \tag{2.52}$$

where covariant derivatives for the Higgs doublet H and singlet scalars ϕ_is are defined as

$$\begin{aligned}
D_{H\mu} H \;&=\; \left(\partial_\mu + i\, \frac{g}{2}\, \sigma_a\, W^a_\mu + i\, \frac{g'}{2}\, B_\mu \right) H\,, \\
D_{\phi_\mu} \phi_i \;&=\; \left(\partial_\mu + i\, g_{BL}\, n_{\phi_i} Z_{BL\mu} \right) \phi_i\,.
\end{aligned} \tag{2.53}$$

The quantity $D_{H\mu}$ is the usual covariant derivative of the SM Higgs doublet with g and g' are gauge couplings of $SU(2)_L$ and $U(1)_Y$ respectively and the corresponding gauge bosons are denoted by W^a_μ ($a = 1,\, 3$) and B_μ. The covariant derivative of H does not include $B-L$ gauge boson Z_{BL} as the corresponding gauge charge of H is zero. On the other hand, being a SM gauge singlet, covariant derivative of ϕ_i only contains Z_{B-L} with n_{ϕ_i} is the respective $B-L$ charge of ϕ_i and g_{BL} is the new gauge coupling. After breaking of both $B-L$ symmetry and electroweak symmetry by the VEVs of H and ϕ_is, the doublet and all three singlets are given by

$$H = \begin{pmatrix} H^+ \\ \dfrac{h' + v + iz}{\sqrt{2}} \end{pmatrix}\,, \quad \phi_i = \frac{s'_i + u_i + A'_i}{\sqrt{2}} \;\; (i = 1,\, 2,\, 3)\,, \tag{2.54}$$

where v and u_is ($i = 1,\, 2,\, 3$) are VEVs of H and ϕ_is respectively. For calculational simplicity we have assumed all three VEVs of singlet scalars are equal i.e. $u_1 = u_2 = u_3 = u$.

Therefore, substituting equation (2.54) in equation (2.52) we have a 4×4 mixing matrix for the real scalar fields in the basis $\frac{1}{\sqrt{2}}\,(h'\ s_1'\ s_2'\ s_3')^T$ which has the following form,

$$\mathcal{M}_{rs} = \begin{pmatrix} 2\lambda_H v^2 & \lambda_{H\phi_1} u\, v & \lambda_{H\phi_2} u\, v & \lambda_{H\phi_3} u\, v \\ \lambda_{H\phi_1} u\, v & 2\lambda_{\phi_1} u^2 & u^2(\beta + \lambda_{\phi_1\phi_2}) & u\left(\sqrt{2}\,\delta + u(\beta + \lambda_{\phi_1\phi_3})\right) \\ \lambda_{H\phi_2} u\, v & u^2(\beta + \lambda_{\phi_1\phi_2}) & -\frac{1}{2}u\left(\sqrt{2}\,\zeta + u(\beta - 4\lambda_{\phi_2})\right) & \frac{1}{2}u\left(2\sqrt{2}\,\zeta + u(\beta + 2\lambda_{\phi_2\phi_3})\right) \\ \lambda_{H\phi_3} u\, v & u\left(\sqrt{2}\,\delta + u(\beta + \lambda_{\phi_1\phi_3})\right) & \frac{1}{2}u\left(2\sqrt{2}\,\zeta + u(\beta + 2\lambda_{\phi_2\phi_3})\right) & -\frac{1}{2}u\left(\sqrt{2}\,\delta + u(\beta - 4\lambda_{\phi_3})\right) \end{pmatrix}. \tag{2.55}$$

The physical scalars $(h,\ s_1,\ s_2,\ s_3)$ are obtained by diagonalising the above real symmetric mass matrix and they are related by an orthogonal transformation to the unphysical scalars (i.e. the basis state before diagonalisation) as

$$\begin{pmatrix} h \\ s_1 \\ s_2 \\ s_3 \end{pmatrix} = \mathcal{O}^T \begin{pmatrix} h' \\ s_1' \\ s_2' \\ s_3' \end{pmatrix}, \tag{2.56}$$

where $\mathcal{O}$ is a 4×4 orthogonal matrix which makes $\mathcal{M}_{rs}$ diagonal i.e. $\mathcal{O}^T \mathcal{M}_{rs} \mathcal{O} \Rightarrow$ a diagonal matrix containing all the masses of four physical scalars as diagonal elements. In Appendix A.2, we have expressed all the elements of $\mathcal{O}$ matrix in terms of four mixing angles (assuming mixing among the three singlet scalars are identical). Additionally, for simplicity we also set $\beta = 0$, [2] and $\zeta = \delta$ in equation (2.52).

On the other hand, in our model we have four pseudo scalars as well, which are z, A_1', A_2' and A_3' (see equation (2.54)). Out of these four pseudo scalars, z does not mixes with others and becomes the Goldstone boson corresponding to the SM Z boson after EWSB. However, the pseudo scalars of complex singlet ϕ_is mix among each other when $B - L$ symmetry is broken by the VEVs of ϕ_is. Therefore, unlike the case of real scalars, here we have a 3×3 mixing matrix in the basis $\frac{1}{\sqrt{2}}(A_1'\ \ A_2'\ A_3')^T$ which is written below,

$$\mathcal{M}_{ps} = \begin{pmatrix} -2u\,(u\,\beta + \sqrt{2}\,\delta) & u^2\,\beta & u\,(-u\,\beta + \sqrt{2}\,\delta) \\ u^2\,\beta & -\frac{u}{2}\,(u\,\beta + \sqrt{2}\,\zeta) & \frac{u}{2}\,(u\,\beta + 2\sqrt{2}\,\zeta) \\ u\,(-u\,\beta + \sqrt{2}\,\delta) & \frac{u}{2}\,(u\,\beta + 2\sqrt{2}\,\zeta) & -\frac{u}{2}\,(u\,\beta + \sqrt{2}(\delta + 4\,\zeta)) \end{pmatrix}. \tag{2.57}$$

After diagonalising, this matrix we get two physical pseudo scalars A_2, A_3 and a massless Goldstone boson A_1 corresponding to the extra neutral gauge boson Z_{BL}. This can easily be checked as the pseudo scalar mass matrix has a null determinant. The eigenvalues of the pseudo scalar mass matrix for $\zeta = \delta$, $\beta = 0$ are[3]

[2] β is the coupling of quartic interaction among all four singlet scalars which has less significant impact in DM phenomenology compared to other cubic scalar interaction terms like $\delta\,\phi_1\phi_1\phi_3^\dagger$ and $\zeta\,\phi_3\phi_3\phi_2^\dagger$.

[3] Eigenvalues of $\mathcal{M}_{ps}$ for $\zeta \neq \delta \neq \beta$ are given in Appendix A.3.

$$m^2_{A_2} = -\frac{3\,\zeta\,u}{\sqrt{2}}\,,$$
$$m^2_{A_3} = -\frac{7\,\zeta\,u}{\sqrt{2}}\,, \tag{2.58}$$

where ζ must be less than zero to ensure m_{A_2} and m_{A_3} are real. Further, the physical CP-odd scalars (A_is) and the Goldstone boson A_1 are related to the unphysical basis states (A'_1, A'_2, A'_3) as follows

$$\begin{pmatrix} A_1 \\ A_2 \\ A_3 \end{pmatrix} = \begin{pmatrix} \frac{1}{\sqrt{21}} & \frac{4}{\sqrt{21}} & \frac{2}{\sqrt{21}} \\ \frac{2}{\sqrt{3}} & -\frac{1}{\sqrt{6}} & \frac{1}{\sqrt{6}} \\ -\frac{2}{\sqrt{7}} & -\frac{1}{\sqrt{14}} & \frac{3}{\sqrt{14}} \end{pmatrix} \begin{pmatrix} A'_1 \\ A'_2 \\ A'_3 \end{pmatrix}. \tag{2.59}$$

Moreover, the neutral gauge boson Z_{BL} becomes massive after the breaking of $U(1)_{B-L}$ and the corresponding mass term of Z_{B-L} is given by

$$\begin{aligned} M_{Z_{BL}} &= g_{BL}\sqrt{\left(\sum_{i=1}^{3} n^2_{\phi_i} u_i^2\right)}\,, \\ &= \sqrt{21}\, g_{BL}\, u\,. \end{aligned} \tag{2.60}$$

Now, let us concentrate on the fermionic sector of the present model. Here, in addition to the usual SM fermions, we have four gauge singlet fermions and three $SU(2)_L$ triplet fermions. All these new fermions have appropriate $B-L$ charges. In equation (2.51), $\mathcal{L}_f$ is the Lagrangian for these newly added fermionic fields and it is composed of two parts as

$$\mathcal{L}_f = \mathcal{L}_{Singlet} + \mathcal{L}_{Triplet}\,, \tag{2.61}$$

where, the Lagrangian for the singlet fields are given below

$$\mathcal{L}_{Singlet} = i\sum_{\kappa=1}^{2}[\overline{N_{\kappa L}}\not{D}(Q^L_\kappa)N_{\kappa L} + \overline{N_{\kappa R}}\not{D}(Q^R_\kappa)N_{\kappa R}] - \left(\mathcal{Y}_1\,\overline{N_{1L}}N_{1R}\,\phi_1^\dagger + \mathcal{Y}_2\,\overline{N_{2L}}N_{2R}\,\phi_2 + \text{h.c.}\right). \tag{2.62}$$

In the above $\mathcal{Y}_i$ ($i = 1,\ 2$) are the dimensionless Yukawa couplings and the covariant derivative is defined as

$$\not{D}(Q^{L(R)}_\kappa)\, N_{\kappa L(R)} = \gamma^\mu\left(\partial_\mu + i g_{BL}\, Q^{L(R)}_\kappa\, Z_{BL\mu}\right) N_{\kappa L(R)}\,, \tag{2.63}$$

where $Q_\kappa^{L(R)}$ is the corresponding $B-L$ charge of $N_{\kappa L(R)}$ which is listed in Table 2.7. As mentioned earlier, due to special choice of $B-L$ charges of scalar fields ϕ_1, ϕ_2 and ϕ_3, the Yukawa interactions in equation (2.62) are exactly diagonal in the basis $\xi_1 = N_{1L} + N_{1R}$ and $\xi_2 = N_{2L} + N_{2R}$. In this basis above Lagrangian can be rewritten as,

$$\begin{aligned}\mathcal{L}_{\text{Singlet}} &= i\,\overline{\xi_1}\,\partial\!\!\!/\,\xi_1 + i\,\overline{\xi_2}\,\partial\!\!\!/\,\xi_2 - g_{BL}\left(-\frac{7}{5}\right)\overline{\xi_1}\,Z\!\!\!/_{BL}\,P_L\,\xi_1 - g_{BL}\left(\frac{6}{5}\right)\overline{\xi_2}\,Z\!\!\!/_{BL}\,P_L\,\xi_2 \\ &\quad - g_{BL}\left(-\frac{2}{5}\right)\overline{\xi_1}\,Z\!\!\!/_{BL}\,P_R\,\xi_1 - g_{BL}\left(-\frac{14}{5}\right)\overline{\xi_2}\,Z\!\!\!/_{BL}\,P_R\,\xi_2 - \mathcal{Y}_1\,\overline{\xi_1}\,P_R\,\xi_1\,\phi_1^\dagger \\ &\quad - \mathcal{Y}_2\,\overline{\xi_2}\,P_R\,\xi_2\,\phi_2 - \mathcal{Y}_1\,\overline{\xi_1}\,P_L\,\xi_1\,\phi_1 - \mathcal{Y}_2\,\overline{\xi_2}\,P_L\,\xi_2\,\phi_2^\dagger\,,\end{aligned}$$

which can be further simplified as

$$\begin{aligned}&= i\,\overline{\xi_1}\,\partial\!\!\!/\,\xi_1 + i\,\overline{\xi_2}\,\partial\!\!\!/\,\xi_2 + \frac{g_{BL}}{10}\,\overline{\xi_1}\,Z\!\!\!/_{BL}\,(9-5\gamma_5)\,\xi_1 + \frac{2\,g_{BL}}{5}\,\overline{\xi_2}\,Z\!\!\!/_{BL}\,(2+5\gamma_5)\,\xi_2 \\ &\quad - \mathcal{Y}_1\,\overline{\xi_1}\,P_R\,\xi_1\,\phi_1^\dagger - \mathcal{Y}_2\,\overline{\xi_2}\,P_R\,\xi_2\,\phi_2 - \mathcal{Y}_1\,\overline{\xi_1}\,P_L\,\xi_1\,\phi_1 - \mathcal{Y}_2\,\overline{\xi_2}\,P_L\,\xi_2\,\phi_2^\dagger\,, \qquad (2.64)\end{aligned}$$

where $P_{L,R} = \dfrac{1\pm\gamma_5}{2}$, left and right chiral projection operators. Besides, in the above we have assumed the Yukawa couplings $\mathcal{Y}_i$s are real. Therefore, from the above Lagrangian one can easily notice that both ξ_1 and ξ_2 are decoupled from each other and thus can be stable simultaneously. Hence, they naturally form a two-component DM system stabilises by the $B-L$ symmetry only [4] . On the other hand, $SU(2)_L \times U(1)_{B-L}$ [5] invariant Lagrangian for the triplet fields are given by,

$$\begin{aligned}\mathcal{L}_{\text{Triplet}} &= \frac{i}{2}\sum_{k=1}^{3}\left(\text{Tr}\left[\overline{\Sigma_{kR}}\not{D}\Sigma_{kR}\right] + \text{Tr}\left[\overline{\Sigma_{kR}{}^c}\not{D}'\Sigma_{kR}{}^c\right]\right) - \frac{1}{2}\left(\text{Tr}[\overline{\Sigma_{1R}{}^c}\sqrt{2}\;Y_{\Sigma_1\phi_3}\Sigma_{1R}]\phi_3\right. \\ &+ \text{Tr}[\overline{\Sigma_{2R}{}^c}\sqrt{2}\;Y_{\Sigma_2\phi_3}\Sigma_{2R}]\phi_3 + \text{Tr}[\overline{\Sigma_{3R}{}^c}\sqrt{2}\;Y_{\Sigma_3\phi_2}\Sigma_{3R}]\phi_2^\dagger + h.c.\Big) - \frac{1}{2}\Big\{\Big(\text{Tr}[\overline{\Sigma_{1R}{}^c}\sqrt{2}\;Y_{\Sigma_{13}\phi_1}\Sigma_{3R}] \\ &+ \text{Tr}[\overline{\Sigma_{3R}{}^c}\sqrt{2}\;Y_{\Sigma_{13}\phi_1}\Sigma_{1R}]\Big)\,\phi_1^\dagger + \Big(\text{Tr}[\overline{\Sigma_{2R}{}^c}\sqrt{2}\;Y_{\Sigma_{23}\phi_1}\Sigma_{3R}] + \text{Tr}[\overline{\Sigma_{3R}{}^c}\sqrt{2}\;Y_{\Sigma_{23}\phi_1}\Sigma_{2R}]\Big)\,\phi_1^\dagger \\ &+ \Big(\text{Tr}[\overline{\Sigma_{1R}{}^c}\sqrt{2}\;Y_{\Sigma_{12}\phi_3}\Sigma_{2R}] + \text{Tr}[\overline{\Sigma_{2R}{}^c}\sqrt{2}\;Y_{\Sigma_{12}\phi_3}\Sigma_{1R}]\Big)\,\phi_3 + h.c.\Big\}\,, \qquad (2.65)\end{aligned}$$

where, we consider fermion triplets Σ_{kR} and its CP conjugate $\Sigma_{kR}{}^c$ in 2×2 representation as

$$\Sigma_{kR} = \begin{pmatrix}\Sigma_{kR}^0/\sqrt{2} & \Sigma_{kR}^+ \\ \Sigma_{kR}^- & -\Sigma_{kR}^0/\sqrt{2}\end{pmatrix}\,,\quad \Sigma_{kR}{}^c = \mathbb{C}\,\overline{\Sigma_{kR}}^T = \begin{pmatrix}\Sigma_{kR}^0{}^c/\sqrt{2} & \Sigma_{kR}^-{}^c \\ \Sigma_{kR}^+{}^c & -\Sigma_{kR}^0{}^c/\sqrt{2}\end{pmatrix} \qquad (2.66)$$

where $\mathbb{C}$ is the charge conjugation matrix. The covariant derivatives used in the kinetic terms of Σ_{kR} and Σ_{kR}^c can be defined as

[4] Actually, we consider the $B-L$ charges of ϕ_1, ϕ_2 and ϕ_3 in such a way that $U(1)_{B-L}$ breaks into a $\mathbb{Z}_2\times\mathbb{Z}_2'$ symmetry where ξ_1 and ξ_2 have following charges $(-,+)$ and $(+,-)$ under the $\mathbb{Z}_2\times\mathbb{Z}_2'$ symmetry respectively.

[5] Triplet fermion fields have no colour charge and hypercharge.

$$D_\mu^{(\prime)}\Sigma_{kR}{}^{(c)} = \left(\partial_\mu + i\,\frac{g}{2}\,\sigma_a\,W_\mu^a + (-)i\,g_{BL}\,n_\Sigma^k\,Z_{BL\mu}\right)\Sigma_{kR}{}^{(c)}\,, \tag{2.67}$$

where n_Σ^k is the $B-L$ charge of Σ_{kR} and there is a sign flip as the $B-L$ charges of Σ_{kR} and its CP conjugate are equal but opposite in sign. Now, we define $\psi_k^0 = \Sigma_{kR}^0 + \Sigma_{kR}^{0\,c}$, a Majorana fermion and a Dirac fermion $\psi_k^- = \Sigma_{kR}^- + \Sigma_{kR}^{+\,c}$. Following [308], we have written the triplet Lagrangian in terms of ψ_k^0 and ψ_k^- as

$$\begin{aligned}
\mathcal{L}_{Triplet} \quad &= \sum_{k=1}^{3}\left\{\frac{i}{2}\overline{\psi_k^0}\not{\partial}\psi_k^0 + i\,\overline{\psi_k^-}\not{\partial}\psi_k^- - g\left(\overline{\psi_k^-}\not{W}^-\psi_k^0 + h.c.\right) + g\sin\theta_W\overline{\psi_k^-}\not{A}\psi_k^-\right.\\
&\left. + g\cos\theta_W\overline{\psi_k^-}\not{Z}\psi_k^- - g_{BL}\,n_\Sigma^k\left(\frac{1}{2}\,\overline{\psi_k^0}\not{Z}_{BL}\gamma_5\psi_k^0 + \overline{\psi_k^-}\not{Z}_{BL}\gamma_5\psi_k^-\right)\right\}\\
&- \sum_{i=1}^{2} Y_{\Sigma_i\phi_3}\left\{\left(\frac{1}{2}\overline{\psi_i^0}\psi_i^0 + \overline{\psi_i^-}\psi_i^-\right)s_3' + i\left(\frac{1}{2}\overline{\psi_i^0}\gamma_5\psi_i^0 + \overline{\psi_i^-}\gamma_5\psi_i^-\right)A_3'\right\}\\
&- Y_{\Sigma_3\phi_2}\left\{\left(\frac{1}{2}\overline{\psi_3^0}\psi_3^0 + \overline{\psi_3^-}\psi_3^-\right)s_2' - i\left(\frac{1}{2}\overline{\psi_3^0}\gamma_5\psi_3^0 + \overline{\psi_3^-}\gamma_5\psi_3^-\right)A_2'\right\}\\
&- Y_{\Sigma_{13}\phi_1}\left\{\left(\frac{1}{2}\overline{\psi_1^0}\psi_3^0 + \overline{\psi_1^-}\psi_3^-\right)s_1' - i\left(\frac{1}{2}\overline{\psi_1^0}\gamma_5\psi_3^0 + \overline{\psi_1^-}\gamma_5\psi_3^-\right)A_1' + h.c.\right\}\\
&- Y_{\Sigma_{23}\phi_1}\left\{\left(\frac{1}{2}\overline{\psi_2^0}\psi_3^0 + \overline{\psi_2^-}\psi_3^-\right)s_1' - i\left(\frac{1}{2}\overline{\psi_2^0}\gamma_5\psi_3^0 + \overline{\psi_2^-}\gamma_5\psi_3^-\right)A_1' + h.c.\right\}\\
&- Y_{\Sigma_{12}\phi_3}\left\{\left(\frac{1}{2}\overline{\psi_1^0}\psi_2^0 + \overline{\psi_1^-}\psi_2^-\right)s_3' + i\left(\frac{1}{2}\overline{\psi_1^0}\gamma_5\psi_2^0 + \overline{\psi_1^-}\gamma_5\psi_2^-\right)A_3' + h.c.\right\}
\end{aligned} \tag{2.68}$$

$\theta_W = \tan^{-1}\dfrac{g'}{g}$ is the weak mixing angle (Weinberg angle). The last two terms of the above Lagrangian introduce off-diagonal elements in the mass matrices of both ψ_k^0 and ψ_k^- (k runs from 1 to 3) when s_1' gets a nonzero VEV. As a result, one needs to diagonalise both the mass matrices using bi-unitary transformations in order to get the physical fermionic states. However, in this work we have not considered this. We have worked in a limit when $Y_{\Sigma_1\phi_3}$, $Y_{\Sigma_2\phi_3}$ and $Y_{\Sigma_3\phi_2}$ >> $Y_{\Sigma_{13}\phi_1}$ and $Y_{\Sigma_{23}\phi_1}$, so that mass matrices of both charged and neutral fermions are effectively diagonal and thus, there is no need for basis transformation. Here, two triplet fermions having $B-L$ charge -1 will play crucial role in generating observed neutrino masses and mixings via Type-III seesaw mechanism. The Yukawa Lagrangian involving the leptons is given by

$$\mathcal{L}_{\text{Yukawa}} \supset \left(\sum_{\alpha=1,2,3,\,\beta=1,2}\sqrt{2}y_\Sigma^{\alpha\beta}\,\overline{l_{\alpha L}}\Sigma_{\beta\,R}\tilde{\Phi} + h.c.\right) \tag{2.69}$$

The light neutrino mass matrix is generated from the type III seesaw mechanism as

$$M_\nu = -M_D M_R^{-1} M_D^T \tag{2.70}$$

where the Dirac neutrino mass matrix M_D and neutral triplet fermion mass matrix M_R are given by

$$M_D = \begin{pmatrix} y_\Sigma^{11} v & y_\Sigma^{12} v & 0 \\ y_\Sigma^{21} v & y_\Sigma^{22} v & 0 \\ y_\Sigma^{31} v & y_\Sigma^{32} v & 0 \end{pmatrix}, \; M_R = \begin{pmatrix} Y_{\Sigma_1\phi_3} u_3 & Y_{\Sigma_{12}\phi_3} u_3 & Y_{\Sigma_{13}\phi_1} u_1 \\ Y_{\Sigma_{12}\phi_3} u_3 & Y_{\Sigma_2\phi_3} u_3 & Y_{\Sigma_{23}\phi_1} u_1 \\ Y_{\Sigma_{13}\phi_1} u_1 & Y_{\Sigma_{23}\phi_1} u_1 & Y_{\Sigma_3\phi_2} u_2 \end{pmatrix}. \tag{2.71}$$

Diagonalisation of the light neutrino mass matrix using the above forms of M_D, M_R gives one vanishing mass eigenvalue. This is same as the prediction of the recent work [262] as well as the littlest seesaw model [265] mentioned earlier. If we simplify our neutral fermion triplet mass matrix M_R by incorporating the smallness on off-diagonal Yukawa couplings mentioned earlier $Y_{\Sigma_1\phi_3}, Y_{\Sigma_2\phi_3}, Y_{\Sigma_3\phi_2} >> Y_{\Sigma_{13}\phi_1}, Y_{\Sigma_{23}\phi_1}, Y_{\Sigma_{12}\phi_3}$ and equality of singlet VEVs, we can approximate M_R to be a diagonal matrix leading to a relatively simple light neutrino mass matrix given as

$$M_\nu = -\frac{v^2}{u} \begin{pmatrix} \frac{(y_\Sigma^{11})^2}{Y_{\Sigma_1\phi_3}} + \frac{(y_\Sigma^{12})^2}{Y_{\Sigma_2\phi_3}} & \frac{y_\Sigma^{11} y_\Sigma^{21}}{Y_{\Sigma_1\phi_3}} + \frac{y_\Sigma^{12} y_\Sigma^{22}}{Y_{\Sigma_2\phi_3}} & \frac{y_\Sigma^{11} y_\Sigma^{31}}{Y_{\Sigma_1\phi_3}} + \frac{y_\Sigma^{12} y_\Sigma^{32}}{Y_{\Sigma_2\phi_3}} \\ \frac{y_\Sigma^{11} y_\Sigma^{21}}{Y_{\Sigma_1\phi_3}} + \frac{y_\Sigma^{12} y_\Sigma^{22}}{Y_{\Sigma_2\phi_3}} & \frac{(y_\Sigma^{21})^2}{Y_{\Sigma_1\phi_3}} + \frac{(y_\Sigma^{22})^2}{Y_{\Sigma_2\phi_3}} & \frac{y_\Sigma^{21} y_\Sigma^{31}}{Y_{\Sigma_1\phi_3}} + \frac{y_\Sigma^{22} y_\Sigma^{32}}{Y_{\Sigma_2\phi_3}} \\ \frac{y_\Sigma^{11} y_\Sigma^{31}}{Y_{\Sigma_1\phi_3}} + \frac{y_\Sigma^{12} y_\Sigma^{32}}{Y_{\Sigma_2\phi_3}} & \frac{y_\Sigma^{21} y_\Sigma^{31}}{Y_{\Sigma_1\phi_3}} + \frac{y_\Sigma^{22} y_\Sigma^{32}}{Y_{\Sigma_2\phi_3}} & \frac{(y_\Sigma^{31})^2}{Y_{\Sigma_1\phi_3}} + \frac{(y_\Sigma^{32})^2}{Y_{\Sigma_2\phi_3}} \end{pmatrix}. \tag{2.72}$$

This simplified light neutrino mass matrix also leads to a vanishing lightest neutrino mass while the three mixing angles can be satisfied by suitable tuning of the Yukawa couplings. Since for TeV scale triplet fermions, the Dirac Yukawa couplings $y_\Sigma^{\alpha\beta}$ have to be fine tuned at the level of $\leq 10^{-4}$, they do not impact the DM analysis discussed in this work. Hence, we do not take such couplings into our subsequent discussions.

2.4.2 Constraints on the model parameters

Before going into the detailed calculation of DM relic abundance and relevant parameter scan, we note the existing theoretical as well as experimental constraints on the model parameters.

In order to keep the scalar potential (given in equation (2.52) within the square brackets) bounded from below, the quartic couplings must satisfy the following inequalities:

$$\begin{aligned} \lambda_H, \lambda_{\phi_1}, \lambda_{\phi_2}, \lambda_{\phi_3} \geq 0\,, \\ \lambda_{H\phi_1} + \sqrt{\lambda_H \lambda_{\phi_1}} \geq 0\,, \lambda_{H\phi_2} + \sqrt{\lambda_H \lambda_{\phi_2}} \geq 0\,, \\ \lambda_{H\phi_3} + \sqrt{\lambda_H \lambda_{\phi_3}} \geq 0\,, \lambda_{\phi_1\phi_2} + \sqrt{\lambda_{\phi_1} \lambda_{\phi_2}} \geq 0\,, \\ \lambda_{\phi_1\phi_3} + \sqrt{\lambda_{\phi_1} \lambda_{\phi_3}} \geq 0\,, \lambda_{\phi_2\phi_3} + \sqrt{\lambda_{\phi_2} \lambda_{\phi_3}} \geq 0\,. \end{aligned} \tag{2.73}$$

To prevent perturbative breakdown of the model, all quartic, Yukawa and gauge couplings should obey the following limits at any energy scale:

$$
\begin{aligned}
|\lambda_H| < 4\pi,\ |\lambda_{\phi_{1,2,3}}| < 4\pi,\ |\lambda_{H\phi_{1,2,3}}| < 4\pi,\\
|\lambda_{\phi_1\phi_2}| < 4\pi,\ |\lambda_{\phi_1\phi_3}| < 4\pi,\ |\lambda_{\phi_2\phi_3}| < 4\pi,\\
|\mathcal{Y}_i| < \sqrt{4\pi},\ |Y_{\Sigma_{1,2}\phi_3}| < \sqrt{4\pi},\ |Y_{\Sigma_3\phi_2}| < \sqrt{4\pi},\\
|Y_{\Sigma_{13}\phi_1}| < \sqrt{4\pi},\ |Y_{\Sigma_{23}\phi_1}| < \sqrt{4\pi},\ |Y_{\Sigma_{12}\phi_3}| < \sqrt{4\pi}\\
|g, g'| < \sqrt{4\pi},\ |g_{BL}| < \sqrt{4\pi},
\end{aligned}
\tag{2.74}
$$

Experimental limits from LEP II constrains such new gauge sector by putting a lower bound on the ratio of new gauge boson mass to the new gauge coupling $M_{Z'}/g' \geq 7$ TeV [260, 261]. The corresponding bounds from the LHC experiment have become stronger than this by now. Search for high mass dilepton resonances have put strong bounds on mass of such gauge boson coupling to first two generations of leptons with couplings similar to electroweak ones. The latest bounds from the ATLAS experiment [295, 309] and the CMS experiment [310] at the LHC rule out such gauge boson masses below 4-5 TeV from analysis of 13 TeV data. Such bounds get weaker, if the corresponding gauge couplings are weaker [295] than the electroweak gauge couplings. Also, if the Z' gauge boson couples only to the third generation of leptons, all such collider bounds become much weaker, as explored in the context of DM and collider searches in a recent work [311].

Similarly, the additional scalars in the model also face stringent constraints which typically arise due to their mixing with the SM Higgs boson which enable them to couple with the SM particles. The bound on such scalar mixing angles would come from both theoretical and experimental constraints [312, 313]. In case of scalar singlet extension of SM, the strongest bound on scalar-SM Higgs mixing angle ($\theta_{1j}, j = 2, 3, 4$) comes form W boson mass correction [314] at NLO for 250 GeV $\lesssim M_{s_i} \lesssim$ 850 GeV as ($0.2 \lesssim \sin\theta_{1j} \lesssim 0.3$) where M_{s_i} is the mass of other physical Higgs. Whereas, for $M_{s_i} > 850$ GeV, the bounds from the requirement of perturbativity and unitarity of the theory turn dominant which gives $\sin\theta_{1j} \lesssim 0.2$. For lower values *i.e.* $M_{s_i} < 250$ GeV, the LHC and LEP direct search [315, 316] and measured Higgs signal strength [316] restrict the mixing angle $\sin\theta_{1j}$ dominantly ($\lesssim 0.25$). The bounds from the measured value of EW precision parameter are mild for $M_{s_i} < 1$ TeV. While these constraints restrict the singlet scalar mixing with SM Higgs denoted by ($\theta_{1j}, j = 2, 3, 4$), the other three angles ($\theta_{23}, \theta_{24}, \theta_{34}$) remain unconstrained. We choose our benchmark values of singlet scalar masses and their mixing with SM Higgs boson in such a way that these constraints are automatically satisfied.

2.4.3 The Boltzmann Equations for Two-component DM

In this work, as we already know that we are dealing with two stable DM candidates ξ_1 and ξ_2. To find the present number densities of DM candidates we need to solve two Boltzmann equations one for each candidate. The collision term of each Boltzmann equation contains all possible number changing interactions of that particular DM candidate allowed by the symmetries. In the present model, there are two types of number changing interactions for a DM candidate. First one is the pair annihilation where ξ_i and $\bar{\xi}_i$ annihilate in a pair into all possible final states (X) except a pair of other DM candidate $\xi_j\bar{\xi}_j$ ($j \neq i$). These

processes reduce the number of ξ_i and $\bar{\xi}_i$ by one unit (assuming there is no asymmetry in the number densities of DM and its anti-particle). The other type of number changing process is $\xi_i\bar{\xi}_i \to \xi_j\bar{\xi}_j$ $(i \neq j)$. This is actually the conversion process where one type of DM converts into another. It increases the number of lighter DM candidate by two unit while reducing the number of heaver one by the same amount. This conversion process acts as a coupling between the individual Boltzmann equations of ξ_1 and ξ_2. Let $n_2 = n_{\xi_2} + n_{\bar{\xi}_2}$ and $n_1 = n_{\xi_1} + n_{\bar{\xi}_1}$ are the total number densities of two DM candidates respectively. Assuming there is no asymmetry in number densities of ξ_i and $\bar{\xi}_i$, the two coupled Boltzmann equations in terms of n_2 and n_1 are given below [317–319],

$$\frac{dn_2}{dt} + 3n_2\mathbf{H} = -\frac{1}{2}\langle\sigma \mathrm{v}_{\xi_2\bar{\xi}_2\to X\bar{X}}\rangle\left(n_2^2 - (n_2^{\rm eq})^2\right) - \frac{1}{2}\langle\sigma \mathrm{v}_{\xi_2\bar{\xi}_2\to \xi_1\bar{\xi}_1}\rangle\left(n_2^2 - \frac{(n_2^{\rm eq})^2}{(n_1^{\rm eq})^2}n_1^2\right) \quad (2.75)$$

$$\frac{dn_1}{dt} + 3n_1\mathbf{H} = -\frac{1}{2}\langle\sigma \mathrm{v}_{\xi_1\bar{\xi}_1\to X\bar{X}}\rangle\left(n_1^2 - (n_1^{\rm eq})^2\right) + \frac{1}{2}\langle\sigma \mathrm{v}_{\xi_2\bar{\xi}_2\to \xi_1\bar{\xi}_1}\rangle\left(n_2^2 - \frac{(n_2^{\rm eq})^2}{(n_1^{\rm eq})^2}n_1^2\right) \quad (2.76)$$

where, $n_i^{\rm eq}$ is the equilibrium number density of DM species i. The second term in the left hand side involving the Hubble parameter $\mathbf{H}$ represents dilution of number density due to the expansion of the Universe. The extra half factors in the collision term are due to non-self-conjugate (Dirac fermion) nature of our both DM candidates ξ_1 and ξ_2 [49]. Here we are more interested to study the evolution of number densities of two-component WIMP system due to all possible interactions which change particle numbers of either ξ_1 or ξ_2 or both. Hence, in stead of actual number density n_i, it is convenient to describe the Boltzmann equation for a species in terms of comoving number density $Y_i = n_i/s$ with s representing the entropy density of the Universe. The quantity Y_i is an useful one as it absorbs the effect of the expansion on n_i. In terms of comoving number densities, the above two coupled Boltzmann equations can be written as,

$$\frac{dY_2}{dx_{\xi_2}} = -\frac{1}{2}\sqrt{\frac{\pi}{45\,G}}\frac{m_{\xi_2}}{x_{\xi_2}^2}\sqrt{g_\star}\left(\langle\sigma \mathrm{v}_{\xi_2\bar{\xi}_2\to X\bar{X}}\rangle\left(Y_2^2 - (Y_2^{\rm eq})^2\right) + \langle\sigma \mathrm{v}_{\xi_2\bar{\xi}_2\to \xi_1\bar{\xi}_1}\rangle\left(Y_2^2 - \frac{(Y_2^{\rm eq})^2}{(Y_1^{\rm eq})^2}Y_1^2\right)\right), \quad (2.77)$$

$$\frac{dY_1}{dx_{\xi_1}} = -\frac{1}{2}\sqrt{\frac{\pi}{45\,G}}\frac{m_{\xi_1}}{x_{\xi_1}^2}\sqrt{g_\star}\left(\langle\sigma \mathrm{v}_{\xi_1\bar{\xi}_1\to X\bar{X}}\rangle\left(Y_1^2 - (Y_1^{\rm eq})^2\right) - \langle\sigma \mathrm{v}_{\xi_2\bar{\xi}_2\to \xi_1\bar{\xi}_1}\rangle\left(Y_2^2 - \frac{(Y_2^{\rm eq})^2}{(Y_1^{\rm eq})^2}Y_1^2\right)\right), \quad (2.78)$$

where, G is the Gravitational constant and $x_{\xi_i} = \frac{m_{\xi_i}}{T}$, is a dimensionless variable with T being the temperature of the Universe. The quantity $g_\star$ is expressed as,

$$\sqrt{g_\star} = \frac{h_{\rm eff}(T)}{\sqrt{g_{\rm eff}(T)}}\left(1 + \frac{1}{3}\frac{d\ln(h_{\rm eff}(T))}{d\ln(T)}\right), \quad (2.79)$$

where, $h_{\rm eff}(T)$ and $g_{\rm eff}(T)$ are the effective degrees of freedom related to the entropy and energy densities of radiation. In the collision of term of the Boltzmann equation, the first term represents pair annihilations of ξ_i and $\bar{\xi}_i$ into particles which are in thermal equilibrium

(including the SM particles also) while the second term is due to the DM conversion process $\xi_2\bar{\xi}_2 \to \xi_1\bar{\xi}_1$ where none of them are in thermal equilibrium during freeze-out. Detailed derivation of this term when both initial as well as final state particles are not in thermal contact with the visible world is given in Appendix A.4. In the collision term, the thermal averaged annihilation cross section of a particular process $AA' \to BB'$ has been denoted by $\langle \sigma v_{AA' \to BB'} \rangle$. The possible annihilation channels of both the DM candidates in our model are shown in figure 2.19. This figure not only contains the Feynman diagrams for individual DM annihilations into other particles, but also the conversion of one particular DM pair into a pair of the other DM. We have solved these two coupled Boltzmann equations using `micrOMEGAs` [320] where the model information has been supplied to `micrOMEGAs` using `FeynRules` [321]. All the relevant annihilation cross sections of DM number changing processes required to solve the coupled equations are calculated using `CalcHEP` [322]. Finally, after solving the Boltzmann equations we get the comoving number density $Y_i(T_0)$ of each DM candidate at the present epoch (at $T = T_0$). Thereafter, one can easily calculate the total DM relic density which is sum of relic densities of all DM candidates,

$$\Omega_{\rm DM} h^2 = 2.755 \times 10^8 \sum_{i=1}^{2} \left(\frac{m_{\xi_i}}{\rm GeV} \right) Y_i(T_0) \,. \tag{2.80}$$

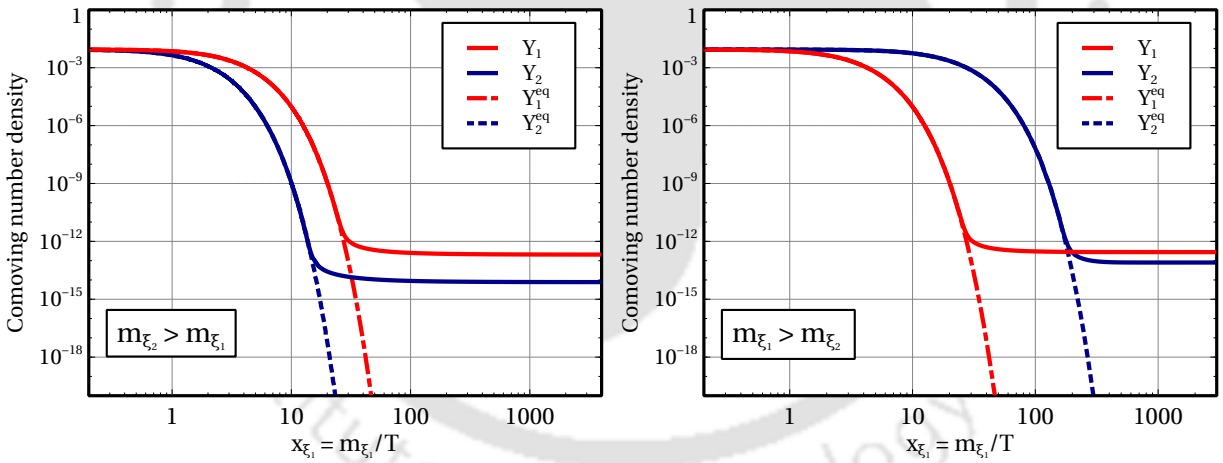

Figure 2.18: Evolution of comoving number densities of both ξ_1 and ξ_2 for two cases (a) $m_{\xi_2} > m_{\xi_1}$ (left panel) and (b) $m_{\xi_1} > m_{\xi_2}$ (right panel).

In order to understand how the comoving number densities are varying with respect to the temperature T, we have shown two plots in the both panels of figure 2.18 illustrating the thermal evolution of Y_1 and Y_2 for $m_{\xi_2} > m_{\xi_1}$ (left panel) and $m_{\xi_1} > m_{\xi_2}$ (right panel) respectively. In the left panel, we consider $m_{\xi_2} = 2m_{\xi_1}$ with $m_{\xi_1} = 2110$ GeV. Here, the red solid line represents the variation of Y_1 with $x_{\xi_1} = \frac{m_{\xi_1}}{T}$ while the same for heavier component ξ_2 has been indicated by the blue solid line. The corresponding equilibrium number densities computed using the Maxwell-Boltzmann distribution are shown by red dash-dotted and blue dotted lines respectively. Form this plot it is seen that initially for low x_{ξ_1} (i.e. for

high T) the comoving number density of each component follows their respective equilibrium number density upto a certain temperature T (different for ξ_1 and ξ_2) and thereafter Y_i departs significantly from the corresponding equilibrium distribution function $Y_i^{\rm eq}$ and remains constant with respect to the variation of T. This is nothing but the well known freeze-out point of a WIMP and it depends on when the interaction rate corresponding to the number changing processes of a particular DM component goes below the expansion rate of the Universe governed by the Hubble parameter **H**. In this particular situation, freeze-out of ξ_1 occurs at $x_{\xi_1} \sim 25$ while that for the heavier component is $\frac{m_{\xi_2}}{T} \sim 30$ ($x_{\xi_2} = 2x_{\xi_1}$). Furthermore, the interactions of ξ_1 and ξ_2 are such that ξ_2 which freezes-out earlier has less relic abundance compared to its lighter counter part ξ_1. The opposite situation is presented in the right panel of figure 2.18, where ξ_1 is the heavier DM component. Here we consider the model parameters in such a way that although the heavier component ξ_1 has earlier freeze-out, ends up with a greater abundance.

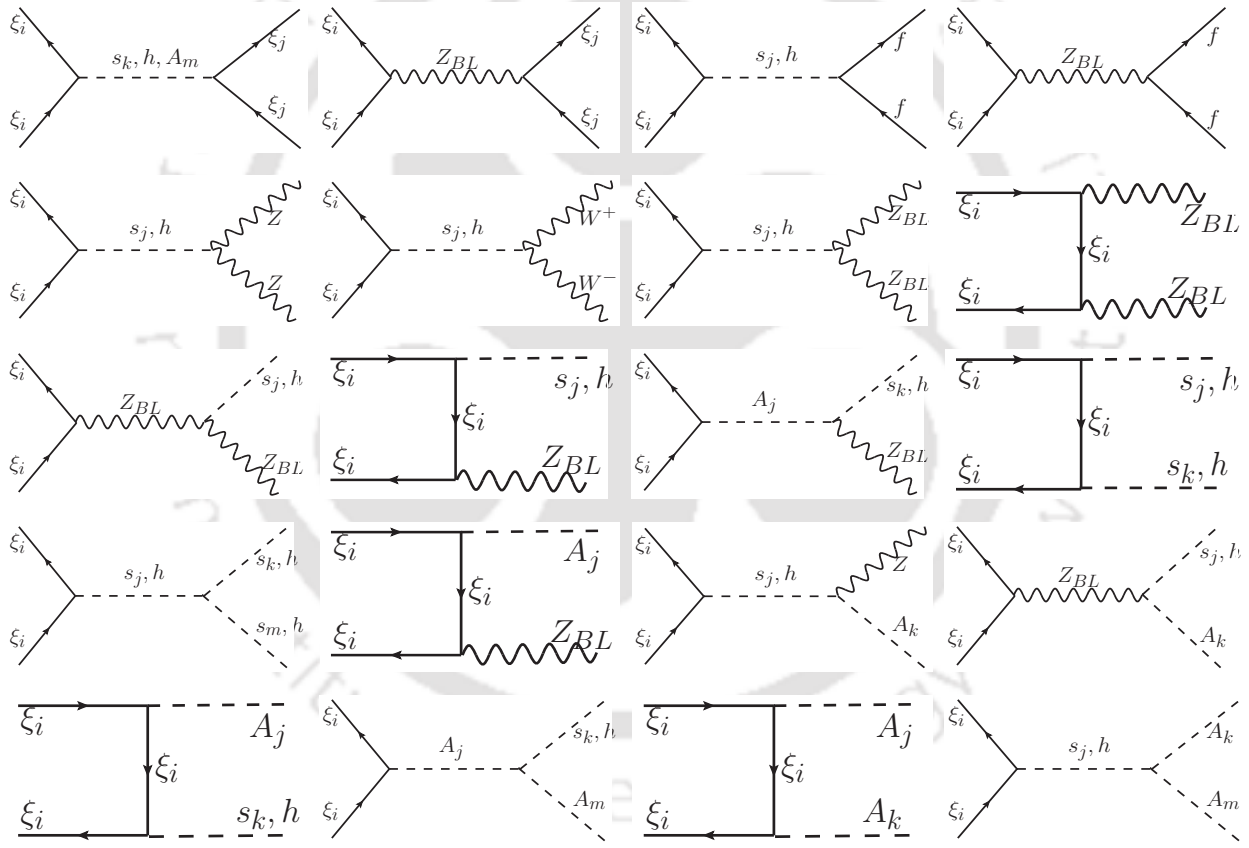

Figure 2.19: Feynman diagrams for all possible annihilation channels of two DM candidates.

2.4.4 Direct Detection

Since each of the DM candidates in our model is a Dirac fermion, there exists Z_{BL} as well as scalar mediated spin independent elastic scattering processes off nucleons. The relevant Feynman diagrams are shown in figure 2.20. Since several ongoing experiments like LUX

[53], PandaX-II [56, 57] and Xenon1T [6, 55] are looking for such processes, regularly giving stringent upper bounds on DM-nucleon scattering cross section, we can further constrain our model parameters from these data. Parametrising DM and quark interactions with Z_{BL} as

$$\mathcal{L} \supset [\overline{\xi_i}\gamma^\mu(g_{\xi_i v} + g_{\xi_1 a}\gamma^5)\xi_i + \overline{q}\gamma^\mu(g_{qv} + g_{qa}\gamma^5)q](Z_{BL})_\mu,$$

the dominant spin independent DM-nucleus scattering cross section can be written down as [293]

$$\sigma^{\rm SI}_{\xi_i} = \frac{\mu^2_{\xi_i N} g^2_{\xi_i v}}{\pi M^4_{Z_{BL}}}\left[Z(2\tilde{b}_u + \tilde{b}_d) + (A - Z)(\tilde{b}_u + 2\tilde{b}_d)\right]^2 \tag{2.81}$$

where $\mu_{\xi_i N}$ is the reduced mass of DM nucleus system, $\tilde{b}_q$ are the quark-Z_{BL} couplings which is same for all quarks in $B - L$ gauge model. Also, A, Z are mass number and atomic number of the nucleus. From the Lagrangian of DM given in (2.64), we can write

$$g_{\xi_1 v} = \frac{9}{10} g_{BL},\ g_{\xi_2 v} = \frac{4}{5} g_{BL}$$

which can be used in the expression above to find the DM-nucleus scattering cross section numerically for different values of $g_{BL}, M_{Z_{BL}}$. Similarly, if the scalar (s_j) mediated interactions are parametrised as

$$\mathcal{L} \supset [\overline{\xi_i}(\lambda_{\xi_i s} + \lambda_{\xi_1 p}\gamma^5)\xi_i + \overline{q}(\lambda_{qs} + \lambda_{qp}\gamma^5)q]s_j$$

the corresponding spin-independent DM-nucleus scattering cross section can be written as

$$\sigma^{\rm SI}_{\xi_i} = \frac{\mu^2_{\xi_i N} \lambda^2_{\xi_i s}}{\pi M^4_{s_j}}\left[Z\tilde{f}_p + (A - Z)\tilde{f}_n\right]^2. \tag{2.82}$$

Here $\tilde{f}_{p,n}$ are defined as

$$\frac{\tilde{f}_{p,n}}{m_{p,n}} = \sum_{q=u,d,s} f^{p,n}_{T_q}\frac{\tilde{f}_q}{m_q} + \frac{2}{27} f_{TG} \sum_{q=c,b,t} \frac{\tilde{f}_q}{m_q} \tag{2.83}$$

with $\tilde{f}_q = \lambda_{s_i} m_q/\text{GeV}$ and $f_{TG} = 1 - f^{p,n}_{T_u} - f^{p,n}_{T_d} - f^{p,n}_{T_d}$. Here λ_{s_i} denotes the quark-singlet scalar couplings which can be derived by using the singlet scalar-SM Higgs mixing shown in Appendix A.2. We take the standard values of other parameters appearing in the above formula as $f^p_{T_u} = 0.020, f^p_{T_d} = 0.026$ (and opposite for $f^n_{T_{u,d}}$), $f_{T_s} = 0.043$ which further gives $f_{TG} \approx 0.91$. We extract the spin independent elastic scattering cross section for both the DM candidates off nucleons from `micrOMEGAs`. Keeping the fact in mind that we are analysing a two-component DM scenario we have multiplied the elastic scattering cross-section by the relative number density of each DM candidate to find the individual effective DM-nucleon scattering cross section.

As mentioned earlier, both gauge interactions as well as Yukawa interactions will contribute in the direct detection cross sections. However, the gauge mediated interaction is proportional to g^4_{BL} whereas the scalar mediated processes are mixing suppressed as well as Yukawa coupling suppressed (the Yukawa couplings of first generation of quarks are $\mathcal{O}(10^{-6})$). Hence, in our present model DM scattering off nucleons through Z_{BL} will have dominant contribution.

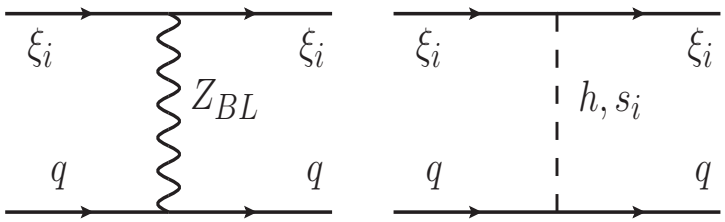

Figure 2.20: Feynman diagrams for spin-independent elastic scattering processes of DM with nucleons (or quarks) in the model.

2.4.5 Results

As we have discussed in the previous section, this model predicts two automatically stable DM candidates ξ_1 and ξ_2. The total relic density of DM can be expressed as, the sum of the relic densities of ξ_1 and ξ_2, $\Omega_{\rm DM}h^2 = \Omega_{\xi_1}h^2 + \Omega_{\xi_2}h^2$ where $\Omega_{\xi_1}h^2$ and $\Omega_{\xi_2}h^2$ are the relic abundances of ξ_1 and ξ_2 respectively. Let us now investigate the dependence of the relic densities, Ω_{ξ_1} and Ω_{ξ_2}, on the parameters of the model. In figure 2.21, we have shown the variation of relic density with the DM mass by assuming $M_{\xi_2} = M_{\xi_1}$. The other parameters of the model were chosen as $M_{\psi_1} = 1.5$ TeV, $M_{\psi_2} = 2$ TeV, $M_{\psi_3} = 750$ GeV, $M_{s_1} = M_{s_2} = M_{s_3} =$ 1 TeV, $M_{A_3} = 10$ TeV, $s_{12} = s_{13} = s_{14} = s_{24} = 0.2$, $M_{Z_{BL}} = 5$ TeV, $g_{BL} = 0.3$. The dashed (blue) and dotted (red) lines denote the relic densities of each DM candidate,$\Omega_{\xi_1}h^2$ and $\Omega_{\xi_2}h^2$, whereas the solid (green) line is their sum ($\Omega_{DM}h^2$). The horizontal magenta line represents the relic density bound from PLANCK data [50]. Some important features of the model can be indicated here. The resonances due to the s-channel annihilation through Z_{BL} and the different scalars (s_1, s_2, s_3, A_2, A_3) has reduced the relic density as expected. Figure 2.21 clearly shows four different scalars and Z_{BL} resonances, as we have assumed all the scalars have the same mass, at a DM mass of 500 GeV, 2.5 TeV, 3.27 TeV, and 5 TeV respectively. At DM mass of 1 TeV, DM particles starts annihilating into the two scalars final state giving a sudden reduction in the relic density. Similar behaviour can be found at the DM mass around 3.77 TeV, and 5.5 TeV where DM starts annihilating into one scalar ($M_{s_i} = 1$ TeV) plus one pseudo scalar ($M_{A_2} = \sqrt{\frac{3}{7}}M_{A_3} = 6.54$ TeV and $M_{A_3} = 10$ TeV) final states(Feynman diagrams in figure 2.19). One can expect similar reduction for the annihilation into one scalar ($M_{s_i} = 1$ TeV) and one Z_{BL} ($M_{Z_{BL}} = 5$ TeV) final state near 3 TeV mass. However, because of the resonance that effect is not visible. Another important point to note here is that, Ω_{ξ_2} is subdominant throughout the whole mass range. That can be explained as follows, ξ_2 has formed by combining N_{2L} and N_{2R} where as ξ_1 has formed from N_{1L} and N_{1R}. The $B-L$ quantum number assigned for N_{2L} and N_{2R} is greater than the quantum number for N_{1L} and N_{1R} and that increases the annihilation cross section of ξ_2 by some numerical factor which results to smaller abundance.

One point to note here is that both the gauge coupling g_{BL} as well as Yukawa couplings $\mathcal{Y}_1$, $\mathcal{Y}_2$ play important roles in the DM annihilation. The gauge coupling g_{BL} is involved in the annihilation channels mediated by gauge boson Z_{BL} while the scalar mediated annihilation cross sections depend on Yukawa couplings $\mathcal{Y}_1$, $\mathcal{Y}_2$. In the lower mass region of DM g_{BL} plays the main role whereas in the high mass region $\mathcal{Y}_i$ also gives a significant contribution

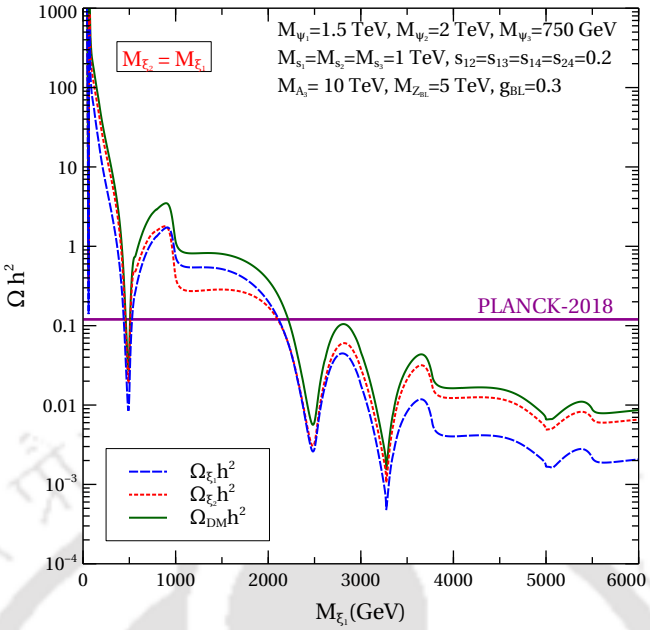

Figure 2.21: Relic abundance of two DM candidates with degenerate masses keeping all other model parameters fixed to benchmark values.

as $\mathcal{Y}_i = \sqrt{2}M_{\xi_i}/u$. In figure 2.22, we have shown the variation of the relic density for two different relations between M_{ξ_1} and M_{ξ_2}. In left panel, we have assumed $M_{\xi_2} = 2\ M_{\xi_1}$ and in right panel $M_{\xi_2} = M_{\xi_1}/2$ – other parameters remain same as in figure 2.21. In figure 2.22a, the resonances have occurred at different positions for Ω_{ξ_2}, at 250 GeV, 1.25 TeV, 1.63 TeV, and 2.5 TeV, whereas, Ω_{ξ_1} has the same behaviour as in 2.21 which is expected as we have assumed the $M_{\xi_2} = 2\ M_{\xi_1}$. Figure 2.22b can be explained in a similar way.

In figure 2.23 we have shown the variation of the total relic density as a function of m_{ξ_1} for three benchmark values of g_{BL} (0.01, 0.09, 0.4) and mixing angle (0.001, 0.01, 0.1). The left panel shows that the total DM abundance increases as we choose smaller values of gauge coupling. It is because small g will decrease the annihilation cross section and eventually increase the DM abundance. The right panel shows that the relic abundance hardly depends on the mixing angle. Here for simplicity we have assumed all the mixing angle to be same. In both the cases, we have assumed $M_{\xi_2} = 2\ M_{\xi_1}$ and the other parameters remain same as in figure 2.21.

As seen from the above plots, the relic abundance of both the DM candidates primarily depend upon the strength of their annihilation cross sections via scalar or gauge portal interactions. After understanding this behaviour from the plots with benchmark choices of model parameters, we now move onto performing a random scan over a set of free parameters mentioned in table 2.9. While the physical masses of DM and all new particles in the model are varied in the mentioned range along with g_{BL}, the singlet scalar mixing angles with SM Higgs boson as well as among themselves are kept fixed at 0.2. We then apply the relevant constraints one by one to arrive at the final allowed parameter space from all relevant bounds. We first show the parameter space in $M_{\xi_1} - M_{\xi_2}$ plane allowed from total DM relic abundance, perturbativity, bounded from below criteria of the scalar potential in figure 2.24. In figure

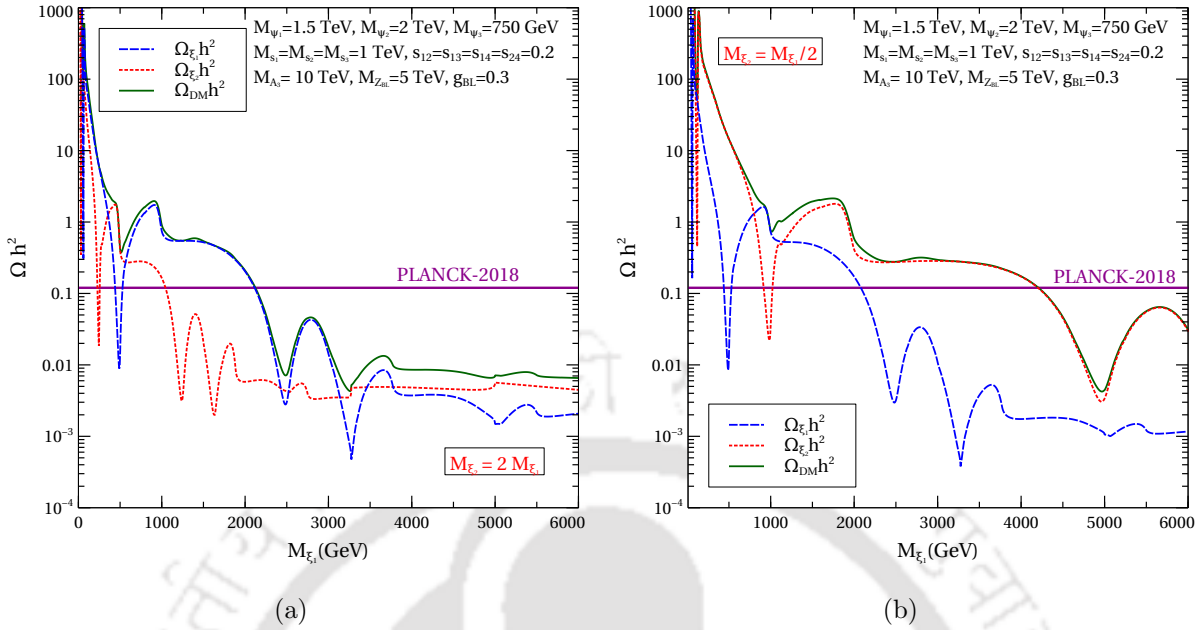

Figure 2.22: Relic abundance of two DM candidates with non-degenerate masses: $M_{\xi_2} = 2M_{\xi_1}$ (left panel) and $M_{\xi_2} = M_{\xi_1}/2$ (right panel), keeping all other model parameters fixed to benchmark values.

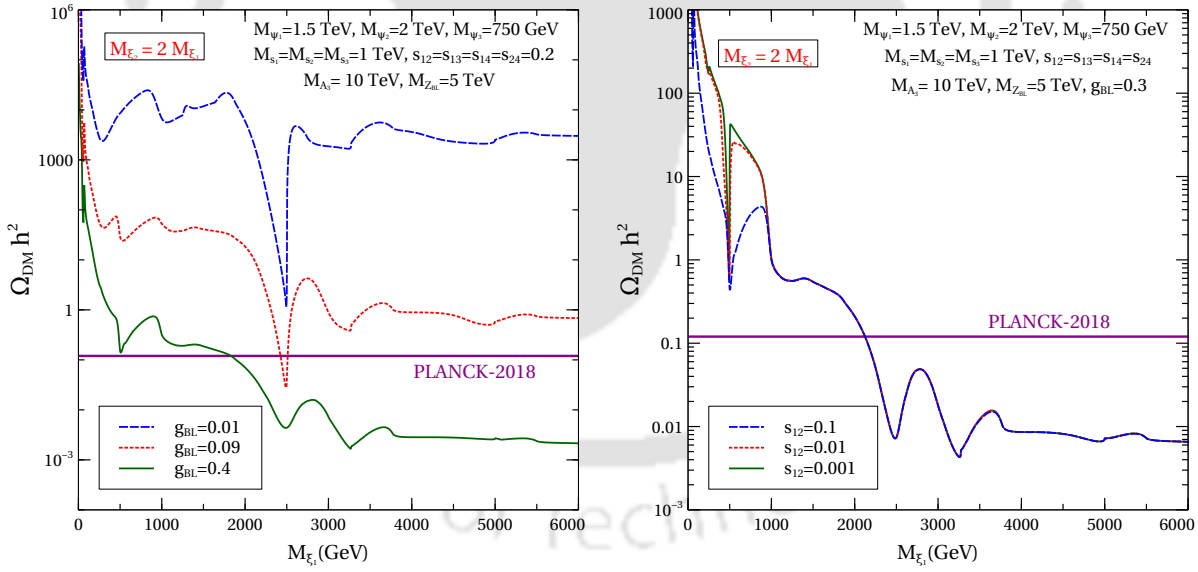

Figure 2.23: Relic abundance of two DM candidates with non-degenerate masses ($M_{\xi_2} = 2M_{\xi_1}$) for different benchmark values of: gauge coupling g_{BL} (left panel), singlet scalar-SM Higgs mixing (right panel).

2.25, we then show the parameter space in $g_{BL} - M_{Z_{BL}}$ plane allowed from total DM relic abundance, perturbativity, bounded from below criteria of the scalar potential. The bounds

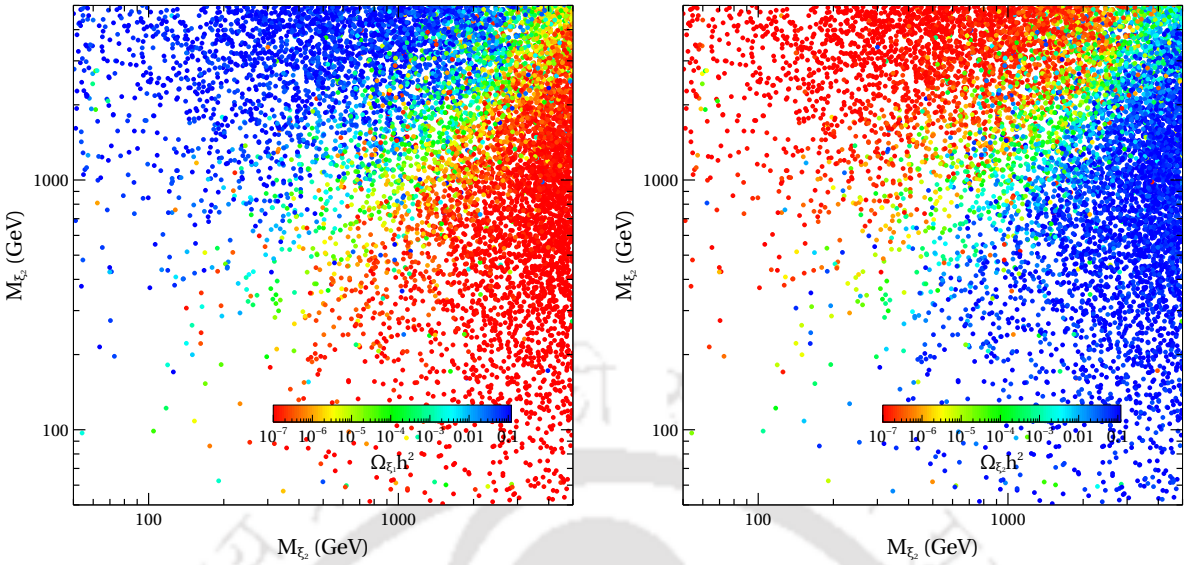

Figure 2.24: Scan plot showing the parameter space in $M_{\xi_1} - M_{\xi_2}$ plane allowed from total DM relic abundance, perturbativity, bounded from below criteria of the scalar potential.

from the LEP and the LHC[6] are separately shown by the respective shaded regions which are excluded. The coloured bar in the two plots shown in figure 2.25 correspond to the relative abundances of two DM candidates ξ_1 (left panel) and ξ_2 (right panel) respectively.

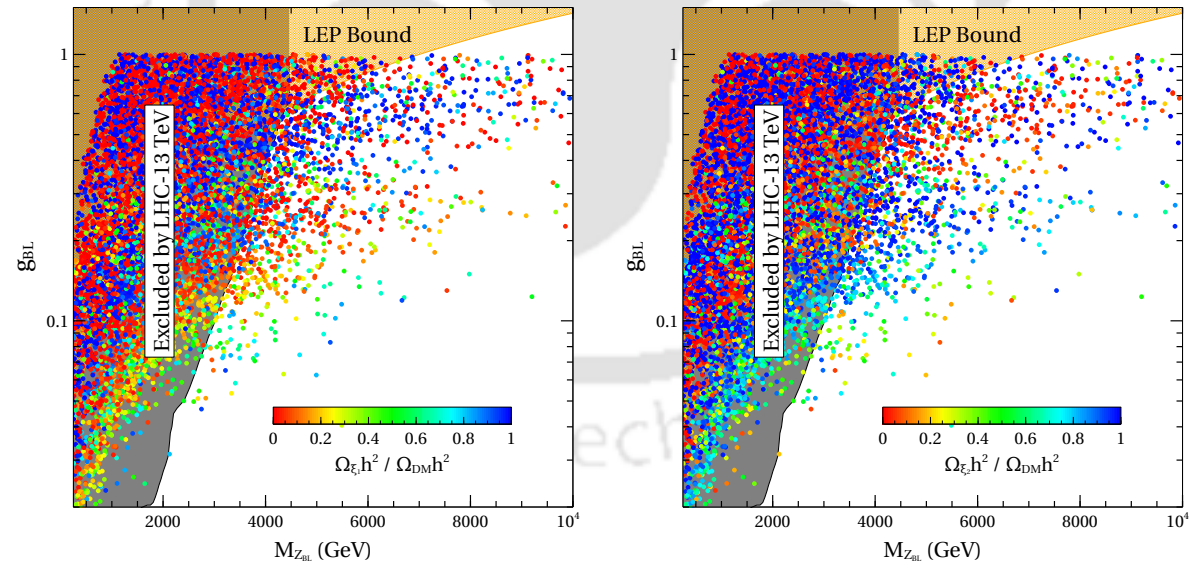

Figure 2.25: Scan plot showing the parameter space in $g_{BL} - M_{Z_{BL}}$ plane allowed from total DM relic abundance, perturbativity, bounded from below criteria of the scalar potential.

[6]Note that we have used the LHC bound in $M_{Z_{BL}} - g_{BL}$ plane from the ATLAS collaboration results [295]. The more recent limits from the ATLAS collaboration with increased luminosity but with same centre of mass energy [309] have small deviations from the limits we apply here.

Parameters	Range
M_{ξ_1}	(10 GeV, 8 TeV)
M_{ξ_2}	(10 GeV, 8 TeV)
$M_{Z_{BL}}$	(100 GeV, 10 TeV)
g_{BL}	(0.0001, 1)
M_{s_1}	(100 GeV, 10 TeV)
M_{s_2}	(100 GeV, 10 TeV)
M_{s_3}	(100 GeV, 10 TeV)
M_{A_3}	(1 TeV, 20 TeV)
M_{A_2}	$\sqrt{\frac{3}{7}}\ M_{A_3}$
M_{ψ_3}	(1 TeV, 2.5 TeV)
M_{ψ_2}	750 GeV + M_{ψ_3}
M_{ψ_1}	1.5 TeV + M_{ψ_3}

Table 2.9: The parameters of our model and ranges used in the random scan

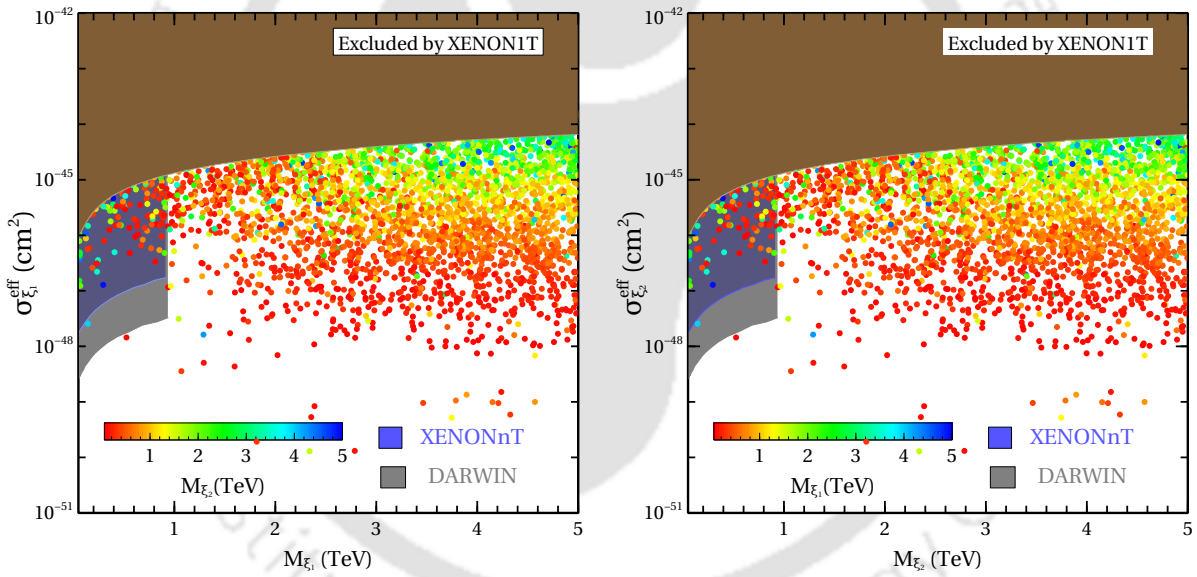

Figure 2.26: Effective spin-independent scattering cross section off nucleons for individual DM candidates. All the points satisfy total DM relic, perturbativity, bounded from below criteria of the scalar potential. The projected sensitivities of XENONnT (blue region) and DARWIN (gray region) experiments have been shown in both the plots.

In figure 2.26, we show the spin independent DM-nucleon scattering cross section for individual DM candidates as functions of their mass. All the points satisfy the total DM relic, perturbativity, bounded from below criteria of the scalar potential. We have also shown the projected sensitivities of XENONnT (blue region) and DARWIN (grey region) experiments in both the plots which clearly show that these two future experiments can probe a large region of parameter space of the model. As mentioned earlier, the actual scattering

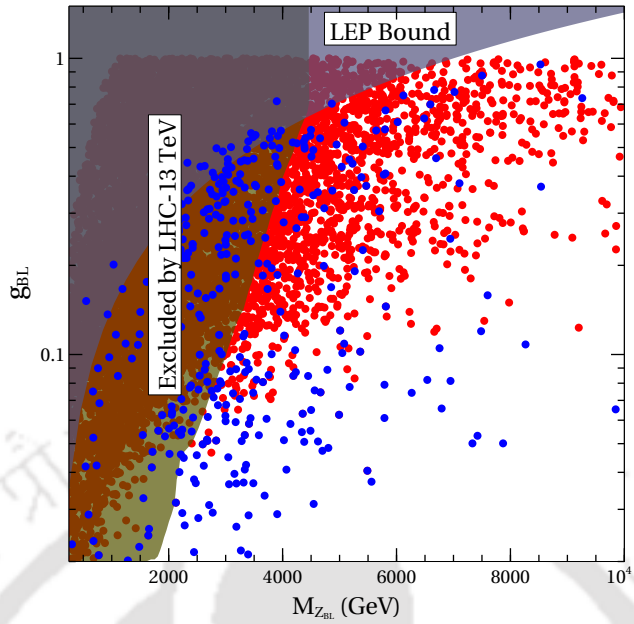

Figure 2.27: Summary plot showing the allowed points with and without applying the direct detection bounds from XENON1T experiment.

cross section is multiplied by individual relative number densities $n_{\xi_{1,2}}/(n_{\xi_1} + n_{\xi_2})$ in order to compare with the XENON1T bounds [6] derived for single DM component. This clearly shows that the model remains very much sensitive to the direct detection experiments with many parts of parameter space already being ruled out. We then superimpose the collider bounds also on these points and show the resulting parameter space in figure 2.27. The severe impact of XENON1T constraints is clearly visible here with a very few points allowed compared to the points allowed without applying the XENON1T bounds. Although the individual DM-nucleon scattering bound allowed several points in the parameter space to survive, as seen from figure 2.26, when we impose the condition that both the DM candidates must satisfy the XENON1T bounds, it results in a much smaller allowed parameter space, seen in figure 2.27. This may be due to the fact that the elastic scatterings of both DM components (ξ_1 and ξ_2) with the detector nuclei occur predominantly through Z_{BL} exchange and hence, $\sigma^{\rm SI}_{\xi_i}$ $(i = 1, 2)$ are extremely sensitive to both g_{BL} and $M_{Z_{BL}}$. On the other hand, Z_{BL} as well as scalar bosons mediated annihilation processes have significant impact in the relic densities of ξ_1 and ξ_2. Therefore, in the latter case we have more parameters (Yukawa couplings, g_{BL} etc.) and consequently the large portion of $g_{BL} - M_{Z_{BL}}$ plane is allowed. The allowed points in the chosen range of random scan will face further constraints from future LHC runs as well as direct detection experiments like LZ [323], XENONnT [324], DARWIN [325].

2.4.6 LHC signatures of fermion triplets

Although typical LHC signatures of a $U(1)_{B-L}$ model is via search for dilepton resonance mediated by Z_{BL} mentioned before, the present model can have additional prospects of being

discovered at the LHC due to the presence of triplet fermions. While the neutral components of fermion triplets play the role of generating light neutrino masses through type III seesaw mechanism, the charged components can leave interesting signatures at colliders. Although a detailed study of collider aspects of such fermion triplets is beyond the scope of this present work and can be found elsewhere, we briefly highlight the additional advantage of having such triplets in a gauged $B-L$ model. Detailed collider studies of charged components of fermion triplet can be found in the context of long lived wino in supersymmetric models; for example, see [326] and references therein. In the context of non-supersymmetric models, collider studies of such long lived fermion triplets can be found in [327, 328] and references therein. We consider the third fermion triplet and its charged component as it can have enhanced production cross section at colliders due to larger $B-L$ charge. It should be noted that unlike in usual type III seesaw model, here the charged components of fermion triplets can be produced at the LHC via both Z and Z_{BL} gauge bosons, apart from usual photon mediation. The charged components can then decay into (i) charged lepton and Higgs boson or (ii) neutral fermion triplet plus on or off-shell W boson depending upon the mass splitting $\Delta M \gtrsim 80$ GeV or $\Delta M \lesssim 80$ GeV. Although the components of a particular fermion triplet have degenerate masses (M_{k0}) at tree level, one can make the charged components $\psi_k^\pm$ heavier by considering one loop electroweak radiative corrections [329, 330], which result in a mass splitting $\Delta M \sim 166$ MeV between $M_{\psi_k^\pm}$ and $M_{\psi_k^0}$ for $M_{k0} \gtrsim 1$ TeV. Thus, in the second possible decay channel mentioned above, only the off-shell W boson is possible. The first decay mode is typically sub-dominant by the constraints from light neutrino masses, which require TeV scale fermion triplet Yukawa couplings with the SM leptons to be as small as around $10^{-6}-10^{-5}$. Therefore we consider the second decay mode only where the charged component of triplet decays into the neutral component and an off-shell W boson. Due to the small mass splitting, the dominant decay mode has final states $\psi_k^0, \pi^\pm$. The decay width of $\psi_3^\pm$ to ψ_3^0 and $\pi^\pm$ can be written as

$$\Gamma_{\psi_3^\pm \to \psi_3^0 \pi^\pm} = \frac{g^4 f_\pi^2 V_{ud}^2}{128\pi M_W^4 M_{\psi_3^\pm}} \Delta M^2 \left((M_{\psi_3^0} + M_{\psi_3^\pm})^2 - M_\pi^2 \right) \times \sqrt{1 - \frac{(M_{\psi_3^0} - M_\pi)^2}{M_{\psi_3^\pm}^2}} \sqrt{1 - \frac{(M_{\psi_3^0} + M_\pi)^2}{M_{\psi_3^\pm}^2}}, \tag{2.84}$$

where $\Delta M = M_{\psi_3^\pm} - M_{\psi_3^0} \simeq 166$ MeV, g is the $\mathrm{SU(2)_L}$ gauge coupling, $f_\pi = 131$ MeV [329] is the pion decay constant, and the first diagonal element of the CKM matrix $V_{ud} \simeq 0.974$ respectively. Such tiny decay width keeps the lifetime of $\psi_3^\pm$ considerably long enough so that it can reach the detector before decaying. In fact, the ATLAS experiment at the LHC has already searched for such long-lived charged particles with lifetime ranging from 10 ps to 10 ns, with maximum sensitivity around 1 ns [331]. In the decay $\psi_3^\pm \to \psi_3^0 \pi^\pm$, the final state pion typically has very low momentum and it is not reconstructed in the detector. On the other hand ψ_3^0 is a long lived particle as it can decay to SM leptons through the small mixing with the other triplet fermions and leaves the detector without interacting. Therefore, it gives rise to a signature where a charged particle leaves a track in the inner parts of the detector and then disappears leaving no tracks in the portions of the detector at higher radii.

Another crucial difference from usual type III seesaw extension of the SM is that here the production cross section of fermion triplets gets enhanced. The presence of Z_{BL} significantly increases the production cross-section of the charged $\psi_3^\pm$ pairs at the collider. This is due to the fact that the decay of the BSM neutral gauge boson to the $\psi_3^\pm$ now happens on-shell in contrast to models where this decay takes place off-shell via SM Z boson and photon. Also, as there is no negative interference between the Z and Z_{BL} mediated charged $\psi_3^\pm$ production channels, hence the addition of new channel always improves the production cross-section. In order to illustrate this improvement, we first show the variation of production cross-section $\sigma_{pp\to\psi_3^+\psi_3^-}$ in the left panel of figure 2.28 for two different choices of centre of mass energy. As can be seen, the improvement in production cross section is more significant in 100 TeV centre of mass energies of proton proton collisions. Once produced, $\psi_3^\pm$ can give rise to disappearing charged track signatures mentioned above. The ATLAS experiment at the LHC put constraints on such disappearing charged track signatures for a long lived chargino decaying into a pion and wino DM, which is shown as the solid black line in right panel of figure 2.28. Although ψ_3^0 is not the DM candidate in our model, it effectively behaves like one at the LHC due to its long life. It can be seen that the existing LHC constraint can already rule out $\psi_3^\pm$ masses below 500 GeV from its searches for disappearing charged tracks, keeping the parameter space considered in this study within near future sensitivity. Also, the bounds will get slightly tighter in our model due to enhanced production cross section. We leave a detailed study of such type III seesaw signatures at the LHC in the framework of a $B-L$ gauge model.

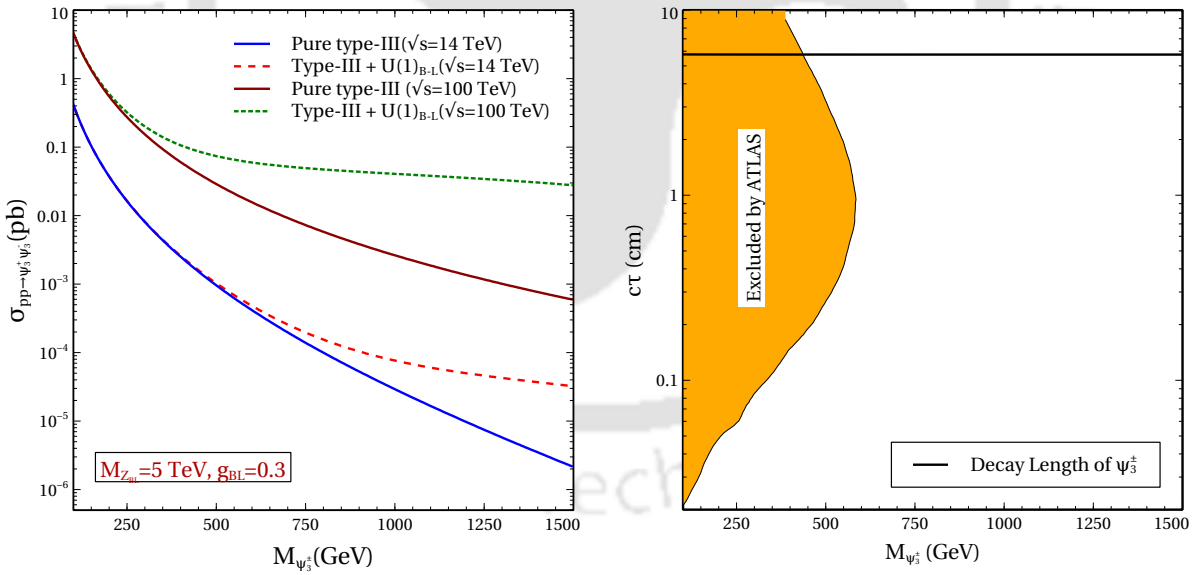

Figure 2.28: Left panel: Plot showing improvement in production cross-section of the $\psi_3^\pm$ pairs due to Z_{BL} mediation for two choices of centre of mass energies in proton proton collisions. Right panel: Decay length of $\psi_3^\pm$ versus its mass compared with the ATLAS bound on disappearing charge track searches at 13 TeV centre of mass energy.

$M_{Z_{BL}} = 5TeV\,, g_{BL} = 0.3\,, M_{\psi_1} = 2.5TeV\,, M_{\psi_2} = 2TeV\,, M_{s_i} = 1TeV\,, M_{A_1} = 10TeV$	
Case - I	$M_{\psi_3} = M_{\xi_i} = (600GeV - 2500GeV)$
Case - II	$M_{\xi_i} = 3TeV,\ M_{\psi_3} = (600GeV - 2500GeV)$
Case - III	$M_{\psi_3} = 2.6TeV,\ M_{\xi_i} = (600GeV - 2500GeV)$

Table 2.10: Benchmark scenarios considered for calculating decay widths of Z_{BL}.

Mass (GeV)	Total Decay Width $\Gamma_{Z_{BL}}$ (GeV)		
	Case-I	**Case -II**	**Case -III**
600	249.2	181.2	177.6
700	249.0	181.1	177.6
800	248.8	181.0	177.4
900	248.4	180.8	177.3
1000	247.9	180.6	177.0
1100	247.2	180.2	176.7
1200	246.3	179.7	176.2
1300	245.1	179.1	175.6
1400	243.5	178.3	174.9
1500	241.5	177.3	173.9
1600	239.0	176.0	172.7
1700	235.7	174.3	171.1
1800	231.7	172.3	169.1
1900	226.7	169.7	166.7
2000	220.3	166.4	163.6
2100	212.2	162.2	159.6
2200	201.7	156.9	154.5
2300	187.6	149.6	147.6
2400	166.8	139.0	137.5
2500	109.7	109.7	109.7

Table 2.11: Decay widths of Z_{BL} for different benchmark values of DM and fermion triplet masses.

It should be noted that here we have adopted the narrow width approximation for Z_{BL} which implies $\Gamma_{Z_{BL}}/M_{Z_{BL}} \ll 1$. To justify this, we consider three benchmark scenarios namely, (i) Z_{BL} can decay into both the DM candidates as well as the fermion triplet, (ii) Z_{BL} can decay into the fermion triplet but not to the DM candidates, (iii) Z_{BL} can decay into both the DM candidates but not to the fermion triplet. The corresponding widths, considering $M_{Z_{BL}} = 5TeV\,, g_{BL} = 0.3$ are shown below in Tables 2.10 and 2.11 respectively. As can be seen from these results, even for the maximum possible decay width of Z_{BL} we can have $\Gamma_{Z_{BL}}/M_{Z_{BL}} < 5\%$. As discussed in several earlier works including [332, 333] and references therein, narrow width approximation remains valid for such small decay widths.

2.5 Two-component dark matter and Dirac neutrino mass in $\mathrm{U(1)_{B-L}}$ model

In this section, we studied the possibility of realising light Dirac neutrinos in a gauged $B-L$ model along with stable DM candidate without incorporating any additional discrete symmetries. In the minimal $U(1)_{B-L}$ model with three right handed neutrinos having $B-L$ charge -1 each, we can not have light Dirac neutrinos naturally as left and right handed neutrinos couple to the SM Higgs field. Even if we forbid the Majorana mass term of right handed neutrinos by suitable choice of singlet scalars, light Dirac neutrino mass of sub-eV order will require extreme fine tuning of Yukawa couplings of the order $\mathcal{O}(10^{-12})$. Even if we tolerate such extreme fine tunings, the model does not have a DM candidate. In earlier works [224, 243], radiative light Dirac neutrino mass and a stable DM candidate were shown to exist in a gauged $B-L$ model, but with several additional global symmetries. Here we consider different $U(1)_{B-L}$ charge (other than -1) for right handed neutrinos in order to prevent the Dirac Yukawa coupling with the SM Higgs. If the right handed neutrinos are assigned $B-L$ charge -2, then the remaining anomalies are

$$\begin{aligned} \mathcal{A}_1\left[U(1)^3_{B-L}\right] &= 21 \\ \mathcal{A}_2\left[(\text{gravity})^2 \times U(1)_{B-L}\right] &= 3 \end{aligned} \tag{2.85}$$

These can be cancelled after introducing four chiral fermions $\chi_L, \chi_R, \psi_L, \psi_R$ having $B-L$ charges 13/9, 22/9, 1/9, 19/9 respectively. This can be seen as

$$\begin{aligned} \mathcal{A}_1\left[U(1)^3_{B-L}\right] &= \left(\frac{13}{9}\right)^3 + \left(-\frac{22}{9}\right)^3 + \left(\frac{1}{9}\right)^3 + \left(-\frac{19}{9}\right)^3 = -21 \\ \mathcal{A}_2\left[(\text{gravity})^2 \times U(1)_{B-L}\right] &= \left(\frac{13}{9}\right) + \left(-\frac{22}{9}\right) + \left(\frac{1}{9}\right) + \left(-\frac{19}{9}\right) = -3 \end{aligned} \tag{2.86}$$

It should be noted that the anomaly cancellation conditions we are solving here are same as the ones adopted in the work [277] leading to type III seesaw for Majorana neutrinos. However, we are using a different solution to the anomaly conditions here from the earlier work. This is due to the fact that a singlet scalars of $B-L$ charges $1, 4$ were required to generate the masses of singlet chiral fermions $-7/5, -2/5, 6/5, -14/5$. However, in our model, we can not have a singlet scalar with $B-L$ charge 4 as with the chosen $B-L$ charge of right handed neutrinos (2 in our model), such a singlet scalar will generate a Majorana mass after spontaneous symmetry breaking, making it impossible to realise light Dirac neutrino scenario.

2.5.1 The Model

In this section, we have discussed about our model in detail. We have extended the SM gauge group with an additional local $\mathrm{U(1)_{B-L}}$ gauge group where B and L are denoting baryon and lepton numbers respectively of a particular field. Addition of this new gauge group introduces anomalies in the theory which can be canceled by including additional fermionic degrees of freedom in the theory. We have discussed the details of anomaly cancellation in the previous

Particles	$SU(3)_c \times SU(2)_L \times U(1)_Y \times U(1)_{B-L}$
$q_L = \begin{pmatrix} u_L \\ d_L \end{pmatrix}$	$(3, 2, \frac{1}{6}, \frac{1}{3})$
u_R	$(3, 1, \frac{2}{3}, \frac{1}{3})$
d_R	$(3, 1, -\frac{1}{3}, \frac{1}{3})$
$\ell_L = \begin{pmatrix} \nu_L \\ e_L \end{pmatrix}$	$(1, 2, -\frac{1}{2}, -1)$
e_R	$(1, 1, -1, -1)$
ν_R	$(1, 1, 0, -2)$
χ_L	$(1, 1, 0, \frac{13}{9})$
χ_R	$(1, 1, 0, \frac{22}{9})$
ψ_L	$(1, 1, 0, \frac{1}{9})$
ψ_R	$(1, 1, 0, \frac{19}{9})$

Table 2.12: Fermion Content of the Model

Particles	$SU(3)_c \times SU(2)_L \times U(1)_Y \times U(1)_{B-L}$
$H = \begin{pmatrix} H^+ \\ H^0 \end{pmatrix}$	$(1, 2, \frac{1}{2}, 0)$
$\eta = \begin{pmatrix} \eta^+ \\ \eta^0 \end{pmatrix}$	$(1, 2, \frac{1}{2}, -1)$
ϕ_1	$(1, 1, 0, 1)$
ϕ_2	$(1, 1, 0, 2)$

Table 2.13: Scalar content of the Minimal Model

section. We have already mentioned that our main motivation is to generate the Dirac neutrino mass along with the stable DM candidate in the theory. Keeping this in mind, we have added three copies of right handed neutrinos with $B - L$ charge -2 each. They couple to lepton doublets via an additional Higgs doublet η with $B - L$ charge -1 generating three Dirac neutrinos with sub-eV mass. However, the addition of these new fermionic fields will increase the anomaly which can be cancelled by adding four SM gauge singlet chiral fermions with fractional $B - L$ charges. We need at least two singlet scalars and one extra scalar doublet to generate the masses all new fermions. The fermion and scalar content of the model are shown in table 2.12 and 2.13 respectively. The necessity of the individual scalar fields will be discussed later.

The Lagrangian of this model can be written as

$$\mathcal{L} \;=\; \mathcal{L}_{SM} - \frac{1}{4} B'_{\alpha\beta}\, B'^{\alpha\beta} + \mathcal{L}_{scalar} + \mathcal{L}_{fermion}\,. \tag{2.87}$$

Here, $\mathcal{L}_{SM}$ represents the Lagrangian involving charged leptons, left handed neutrinos, quarks, gluons and electroweak gauge bosons. Second term denotes the kinetic term of new gauge boson (Z_{BL}) expressed in terms of field strength tensor $B'^{\alpha\beta} = \partial^\alpha Z^\beta_{BL} - \partial^\beta Z^\alpha_{BL}$. Please note that, in principle, the symmetry of the model allows a kinetic mixing term

between $U(1)_Y$ of SM and $U(1)_{B-L}$ of the form $\frac{\epsilon}{2}B^{\alpha\beta}B'_{\alpha\beta}$ where $B^{\alpha\beta} = \partial^\alpha B^\beta - \partial^\beta B^\alpha$ and ϵ is the mixing parameter. Even if we turn off such mixing at tree level as we have done here, one can generate such mixing at one loop level since there are particles in the model which are charged under both $U(1)_Y$ and $U(1)_{B-L}$. Such one loop mixing can be approximated as $\epsilon \approx g_{\rm BL}g'/(16\pi^2)$ [334]. As we will see from final allowed parameter space in our numerical analysis, we have $g_{\rm BL} \leq 0.2$ for few TeV $B-L$ gauge boson mass and with such small values of $g_{\rm BL}$, the mixing parameter ϵ will be of the order of 10^{-3} or smaller. Such small mixing has very little effect on the final allowed parameter space in our model, to be discussed in details in upcoming sections. Therefore, for simplicity, we ignore such kinetic mixing for the rest of our analysis.

The gauge invariant scalar interactions described by $\mathcal{L}_{scalar}$ can be written as

$$\begin{aligned}
\mathcal{L}_{scalar} = & \left(D_{H\mu}H\right)^\dagger \left(D_H{}^\mu H\right) + \left(D_{\eta_\mu}\eta\right)^\dagger \left(D_\eta{}^\mu \eta\right) + \sum_{i=1}^{2}\left(D_{\phi_i\,\mu}\phi_i\right)^\dagger \left(D_{\phi_i}{}^\mu\,\phi_i\right) - \Big\{ -\mu_H^2|H|^2 \\
& + \lambda_H|H|^4 + \left(\mu_\eta^2|\eta|^2 + \lambda_\eta|\eta|^4\right) + \sum_{i=1,2}\left(-\mu_{\phi_i}^2|\phi_i|^2 + \lambda_{\phi_i}|\phi_i|^4\right) + \lambda_{H\eta}(\eta^\dagger\eta)(H^\dagger H) \\
& + \lambda'_{H\eta}(\eta^\dagger H)(H^\dagger\eta) + \sum_{i=1,2}\lambda_{H\phi_i}(\phi_i^\dagger\phi_i)(H^\dagger H) + \left(\lambda_{H\eta\phi}H^\dagger\eta\phi_1^*\phi_2 + \text{h.c.}\right) \\
& + \left(\mu_{H\eta}H^\dagger\eta\phi_1 + \text{h.c.}\right) + \sum_{i=1,2}\lambda_{\eta\phi_i}(\eta^\dagger\eta)(\phi_i^\dagger\phi_i) + \lambda_\phi(\phi_1^\dagger\phi_1)(\phi_2^\dagger\phi_2) \\
& + \left(\mu_\phi\phi_1\phi_1\phi_2^\dagger + \text{h.c.}\right)\Big\}
\end{aligned} \tag{2.88}$$

Where $D_H{}^\mu$, $D_\eta{}^\mu$ and $D_\phi{}^\mu$ denote the covariant derivatives for the scalar doublets H, η and scalar singlets ϕ_i respectively and can be written as

$$\begin{aligned}
D_{H\mu}\,H &= \left(\partial_\mu + i\,\frac{g}{2}\,\sigma_a\,W_\mu^a + i\,\frac{g'}{2}\,B_\mu\right)H\,, \\
D_{\eta_\mu}\,\eta &= \left(\partial_\mu + i\,\frac{g}{2}\,\sigma_a\,W_\mu^a + i\,\frac{g'}{2}\,B_\mu + i\,g_{BL}\,n_\eta Z_{BL\mu}\right)\eta\,, \\
D_{\phi_\mu}\,\phi_i &= \left(\partial_\mu + i\,g_{BL}\,n_{\phi_i}Z_{BL\mu}\right)\phi_i\,.
\end{aligned} \tag{2.89}$$

where $g_{\rm BL}$ is the new gauge coupling and n_η and n_{ϕ_i} are the charges under $U(1)_{B-L}$ for η and ϕ_i respectively. After both $B-L$ and electroweak gauge symmetries get spontaneously broken by the vacuum expectation value (VEV) of H and ϕ_is, the doublet and singlet scalars can be written as

$$H = \begin{pmatrix} H^+ \\ \dfrac{h' + v + iz}{\sqrt{2}} \end{pmatrix}\,, \quad \eta = \begin{pmatrix} \eta^+ \\ \dfrac{\eta'_R + i\eta'_I}{\sqrt{2}} \end{pmatrix}\,, \quad \phi_i = \frac{s'_i + u_i + A'_i}{\sqrt{2}} \;\; (i = 1,\,2)\,. \tag{2.90}$$

From equation (2.90), it is clear that the neutral component of the scalar doublet H and the scalar singlets ϕ_i acquire non-zero VEV whereas the neutral component of η does not.

This can be assured by suitably choosing the sign of bare mass squared term of η field to be positive definite ($\mu_\eta^2 > 0$). Even after the spontaneous symmetry breaking of $U(1)_{B-L}$, the effective bare mass squared term for η can be assumed to be positive definite by appropriate choice of quartic couplings in the scalar potential. However, one crucial point to note here is that the neutral component of η will get a very tiny induced VEV after electroweak symmetry breaking because of the presence of trilinear term $\mathrm{H}^\dagger\eta\phi_1$ as well as the quartic term $\lambda_{H\eta\phi}H^\dagger\eta\phi_1^*\phi_2$ in the Lagrangian (2.88). This can be realised by minimising the scalar potential with respect to η. This leads to

$$\langle\eta_R'\rangle = v_\nu \approx \frac{\mu_{H\eta}vu_1/\sqrt{2} + \lambda_{H\eta\phi}vu_1u_2/2}{2\mu_\eta^2} \tag{2.91}$$

To simplify the calculation we have assumed all two VEVs of singlet scalars are equal, i.e. $u_1 = u_2 = u$ and also assumed the induced VEV to be negligible. The mass of the new gauge boson after spontaneous symmetry breaking is

$$M_{Z_{BL}} = \sqrt{5}g_{BL}u \tag{2.92}$$

where we have ignored the contribution due to v_ν as it is negligible compared to that from u.

After putting equation (2.90) in equation (2.88) we have found out the 4×4 mixing matrix for the real scalar fields in the basis $\frac{1}{\sqrt{2}}\left(h'\ s_1'\ s_2'\ \eta_R'\right)^T$ which has the following form,

$$\begin{pmatrix} 2v^2\lambda_H & u\,v\lambda_{H\phi_1} & u\,v\lambda_{H\phi_2} & 0 \\ u\,v\lambda_{H\phi_1} & 2u^2\lambda_{\phi_1} & u\left(u\lambda_\phi + \mu_\phi\sqrt{2}\right) & 0 \\ u\,v\lambda_{H\phi_2} & u\left(u\lambda_\phi + \mu_\phi\sqrt{2}\right) & \frac{1}{2}u\left(4u\lambda_{\phi_2} - \sqrt{2}\mu_\phi\right) & \frac{u\,v\lambda_{H\eta\phi}}{2} \\ 0 & 0 & \frac{u\,v\lambda_{H\eta\phi}}{2} & \frac{1}{2}\left(\lambda_{\eta\phi_1} + \lambda_{\eta\phi_2}\right)u^2 + v^2(\lambda_{H\eta} + \lambda'_{H\eta}) + 2\mu_\eta^2 \end{pmatrix} \tag{2.93}$$

The physical scalars $\frac{1}{\sqrt{2}}\left(h\ s_1\ s_2\ \eta_R\right)$ can be obtained by diagonalising this real symmetric mass matrix and that can be done by the orthogonal matrix $\mathcal{O}_S$ and the physical states can be expressed as

$$\begin{pmatrix} h \\ s_1 \\ s_2 \\ \eta_R \end{pmatrix} = {\mathcal{O}_S}^T \begin{pmatrix} h' \\ s_1' \\ s_2' \\ \eta_R' \end{pmatrix}, \tag{2.94}$$

In a similar manner, the 3×3 pseudo scalar mass matrix can be written as

$$\begin{pmatrix} -2\sqrt{2}u\,\mu_\phi & \sqrt{2}u\,\mu_\phi & u\,v\lambda_{H\eta\phi} \\ \sqrt{2}u\,\mu_\phi & -\frac{u\mu_\phi}{\sqrt{2}} & -\frac{1}{2}u\,v\,\lambda_{H\eta\phi} \\ u\,v\,\lambda_{H\eta\phi} & -\frac{1}{2}u\,v\lambda_{H\eta\phi} & \frac{1}{2}\left((\lambda_{\eta\phi_1} + \lambda_{\eta\phi_2})u^2 + v^2(\lambda_{H\eta} + \lambda'_{H\eta}) + 2\mu_\eta^2\right) \end{pmatrix} \tag{2.95}$$

The physical pseudo-scalars and the Goldstone boson $\frac{1}{\sqrt{2}}\left(A_1\ A_2\ \eta_I\right)$ can be obtained by diagonalising the above mass matrix and that can be done by the orthogonal matrix $\mathcal{O}_\mathcal{P}$ and the states can be expressed as

$$\begin{pmatrix} A_1 \\ A_2 \\ \eta_I \end{pmatrix} = {\mathcal{O}_\mathcal{P}}^T \begin{pmatrix} A_1' \\ A_2' \\ \eta_I' \end{pmatrix}, \tag{2.96}$$

After the analysing of the scalar potential and diagonalising the mass matrices there will be four independent quartic couplings left (λ_η , $\lambda_{\mathrm{H}\eta}$, $\lambda_{\eta\phi_1}$, $\lambda_{\eta\phi_2}$). All the other couplings in the potential can be expressed in terms of the VEVs, scalar masses and the mixing angles. In principle there should be nine different mixing angles ($\sin\theta_{ij}$) present in the scalar sector out of which six will come from the real sector and three will come from the pseudo scalar sector. Later we have shown that the result in the DM sector is almost independent of these mixing angles ($\sin\theta_{ij}$) and through our discussion to simplify the numerical analysis we have assumed all of them to be equal to 0.1. The parametrisation of the orthogonal matrices $\mathcal{O}_{\mathcal{S}}, \mathcal{O}_{\mathcal{P}}$ are shown in Appendix A.5 and A.6.

Lets discuss the fermionic sector of our model. We have three generations of right handed neutrinos and four chiral fermions and the corresponding interactions can be written as

$$\mathcal{L}_{fermion} = \mathcal{L}_{\nu_R} + \mathcal{L}_{\mathrm{DM}} \tag{2.97}$$

where $\mathcal{L}_{\nu_R}$ is the interactions related to the right handed neutrinos can be expressed as

$$\mathcal{L}_{\nu_R} = i\,\overline{\nu_{Rj}}\not{D}(Q^R_\nu)\nu_{Rj} + \left(Y_{ij}(\overline{\ell_L})_i i\tau_2\eta^*\nu_{Rj} + \mathrm{h.c.}\right) \tag{2.98}$$

The first term in the equation (2.98) represents the kinetic part of ν_{R} and the second term is the Yukawa interaction between SM lepton doublet ℓ_{L} , ν_{R} , and η which is responsible for generating neutrino mass. As discussed above, the neutral component of η will get a small induced VEV v_ν through the trilinear interaction present in the potential. This will generate a tiny Dirac neutrino mass as

$$(m_\nu)_{ij} = \frac{Y_{ij}v_\nu}{\sqrt{2}} \tag{2.99}$$

As can be seen from equation (2.91), a tiny induced VEV $v_\nu \approx \mathcal{O}(\mathrm{eV})$ can be generated by appropriate tuning of the trilinear coupling $\mu_{H\eta}$, quartic coupling $\lambda_{H\eta\phi}$ as well as bare mass squared term μ_η^2. Since $u \sim 10$ TeV, $v \sim 100$ GeV, we can have $v_\nu \sim 0.1$ eV by choosing $\mu_{H\eta}/\mu_\eta^2 \sim 10^{-16}$ GeV^{-1} and $\lambda_{H\eta\phi}/\mu_\eta^2 \sim 10^{-20}$ GeV^{-2} which can be ensured by choosing very large μ_η^2. This also ensures that the components of η decouple from the low energy particle spectra as well as their relevant phenomenology. The hierarchy between $\mu_{H\eta}$ and μ_η can be reduced to bring the ratio to $\mu_{H\eta}/\mu_\eta^2 \sim 10^{-11}$ GeV^{-1} if we tune the Dirac Yukawa couplings to be as small as electron Yukawa coupling. Without any fine-tuning of parameters, we consider $\mu_{H\eta} \sim u, \lambda_{H\eta\phi} \sim \mathcal{O}(1)$ so that μ_η is required to be very large ($\geq 10^{10}$ GeV) thereby decoupling the neutrinophillic scalar doublet η from low energy spectrum. Fine tuning of these parameters will enable the scalar doublet η to have lighter mass having consequences at colliders as well as for thermalisation of right handed part of light Dirac neutrinos. However, we do not pursue such aspects in our studies. Similar way of generating sub-eV Dirac neutrino mass from induced VEV of neutrinophilic Higgs was proposed earlier by the authors of [221, 222, 245].

The term $\mathcal{L}_{\mathrm{DM}}$ is the interactions correspond to the chiral fermions can be written as

$$\begin{aligned}\mathcal{L}_{\mathrm{DM}} &= i[\overline{\chi_L}\not{D}(Q^L_\chi)\chi_L + \overline{\chi_R}\not{D}(Q^R_\chi)\chi_R + \overline{\psi_L}\not{D}(Q^L_\psi)\psi_L + \overline{\psi_R}\not{D}(Q^R_\psi)\psi_R] - \\ &\left(f_1\,\overline{\chi_L}\chi_R\,\phi_1^* + f_2\,\overline{\psi_L}\psi_R\,\phi_2^* + \mathrm{h.c.}\right).\end{aligned} \tag{2.100}$$

We now rewrite the above Lagrangian in the basis $\xi_1 = \chi_L + \chi_R$ and $\xi_2 = \psi_L + \psi_R$. In the basis of ξ_1 and ξ_2, the above Lagrangian (2.100) can be written as

$$\begin{aligned}\mathcal{L}_{\rm DM} &= i\,\overline{\xi_1}\,\partial\!\!\!/\,\xi_1 + i\,\overline{\xi_2}\,\partial\!\!\!/\,\xi_2 - g_{BL}\left(\frac{13}{9}\right)\overline{\xi_1}\,Z\!\!\!/_{BL}\,P_L\,\xi_1 - g_{BL}\left(\frac{1}{9}\right)\overline{\xi_2}\,Z\!\!\!/_{BL}\,P_L\,\xi_2 \\ &\quad - g_{BL}\left(\frac{22}{9}\right)\overline{\xi_1}\,Z\!\!\!/_{BL}\,P_R\,\xi_1 - g_{BL}\left(\frac{19}{9}\right)\overline{\xi_2}\,Z\!\!\!/_{BL}\,P_R\,\xi_2 - f_1\,\overline{\xi_1}\,P_R\,\xi_1\,\phi_1^\dagger \\ &\quad - f_2\,\overline{\xi_2}\,P_R\,\xi_2\,\phi_2 - f_1\,\overline{\xi_1}\,P_L\,\xi_1\,\phi_1 - f_2\,\overline{\xi_2}\,P_L\,\xi_2\,\phi_2^\dagger\,, \end{aligned} \tag{2.101}$$

where $P_{L,R} = \dfrac{1 \pm \gamma_5}{2}$, left and right chiral projection operators. From the above Lagrangian (2.101) it is clear that DM particles will get mass after the breaking of $B - L$ symmetry spontaneously by the VEV's of the singlet scalars (ϕs). ξ_1 and ξ_2 can annihilate to the SM particles through the interaction with Z_{BL} and the singlet scalars. Due to the suitable choice of the scalar sector of the model, in the basis $\xi_1 = \chi_L + \chi_R$ and $\xi_2 = \psi_L + \psi_R$, all the interactions in equation (2.101) are exactly diagonal in (ξ_1, ξ_2) basis. This is similar to imposing two different $\mathbb{Z}_2$ symmetries to two different DM candidates as: $\mathbb{Z}_2 : \xi_1 \to -\xi_1, Z_2' : \xi_2 \to -\xi_2$ while all other particles being even under these symmetries. Clearly, the complete Lagrangian of our model is invariant under these two remnant discrete symmetries. Therefore, ξ_1 and ξ_2 are completely stable and will play the roles of two DM candidates in this model.

2.5.2 Constraints on the model parameters

Before discussing our results, we first note down the existing constraints on the model parameters from both theory and experiments. We discuss them one by one in this section as follows.

2.5.3 Boundedness of Scalar Potential

The scalar potential of the model has to be bounded from below and that can be ensured by the following inequalities.

$$\begin{aligned} \lambda_H, \lambda_\eta, \lambda_{\phi_1}, \lambda_{\phi_2}, \lambda'_{H\eta}, \lambda_{H\eta\phi} \geq 0\,, \\ \lambda_{H\phi_2} + \sqrt{\lambda_H \lambda_{\phi_2}} \geq 0\,, \lambda_{H\phi_1} + \sqrt{\lambda_H \lambda_{\phi_1}} \geq 0\,, \\ \lambda_{H\eta} + \sqrt{\lambda_H \lambda_\eta} \geq 0\ , \lambda_\phi + \sqrt{\lambda_{\phi_1} \lambda_{\phi_2}} \geq 0\,, \\ \lambda_{\eta\phi_1} + \sqrt{\lambda_\eta \lambda_{\phi_1}} \geq 0\,, \lambda_{\eta\phi_2} + \sqrt{\lambda_\eta \lambda_{\phi_2}} \geq 0\,. \end{aligned} \tag{2.102}$$

2.5.4 Perturbativity of Couplings

We have to also take care of the perturbative breakdown of the model and to to guarantee that all quartic, Yukawa and gauge couplings should obey the following conditions.

$$\begin{aligned} |\lambda_H| < 4\pi,\ |\lambda_{\phi_{1,2}}| < 4\pi,\ |\lambda_\eta| < 4\pi, \\ |\lambda_{H\phi_{1,2}}| < 4\pi, |\lambda_{\eta\phi_{1,2}}| < 4\pi,\ |\lambda_\phi| < 4\pi, \\ |\lambda_{H\eta}| < 4\pi,\ |\lambda'_{H\eta}| < 4\pi,\ |\lambda_{H\eta\phi}| < 4\pi, \\ |f_i| < \sqrt{4\pi},\ |Y_{i,j}| < \sqrt{4\pi}, \\ |g, g'| < \sqrt{4\pi},\ |g_{BL}| < \sqrt{4\pi}, \end{aligned} \tag{2.103}$$

2.5.5 Collider Constraints

Apart from the theoretical constraints mentioned above, there exists stringent experimental constraints on the $B-L$ gauge sector. The limits from LEP II data constrains such additional gauge sector by imposing a lower bound on the ratio of new gauge boson mass to the new gauge coupling $M_{Z'}/g' \geq 7$ TeV [260, 261]. The bounds from ongoing LHC experiment have already surpassed the LEP II bounds. In particular, search for high mass dilepton resonances have put strict bounds on such additional gauge sector coupling to all generations of leptons and quarks with coupling similar to electroweak ones. The latest bounds from the ATLAS experiment [295,309] and the CMS experiment [310] at the LHC rule out such gauge boson masses below 4-5 TeV from analysis of 13 TeV data. Such bounds get weaker, if the corresponding gauge couplings are weaker [295] than the electroweak gauge couplings. Also, if the Z' gauge boson couples only to the third generation of leptons, all such collider bounds become much weaker, as explored in the context of DM and collider searches in a recent work [311]. Apart from the additional gauge boson, the additional singlet scalar spectrum is also constrained by experimental data. Though the singlet scalars do not directly couple to the SM particles, they can do so by virtue of their mixing with the SM Higgs. Such singlet scalar - Higgs mixing faces both theoretical and experimental constraints [312, 313]. In case of scalar singlet extension of SM, the strongest bound on scalar-SM Higgs mixing angle ($\theta_{1j}, j = 2, 3, 4$) comes form W boson mass correction [314] at NLO for 250 GeV $\lesssim M_{s_i} \lesssim$ 850 GeV as ($0.2 \lesssim \sin\theta_{1j} \lesssim 0.3$) where M_{s_i} is the mass of other physical Higgs. Whereas, for $M_{s_i} > 850$ GeV, the bounds from the requirement of perturbativity and unitarity of the theory turn dominant which gives $\sin\theta_{1j} \lesssim 0.2$. For lower values *i.e.* $M_{s_i} < 250$ GeV, the LHC and LEP direct search [315,316] and measured Higgs signal strength [316] restrict the mixing angle $\sin\theta_{1j}$ dominantly ($\lesssim 0.25$). The bounds from the measured value of EW precision parameter are mild for $M_{s_i} < 1$ TeV. While these constraints restrict the singlet scalar mixing with SM Higgs denoted by ($\theta_{1j}, j = 2, 3, 4$), the other three angles ($\theta_{23}, \theta_{24}, \theta_{34}$) remain unconstrained. We choose our benchmark values of singlet scalar masses and their mixing with SM Higgs boson in such a way that these constraints are automatically satisfied.

2.5.6 Cosmological Bound on Additional Light Degrees of Freedom

Another interesting way to constrain the model parameters is by calculating the additional relativistic degrees of freedom due to the presence of right handed neutrinos at sub-eV scale having sizeable gauge interactions. Through these gauge interactions, they will achieve the thermal equilibrium in the early Universe and will contribute to the total relativistic degrees of freedom of the thermal plasma. However, the total effective degrees of freedom for neutrinos are already very much constrained from cosmological observations, more specifically from BBN and CMB. We have used this fact to constrain the parameter space of the model. Recent data from the CMB measurement by the Planck [50] suggests that the effective degrees of freedom for neutrinos as

$$\mathrm{N_{eff}} = 2.99^{+0.34}_{-0.33} \tag{2.104}$$

In this scenario the effective contribution from the right-handed neutrinos can be written as [335, 336]

$$\Delta \mathrm{N_{eff}} = \mathrm{N_{eff}} - \mathrm{N_{eff}^{SM}} = \mathrm{N_{\nu_R}} \left(\frac{\mathrm{T_{\nu_R}}}{\mathrm{T_{\nu_L}}}\right)^4 = \mathrm{N_{\nu_R}} \left(\frac{\mathrm{g}\left(\mathrm{T_{\nu_L}^{dec}}\right)}{\mathrm{g}\left(\mathrm{T_{\nu_R}^{dec}}\right)}\right)^{4/3} \tag{2.105}$$

where $\mathrm{N_{\nu_R}}$ represents the number of relativistic right-handed neutrinos, g(T) corresponds to the relativistic degrees of freedom at temperature T, and $\mathrm{T_{\nu_R}^{dec}}$, $\mathrm{T_{\nu_L}^{dec}}$ are the decoupling temperatures for ν_R and ν_L respectively. From equation (2.104) one can write

$$\Delta \mathrm{N_{eff}} = \mathrm{N_{eff}} - \mathrm{N_{eff}^{SM}} \leq 0.285 \tag{2.106}$$

where we have used $\mathrm{N_{eff}^{SM}} = 3.045$ [337] and considered the maximum allowed $\mathrm{N_{eff}}$ from CMB bound mentioned above in equation (2.104). Now, to predict $\Delta \mathrm{N_{eff}}$ one needs to know the decoupling temperature of ν_R which remains in thermal equilibrium until the interaction rate becomes smaller than the Hubble expansion of the Universe.

$$\Gamma_{\nu_\mathrm{R}}(\mathrm{T_{\nu_R}^{dec}}) = \mathrm{H}(\mathrm{T_{\nu_R}^{dec}}) \tag{2.107}$$

Here the Hubble rate can be written as [336]

$$H(T) = \sqrt{\frac{8\pi G_N \rho(T)}{3}} = \sqrt{\frac{4\pi^3 G_N}{45}\left(g(T) + 3\frac{7}{8} g_{\nu_R}\right)}\, T^2, \tag{2.108}$$

where g_{ν_R} is the internal degrees of freedom for right-handed neutrinos. In this scenario, the interaction rate can be written as [336]

$$\begin{aligned} \Gamma_{\nu_R}(T) &= n_{\nu_R}(T) \langle \sigma(\bar{\nu}_R \nu_R \to \bar{f} f)\, v_M \rangle \\ &= \frac{g_{\nu_R}^2}{n_{\nu_R}(T)} \int \frac{d^3\vec{p}}{(2\pi)^3} f_{\nu_R}(p) \int \frac{d^3\vec{k}}{(2\pi)^3} f_{\nu_R}(k) \sigma_f(s) v_M, \end{aligned} \tag{2.109}$$

where f($\nu_{\rm R}$) is the Fermi-Dirac distribution of right-handed neutrinos. As we have discussed earlier, $\nu_{\rm R}$ will achieve thermal equilibrium only through $Z_{\rm BL}$ interactions and the cross-section can be written as

$$\sigma_{\bar{\nu}_R\nu_R\to\bar{f}f} = \frac{g_{BL}^4}{12\pi\sqrt{s}}\frac{1}{(s-M_{Z_{BL}}^2)^2+\Gamma_{Z_{BL}}^2 M_{Z_{BL}}^2}\sum_f N_f^C n_f^2\sqrt{s-4M_f^2}\,(2M_f^2+s), \qquad (2.110)$$

where n_f is is the charge of the SM fermions under $U(1)_{B-L}$, N_f^C is the colour multiplicity of the fermions. Inserting the required input in equation (2.107) one can find out the decoupling temperature for right-handed neutrinos and using equations (2.105), (2.106) we can derive a bound on the unknown parameters of the model and in this case these are g_{BL} and $M_{Z_{BL}}$. In fact, this is not a feature of this model but can be applicable to any gauge symmetric model with additional light degrees of freedom having sizeable gauge interactions. For example, in left-right symmetric models with light Dirac neutrinos or light right handed neutrinos one can derive similar bounds on additional gauge sector, as discussed by several earlier works including [228, 231] and references therein. It should be noted that the right handed neutrinos can also thermalise via Yukawa couplings $Y_{ij}(\overline{\ell_L})_i i\tau_2\eta^*\nu_{Rj}$ depending upon its relative strength compared to gauge coupling. However, since we consider η and its components to be very heavy and hence decoupled from low energy spectrum, the bounds on such Yukawa coupling from CMB-BBN constraints will be much weaker and hence we do not discuss it here.

2.5.7 Dark Matter: Relic Density and Direct Detection

Relic abundance of two-component DM in our model $\chi_{1,2}$ can be found by numerically solving the corresponding Boltzmann equations. Let $n_2 = n_{\xi_2} + n_{\bar{\xi}_2}$ and $n_1 = n_{\xi_1} + n_{\bar{\xi}_1}$ are the total number densities of two DM candidates respectively. Assuming there is no asymmetry in number densities of ξ_i and $\bar{\xi}_i$, the two coupled Boltzmann equations in terms of n_2 and n_1 are given below [277],

$$\frac{dn_2}{dt}+3n_2H = -\frac{1}{2}\langle\sigma v_{\xi_2\bar{\xi}_2\to X\bar{X}}\rangle\left(n_2^2-(n_2^{\rm eq})^2\right)-\frac{1}{2}\langle\sigma v_{\xi_2\bar{\xi}_2\to\xi_1\bar{\xi}_1}\rangle\left(n_2^2-\frac{(n_2^{\rm eq})^2}{(n_1^{\rm eq})^2}n_1^2\right) \qquad (2.111)$$

$$\frac{dn_1}{dt}+3n_1H = -\frac{1}{2}\langle\sigma v_{\xi_1\bar{\xi}_1\to X\bar{X}}\rangle\left(n_1^2-(n_1^{\rm eq})^2\right)+\frac{1}{2}\langle\sigma v_{\xi_2\bar{\xi}_2\to\xi_1\bar{\xi}_1}\rangle\left(n_2^2-\frac{(n_2^{\rm eq})^2}{(n_1^{\rm eq})^2}n_1^2\right) \qquad (2.112)$$

where, $n_i^{\rm eq}$ is the equilibrium number density of DM species i and H denotes the Hubble parameter, defined earlier. For further details of these Boltzmann equations for two-component Dirac fermion DM and their annihilation channels ($\xi_i\bar{\xi}_i\to X\bar{X}$, X being all particles where DM can annihilate into) contributing to $\langle\sigma v\rangle$, please refer to [277] where a similar scenario was discussed recently. We have solved these two coupled Boltzmann equations using `micrOMEGAs` [320] where the model information has been supplied to `micrOMEGAs` using `FeynRules` [321]. All the relevant annihilation cross sections of DM number changing processes required to solve the coupled equations are calculated using `CalcHEP` [322]. The most important DM annihilation channels are the ones mediated by Z_{BL} and the singlet scalars. Since the two DM candidates are stabilised by two separate and accidental $\mathbb{Z}_2$ symmetries,

there is no coannihilation between them. On the other hand a pair of one DM can annihilate into a pair of the other, if kinematically allowed, as shown by the last terms on the right hand side of above two equations.

Just like the new gauge boson and singlet scalars mediate DM annihilation into SM particles, similarly, they can also mediate spin independent DM-nucleon scatterings. The Feynman diagrams corresponding to such direct detection (DD) processes are shown in the figure 2.29. Different ongoing experiments like Xenon1T [6,55], LUX [53], PandaX-II [56,57]

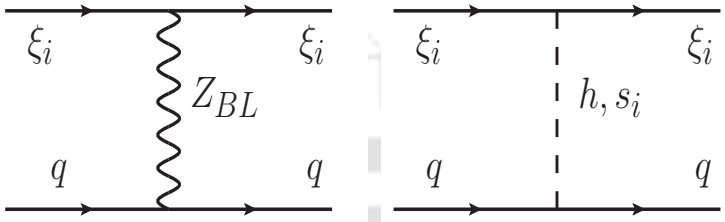

Figure 2.29: Feynman diagrams for spin-independent elastic scattering processes of DM with nucleons (or quarks) in the model.

are trying to detect the DM in the lab-based experiments and give a strong upper bound on the spin-independent (SI) DD cross-section as a function of DM mass. We have extracted the SI elastic scattering cross-section for both the DM candidates from micrOmegas. DD analysis for two-component DM is slightly different from the single component scenario. To compare the result of our model with Xenon1T bound, we have multiplied the elastic scattering cross-section by the relative number density of each DM candidate and used the following conditions

$$\begin{aligned}\sigma^{\rm eff}_{\xi_1} &= \frac{n_{\xi_1}}{n_{\xi_1}+n_{\xi_2}}\sigma^{\rm SI}_{\xi_1} \leq \sigma_{\rm Xenon1T}\\ \sigma^{\rm eff}_{\xi_2} &= \frac{n_{\xi_2}}{n_{\xi_1}+n_{\xi_2}}\sigma^{\rm SI}_{\xi_2} \leq \sigma_{\rm Xenon1T}\end{aligned} \tag{2.113}$$

2.5.8 Results and Discussion

Since we have two stable DM candidates i.e. ξ_1 and ξ_2 in this model, the total relic abundance can be expressed as the sum of the individual candidates, $\Omega_{\rm DM}h^2 = \Omega_{\xi_1}h^2 + \Omega_{\xi_2}h^2$. Equation (2.101) clearly shows that ξ_1 and ξ_2 have interactions with Z_{BL} and the new singlet scalars ϕ_1 and ϕ_2. Through these interactions they will achieve the thermal equilibrium in the early Universe (unless the gauge and Yukawa couplings are extremely small) and eventually freeze-out as the Universe expands. In figure 2.30 and 2.31, we have shown the dependence of relic abundance on DM mass by keeping the other parameters fixed at some benchmark values. For these two plots we assumed both the DM to have equal masses ($M_{\xi_1} = M_{\xi_2}$), although in principle, they can have different masses. The left panel of figure 2.30 shows the variation of relic abundance as a function of DM mass and the other parameters were chosen as $M_{\eta_R} = M_{\eta_I} = 1.5$ TeV, $M_{A_1} = 2$ TeV, $M_{\eta^\pm} = 750$ GeV, $M_{s_1} = M_{s_2} = 1$ TeV, $M_{Z_{BL}} = 6$ TeV, $g_{BL} = 0.21$ while all the scalar mixing angles ($\sin\theta_{ij}$) and the independent quartic couplings

are assumed to be equal to 0.1. Figure 2.30a clearly shows the dip in the relic densities due to different scalars and Z_{BL} resonances, at DM mass of 62.5 GeV, 250 GeV, 1 TeV, 1.5 TeV, and 3 TeV respectively. The dotted blue line and the dashed red line represent the $\Omega_{\xi_1}h^2$ and $\Omega_{\xi_2}h^2$ respectively whereas the green solid line shows the total DM relic density. One important point to note here is that ξ_2 has dominant contribution throughout the whole mass range and that is because of the $B-L$ charges assigned for the individual chiral fermions which constitute the two Dirac fermion DM candidates. In figure 2.30b we have shown the dependence of total DM abundance on the gauge coupling g_{BL} which shows that the total relic abundance is decreasing as we are increasing the gauge coupling as expected.

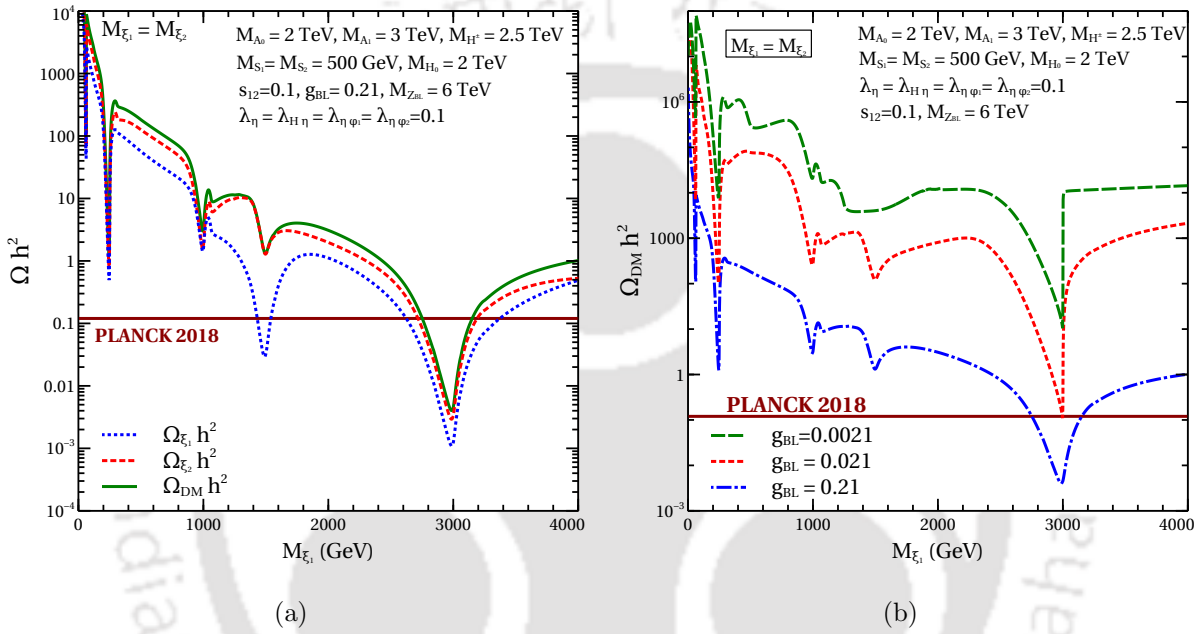

Figure 2.30: Left panel: Relic abundance of two DM candidates with degenerate masses keeping all other model parameters fixed to benchmark values. Right panel: Total relic abundance of two DM candidates ($\Omega_{DM}h^2 = \Omega_{\xi_1}h^2 + \Omega_{\xi_2}h^2$) with degenerate masses $M_{\xi_1} = M_{\xi_2}$ for different benchmark values of $U(1)_{B-L}$ gauge coupling.

Figure 2.31 shows the dependence of DM abundance on the parameters from the scalar sector. The left panel of figure 2.31 is for different values of scalar mixing angle, (0.1, 0.01, 0.001) whereas the right one is for different quartic couplings (0.1,0.01,0.001). Both the figures clearly show that the total DM abundance does not have strong dependence on these two parameters.

After analysing the dependence on different model parameters from the above benchmark plots we have now performed a random scan over the model parameters shown in the table 2.14. As mentioned earlier, we have kept the quartic couplings and the mixing angles fixed at 0.1 throughout our analysis unless otherwise specified. In figure 2.32 we have shown the final parameter space of this model in the $g_{BL} - M_{Z_{BL}}$ plane where we have constrained the allowed parameter space from different relevant upper bounds coming from LHC, LEP, BBN-CMB and also XENON1T. The blue points showing in the above figure are allowed from all these experimental bounds. Apart from the experimental bounds, we also apply the bounded from

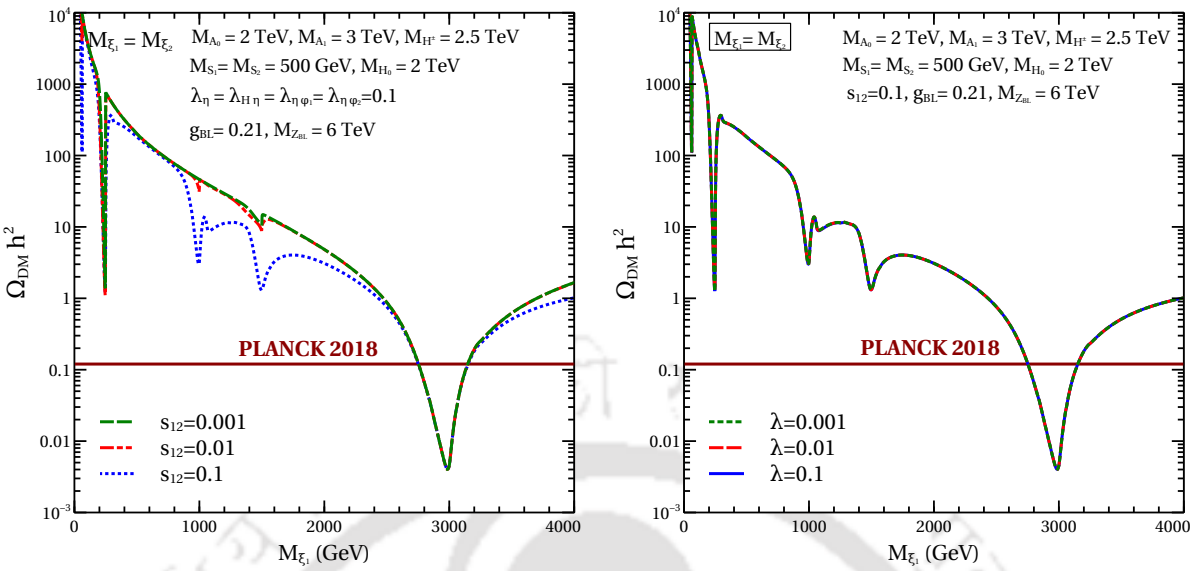

Figure 2.31: Total relic abundance of two DM candidates ($\Omega_{\rm DM}h^2 = \Omega_{\xi_1}h^2 + \Omega_{\xi_2}h^2$) with degenerate masses $M_{\xi_1} = M_{\xi_2}$ for different benchmark values of: mixing angle (left panel) and (b) quartic couplings (right panel).

below criteria of the scalar potential as well as perturbativity of all dimensionless couplings. One interesting point to note here is that the BBN-CMB bound on $\Delta N_{\rm eff}$ is putting much stronger bound in the high mass region of $M_{Z_{\rm BL}}$ compared to the other bounds like collider or direct detection.

In order to show the prospects of probing such a scenario at ongoing and upcoming direct detection experiments, we have shown the effective spin-independent DD cross-section (see equation (2.113)) as function of individual DM mass in figure 2.33. Points showed in green satisfy perturbativity of couplings, bounded from below criteria of the scalar potential, and the total DM relic density constraint whereas the black points are allowed from all other relevant constraints such as XENON1T, LHC, LEP and CMB bound on $\Delta N_{\rm eff}$ as well. From this figure, it is clear that the parameter space of this model has promising scope of being detected. We have also shown the projected sensitivities from future experiments such as XENONnT [324] (blue region) and DARWIN [325] (yellow region) in both plots which clearly indicate that these two experiments can probe a large region of parameter space. For a comparison, we also show the neutrino floor by the red solid line, corresponding to coherent neutrino-nucleus scattering cross section [338].

In figure 2.34 we have shown the allowed parameter space in $M_{\xi_1} - M_{\xi_2}$ plane where the variation of $g_{\rm BL}$ (right panel) and $M_{Z_{\rm BL}}$ (left panel) have also been shown through colour coding. One can see that the region becomes broader as we go to the high mass region of both DM candidates whereas in the low DM mass region it becomes narrower. This can be explained by noting the fact that the DM Yukawa couplings with singlet scalars namely, f_i $(i = 1, 2)$ can be written as $\sqrt{2}\ M_{\rm DM_i}/u$ which will increase with $M_{\rm DM_i}$ for fixed u. So, in the low DM mass region, only gauge coupling ($g_{\rm BL}$) is playing the major role

Parameters	Range
M_{ξ_1}	(10 GeV, 5 TeV)
M_{ξ_2}	(10 GeV, 5 TeV)
$M_{Z_{BL}}$	(100 GeV, 10 TeV)
g_{BL}	(0.0001, 1)
M_{s_1}	(100 GeV, 2 TeV)
M_{s_2}	(100 GeV, 2 TeV)
M_{A_1}	(100 GeV, 2 TeV)
$M_{\eta_R} = M_{\eta_I}$	(1 TeV, 2 TeV)
$M_{\eta^\pm}$	2.5 TeV

Table 2.14: The parameters of the model and ranges used in the random scan

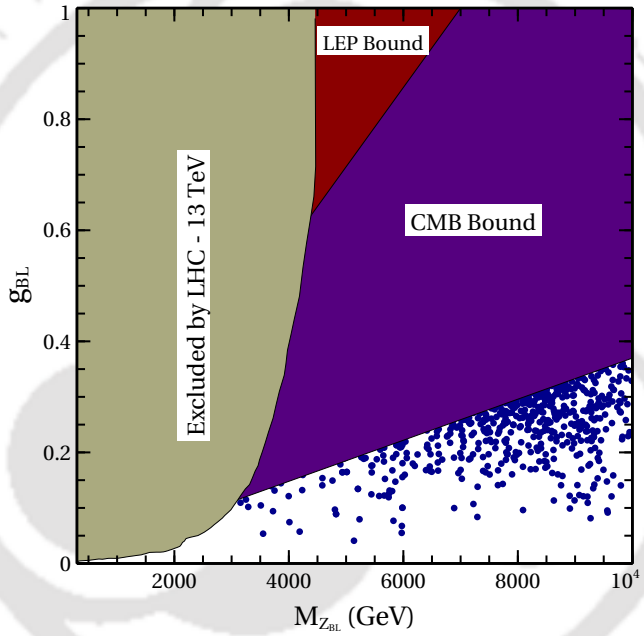

Figure 2.32: Summary plot showing allowed parameter space of the model from all relevant experiments and observations.

in DM annihilation processes thereby deciding its relic. As discussed earlier, $B-L$ gauge boson portal interactions typically lead to correct DM relic around the resonance region $M_{DM_i} \approx M_{Z_{BL}}/2$. However, as the DM mass increases, Yukawa coupling corresponding to each DM candidate also increases and starts to contribute significantly taking the allowed parameter space away from the resonance region $M_{DM_i} \approx M_{Z_{BL}}/2$ mentioned before. As a result the region becomes broader as we go to the high mass region due to reduced dependence on the gauge boson mediated annihilation channels.

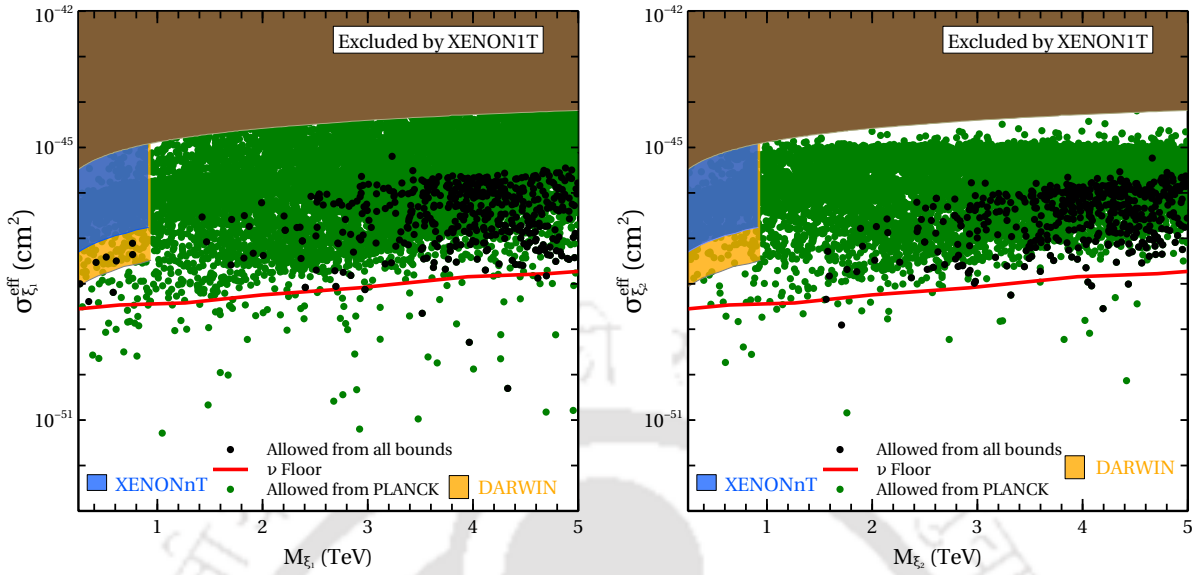

(a) (b)

Figure 2.33: Effective spin-independent direct detection scattering cross-section of individual DM candidates. Green points are satisfying the boundedness of potential, perturbativity of couplings and the total DM relic density constraint whereas the black points are allowed from all relevant constraint such as direct detection, LHC, LEP and CMB bound on $\Delta N_{\rm eff}$.

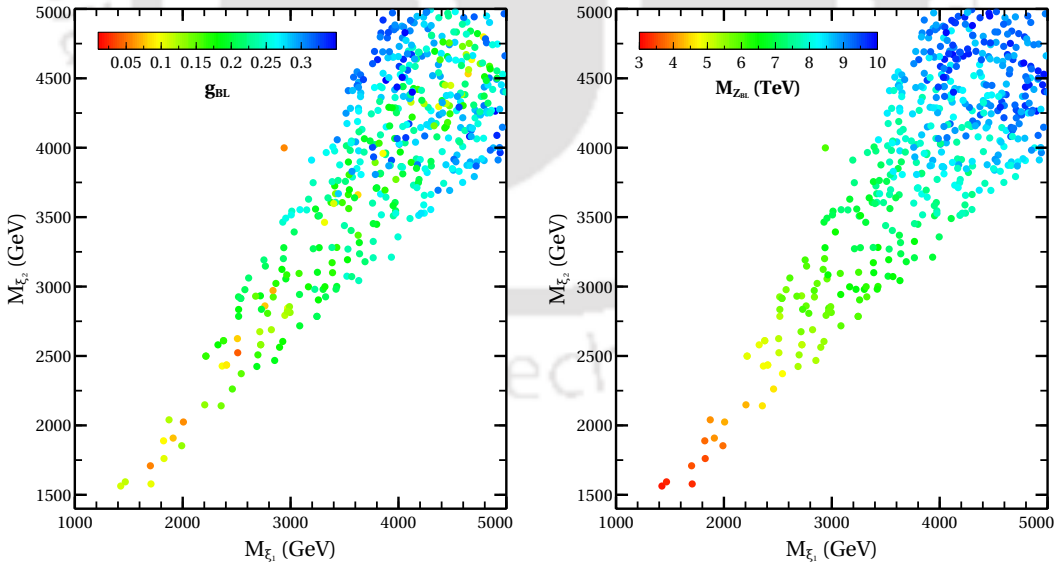

(a) (b)

Figure 2.34: DM parameter in terms of DM masses space satisfying all relevant constraints. The colour coding is used to denote $g_{\rm BL}$, $M_{Z_{\rm BL}}$ in left and right panels respectively.

CHAPTER 3

Light Dirac neutrinos with dark matter in left-right symmetric model.

3.1 Introduction

Left-right symmetric models (LRSM) [204, 246, 339–348] have been one of the most popular BSM frameworks studied in the literature. Here the gauge symmetry of the SM is extended to $\mathrm{SU(3)_c \times SU(2)_L \times SU(2)_R \times U(1)_{B-L}}$ so that the right-handed fermions (which are singlet in SM) can form doublets under the new $SU(2)_R$. This not only makes the inclusion of right-handed neutrino automatic, but also puts the left and right-handed fermions on equal footing. Incorporating an additional discrete symmetry (or left-right parity) ensures that the theory is invariant under $SU(2)_L \leftrightarrow SU(2)_R$. Thus, the model not only explains the origin of parity violation in electroweak interactions through spontaneous breaking of a parity symmetric theory at high energy scale but also incorporates right handed neutrino, crucial to generate light neutrino masses and mixing observed at neutrino oscillation experiments [142, 349]. Apart from the possibility of realising left-right symmetry as an intermediate symmetry in popular grand unified theories (GUT) like SO(10), a TeV scale realisation of LRSM can also have very interesting consequences at collider experiments like the large hadron collider (LHC) [350–356].

Conventionally, the very first proposals and studies of LRSM [339–343] considered a scalar bidoublet for generating fermion masses and also for electroweak symmetry breaking whereas a pair of scalar doublets were introduced for the purpose of left-right symmetry breaking at high energy scale. A very recent detailed study of this model can be found in [357]. On the other hand, the LRSM proposals put forward later [204, 246, 345–348] received much more attention due to the possibility of seesaw origin of light neutrino masses through a combination of type I seesaw [200–203] and type II seesaw [204–208] or type III seesaw [209]. In the doublet left-right model (DLRM), in its minimal version, there is no such seesaw mechanism as all fermions including neutrinos acquire Dirac masses by virtue of their couplings to the bidoublet scalar. While generating sub-eV neutrino mass in this fashion requires relevant Yukawa couplings at the level of $< 10^{-12}$, we adopt this minimal scenario to study some of the interesting phenomenological consequences. Radiative generation of light Dirac neutrinos in different left-right symmetric models have also been discussed over last few decades [210, 226–228, 230, 231, 358, 359] which may provide a UV completion of the

minimal DLRM we discuss here. Since such UV completions do not drastically change the conclusions we reach in the present work, we stick to the DLRM for the sake of simplicity.

The Dirac nature of light neutrinos in DLRM gives rise to additional relativistic degrees of freedom which can be thermalised in the early Universe due to their gauge interactions mediated by right sector gauge bosons. Such additional light degrees of freedom can be probed by precise measurements of the cosmic microwave background (CMB) anisotropies. Recent 2018 data from the CMB measurement by the Planck satellite [50] suggests that the effective degrees of freedom for neutrinos as

$$\mathrm{N_{eff}} = 2.99^{+0.34}_{-0.33} \tag{3.1}$$

at 2σ or 95% CL including baryon acoustic oscillation (BAO) data. At 1σ CL it becomes more stringent to $N_{\rm eff} = 2.99 \pm 0.17$. Both these bounds are consistent with the SM prediction $N_{\rm eff}^{\rm SM} = 3.045$ [337, 360, 361]. Upcoming CMB Stage IV (CMB-S4) experiments are expected to put much more stringent bounds than Planck due to their potential of probing all the way down to $\Delta N_{\rm eff} = N_{\rm eff} - N_{\rm eff}^{\rm SM} = 0.06$ [362]. We use the existing constraints and put strong limits on the scale of left-right symmetry or equivalently the right sector gauge bosons W_R, Z_R. For comparison, we also check the corresponding bounds for left-right asymmetric scenario by considering different $SU(2)_R$ gauge couplings. Interestingly, we find that the bounds on W_R, Z_R mass from Planck 2018 bound on $\Delta N_{\rm eff}$ at 2σ CL are equally competitive as the latest LHC bounds [351, 352, 355] and much stronger that the corresponding bounds from flavour physics [363]. On the other hand the same Planck 2018 bound at 1σ CL can rule out a much larger mass window for W_R, Z_R out of reach of present collider experiments. In fact CMB-S4 will be able to probe a much larger region of W_R, Z_R masses out of existing collider's reach and hence can probe or rule out the minimal model. Since there have been a few recent studies on gauged $B - L$ model with light Dirac neutrinos [278, 335, 336, 364]and corresponding constraints due to Planck 2018 bound on $\Delta N_{\rm eff}$, we also reproduce the corresponding parameter space in gauged $B - L$ model and compare with the one obtained in DLRM. We point out the important difference due to the restricted range of DLRM gauge couplings g_R, g_{BL} unlike that in gauged $B - L$ model. We also show the impact of these constraints on DM parameter space in DLRM by considering a right handed fermion quintuplet to be the dominant component of DM which can thermalise by virtue of its interactions with SM mediated by right sector gauge bosons. We calculate the parameter space allowed from observed DM relic and find the leftover parameter space after applying the $\Delta N_{\rm eff}$ bound. Finally, we comment on the more stringent Planck 2018 1σ bound which can be satisfied if more light fields below the scale of left-right symmetry breaking in addition to SM plus three right handed neutrinos exist. In fact, we show that DLRM with right handed fermion quintuplet DM can give rise to sufficient number of additional degrees of freedom to serve this purpose.

This chapter is organised as follows. In section 3.2, we discuss the doublet left-right symmetric model followed by discussion of additional relativistic degrees of freedom due to light Dirac neutrinos in section 3.3. In section 3.4 we briefly discuss DM in DLRM particularly focusing on fermion quintuplet DM followed by results and discussion in section 3.5.

Particles	$SU(3)_c \times SU(2)_L \times SU(2)_R \times U(1)_{B-L}$
$Q_L = \begin{pmatrix} u_L \\ d_L \end{pmatrix}$	$(3, 2, 1, \frac{1}{3})$
$Q_R = \begin{pmatrix} u_R \\ d_R \end{pmatrix}$	$(3, 1, 2, \frac{1}{3})$
$\ell_L = \begin{pmatrix} \nu_L \\ e_L \end{pmatrix}$	$(1, 2, 1, -1)$
$\ell_R = \begin{pmatrix} \nu_R \\ e_R \end{pmatrix}$	$(1, 1, 2, -1)$

Table 3.1: Fermionic fields of the present Model including the SM fermions.

Particles	$SU(3)_c \times SU(2)_L \times SU(2)_R \times U(1)_{B-L}$
$\Phi = \begin{pmatrix} \phi^0 & \phi'^+ \\ \phi^- & \phi'^0 \end{pmatrix}$	$(1, 2, 2, 0)$
χ_L	$(1, 2, 1, 1)$
χ_R	$(1, 1, 2, 1)$

Table 3.2: Scalar fields and their corresponding charges under all the symmetry groups.

3.2 The DLRM

We briefly discuss the doublet left-right symmetric model in this section. The fermion and scalar content of the model are given in table 3.1 and 3.2 respectively. The relevant Yukawa Lagrangian giving masses to the three generations of leptons is given by,

$$\mathcal{L} = h_{ij}\bar{l}_{L,i}\Phi l_{R,j} + \widetilde{h_{ij}}\bar{l}_{L,i}\widetilde{\Phi} l_{R,j} + \text{h.c}, \tag{3.2}$$

where the indices $i, j = 1, 2, 3$ represent the family indices for the three generations of fermions, $\widetilde{\Phi} = \tau_2\phi^*\tau_2$ and τ_2 is Pauli matrix. The gauge structure of the model prevents any renormalisable Yukawa couplings involving the scalar doublets $\chi_{L,R}$. The scalar potential V_{scalar} is given by [357]

$$\begin{aligned}
V_{\text{scalar}} = & -\mu_1^2 \text{Tr}\left[\Phi^\dagger\Phi\right] - \mu_2^2 \text{Tr}\left[\Phi^\dagger\tilde{\Phi} + \tilde{\Phi}^\dagger\Phi\right] - \mu_3^2(\chi_L^\dagger\chi_L + \chi_R^\dagger\chi_R) + \lambda_1\Big(\text{Tr}\left[\Phi^\dagger\Phi\right]\Big)^2 \\
& + \lambda_2\Big\{\Big(\text{Tr}\left[\Phi^\dagger\tilde{\Phi}\right]\Big)^2 + \Big(\text{Tr}\left[\tilde{\Phi}^\dagger\Phi\right]\Big)^2\Big\} + \lambda_3 \text{Tr}\left[\Phi^\dagger\tilde{\Phi}\right]\text{Tr}\left[\tilde{\Phi}^\dagger\Phi\right] + \lambda_4 \text{Tr}\left[\Phi^\dagger\Phi\right]\text{Tr}\left[\Phi^\dagger\tilde{\Phi} + \tilde{\Phi}^\dagger\Phi\right] \\
& + \mu_1'(\chi_L^\dagger\Phi\chi_R + \chi_R^\dagger\Phi^\dagger\chi_L) + \mu_2'(\chi_L^\dagger\tilde{\Phi}\chi_R + \chi_R^\dagger\tilde{\Phi}^\dagger\chi_L) + \rho_1\Big[(\chi_L^\dagger\chi_L)^2 + (\chi_R^\dagger\chi_R)^2\Big] \\
& + \alpha_1 \text{Tr}\left[\Phi^\dagger\Phi\right]\Big[(\chi_L^\dagger\chi_L) + (\chi_R^\dagger\chi_R)\Big] + \alpha_2 e^{i\delta}\Big[\text{Tr}\left[\tilde{\Phi}\Phi^\dagger\right](\chi_L^\dagger\chi_L) + \text{Tr}\left[\Phi\tilde{\Phi}^\dagger\right](\chi_R^\dagger\chi_R)\Big] \\
& + \alpha_2 e^{-i\delta}\Big[\text{Tr}\left[\tilde{\Phi}^\dagger\Phi\right](\chi_L^\dagger\chi_L) + \text{Tr}\left[\Phi^\dagger\tilde{\Phi}\right](\chi_R^\dagger\chi_R)\Big] + \alpha_3(\chi_L^\dagger\Phi\Phi^\dagger\chi_L + \chi_R^\dagger\Phi^\dagger\Phi\chi_R) \\
& + \alpha_4(\chi_L^\dagger\tilde{\Phi}\tilde{\Phi}^\dagger\chi_L + \chi_R^\dagger\tilde{\Phi}^\dagger\tilde{\Phi}\chi_R).
\end{aligned} \tag{3.3}$$

For details of the minimisation of the scalar potential and resulting symmetry breaking, please refer to [357]. In the symmetry breaking pattern, the neutral component of the Higgs doublet χ_R acquires a vacuum expectation value (VEV) to break the gauge symmetry of the DLRM into that of the SM and then to the $U(1)$ of electromagnetism by the VEV of the neutral components of Higgs bidoublet Φ:

$$SU(2)_L \times SU(2)_R \times U(1)_{B-L} \xrightarrow{\langle \chi_R \rangle} SU(2)_L \times U(1)_Y \xrightarrow{\langle \Phi \rangle} U(1)_{\rm em}.$$

The VEVs of the neutral components of the Higgs fields can be denoted as

$$\langle \Phi \rangle = \begin{pmatrix} \frac{k_1}{\sqrt{2}} & 0 \\ 0 & \frac{k_2}{\sqrt{2}} \end{pmatrix} \ , \ \langle \chi_L \rangle = \begin{pmatrix} 0 \\ \frac{v_L}{\sqrt{2}} \end{pmatrix} \ , \ \langle \chi_R \rangle = \begin{pmatrix} 0 \\ \frac{v_R}{\sqrt{2}} \end{pmatrix}$$

where the VEV's k_1, k_2 satisfy the VEV of the SM namely, $v_{\rm SM} = \sqrt{k_1^2 + k_2^2} \approx 246$ GeV. The spontaneous breaking of DLRM gauge symmetry down to $U(1)_{\rm em}$ results in two charged massive vector bosons W_L, W_R, two neutral massive bosons Z_L, Z_R and a massless photon as expected. The details of the mass spectrum of gauge bosons are shown in Appendix B.1.

Light Dirac neutrino mass and charged lepton mass are given by

$$M_\nu = \frac{1}{\sqrt{2}}(k_1 h + k_2 \widetilde{h}), M_l = \frac{1}{\sqrt{2}}(k_2 h + k_1 \widetilde{h}) \tag{3.4}$$

where the family indices are suppressed. Without any loss of generality, we make use of rotation in the $SU(2)_L \times SU(2)_R$ space so that only one of the neutral components of the Higgs bidoublet acquires a large vacuum expectation value, $k_1 \approx v_{\rm SM}$ and $k_2 \approx 0$. Under these assumptions, the Dirac neutrino mass matrix is

$$M_\nu = \frac{1}{\sqrt{2}}(k_1 h) \tag{3.5}$$

while the charged lepton mass matrix is

$$M_l = \frac{1}{\sqrt{2}}(k_1 \widetilde{h}) \tag{3.6}$$

Therefore, tiny sub-eV Dirac neutrino mass arises due to smallness of Yukawa coupling h while charged lepton masses are generated by corresponding Yukawa coupling $\widetilde{h}$. The details of fermion-gauge boson couplings are shown in Appendix B.2. The details of the scalar mass spectrum is not derived here as we do not need them for our analysis and we refer to [357] for details of the same.

3.3 $\Delta N_{\rm eff}$ in DLRM

Effective number of relativistic degrees of freedom is defined as

$$N_{\rm eff} \equiv \frac{8}{7}\left(\frac{11}{4}\right)^{4/3}\left(\frac{\rho_{\rm rad} - \rho_\gamma}{\rho_\gamma}\right)$$

where $\rho_{\rm rad} = \rho_\gamma + \rho_\nu$ is the net radiation content of the Universe. As mentioned earlier, the SM prediction is $N_{\rm eff}^{\rm SM} = 3.045$ [337, 360, 361] which is also consistent with the constraint from precision measurement of Z boson decay width at LEP $N_\nu = 2.984 \pm 0.008$ [142]. Any deviation of $N_{\rm eff}$ from $N_{\rm eff}^{\rm SM}$ will therefore indicate the presence of additional relativistic species thermalised in the early Universe. While these additional relativistic degrees of freedom can not fully thermalise with the SM bath through interactions mediated by Z boson due to strong LEP bound, they can thermalise via additional interactions or mediating particles not yet observed in direct search experiments. The right handed neutrinos in DLRM provides such an example. They can thermalise with the SM bath in the early Universe due to the interactions mediated by right sector gauge bosons, as depicted by the Feynman diagrams shown in figure 3.1. We consider negligible mixing between left and right sector gauge bosons and hence ignore the contributions coming from processes like $\bar{\nu_R}\nu_L \to f\bar{f}, \bar{\nu_L}\nu_R \to f\bar{f}$. Additionally, the scalar mediated interactions are negligible due to tiny Dirac Yukawa couplings.

To estimate the contribution in $\Delta N_{\rm eff}$ we need to check the decoupling temperature of the right handed neutrinos. The decoupling occurs when the expansion rate of the Universe becomes more than the interaction rate. Hence, the decoupling temperature can be calculated from the following equality

$$\Gamma(T^{\rm d}_{\nu_R}) = H(T^{\rm d}_{\nu_R}) \tag{3.7}$$

where $\Gamma(T)$ is the interaction rate and $H(T)$ is the expansion rate of the Universe. The interaction rate can be written as

$$\Gamma(T) = n_{\nu_R}(T)\,\langle\sigma_{\rm Tot} v\rangle \tag{3.8}$$

where the number density n_{ν_R} for a relativistic neutrino can be written as

$$n_{\nu_R}(T) = \frac{3\ g_{\nu_R}}{4\ \pi^2}\ \zeta(3)\ T^3 \tag{3.9}$$

and the annihilation cross sections of right handed neutrinos are given in Appendix B.3.

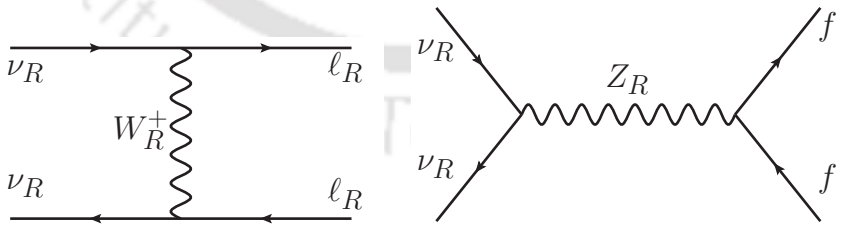

Figure 3.1: Feynman diagrams of ν_R annihilation. Here $l_R \equiv e_R, \mu_R, \tau_R$, $f \equiv e_R, \mu_R, \tau_R, q_R$ with q being quark.

The expansion rate of the Universe can be written as

$$H(T) = \sqrt{\frac{8\,\pi\,G_N\,\rho(T)}{3}} = \sqrt{\frac{4\pi^3 G_N}{45}\left(g_*(T) + 3\frac{7}{8}g_{\nu_R}\right)}T^2 \tag{3.10}$$

where g_{ν_R} is the internal degrees of freedom for right-handed neutrinos. Thus, the contribution of ν_R to effective relativistic degrees of freedom can be estimated as

$$\Delta N_{\rm eff} = N_{\rm eff} - N_{\rm eff}^{\rm SM} = N_{\nu_R} \left(\frac{T_{\nu_R}}{T_{\nu_L}}\right)^4 = N_{\nu_R} \left(\frac{g_{*s}(T^{\rm d}_{\nu_L})}{g_{*s}(T^{\rm d}_{\nu_R})}\right)^{\frac{4}{3}} \tag{3.11}$$

where $\rm N_{\nu_R}$ represents the number of relativistic right-handed neutrinos, $g_*(T)$ corresponds to the relativistic degrees of freedom at temperature T, $g_{*s}(T)$ corresponds to the relativistic entropy degrees of freedom at temperature T [1] and $\rm T^d_{\nu_R}$, $\rm T^d_{\nu_L}$ are the decoupling temperatures for $\nu_{\rm R}$ and $\nu_{\rm L}$ respectively. Thus, depending upon the decoupling temperature of ν_R and hence $g_*(T^{\rm d}_{\nu_R})$, the additional contribution to $\Delta N_{\rm eff}$ can be kept within experimental upper limits. Lower the strength of ν_R interaction with SM bath or higher the mediator mass of ν_R-SM interactions, larger will be $g_*(T^{\rm d}_{\nu_R})$ and hence smaller will be $\Delta N_{\rm eff}$. Similar analysis for $U(1)_{B-L}$ extension of the SM can be found in [278, 335, 336, 364] whereas some estimates in the context of radiative Dirac neutrino mass in LRSM were made in [228, 231].

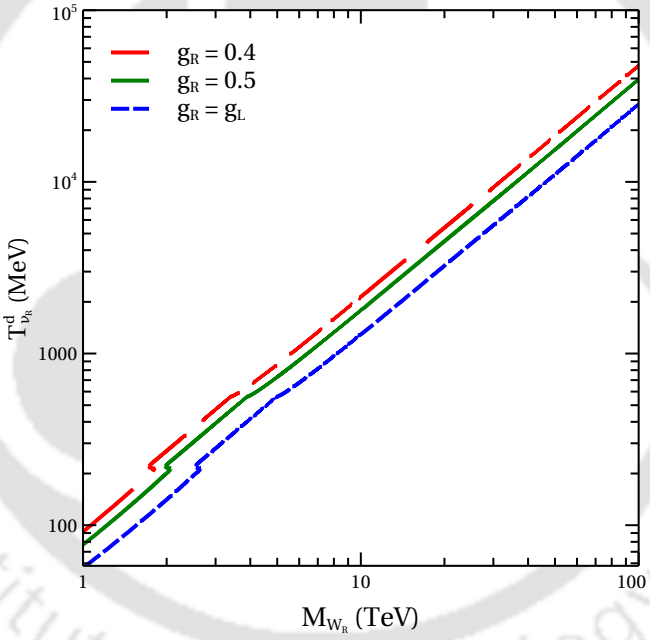

Figure 3.2: Decoupling temperature of right handed neutrinos as a function of W_R mass for different gauge couplings g_R.

3.4 Dark Matter in DLRM

The data from Planck experiment which restricts the effective relativistic degrees of freedom in our Universe also reveal that more than 26% of present Universe's energy density is composed of a non-luminous and non-baryonic form of matter, known as DM. Apart from recent

[1] We use g_* and g_{*s} interchangeably, which is true in SM at high temperatures.

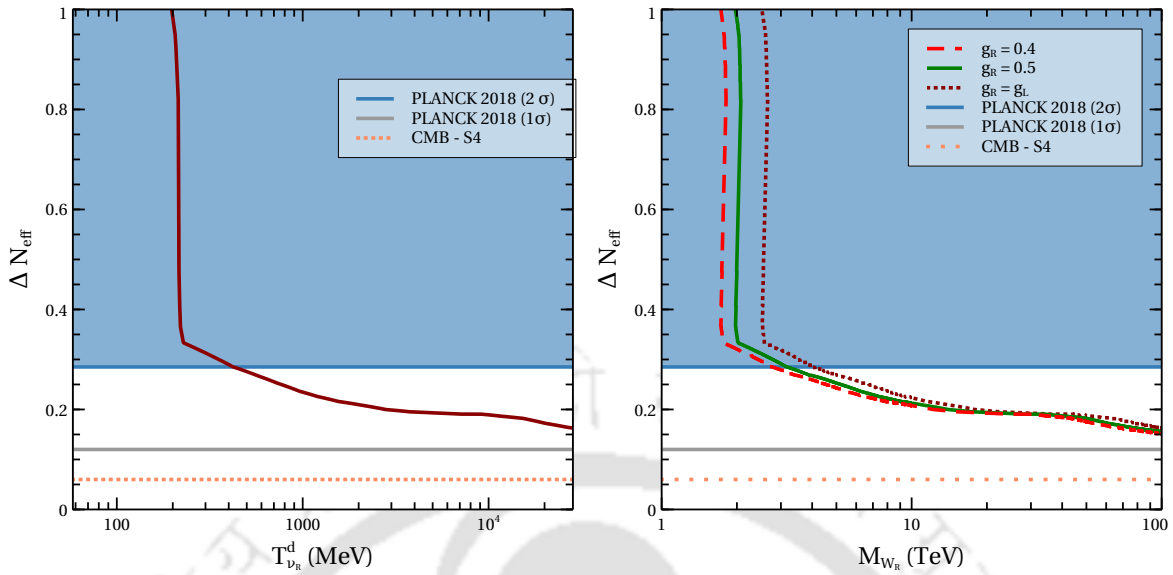

Figure 3.3: $\Delta N_{\rm eff}$ as a function of decoupling temperature (left panel) and W_R mass (right panel).

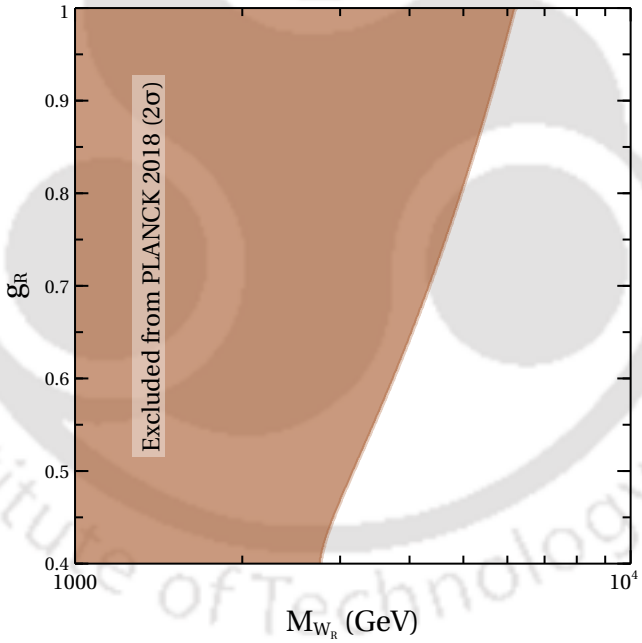

Figure 3.4: Parameter space in $g_R - M_{W_R}$ plane from Planck 2018 2σ constraints on $\Delta N_{\rm eff}$.

cosmology based experiments like Planck, there have been several astrophysical evidences for many decades suggesting the presence of DM [2, 17, 365]. In terms of density parameter $\Omega_{\rm DM}$ and h = Hubble Parameter/(100 km s^{-1}Mpc^{-1}), the present DM abundance is conventionally reported as [50]: $\Omega_{\rm DM}h^2 = 0.120 \pm 0.001$ at 68% CL. Given that none of the SM particles can be a viable DM candidate, several BSM proposals have been put forward among which the weakly interacting massive particle (WIMP) paradigm is the most popular one.

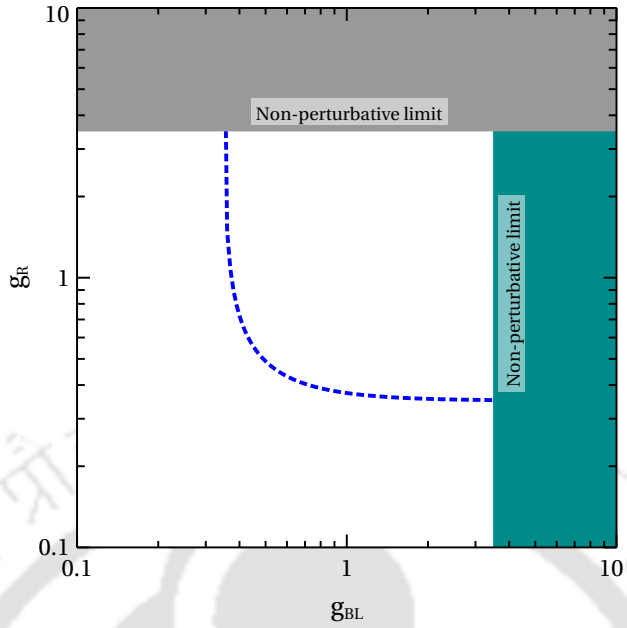

Figure 3.5: Allowed values of g_{BL} and g_R which will reproduce the value g_Y after the spontaneous breaking of $\mathrm{SU(2)_R \times U(1)_{B-L}}$ to the remaining $U(1)_Y$.

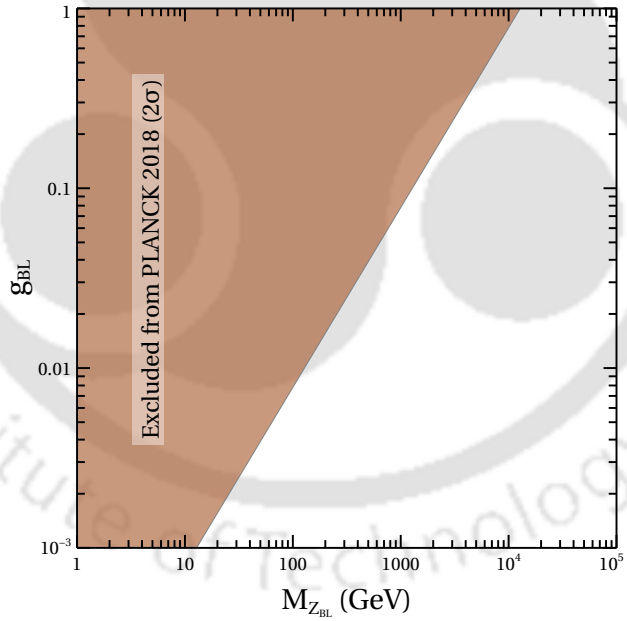

Figure 3.6: Allowed $g_{BL} - M_{Z_{BL}}$ parameter space from Planck 2018 bound on $\Delta N_{\rm eff}$ at 2σ in minimal $U(1)_{B-L}$ gauge model with light Dirac neutrinos.

In this framework, a DM particle having masses and interactions similar to those around the electroweak scale gives rise to the observed relic after thermal freeze-out, a remarkable coincidence often referred to as the *WIMP Miracle* [5].

The minimal DLRM discussed above does not have a stable DM candidate. One can

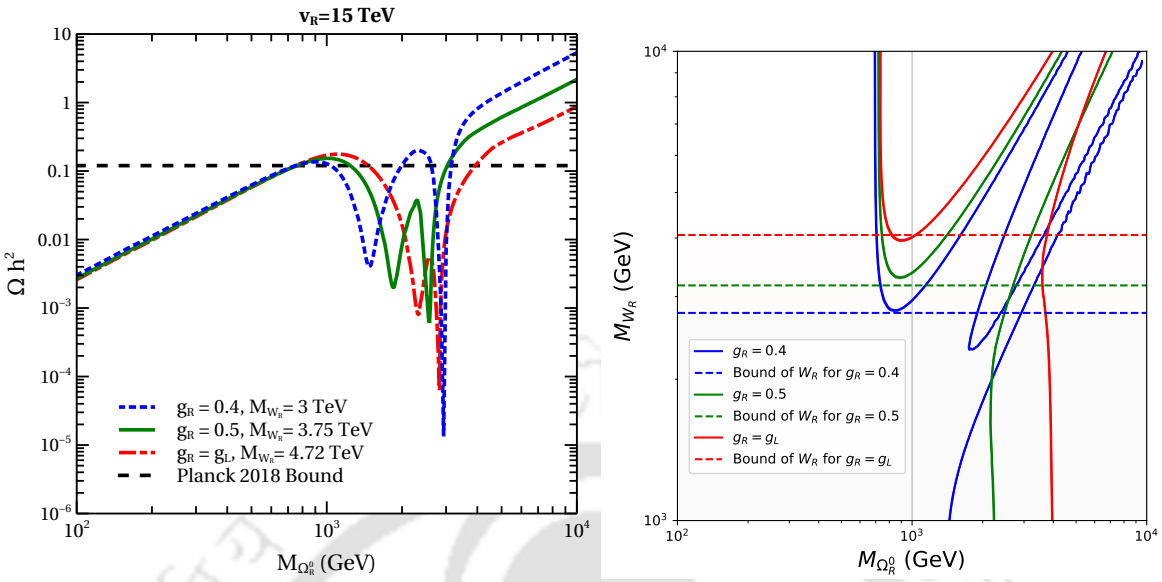

Figure 3.7: Left panel: DM relic as a function of DM mass for different benchmark combinations of g_R, W_R). Right panel: Parameter space satisfying relic abundance criteria of right handed fermion quintuplet DM in DLRM. The shaded regions are ruled out by Planck 2018 bound on $\Delta N_{\rm eff}$ at 2σ for respective values of g_R.

however, minimally extend the model by including additional scalar or fermionic multiplets in the spirit of minimal DM scenario [329, 366, 367]. In these models, the DM candidate is stabilised either by a $\mathbb{Z}_2 = (-1)^{B-L}$ subgroup of the $U(1)_{B-L}$ gauge symmetry or due to an accidental symmetry at the renormalisable level due to the absence of any renormalisable operator leading to DM decay. Such minimal DM scenario in LRSM has been studied recently by the authors of [368, 369]. Some more recent works on DM in LRSM can be found in [110, 228, 230, 231, 370–376]. Unlike in triplet LRSM where $SU(2)_R \times U(1)_{B-L}$ gauge symmetry is spontaneously broken by scalar triplet with even $(B-L)$ charge (± 2), in DLRM the same happens due to scalar doublet with odd $(B-L)$ charge (± 1). Thus, there is no stabilising symmetry like $\mathbb{Z}_2 = (-1)^{B-L}$ in DLRM to stabilise DM. Therefore some DM candidates like fermion triplet, fermion bidoublet, scalar doublet discussed in the context of triplet LRSM [368, 369] are no longer stable in DLRM due to the presence of renormalisable interactions with lighter fields. We therefore consider the option of larger fermion multiplet as DM, and the minimal scenario is to consider a real fermion quintuplet of $B-L$ charge 0. Since we want to constrain the right sector gauge bosons from cosmology bound on $\Delta N_{\rm eff}$, we particularly focus on right handed fermion quintuplet DM whose relic abundance depends upon the strength of its annihilation through right sector gauge bosons.

In the pure left-right symmetric setup, one has to introduce a pair of left and right handed

fermion quintuplets (having same mass) which can be written in component form as

$$\Omega_L = \begin{pmatrix} \Omega_L^{++} \\ \Omega_L^{+} \\ \Omega_L^{0} \\ \Omega_L^{-} \\ \Omega_L^{--} \end{pmatrix}, \quad \Omega_R = \begin{pmatrix} \Omega_R^{++} \\ \Omega_R^{+} \\ \Omega_R^{0} \\ \Omega_R^{-} \\ \Omega_R^{--} \end{pmatrix}. \tag{3.12}$$

Since we are discussing a general scenario with $g_L \neq g_R$, we consider the left fermion quintuplet to be very heavy and decoupled from the low energy phenomenology. Even in the pure left-right symmetric limit $g_L = g_R$, one can make the left quintuplet decouple from the low energy phenomenology by introducing a parity odd scalar singlet whose non-zero VEV at a very high scale splits the right and left fermion masses. Such proposals where the left-right discrete symmetry or parity gets broken spontaneously before $SU(2)_R \times U(1)_{B-L}$ gauge symmetry were put forward long ago in [377–379]. While all the components of fermion multiplet have same tree level masses, at radiative level, there arises a mass splitting between charged (with Q) and neutral components given by [368, 369],

$$M_{\Omega_R^Q} - M_{\Omega_R^0} \simeq \frac{\alpha_2}{4\pi} \frac{g_R^2}{g_L^2} M Q^2 \left[f(r_{W_R}) - c_M^2 f(r_{Z_R}) - s_W^2 s_M^2 f(r_{Z_L}) - c_W^2 s_M^2 f(r_\gamma) \right], \tag{3.13}$$

where $s_M = \sin\theta_M \equiv \tan\theta_W \frac{g_L}{g_R}$, $s_W = \sin\theta_W$, $r_X = M_X/M$ and

$$f(r) \equiv 2 \int_0^1 dx (1+x) \log\left[x^2 + (1-x)x^2\right].$$

The bare mass of the multiplet is denoted by M. Here the one loop self-energy corrections through mediations of gauge bosons are presented within the square bracket of the second expression. Due to such tiny one loop mass splitting, the next to lightest component of each DM multiplet can be thermally accessible during the DM freeze-out and hence the coannihilation effects play a crucial role [282]. While in triplet LRSM, there exists the possibility that for $M \gg M_{W_R}$, the neutral component of the multiplet can become heavier compared to the charged components, such possibilities do not arise in DLRM. This was noted in [376] which we also confirm. Apart from its role in enhancing DM coannihilations, such mass splitting, if small enough, may also induce inelastic DM-nucleon scattering mediated by W_R bosons. However, for our region of interest, such tiny mass splitting does not arise. This ensures that W_R mediated DM-nucleon scattering occurs only at one loop level and hence remain suppressed. Spin-independent elastic DM nucleon scattering mediated by Z_R at tree level remains absent due to vanishing $B-L$ charge of fermion quintuplet discussed in this work. Thus, the DM phenomenology of right handed fermion quintuplet is mainly governed by its gauge interactions which are given by [376]

$$\begin{aligned} \mathcal{L}_{\Omega_R} \supset & -s_W s_M g_R Q \overline{\Omega_R^Q} Z_L^\mu \gamma_\mu \Omega_R^Q + c_M g_R Q \overline{\Omega_R^Q} Z_R^\mu \gamma_\mu \Omega_R^Q \\ & + c_W s_M g_R Q \overline{\Omega_R^Q} A^\mu \gamma_\mu \Omega_R^Q + \frac{g_R}{\sqrt{2}} \left(c_Q \overline{\Omega_R^{Q+1}} W_R^\mu \gamma_\mu \Omega_R^Q + \text{h.c.} \right) \end{aligned} \tag{3.14}$$

where $c_Q = \sqrt{(2+Q+1)(2-Q)}$ and Q is the electromagnetic charge of the quintuplet component.

3.5 Results and Discussion

Using the recipe discussed in previous section, we first calculate the decoupling temperature of right handed neutrinos from the thermal bath for different values of W_R, Z_R mass and gauge coupling g_R. The variation of decoupling temperature with W_R mass for different values of g_R is shown in figure 3.2. Although both W_R and Z_R masses play role in right handed neutrino interactions with the thermal bath, we show the variation of decoupling temperature as well as other physical quantities only in terms of W_R mass. This is due to the fact that Z_R mass typically depends upon W_R mass and is heavier than it, similar to Z and W masses of the SM. Also, we are not restricting ourselves to pure left-right symmetric limit $g_R = g_L$ and considering different values of g_R as well. Decoupling temperature rises for lower values of gauge coupling as well as higher values of W_R mass as seen from figure 3.2 which is expected as the corresponding rate of interactions decreases. Typically the interaction cross section $\langle \sigma v \rangle$ of right handed neutrinos depends upon temperature as $g_R^4 T^2/M_{W_R}^4$ and hence the rate of interaction is $\Gamma(T) \propto g_R^4 T^5/M_{W_R}^4$. When this is compared with the Hubble parameter $H(T) \propto T^2$ as in equation (3.7) to find the decoupling temperature $\mathrm{T}^{\mathrm{d}}_{\nu_{\mathrm{R}}}$, it is clear that with increase in W_R mass, the decoupling temperature will also rise. Similarly, decrease in g_R will lead to an increase in decoupling temperature for same value of M_{W_R}. This conclusion reached from approximate analytical formulas for cross section and Hubble parameter also agrees with our numerical results shown in figure 3.2.

We then show the contribution to ΔN_{eff} in figure 3.3 as functions of decoupling temperature as well as W_R mass.The dependance of ΔN_{eff} on $\mathrm{T}^{\mathrm{d}}_{\nu_{\mathrm{R}}}$ in the left panel of figure 3.3 can be understood from equation (3.11). The total number of relativistic degrees of freedom at decoupling temperature $g_{*s}(T^{\mathrm{d}}_{\nu_R})$ increases with the increasing $\mathrm{T}^{\mathrm{d}}_{\nu}$ which thereby decreases the value of ΔN_{eff}. However, at some point g_{*s} it will reach its maximum value and ΔN_{eff} becomes almost constant, as seen from the plateau region on bottom left corner of left panel plot in figure 3.3. Since $T^d_{\nu_R}$ is being varied independently and corresponding $g_{*s}(T^{\mathrm{d}}_{\nu_R})$ is used to find ΔN_{eff} using equation (3.11), the behaviour of this plot does not depend upon g_R, M_{W_R}. To show the dependence of ΔN_{eff} on such model parameters, we have made the plot shown in right panel of figure 3.3. The right panel of figure 3.3 represents the dependance of ΔN_{eff} on $\mathrm{M_{W_R}}$ for three benchmark values of g_R. One can see that the contribution to the ΔN_{eff} decreases with increasing M_{W_R}. This is because, for higher values of M_{W_R}, ν_R will decouple at some higher temperature and the contribution to the ΔN_{eff} will become smaller. Along with the Planck 2018 bound mentioned earlier, we also show the CMB-S4 sensitivity [380] as well as the Planck 2018 1σ limit while the latter is same as SPT-3G sensitivity [381]. Clearly, Planck 2018 bound at 2σ CL itself rules out W_R mass below 4.06 TeV with gauge coupling $g_R = g_L$. On the other hand, future probe will be able to either confirm or rule out the model, even for very high W_R masses, out of reach of direct search experiments. Finally we show the final parameter space in $g_R - M_{W_R}$ plane after applying Planck 2018 2σ constraints in figure 3.4.

Unlike in [278, 335, 336, 364] where similar constraints on $U(1)_{B-L}$ gauge boson was obtained, the crucial difference in DLRM is that here one can not tune the gauge couplings for a particular value of gauge boson mass in order to suppress the contribution to ΔN_{eff}. This is because the gauge couplings of $SU(2)_R$ and $U(1)_{B-L}$ are not arbitrary but related to the

gauge coupling of $U(1)_Y$ (at the scale of left-right symmetry breaking) as

$$\frac{1}{g_Y^2} = \frac{1}{g_R^2} + \frac{1}{g_{BL}^2} \tag{3.15}$$

Since g_Y is known, one can not change g_R, g_{BL} arbitrarily within their perturbative limits[2]. We show the allowed region of these two gauge couplings in figure 3.5. While we still have a large region within perturbative limits, we have chosen g_R to be either equal to g_L or smaller while keeping g_{BL} also below order one for our benchmark analysis. For $g_R > g_R$ the Planck bound becomes even more stringent, as we found in the scan plot shown in $g_R - M_{W_R}$ plane in figure 3.4. Thus, compared to $U(1)_{B-L}$ or other Abelian gauge models of Dirac neutrinos, DLRM is much more constrained. For a comparison we show the parameter space for gauged $U(1)_{B-L}$ model with Dirac neutrinos in figure 3.6. This is a minimal gauged $B-L$ model where there are three right handed neutrinos having $B-L$ charge -1 each apart from the SM fermion content and neutrinos get sub-eV Dirac mass by virtue of their tiny couplings with SM Higgs. Since the $B-L$ gauge coupling is a free parameter and not related to SM gauge couplings in this model, one can tune the gauge coupling arbitrarily to evade the stringent Planck bound on $\Delta N_{\rm eff}$ as can be seen from figure 3.6.

To check the impact of these constraints on DM parameter space, we then calculate relic of right fermion quintuplet DM. For DM relic calculation, we first implement the model in `SARAH` [383] and then feed the model files into `micrOMEGAs` [384] for relic calculations. We then consider three benchmark combinations of (g_R, W_R) while keeping the scale of left-right gauge symmetry breaking v_R fixed. The resulting variation of DM relic as a function of DM mass is shown in left panel plot of figure 3.7. The resonance corresponding to W_R, Z_R masses are clearly visible in this plot. Note that in LRSM, the ratio between the two new gauge bosons crucially depends on the way $SU(2)_R \times U(1)_{B-L}$ is broken to the hypercharge group $U(1)_Y$. Unlike in quintuplet DM scenario in triplet LRSM [369], here the two resonances are quite close to each other due to smaller ratio of Z_R to W_R mass in DLRM. The results shown in left panel plot of figure 3.7 also agree with that shown in [376]. We then scan the parameter space of W_R, Ω_R^0 masses and show the region satisfying correct DM relic in right panel plot of figure 3.7. Multiple allowed values of DM mass for a fixed W_R mass are arising due to annihilation and coannihilations of $\Omega_R^0, \Omega_R^\pm, \Omega_R^{\pm\pm}$ mediated by W_R, Z_R bosons where Z_R is slightly heavier than W_R ($M_{Z_R} \approx 1.2 M_{W_R}$ in pure left-right symmetric limit $g_R = g_L$). Further, red and green solid lines on the right panel plot of figure 3.7 has shows the possibility of having three different values of DM mass with correct relic abundance for a fixed W_R mass. The same behaviour is also seen on the left panel plot of figure 3.7 with fixed W_R mass where the red and green lines satisfy relic at three different values of DM masses. On the other hand, the blue dashed line on the left panel plot of figure 3.7 satisfies correct relic abundance for five different values of DM masses, a feature which is also depicted by the blue solid line in the scan plot (right panel of figure 3.7). We also apply the corresponding bounds on W_R mass from Planck constraints on $\Delta N_{\rm eff}$ at 2σ CL as horizontal shaded lines so that the region below the respective lines are disallowed. Clearly, some part of the DM parameter space on the right side of the scan plot (right panel of figure 3.7) gets disfavoured

[2]For discussion related to perturbativity constraints on similar models, please refer to [382] and references therein.

for all three values of g_R by $\Delta N_{\rm eff}$ bounds as the lower region of the dashed lines are excluded from Planck constraints on $\Delta N_{\rm eff}$ at 2σ CL. In the parabolic part of the parameter space in the scan plot, a small part of the parameter space for $g_R = g_L$ case is disfavoured by $\Delta N_{\rm eff}$ bounds while the parabolic lines corresponding to $g_R \neq g_L$ still remains allowed from respective $\Delta N_{\rm eff}$. We do not show other existing bounds on W_R mass from flavour or LHC data as they are either equally or less strong compared to the bounds derived here.

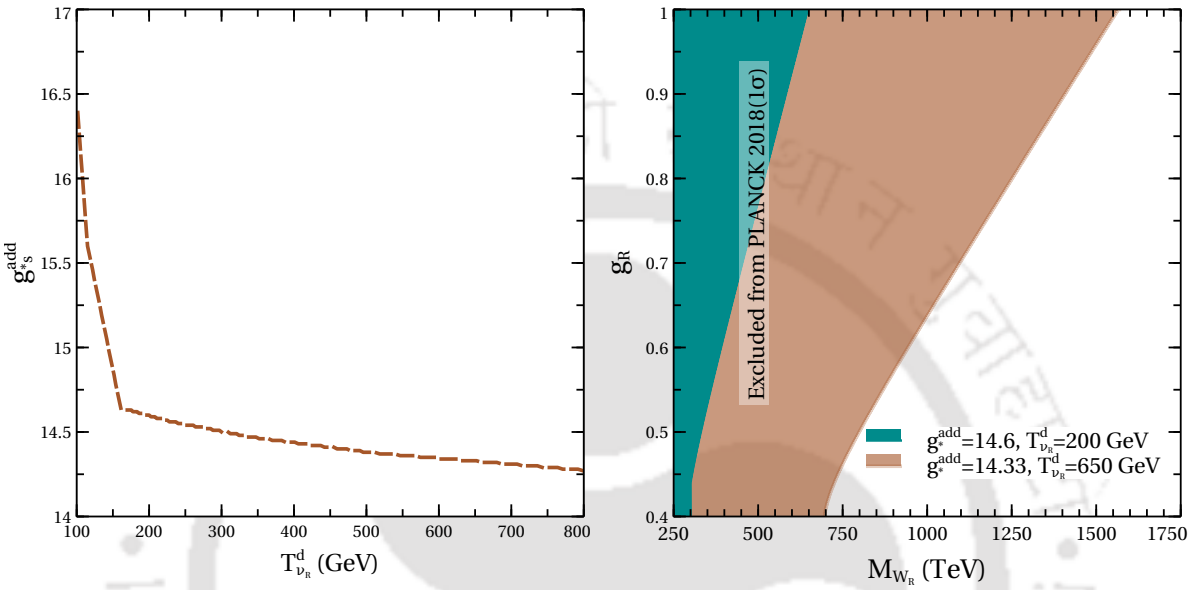

Figure 3.8: Left panel: Additional relativistic degrees of freedom required to bring $N_{\rm eff}$ within Planck 2018 1σ bound $N_{\rm eff} = 2.99 \pm 0.17$. Right panel: Allowed parameter space in $g_R - M_{W_R}$ plane from Planck 2018 1σ bound $N_{\rm eff} = 2.99 \pm 0.17$ after considering additional relativistic degrees of freedom.

One important point to note here is that the 1σ bound of $N_{\rm eff}$ rules out all the parameter space if we assume only SM plus three right- handed neutrinos to be contributing to the relativistic degrees of freedom (DOF) below the scale of left-right symmetry breaking. However, this can be relaxed if we have more relativistic degrees of freedom at the early universe. The left panel of figure 3.8 shows the required additional DOF in as a function of right-handed neutrino decoupling temperature. All the points on the dashed line in the left panel of figure 3.8 gives rise to $\Delta N_{\rm eff} = 0.12$ so that the points below this line are ruled out. This DOF can arise from DLRM with right-handed fermion quintuplet DM. For example, the scalar bidoublet has four physical DOF apart from the SM Higgs, while the pair of Higgs doublets can give rise to five more physical DOF. Similarly, right-handed fermion quintuplet DM has approximately ten DOF. Thus, one can have 19 additional DOF in DLRM with right-handed fermion quintuplet DM. Similar ways of avoiding such strict cosmological bounds on $\Delta N_{\rm eff}$ have also been discussed in the recent work [434]. On the right panel of figure 3.8, we show the allowed parameter space on $g_R - M_{W_R}$ plane from Planck 2018 1σ bound after considering the required additional relativistic DOF at decoupling temperatures of 200 GeV and 650 GeV, respectively. Since decoupling temperature of 200 GeV can be achieved with a lighter W_R gauge boson, therefore we get more allowed parameter space compared to the

case with higher decoupling temperature of right-handed neutrinos. However, the presence of such additional light degrees of freedom will face stringent tests from collider as well as flavour physics constraints.

CHAPTER 4

Dark matter and neutrino mass with discrete flavour symmetries

4.1 Introduction

After discussing different aspects of dark matter and connection to the origin of light neutrino masses within gauged extensions of the standard model, in this chapter, we elaborate upon two different BSM scenarios with discrete and global symmetries dictating the interplay of DM and neutrino phenomenology. At first, we discuss a hybrid scenario where both thermal (freeze-out) and non-thermal (freeze-in) contributions to DM relic abundance can be important. To be more specific, DM can have sizeable interactions to be thermally produced in the early Universe but also needs a non-thermal source to satisfy the correct relic abundance in the present epoch. This idea was explored in several earlier works including [385–388] and references therein. Recently, such a work was performed for the inert Higgs doublet DM model [389] where the SM is extended by an additional scalar doublet odd under an in-built $\mathbb{Z}_2$ symmetry so that the lightest $\mathbb{Z}_2$-odd component is a stable DM candidate. In that work the thermally under-abundant DM parameter space was revisited and it was shown that a non-thermal contribution from an additional $\mathbb{Z}_2$-odd singlet neutral fermion can fill this deficit while the other two cousins of this singlet neutral fermion along with the inert scalar doublet can play a role in generating one loop radiative neutrino masses in scotogenic fashion [12]. While the addition of singlet right handed neutrinos to the SM content can give rise to the usual seesaw mechanism [200, 202, 203] for neutrino mass at tree level, the scotogenic framework can explain the origin of neutrino mass and DM in a unified manner. In the earlier work [389] where both thermal and non-thermal contributions to scalar DM abundance were studied, the initial abundance of the heavy singlet fermion was not explained, but was fixed suitably in order to generate the required non-thermal contribution.

In the present work, we consider a more general study of this hybrid scenario within the framework of another minimal model for DM and neutrino masses but with more observable consequences. Here the singlet neutral fermions of the minimal scotogenic model [12] are replaced by fermion triplets having zero hypercharge, but odd under the $\mathbb{Z}_2$ symmetry. As known from the discussions of fermion triplet DM (FTDM) model proposed by Ma and Suematsu [330], the FTDM is usually under-abundant below 2.2 TeV mass due to its

large annihilation cross section. Inclusion of non-perturbative effects on DM annihilations [390, 391] which are more dominant for heavier DM masses, pushes this bound on fermion triplet DM mass to around 2.7 TeV [369]. In this work, we particularly focus on the fermion triplet DM mass around 1 TeV and check if a non-thermal contribution can fill the deficit coming from thermal freeze-out. In a scotogenic model with fermion triplet, the only non-thermal contribution for such 1 TeV DM can come from the $\mathbb{Z}_2$ odd scalar doublet. Unlike the earlier work [389] where the mother particle was a fermion singlet with tiny Yukawa coupling with the dark mater candidate, here the mother particle has gauge interactions and hence can have thermal abundance due to the usual freeze-out scenario. We solve the coupled Boltzmann equations corresponding to the comoving number densities of the inert scalar doublet as well as fermion triplets to determine the final relic abundance of fermion triplet DM. The inert scalar doublet, being heavier, freezes out first followed by the freeze-out of the fermion triplet. Then a non-thermal contribution from the inert scalar doublet fills the deficit in fermion triplet relic abundance from thermal freeze-out. The requirement for correct fermion triplet DM abundance not only constrains its coupling with the inert scalar doublet, but also the freeze-out abundance and hence the parameter space of the latter. The other two cousins of the FTDM can have sizeable coupling with inert scalar doublet and SM leptons to generate tiny neutrino masses at one loop. Since the lightest fermion triplet almost decouples from neutrino mass generation due to tiny Yukawa couplings (required for non-thermal production or freeze-in), the lightest neutrino remains massless in our scenario. We also check the testability of the model and find that such TeV scale fermion triplet DM can have observable consequences and direct, indirect DM detection experiments as well as collider experiments like the large hadron collider (LHC).

In the second scenario, we have discussed the possibility of dynamically generating the tiny coupling constant required for the non-thermal DM production which we had introduced by hand in our earlier work. This work is motivated by the coincidence that the origin of Dirac neutrino masses as well as FIMP DM typically require very small dimensionless couplings $\sim 10^{-12}$ [11]. In the neutrino sector, such couplings can generate 0.1 eV Dirac neutrino mass through neutrino coupling to the SM like Higgs. On the other hand, in the dark sector, such tiny couplings of the DM particle with the mother particle makes sure that it gets produced non-thermally through the freeze-in mechanism. There have been several attempts where the origin of such feeble interactions of DM with the visible sector is generated via higher dimensional effective operators [11, 164, 392]. Very recently, there has been attempt to realise such feeble interactions naturally at renormalisable level also [393]. The coincidence between such tiny FIMP couplings and Dirac neutrino Yukawas was also pointed out, mostly in supersymmetric contexts, by the authors of [11, 394–398]. Here, we consider an A_4 flavour symmetric model[1] where neutrino Dirac mass as well as FIMP coupling with its mother particle get generated through dimension six operators involving the same flavon fields. A global unbroken lepton number symmetry is assumed that forbids the Majorana mass terms of singlet fermions. We show that both freeze-in and freeze-out formalisms are important in generating the DM relic in our scenario. The mother particle,

[1]Similar exercise can be carried out using other discrete groups like A_5, S_4, $\Delta(27)$ etc. However, here we adopt A_4 flavour symmetry as it is the smallest group having a three dimensional representation which in turn helps to realise neutrino mixing in an economical way.

which is long lived in this model and decays only to the DM at leading order, first freezes out and then decays into the DM particle. Therefore, the final abundance of DM particle depends upon the mother particle couplings to the SM particles which can be probed at different ongoing experiments. This is similar to the superWIMP scenario [399] where a metastable WIMP decays into a super-weakly interacting DM at late epochs. Interestingly, we find that ongoing experiments like the large hadron collider (LHC) can probe some part of the parameter space which can give rise to sizeable invisible decay of SM like Higgs boson into the long lived mother particles. We also show that the correct neutrino oscillation data can be reproduced in some specific vacuum alignments of the flavon fields indicating the predictive nature of the model. The model also predicts normal hierarchical neutrino mass ordering and interesting correlations between neutrino parameters requiring the atmospheric mixing angle to be in the lower octant for maximal Dirac CP phase.

4.2 sub-TeV fermion triplet dark matter with radiative neutrino mass

4.2.1 Fermion Triplet Dark Matter (FTDM)

In this section, we discuss a stable fermion triplet of zero hypercharge as a DM candidate, stabilised by an in-built $\mathbb{Z}_2$ symmetry. It is straightforward to realise the need of additional $\mathbb{Z}_2$ symmetry as otherwise the triplet can decay into the SM Higgs and lepton due to renormalisable couplings among them. A $\mathrm{SU(2)_L}$ multiplet of higher dimensions can however be naturally stable without any need of additional symmetries, along the minimal DM spirit [329]. FTDM was also studied by several other groups, the most recent of which can be found in [369] within the framework of another class of models. To be more technical, in a minimal setup of FTDM, the fermionic sector of the SM is extended by a $\mathrm{SU(2)_L}$ triplet $\Sigma_R = (\Sigma_R^1 \;\; \Sigma_R^2 \;\; \Sigma_R^3)^T$ with zero hypercharge. The triplet Σ_R which is in the adjoint representation of $\mathrm{SU(2)_L}$, can also be expressed in the fundamental representation as

$$\Sigma_R \;=\; \frac{\sigma^i \; \Sigma_R^i}{\sqrt{2}} \;=\; \begin{pmatrix} \Sigma_R^0/\sqrt{2} & \Sigma_R^+ \\ \Sigma_R^- & -\Sigma_R^0/\sqrt{2} \end{pmatrix}, \tag{4.1}$$

where σ_i's ($i = 1$ to 3) are the Pauli spin matrices, the generators of the fundamental representation of $\mathrm{SU(2)_L}$ while $\Sigma_R^\pm = (\Sigma_R^1 \mp i\,\Sigma_R^2)/\sqrt{2}$, $\Sigma_R^0 = \Sigma_R^3$. Let us define $\Sigma = \Sigma_R + {\Sigma_R}^c$, where ${\Sigma_R}^c = C\,\overline{\Sigma_R}^T$ is the CP conjugate of Σ_R and C being the charge conjugation operator. Note that, by construction Σ is a Majorana fermion ($\Sigma^c = \Sigma$) however, not all the components of Σ are Majorana fermions. We have shown in the Appendix C.1 that only neutral component of Σ is a Majorana fermion while the charged one is as usual a Dirac fermion. The Lagrangian of the triplet Σ is given by

$$\mathcal{L}_{triplet} \;=\; \frac{i}{2}\mathrm{Tr}[\overline{\Sigma}\,\not{D}\Sigma] - \frac{1}{2}\,\mathrm{Tr}[\overline{\Sigma}\,M_\Sigma\,\Sigma]\,, \tag{4.2}$$

$$= \frac{i}{2}\mathrm{Tr}[\overline{\Sigma_R}\,\not{D}\,\Sigma_R] + \frac{i}{2}\mathrm{Tr}[\overline{{\Sigma_R}^c}\,\not{D}\,{\Sigma_R}^c] - \left(\frac{1}{2}\,\mathrm{Tr}[\overline{{\Sigma_R}^c}\,M_\Sigma\,\Sigma_R] + h.c.\right), \tag{4.3}$$

where, D_μ is the covariant derivative of Σ_R and its expression is given in equation (C.3) of Appendix C.1. Now, inserting equation (4.1) into equation (4.3), and using the relation ${\Sigma_R}^c = C\,\overline{\Sigma_R}^T$, we get

$$\begin{aligned}\mathcal{L}_{triplet} &= \overline{\psi^-}\, i\,\partial\!\!\!/\psi^- + \frac{1}{2}\overline{\psi^0} i\,\partial\!\!\!/\psi^0 - M_\Sigma\,\overline{\psi^-}\,\psi^- - \frac{M_\Sigma}{2}\,\overline{\psi^0}\,\psi^0 - g\left(\overline{\psi^-}\gamma^\mu\,\psi^0\,W_\mu^- + h.c.\right)\\ &\quad + g\,\cos\theta_w\,\overline{\psi^-}\gamma_\mu\psi^-\,Z^\mu + g\,\sin\theta_w\,\overline{\psi^-}\gamma_\mu\psi^-\,A^\mu\,,\end{aligned} \tag{4.4}$$

where, we have defined $\psi^- = \Sigma_R^- + \Sigma_R^{+c}$, a four component Dirac spinor while ψ^0 is a Majorana fermion in four component notation as $\psi^0 = \Sigma_R^0 + \Sigma_R^{0\,c}$ and θ_w is the usual weak mixing angle known as the Weinberg angle. In Appendix C.1, we have explicitly derived equation (4.4) from equation (4.3). Now, if one introduces a $\mathbb{Z}_2$ parity on Σ_R then the neutral component ψ^0, which is a Majorana fermion, can be a viable thermal DM candidate (WIMP). As the Yukawa interaction terms among Σ_R, SM leptons and Higgs boson are forbidden by the $\mathbb{Z}_2$ symmetry hence the DM candidate ψ^0 interacts with the SM particle only through gauge interactions. Moreover, from the Lagrangian (equations (4.3), (4.4)) it is evident that the bare masses for all members of the fermionic triplet Σ_R are identical to M_Σ. However, one can make the charged components $\psi^\pm$ heavier by considering one loop electroweak radiative corrections [329, 330], which result in a mass splitting ~ 166 MeV between $M_{\psi^\pm}$ and M_{ψ^0} for $M_\Sigma \gtrsim 1\,\text{TeV}$. In this framework, the relic density of the lightest $\mathbb{Z}_2$-odd particle ψ^0 is determined by its pair annihilation into W^+W^- final state via t-channel exchange of $\psi^\pm$. Besides, the co-annihilations among ψ^0 and $\psi^\pm$ into SM particles also play a crucial role in relic density calculation as the mass splitting between the members of the fermionic triplet is extremely small ($\sim \mathcal{O}(100\,\text{MeV})$). The co-annihilations include several process like $\psi^0\,\psi^\pm \to W^\pm Z$ (via t-channel exchange of $\psi^\mp$), $\psi^+\,\psi^- \to f\bar{f}$, W^+W^- (via s-channel exchange of Z), $\psi^\pm\,\psi^\pm(\psi^\mp) \to W^\pm W^\pm(W^\mp)$ (via t-channel exchange of ψ^0) etc. After including all these annihilation and co-annihilation channels, the relic density of ψ^0 satisfies the Planck limit [400] for $M_{\psi^0} \sim 2.2$ TeV [330] (see green dashed line in figure 4.4 in Section 4.2.4). Therefore, the DM mass allowed by the observational data from Planck satellite may not be produced efficiently in LHC at the present centre of mass energy and luminosity. This has also led to some recent discussions on FTDM with a singlet admixture, in order to lower the bound on fermion triplet from relic abundance point of view and to enhance its production at colliders, see for example, [401]. It should be noted that such admixture of singlet fermion with the neutral component of fermion triplet as DM candidate was proposed long back by the authors of [402], motivated from its search prospects at LEP collider. We consider another minimal modifications of the present model which is also motivated from neutrino mass point of view, so that one can still have a much lighter triplet fermionic DM which at the same time satisfies all the existing direct and indirect bounds and can have tantalising detection prospects at the LHC. We will present a detailed discussion on this topic in Section 4.2.5.

4.2.2 Scotogenic Extension of FTDM

In order to have nonzero neutrino masses and a light triplet fermionic DM, we have extended the minimal model, described in the previous section, by two more triplets and one inert

doublet. Therefore, besides the usual SM fields, the present model contains three fermionic $\mathrm{SU(2)_L}$ triplets and one extra $\mathrm{SU(2)_L}$ doublet $\Phi = \begin{pmatrix} \phi^+ & \frac{\phi^0 + i\,A^0}{\sqrt{2}} \end{pmatrix}^T$. All these extra BSM fields are odd under the discrete symmetry $\mathbb{Z}_2$. As a result, the Yukawa interaction terms involving fermionic triplet, SM Higgs doublet and lepton doublet are forbidden. Hence, one cannot generate tiny neutrino masses following usual Type-III seesaw mechanism [209, 403, 404], where the above mentioned Yukawa terms play a pivotal role. Instead, in the present model, we can write the Yukawa terms using the inert Higgs doublet Φ. However, the extra doublet Φ, being an inert one (does not interact with SM fermions), does not have any vacuum expectation value (VEV) (in order to maintain $\mathbb{Z}_2$ symmetry unbroken). Hence, there are no neutrino masses at tree level (Type-III seesaw is not possible) and instead, the light neutrino masses can be generated radiatively at one loop level following the scotogenic model [12]. This scotogenic version of Type-III seesaw model is also known as radiative Type-III seesaw model, studied in different contexts by several authors [330, 405, 406].

Further, the Majorana type bare mass terms $\mathrm{Tr}\left[\overline{\Sigma_{\alpha R}{}^c}\, M_\Sigma^{\alpha\beta}\, \Sigma_{\beta_R}\right]$ are although invariant under $\mathbb{Z}_2$ symmetry, the origin of such terms is not obvious in the present scenario. Therefore, to understand a possible origin of bare mass term of fermionic triplet we introduce a scalar field S', which is a singlet under SM gauge group. Moreover, we also impose an additional $\mathbb{Z}_3$ charges to Σ_{β_R} ($\beta = 1$ to 3) and S' such that the bare mass term of Σ_{β_R} is forbidden by $\mathbb{Z}_3$ symmetry while at the same time $\mathrm{Tr}\left[\overline{\Sigma_{\alpha R}{}^c}\, y_s^{\alpha\beta}\, \Sigma_{\beta_R}\right] S'^\dagger$ term is allowed. Thus, when S' gets a VEV, $\langle S' \rangle = \dfrac{v_s}{\sqrt{2}}$, this term will generate the bare mass term $M_\Sigma^{\alpha\beta} \sim y_s^{\alpha\beta}\, v_s$. Apart from that the singlet scalar S' also helps the present model to evade the indirect detection bounds on W^+W^- annihilation channel [8]. This limit is obtained from the non-observation of excess gamma-rays, over the known backgrounds, due to dark matter annihilation from dwarf spheroidal galaxies. Another interesting aspect of including this singlet scalar is to enhance the DM direct detection rate by introducing a tree level scattering while the minimal model had only radiative direct detection scattering at one loop level. We will have a detailed discussion on this topic in Section 4.2.7. Furthermore, we have to impose appropriate $\mathbb{Z}_3$ charges to the SM leptons as well so that the Yukawa interaction terms involving both inert doublet Φ and SM Higgs doublet H remain invariant under $\mathbb{Z}_3$ symmetry. The $\mathbb{Z}_3$ charges of Σ_{β_R} and SM leptons can be ω^2 while that of S' can be ω, where ω^2, ω are the cube roots of unity.

The Lagrangian involving Σ_{β_R}, Φ and S' fields, which is invariant under $\mathrm{SU(2)_L \times U(1)_Y \times}$ $\mathbb{Z}_2 \times \mathbb{Z}_3$ symmetry, is given by

$$\begin{aligned} \mathcal{L}_{\rm BSM} \;\supset\; & \frac{i}{2}\left(\sum_{\beta=1}^{3} \mathrm{Tr}[\overline{\Sigma_{\beta_R}}\, \not{D} \Sigma_{\beta_R}] + \mathrm{Tr}[\overline{\Sigma_{\beta_R}{}^c}\, \not{D} \Sigma_{\beta_R}{}^c]\right) - \left(\sum_{\alpha,\,\beta=1}^{3} \frac{1}{2}\, \mathrm{Tr}[\overline{\Sigma_{\alpha R}{}^c}\, \sqrt{2}\, y_s^{\alpha\beta}\, \Sigma_{\beta_R}]\, S'^\dagger + h.c.\right) \\ & - \left(\sum_{\alpha,\,\beta=1}^{3} y_\Sigma^{\alpha\beta}\, \overline{l_{\alpha L}} \Sigma_{\beta_R} \tilde{\Phi} + h.c.\right) + \mathcal{L}_{\rm scalar}(H,\, \Phi,\, S')\,, \end{aligned} \tag{4.5}$$

where $\tilde{\Phi} = i\sigma_2\Phi^\star$ and the Lagrangian for the scalar fields are given by

$$\begin{aligned}\mathcal{L}_{\rm scalar}(H,\,\Phi,\,S') &= (D_\mu H)^\dagger\,(D^\mu H) + (D_\mu\Phi)^\dagger\,(D^\mu\Phi) + \partial_\mu S'^\dagger\,\partial^\mu S' + \mu_H^2\,H^\dagger H - \lambda_H\,\left(H^\dagger H\right)^2 \\ &- \mu_2^2\,\Phi^\dagger\Phi - \lambda_2(\Phi^\dagger\Phi)^2 + \mu_s^2\,S'^\dagger S' - \mu_3\left(S'^3 + S'^{\dagger 3}\right) - \lambda_s\left(S'^\dagger S'\right)^2 \\ &- \lambda_3\left(H^\dagger H\right)\left(\Phi^\dagger\Phi\right) - \lambda_4\left(H^\dagger\Phi\right)\left(\Phi^\dagger H\right) - \frac{\lambda_5}{2}\left((H^\dagger\Phi)^2 + h.c.\right) \\ &- \lambda_6\left(H^\dagger H\right)\left(S'^\dagger S'\right) - \lambda_7\left(\Phi^\dagger\Phi\right)\left(S'^\dagger S'\right)\,. \end{aligned} \tag{4.6}$$

where $S' = \dfrac{h_2 + i\,\zeta}{\sqrt{2}}$, h_2 and ζ are the real and imaginary parts of S' respectively while $H = \begin{pmatrix} 0 & \frac{h_1+v}{\sqrt{2}}\end{pmatrix}^T$ is the SM Higgs doublet in the unitary gauge. Following the procedure given in the Appendix C.1, we can write the triplet Lagrangian in terms of $\psi_\beta^- = \Sigma_{\beta\,R}^- + \Sigma_{\beta\,R}^{+\,c}$ and $\psi_\beta^0 = \Sigma_{\beta\,R}^0 + \Sigma_{\beta\,R}^{0\,c}$ as

$$\begin{aligned}\mathcal{L}_{\rm BSM} \supset & \sum_{\beta=1}^{3}\overline{\psi_\beta^-}\,i\,\partial\!\!\!/\psi_\beta^- + \frac{1}{2}\overline{\psi_\beta^0}i\,\partial\!\!\!/\psi_\beta^0 - \left(\sum_{\alpha,\,\beta=1}^{3} y_s^{\alpha\beta}\,\overline{\psi_\alpha^-}\,\psi_\beta^- + \frac{y_s^{\alpha\beta}}{2}\,\overline{\psi_\alpha^0}\,\psi_\beta^0\right)h_2 \\ & -i\left(\sum_{\alpha,\,\beta=1}^{3} y_s^{\alpha\beta}\,\overline{\psi_\alpha^-}\gamma_5\,\psi_\beta^- + \frac{y_s^{\alpha\beta}}{2}\,\overline{\psi_\alpha^0}\gamma_5\,\psi_\beta^0\right)\zeta - g\left(\overline{\psi_\beta^-}\gamma^\mu\,\psi_\beta^0\,W_\mu^- + h.c.\right) \\ & + g\,\cos\theta_w\,\overline{\psi_\beta^-}\gamma_\mu\psi_\beta^-\,Z^\mu + g\,\sin\theta_w\,\overline{\psi_\beta^-}\gamma_\mu\psi_\beta^-\,A^\mu \\ & -\Bigg[\sum_{\alpha,\,\beta=1}^{3} y_\Sigma^{\alpha\beta}\left(\frac{1}{\sqrt{2}}\overline{\nu_{\alpha L}}\,P_R\psi_\beta^0 + \overline{e_{\alpha L}}\,P_R\psi_\beta^-\right)\left(\frac{\phi^0 - i\,A^0}{\sqrt{2}}\right) - y_\Sigma^{\alpha\beta}\,\overline{P_L\,\psi_\beta^-}\,\nu_{\alpha\,L}{}^c\,\phi^- \\ & + \frac{y_\Sigma^{\alpha\beta}}{\sqrt{2}}\overline{e_{\alpha L}}P_R\psi_\beta^0\,\phi^- + h.c.\Bigg] + \mathcal{L}_{\rm scalar}(H,\,\Phi,\,S')\,. \end{aligned} \tag{4.7}$$

As mentioned earlier, when the real part of S' gets VEV v_s, the mass terms for both ψ_α^- and ψ_α^0 are generated from the third and fourth terms of the above Lagrangian as $M_\psi^{\alpha\beta} = y_s^{\alpha\beta}\,v_s$. For simplicity, we have assumed that $M_\psi^{\alpha\beta}$ is a diagonal matrix with real and nonzero elements. Therefore, both ψ_α^0 and ψ_α^- are representing the physical states and the lightest neutral fermion ψ_1^0 can be our DM candidate with mass $M_{\psi_1^0} = y_s\,v_s$ [2]. Furthermore, the first term within the square bracket is responsible for tiny neutrino mass generation at one loop level. We will have a detailed discussion on this topic in the next section (Section 4.2.3). After $\mathrm{SU(2)_L \times U(1)_Y \times \mathbb{Z}_3}$ symmetry breaking, the mass terms for the components of inert Higgs doublet are

$$M_{\phi^\pm}^2 = \mu_2^2 + \frac{1}{2}\left(\lambda_3 v^2 + \lambda_7 v_s^2\right)\,, \tag{4.8}$$

$$M_{A^0}^2 = \mu_2^2 + \frac{1}{2}\left[(\lambda_3 + \lambda_4 - \lambda_5)v^2 + \lambda_7 v_s^2\right]\,, \tag{4.9}$$

$$M_{\phi^0}^2 = \mu_2^2 + \frac{1}{2}\left[(\lambda_3 + \lambda_4 + \lambda_5)v^2 + \lambda_7 v_s^2\right]\,. \tag{4.10}$$

[2] For notational simplicity we choose $y_s^{11} = y_s$.

On the other hand, after symmetry breaking there will be a mixing between the real scalar fields of H and S'. The mixing matrix with respect to the basis $(h_1,\, h_2)$ is given by

$$\mathcal{M}^2_{\rm scalar} = \begin{pmatrix} 2\,\lambda_H v^2 & \lambda_6\, v\, v_s \\ \lambda_6\, v\, v_s & 2\,\lambda_s v_s^2 + \dfrac{3\,\mu_3\, v_s}{\sqrt{2}} \end{pmatrix} . \tag{4.11}$$

Clearly, h_1 and h_2 do not represent physical fields. However, after diagonalising the above mass matrix, one can have two physical scalar fields h and S, which are two orthogonal linear combinations of h_1, h_2 and the corresponding mixing angle is given by

$$\tan 2\xi = \frac{\lambda_6\, v\, v_s}{\lambda_H\, v^2 - \lambda_s\, v_s^2 - \frac{3\,\mu_3\, v_s}{2\sqrt{2}}} . \tag{4.12}$$

We consider h is the SM-Like Higgs boson which was discovered at the LHC [407, 408]. The mass of the pseudo scalar ζ is given by

$$M^2_\zeta = -\frac{3\,\mu_3\, v_s}{\sqrt{2}} , \tag{4.13}$$

where we need $\mu_3 < 0$ for $M^2_\zeta > 0$. The trilinear terms of S' and $S'^\dagger$ allowed by $\mathbb{Z}_3$ symmetry play a crucial role in generating the mass term for the imaginary part of S' after spontaneous symmetry breaking of $\mathbb{Z}_3$. As a result, we can choose the mass of the pseudo scalar (ζ) different than S and also heavier compared to the mass of our DM candidate ψ^0_1, so that it will not affect the relic density of ψ^0_1. From equations (4.13), one can easily find that M_ζ will be heavier than our DM candidate ψ^0_1 when $\mu_3 < -\dfrac{\sqrt{2}\, M^2_{\psi^0_1}}{3\, v_s}$. Now, using $M_{\psi^0_1} = y_s v_s$, we can rewrite the above limit on μ_3 as $\mu_3 < -\dfrac{\sqrt{2}\, y_s^2}{3} v_s$. On the other hand, since μ_3 acts oppositely to the expression of M_s, therefore one can also find a lower bound on self coupling λ_s from the requirement of $M_s > 0$. Therefore, under the approximation of small mixing angle ξ, the quartic coupling λ_s must be greater than $\dfrac{y_s^2}{2}$. In Sections 4.2.4 and 4.2.7, we have considered $y_s = 1.5$ for $M_{\psi^0_1} = 1$ TeV and hence we need $\mu_3 < -707.11$ GeV and $\lambda_s > 1.13$. One thing we want to note here that the considered hierarchy $M_\zeta > M_{\psi^0_1} > M_s$ is solely for the calculational simplification. There may be a situation when $M_{\psi^0_1} > M_\zeta, M_s$, where our DM candidate can annihilate to both ζ as well as S and in that case due to the extra annihilation modes, the thermal contribution to DM relic abundance will be even less compared to the present scenario. The main difference between the minimal model discussed in the previous section and the present model is that here, our DM candidate ψ^0_1, after its thermal freeze-out, gets some non-thermal contribution to the relic abundance mainly from the decay of ϕ^0. This eventually compensates the under abundance of ψ^0_1 in low mass regime $M_{\psi_1} \lesssim 2$ TeV. We also consider the mass of ϕ^0 to be smaller than the heavier cousins of Σ_{1R} so that ϕ^0 decays preferentially to the DM candidate only. This is also important from the point of view of neutrino mass (as we discuss in the next section) because the couplings of $\Sigma_{2R,3R}$ with Φ and SM leptons have to be sizeable in order to generate the correct one loop neutrino mass at sub-eV. Therefore, if $\Sigma_{2R,3R}$ are lighter than Φ, then ϕ^0 will also decay

into these triplets reducing the branching ratio into the DM candidate Σ_{1R}, falling short of providing the required non-thermal contribution. We will discuss in great detail about the thermal as well as non-thermal contributions to the relic density of our DM candidate in Section 4.2.4.

4.2.3 Neutrino mass generation at one loop

In the present model since we have imposed both $\mathbb{Z}_2$ as well as $\mathbb{Z}_3$ charges to all three fermion triplets Σ_{β_R}, neutrino masses can not be generated via tree level Type-III seesaw mechanism. However, in this model we have an inert doublet Φ which is also odd under $\mathbb{Z}_2$ symmetry. Hence we can write a Yukawa interaction term involving fermion triplet Σ_{β_R} inert doublet Φ and SM lepton doublet $l_{\alpha L}$. Such term will be automatically $\mathbb{Z}_2$ invariant. However, $\mathbb{Z}_3$ invariance requires same $\mathbb{Z}_3$ charge to SM leptons as well since Φ does not have any $\mathbb{Z}_3$ charge. Because, any nonzero $\mathbb{Z}_3$ charge of Φ, other than unity, will forbid the mass splitting between A^0 and ϕ^0, which is $\lambda_5 v^2$ (see equations (4.9 and 4.10)). Later in this section, we will see that the light neutrino masses are proportional to the mass splitting between A^0 and ϕ^0, hence we cannot impose any non-trivial $\mathbb{Z}_3$ charge to Φ. Therefore, in this work as mentioned in the previous section, we choose $\mathbb{Z}_3$ charge of Σ_{β_R} and $l_{\alpha L}$ is ω^2. The Yukawa interaction terms invariant under both continuous and discrete symmetries of the model are given as

$$\begin{aligned}
\mathcal{L}_{\text{Yukawa}} \supset & -\sum_{\alpha,\beta=1}^{3} y_\Sigma^{\alpha\beta}\,\overline{l_{\alpha L}}\Sigma_{\beta_R}\tilde{\Phi} + h.c.\,, \\
& -\sum_{\alpha,\beta=1}^{3} y_\Sigma^{\alpha\beta}\left(\frac{1}{\sqrt{2}}\overline{\nu_{\alpha L}}\,P_R\psi_\beta^0 + \overline{e_{\alpha L}}\,P_R\psi_\beta^-\right)\left(\frac{\phi^0 - i\,A^0}{\sqrt{2}}\right) - y_\Sigma^{\alpha\beta}\,\overline{P_L\,\psi_\beta^-}\,\nu_{\alpha L}{}^c\,\phi^- \\
& + \frac{y_\Sigma^{\alpha\beta}}{\sqrt{2}}\overline{e_{\alpha L}}P_R\psi_\beta^0\,\phi^- + h.c.\,,
\end{aligned} \tag{4.14}$$

where we have used the definition of ψ_β^- and ψ_β^0 give in Appendix C.1. As discussed in previous section, the first term in the above Lagrangian is responsible for neutrino mass generation in one loop level following the scotogenic model [12]. The Feynman diagram for neutrino mass generation at one loop level is shown in figure 4.1. In figure 4.1, we have

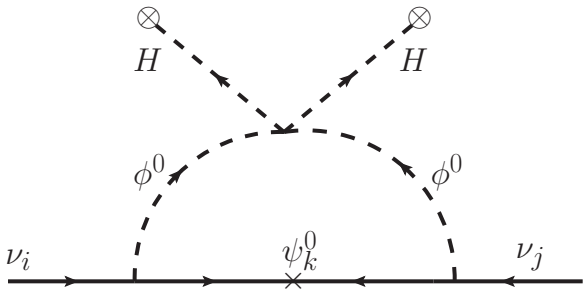

Figure 4.1: Feynman diagram of neutrino mass generation at one loop.

drawn the diagram with ϕ^0 as an intermediate loop particle. However, the same diagram

with ϕ^0 replaced by pseudo scalar A^0 is also possible. These two diagrams will differ by a -ve sign which actually helps us to cancel the divergences of both diagrams. The expression of neutrino mass is then given by [12]

$$\mathcal{M}_\nu{}^{\alpha\beta} = \sum_\rho \frac{y_\Sigma^{\alpha\rho}\, y_\Sigma^{\beta\rho}\, M_{\psi_\rho^0}}{64\pi^2} \left(\frac{M_{\phi^0}^2}{M_{\phi^0}^2 - M_{\psi_\rho^0}^2} \ln \frac{M_{\phi^0}^2}{M_{\psi_\rho^0}^2} - \frac{M_{A^0}^2}{M_{A^0}^2 - M_{\psi_\rho^0}^2} \ln \frac{M_{A^0}^2}{M_{\psi_\rho^0}^2} \right) . \tag{4.15}$$

Now, if we consider the mass splitting between M_A^0 and M_{ϕ^0} is small compared to $(M_A^0 + M_{\phi^0})/2$, which is indeed true for our work (see Section 4.2.4), the expression for $\alpha\beta$ element of neutrino mass matrix simplifies to

$$\mathcal{M}_\nu{}^{\alpha\beta} = \frac{\lambda_5\, v^2}{64\pi^2} \sum_\rho \frac{y_\Sigma^{\alpha\rho}\, y_\Sigma^{\beta\rho}\, M_{\psi_\rho^0}}{M_0^2 - M_{\psi_\rho^0}^2} \left(1 - \frac{M_{\psi_\rho^0}^2}{M_0^2 - M_{\psi_\rho^0}^2} \ln \frac{M_0^2}{M_{\psi_\rho^0}^2} \right) , \tag{4.16}$$

where $M_0^2 = (M_A^0 + M_{\phi^0})/2$ and $M_{A^0}^2 - M_{\phi^0}^2 = \lambda_5\, v^2$ using equations (4.9 and 4.10). It should be noted that the requirement for non-thermal contribution to DM candidate in our model constrains the Yukawa couplings of the lightest fermion triplet with the SM leptons to be very small $y_\Sigma^{11} \approx y_\Sigma^{21} \approx y_\Sigma^{31} \leq 10^{-9}$, as we discuss in details below. As can be seen from the one loop neutrino mass formula given above, such tiny couplings will practically have a negligible contribution to light neutrino masses. This makes the lightest fermion triplet to effectively decouple from the neutrino mass generation mechanism giving rise to one almost massless and two massive light neutrinos which can be tested at experiments which are sensitive to the absolute mass scale of neutrinos.

4.2.4 Relic Abundance of dark matter candidate Σ_{1R}^0 in Scotogenic FTDM

To compute the relic abundance of a DM candidate, one has to find the value of comoving number density of DM species at the present epoch, which can be found by solving the corresponding Boltzmann equation for the DM candidate we are considering i.e. ψ_1^0. Moreover, while solving the Boltzmann equation for ψ_1^0, we need to have the information about the comoving number densities of other particles which are not in thermal equilibrium but have significant impact on the production processes of ψ_1^0. In other words, we need to solve a system of coupled Boltzmann equations for all the out of equilibrium particles. The coupled

Boltzmann equations for our present scenario are given by

$$\frac{dY_{\psi_1^0}}{dx} = -\left(\frac{45\,G}{\pi}\right)^{-1/2}\frac{M_{sc}}{x^2}\sqrt{g_\star}\,\langle\sigma\mathrm{v}\rangle_{\rm Triplet}\left(Y^2_{\psi_1^0}-(Y^{eq}_{\psi_1^0})^2\right) + \left(\frac{4\pi^3 G}{45}\right)^{-1/2}\frac{x}{M_{sc}^2}\frac{\sqrt{g_\star}}{g_s}\left(\langle\Gamma_{\phi^0\to\psi_1^0}\rangle\; Y_{\phi^0}+2\,\langle\Gamma_{\psi_1^\pm\to\psi_1^0}\rangle\; Y_{\psi_1^-}\right), \tag{4.17}$$

$$\frac{dY_{\phi^0}}{dx} = -\left(\frac{45\,G}{\pi}\right)^{-1/2}\frac{M_{sc}}{x^2}\sqrt{g_\star}\,\langle\sigma\mathrm{v}\rangle_{\rm IDM}\left(Y^2_{\phi^0}-(Y^{eq}_{\phi^0})^2\right) - \left(\frac{4\pi^3 G}{45}\right)^{-1/2}\frac{x}{M_{sc}^2}\frac{\sqrt{g_\star}}{g_s}\langle\Gamma^{\rm Total}_{\phi^0}\rangle\; Y_{\phi^0}\,, \tag{4.18}$$

$$\frac{dY_{\psi_1^-}}{dx} = \left(\frac{4\pi^3 G}{45}\right)^{-1/2}\frac{x}{M_{sc}^2}\frac{\sqrt{g_\star}}{g_s}\left(\langle\Gamma_{\phi^0\to\psi_1^-}\rangle\; Y_{\phi^0}-\langle\Gamma_{\psi_1^-\to\psi_1^0}\rangle\; Y_{\psi_1^-}\right), \tag{4.19}$$

where, M_{sc} is some arbitrary mass scale and here we have considered $M_{sc}=M_{\psi_1^0}$. The first Boltzmann equation describes the evolution of comoving number density of ψ_1^0 where the first term in the R.H.S. represents the thermal WIMP contribution to $Y_{\psi_1^0}$ coming from the annihilations and co-annihilations among the ψ_1^0 and $\psi_1^\pm$. As mentioned earlier, since the mass splitting between $\psi_1^\pm$ and ψ_1^0 is $\sim\mathcal{O}(100\,\mathrm{MeV})$, the effect of co-annihilations [282, 283] is significant to $Y_{\psi_1^0}$. In equation (4.17), $\langle\sigma\mathrm{v}\rangle_{\rm Triplet}$ is the thermally averaged cross section for the annihilation and co-annihilation channels which are contributing significantly to the freeze-out process of ψ_1^0. The Feynman diagrams of these processes are shown in figure 4.2. It is worth mentioning that we are not taking any non-perturbative effects on DM annihilations into account here which is justified by the fact that such effects are small for DM masses in the sub TeV regime [390,391]. This is in fact, another motivation for confining our discussion to the sub-TeV mass regime of DM. Here, we have considered the mass difference between ψ_1^0 and other heavier triplet fermions (ψ_β^0, $\psi_\beta^\pm$, $\beta=2,\,3$) to be large so that the co-annihilations of these heavier triplet fermions do not affect the freeze-out process of ψ_1^0.

The second term in the R.H.S. of equation (4.17), which appears with an opposite sign to the first one, is the non-thermal contributions to $Y_{\psi_1^0}$ coming from the decays of ϕ^0 and $\psi_1^\pm$ and the corresponding thermal averaged decay widths are indicated by $\langle\Gamma_{\phi^0\to\psi_1^0}\rangle$ and $\langle\Gamma_{\psi_1^\pm\to\psi_1^0}\rangle$ respectively. The general expression of thermal averaged decay width for a decay process $A\to B\,C$ is $\langle\Gamma_{A\to B\,C}\rangle=\Gamma_{A\to B\,C}\dfrac{K_1(\frac{M_A}{T})}{K_2(\frac{M_A}{T})}$, where M_A is the mass of the mother particle A and K_n is the nth order Modified Bessel function of second kind. These non-thermal contributions proportional to the thermal averaged decay widths $\langle\Gamma_{\phi^0\to\psi_1^0}\rangle$ and $\langle\Gamma_{\psi_1^\pm\to\psi_1^0}\rangle$ respectively, are effective only after the freeze-out of ψ_1^0 before which ψ_1^0 has equilibrium number density governed by the Maxwell-Boltzmann distribution function. The decay of $\phi^0\to\psi_1^0\,\nu$ is due to the Yukawa interaction (first term within the square bracket of equation (4.7)), which is also responsible for the neutrino mass generation radiatively, while the decay of $\psi_1^\pm\to\psi_1^0\,\pi^\pm$ is possible due to an $\mathcal{O}(100\,\mathrm{MeV})$ mass splitting between $\psi_1^\pm$ and ψ_1^0. Although, $\psi_1^\pm$ has some three-body decay modes like $\psi_1^{+(-)}\to\psi_1^0+\bar{l}(l)+\nu(\bar{\nu})$ and $\psi_1^{+(-)}\to\psi_1^0+u(\bar{u})+\bar{d}(d)$, $\psi_1^\pm\to\psi_1^0\,\pi^\pm$ is the dominant decay mode of charged fermion $\psi_1^\pm$ with nearly 97% branching

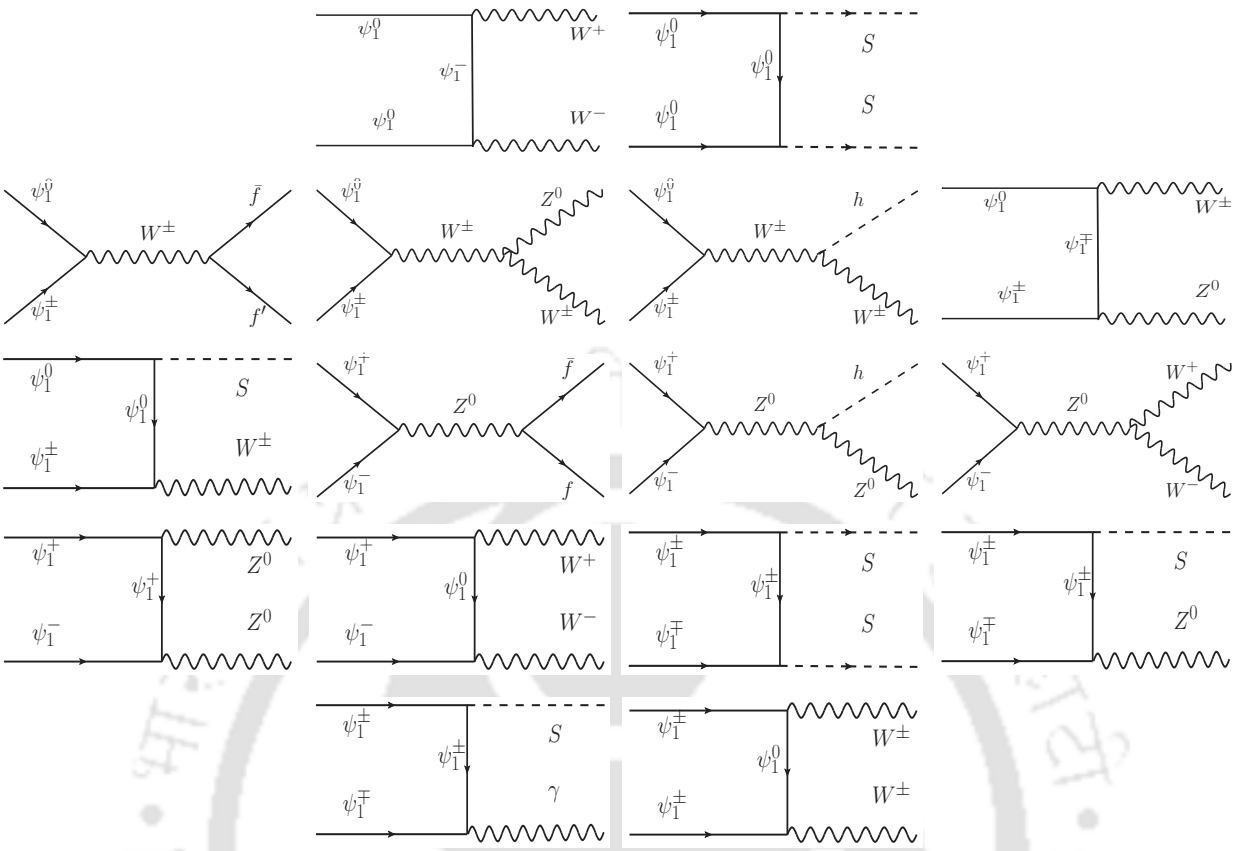

Figure 4.2: Feynman diagrams for all possible annihilation and co-annhilation channels. Two diagrams in first row are annihilation of ψ_1^0 while rest are co-annihilations.

ratio [329]. The expression of decay width for $\psi_1^\pm \to \psi_1^0 \pi^\pm$ is given by

$$\Gamma_{\psi_1^\pm \to \psi_1^0} = \frac{g^4 f_\pi^2 V_{ud}^2}{128\pi M_W^4 M_{\psi_1^\pm}} \Delta M^2_{\text{triplet}} \left((M_{\psi_1^0} + M_{\psi_1^\pm})^2 - M_\pi^2 \right) \times \sqrt{1 - \frac{(M_{\psi_1^0} - M_\pi)^2}{M^2_{\psi_1^\pm}}} \sqrt{1 - \frac{(M_{\psi_1^0} + M_\pi)^2}{M^2_{\psi_1^\pm}}}, \tag{4.20}$$

where $\Delta M_{\text{triplet}} = M_{\psi_1^\pm} - M_{\psi_1^0} \simeq 166$ MeV, g is the $\text{SU}(2)_\text{L}$ gauge coupling, the pion decay constant $f_\pi = 131$ MeV [329] and the first diagonal element of the CKM matrix $V_{ud} \simeq 0.974$ respectively. Since we have assumed that there is no asymmetry between the comoving number densities of ψ_1^+ and ψ_1^- and decay widths $\Gamma_{\psi_1^- \to \psi_1^0} = \Gamma_{\psi_1^+ \to \psi_1^0} = \Gamma_{\psi_1^\pm \to \psi_1^0}$, the non-thermal contribution arising from the decays of ψ_1^+ and ψ_1^- are equal. Therefore, without explicitly showing the contribution of ψ_1^+ in $Y_{\psi_1^0}$, we have multiplied the term for ψ_1^- in equation (4.17) by a factor of 2.

The second Boltzmann equation in equation (4.18), is the evolution equation for ϕ_0. In the R.H.S. of this equation, the first term is the collision term due to the annihilation and co-annihilation processes among the components of inert doublet Φ. These processes were in both thermal as well as chemical equilibrium in the early Universe and the lightest

neutral component ϕ^0 of Φ freezes-out when these interaction rates become less than the expansion rate of the Universe, which is governed by the Hubble parameter $\mathbf{H}(T)$. The effective annihilation cross section, which we have denoted by $\langle\sigma \mathrm{v}\rangle_{\mathrm{IDM}}$ for ϕ^0 and $\langle\sigma \mathrm{v}\rangle_{\mathrm{Triplet}}$ for ψ_1^0 respectively, can be expressed as a weighted sum of individual annihilation and co-annihilation cross sections [282]. We have calculated $\langle\sigma \mathrm{v}\rangle_{\mathrm{IDM}}$ using `micrOMEGAs` package [384]. In the present scenario, although ϕ^0 has a $\mathbb{Z}_2$ charge, it is not the lightest $\mathbb{Z}_2$-odd particle in the model. Hence, it can decay to other lighter $\mathbb{Z}_2$-odd particles such as $\psi_1^\pm$, ψ_1^0 [3]. These decay modes further decrease the number density of ϕ^0 after its thermal freeze-out and this effect has been included in the Boltzmann equation of ϕ^0 by the second term in the R.H.S. of equation (4.18), which is, as expected, proportional to the total decay width $\Gamma_{\phi^0}^{\mathrm{Total}}$ of ϕ^0. Finally, equation (4.19) is the Boltzmann Equation for ψ_1^-. As we know that after the freeze-out of ψ_1^0, the abundance of $\psi_1^\pm$ is zero. However, $\psi_1^\pm$ can again be produced from the late decay of ϕ^0 and those $\psi_1^\pm$ eventually decay to ψ_1^0 and contribute to the non-thermal abundance of ψ_1^0. In the R.H.S. of equation (4.19), the first term is the production term of ψ_1^- from the decay of ϕ^0 while the second one with an opposite sign is the depletion term of ψ_1^-. Like ψ_1^-, one can also write a same Boltzmann equation for ψ_1^+ as well, however since both ψ_1^+ and ψ_1^- have identical interactions with other particles and also we have assumed that there is no asymmetry in the initial number densities of ψ_1^+ and ψ_1^-, hence we do not need to solve an extra Boltzmann equation similar to equation (4.19) for ψ_1^+. Ultimately, we have solved three coupled Boltzmann equations given in equations (4.17-4.19) numerically to find the comoving number density $Y_{\psi_1^0}(T_0)$ of ψ_1^0 at the present epoch, which contains both thermal as well as non-thermal contributions. Finally, the relic density of our DM candidate ψ_1^0 can be computed from the value of $Y_{\psi_1^0}(T_0)$ using the following relation [283]

$$\Omega_{\psi_1^0} h^2 = 2.755 \times 10^8 \left(\frac{M_{\psi_1^0}}{\mathrm{GeV}}\right) Y_{\psi_1^0}(T_0) \ , \tag{4.21}$$

where $T_0 \simeq 2.73$ K, the present temperature of the Universe.

In the left panel of figure 4.3, we show the variation of comoving number densities of ϕ^0, ψ_1^0 and $\psi_1^\pm$ with $x = \dfrac{M_{\psi_1^0}}{T}$. Here, the variation of Y_{ϕ^0} is denoted by green solid line and as mentioned above due to the finite decay width $\Gamma_{\phi^0}^{\mathrm{Total}}$, the comoving number density of ϕ^0, instead of becoming a constant with temperature T, decreases sharply after its freeze-out. Due to this decrement of Y_{ϕ^0} there is an increment in $Y_{\psi_1^0}$ denoted by red solid line as more and more ψ_1^0 are being produced from the decay of ϕ^0 after the thermal freeze-out of ψ_1^0. In this figure, the evolution of $\psi_1^\pm$ is denoted by blue solid line, which gets produced from the decay of ϕ^0 at around $x \sim 25$ and eventually $Y_{\psi_1^\pm}$ becomes negligibly small after having a minute contribution to $Y_{\psi_1^0}$. This plot has been drawn for $M_{\psi_1^0} = 1$ TeV, $M_{\phi^0} = 2$ TeV, $M_s = 200$ GeV, $\Delta M = M_{A^0} - M_{\phi^0} = M_{\phi^\pm} - M_{\phi^0} = 4$ GeV [4], $y_s = 1.5$ and $y_\Sigma = 0.854 \times 10^{-9}$ [5]. In absence of any non-thermal contribution from the decay of ϕ^0, the thermal abundance of ψ_1^0 is denoted by a cyan dashed line, which clearly shows the under abundance of ψ_1^0 for $M_{\psi_1^0} = 1$ TeV due to its large annihilations and co-annihilations. In the right panel of

[3] Here we have assumed other triplet fermions are heavier than ϕ^0.

[4] In this work, we have assumed $M_{\phi^\pm} = M_{A^0}$, which is possible if $\lambda_4 = \lambda_5$.

[5] For simplicity we have assumed Yukawa couplings $y_\Sigma^{11} = y_\Sigma^{21} = y_\Sigma^{31} = y_\Sigma$.

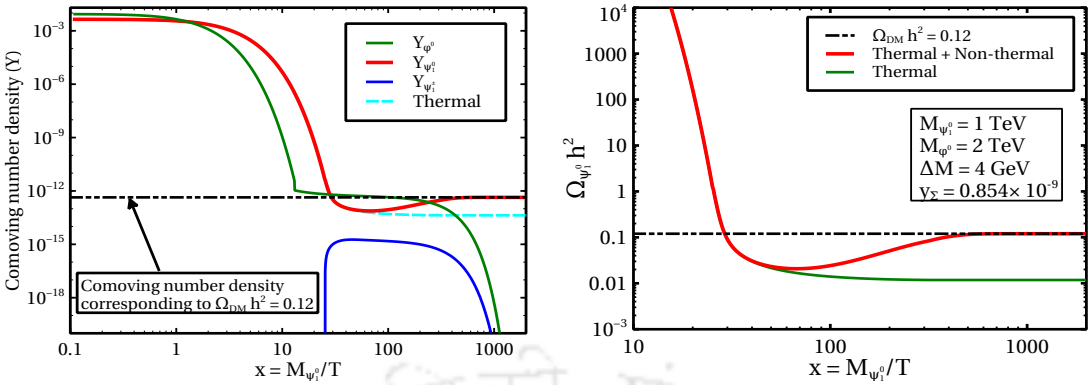

Figure 4.3: Left panel: Solution of coupled Boltzmann equations given in equations (4.17)-(4.19) for a particular benchmark point $M_{\psi_1^0} = 1$ TeV, $M_{\phi^0} = 2$ TeV, $M_s = 200$ GeV, $\Delta M = 4$ GeV, $y_\Sigma = 0.854 \times 10^{-9}$ and $y_s = 1.5$. Right panel: Relic density of ψ_1^0 for thermal interactions ($y_\Sigma = 0$) and thermal plus non-thermal interactions ($y_\Sigma = 0.854 \times 10^{-9}$).

figure 4.3, we plot the variation of relic abundance of ψ_1^0 with x for the same benchmark point mentioned above. Here, the green solid line represents the relic abundance of ψ_1^0 due to thermal freeze-out only for $M_{\psi_1^0} = 1$ TeV, i.e. the relic abundance of ψ_1^0 by considering its all possible annihilation and co-annihilation channels as shown in figure 4.2. From this figure it is clearly seen that for this benchmark point the thermal contribution, which is contributing only around $\sim 10\%$ of the *canonical value* $\Omega_{\rm DM}h^2 = 0.12$, is not enough to reproduce the correct DM relic abundance. Hence there is need of an additional non-thermal contribution from the decay of ϕ^0 to compensate this deficit. Total abundance of ψ_1^0 including contributions from both thermal and non-thermal processes is shown by red solid line.

In figure 4.4 we show how $\Omega_{\psi_1^0}h^2$ varies with the mass of ψ_1^0. In this plot, green dotted line is for the pure FTDM model [330] (discussed in Section 4.2.1) and it is clearly seen that in this model relic density of ψ_1^0 satisfies the Planck limit for $M_{\psi_1^0} \sim 2.2$ TeV which is consistent with the Ref. [330]. The blue dashed dotted line is for the present model without any non-thermal contribution to relic density i.e. Yukawa coupling $y_\Sigma = 0$. The difference between this case with the pure FTDM is that here we have extra annihilation and co-annihilation channels involving one or two S in the final states. In this case, we have chosen $M_s = 200$ GeV and $y_s = 1.5$. Hence, the relic density of ψ_1^0 for a particular mass $M_{\psi_1^0}$ is further suppressed. This is clearly evident from figure 4.4. Finally, the red solid line represents variation of DM relic density, which has both thermal as well as non-thermal contributions, for $\Delta M = 4$ GeV, $M_{\phi^0} = 2$ TeV, $M_s = 200$ GeV, $y_\Sigma = 0.854 \times 10^{-9}$ and $y_s = 1.5$. Moreover, it also shows that for the chosen benchmark point the relic density of triplet fermion ψ_1^0 satisfies the Planck limit for a mass as low as $M_{\psi_1^0} = 1$ TeV. Please note that the plot shown in figure 4.4 is for illustrative purposes only in order to show the difference between possible scenarios discussed here. We have not taken non-perturbative effects into account in DM annihilations which can be significant if we go to high mass regime beyond 1 TeV. If we take them into account, as discussed by the authors of [390, 391], the point in the green and the blue lines where correct relic is satisfied will shift further towards right.

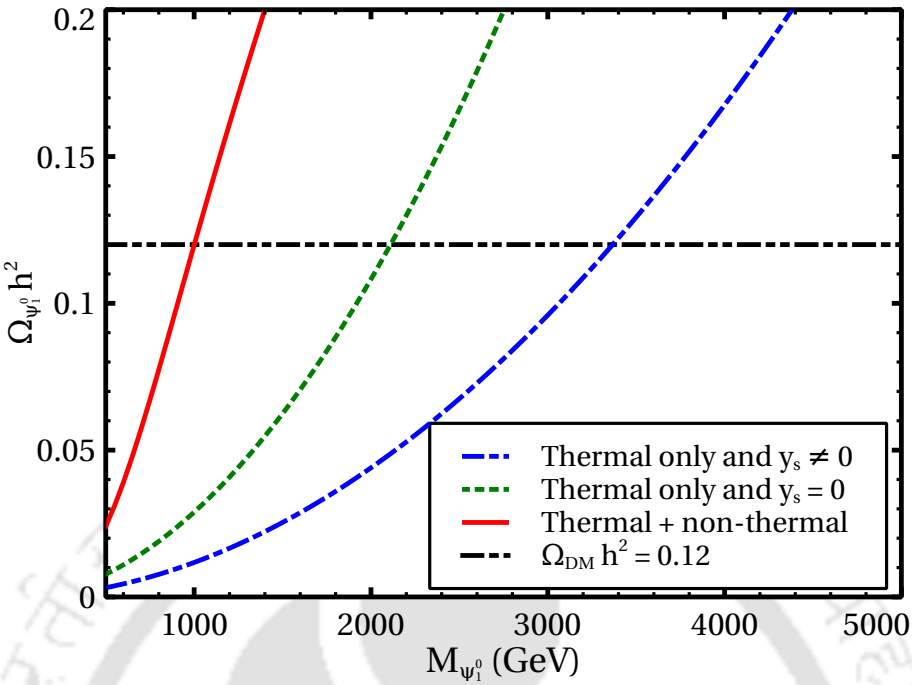

Figure 4.4: Variation of $\Omega_{\psi_1^0} h^2$ with $M_{\psi_1^0}$.

Now, we will present the effect of four model parameters on $Y_{\psi_1^0}$. These four model parameters have significant impacts on the non-thermal contributions to $Y_{\psi_1^0}$. While generating the four plots, we have kept fixed the other parameters (expect the particular one which has been varied) to the same benchmark point we have used to generate figure 4.3. In figure 4.5(a), we show the variation of $Y_{\psi_1^0}$ with x for four different values of $\Delta M = M_{\phi^\pm} - M_{\phi^0} = M_{A^0} - M_{\phi^0}$. From this plot it is seen that the value of $Y_{\psi_1^0}$, after the thermal freeze-out of ψ_1^0, increases as we decrease the mass splitting between ϕ^0 and other components of inert doublet Φ i.e. $\phi^\pm$ and A^0 [6]. This can be understood as follows. From the inert doublet DM model [290, 389, 409–413] we know that the abundance ϕ^0 increases as ΔM decreases and it is due to the cancellation between four point diagram and t, u channel diagrams for annihilation channels of ϕ^0 into gauge boson final states W^+W^-, ZZ and this is also true for the co-annihilation channels of inert scalars. Now, similarly here also Y_{ϕ^0} increases with decreasing ΔM. Again, from equation (4.17) one can easily notice that the non-thermal contribution to $Y_{\psi_1^0}$ coming from the decay of ϕ^0 is proportional to Y_{ϕ^0}. Hence $Y_{\psi_1^0}$ also increases as we decrease the mass splitting ΔM. The dependence of $Y_{\psi_1^0}$ on M_{ϕ^0} is shown in figure 4.5(b), where we have considered four different values of M_{ϕ^0}. From this plot, we see that $Y_{\psi_1^0}$ keeps on increasing as we lower the mass of ϕ^0. This is due to the fact that the non-thermal contribution to $Y_{\psi_1^0}$ is proportional to two quantities. One is the abundance of ϕ^0 during the decay to ψ_1^0, which occurs after the freeze-out of ϕ^0 (see left panel of figure 4.3) and other one is the corresponding decay width $\Gamma_{\phi^0 \to \psi_1^0}$. The behaviour of these two quantities are opposite with respect to M_{ϕ^0}. While decay width $\Gamma_{\phi^0 \to \psi_1^0}$ is proportional to M_{ϕ^0}, the comoving number density of ϕ^0 is less and becomes more suppressed for heavier

[6] In this work, for simplicity we choose $M_{\phi^\pm} = M_{A^0}$.

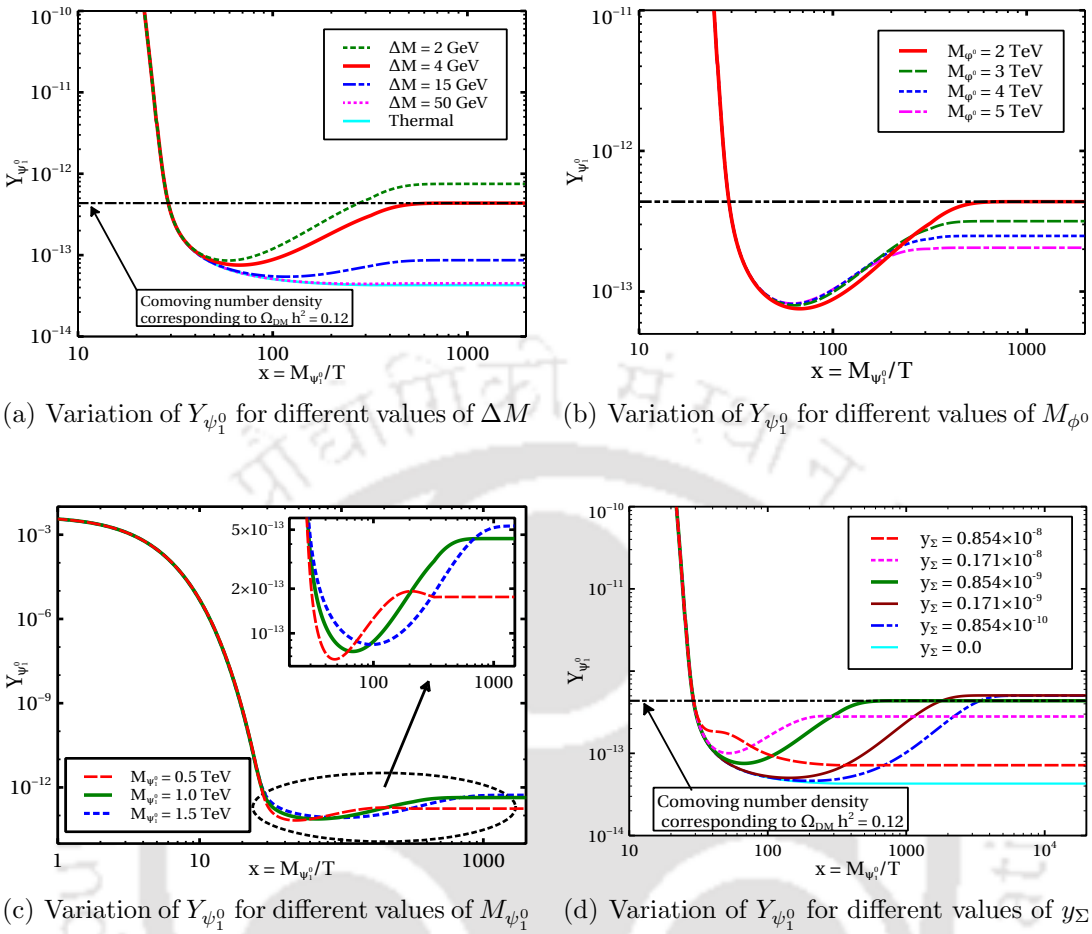

(a) Variation of $Y_{\psi_1^0}$ for different values of ΔM (b) Variation of $Y_{\psi_1^0}$ for different values of M_{ϕ^0}

(c) Variation of $Y_{\psi_1^0}$ for different values of $M_{\psi_1^0}$ (d) Variation of $Y_{\psi_1^0}$ for different values of y_Σ

Figure 4.5: Comparison of $Y_{\psi_1^0}$ with respect to different model parameters.

ϕ^0 during the period when maximum decay to ψ_1^0 occurs. This is because, primarily the comoving number density of ϕ^0 after its freeze-out is less for higher value of M_{ϕ^0} (valid for a fixed value of ΔM and $M_{\phi^0} \gtrsim 1$ TeV) and additionally the total decay width $\Gamma_{\phi^0}^{\text{Total}}$ of ϕ^0 which gets enhanced with M_{ϕ^0}, has a negative impact on Y_{ϕ^0} (see equation (4.18)), which further reduces Y_{ϕ^0} with respect to M_{ϕ^0} in the considered range. Therefore, finally we get a combined effect of both the terms Y_{ϕ^0} and $\Gamma_{\phi^0 \to \psi_1^0}$ on $Y_{\psi_1^0}$, where $Y_{\psi_1^0}$ increases with decreasing M_{ϕ^0}. In figure 4.5(c), we demonstrate how $Y_{\psi_1^0}$ depends on the mass of ψ_1^0. Here, we have shown the variation of $Y_{\psi_1^0}$ with x for three different values of $M_{\psi_1^0}$ such as 500 GeV, 1000 GeV and 1500 GeV. From this plot one can see that the final saturation value of $Y_{\psi_1^0}$ is more for DM candidate with heavier mass. This is due to the reason that the thermal abundance of ψ_1^0, which is approximately inversely proportional to its annihilation and co-annihilation cross sections, is larger for heavier ψ_1^0. Also, we don't get same enhancement in $Y_{\psi_1^0}$ while going from 500 GeV to 1000 GeV and 1000 GeV to 1500 GeV. This is because, the decay width $\Gamma_{\phi^0 \to \psi_1^0}$ becomes phase space suppressed as $M_{\psi_1^0} \to M_{\phi^0}$. As a result, non-thermal contribution, which is proportional to $\Gamma_{\phi^0 \to \psi_1^0}$, decreases with $M_{\psi_1^0}$. Hence, we get the saturation values of $Y_{\psi_1^0}$ for 1000 GeV and 1500 GeV, which are not much different from each other. Finally, we show the dependence of the evolution of $Y_{\psi_1^0}$ with x on Yukawa coupling

y_Σ, where we have considered six different values for the Yukawa coupling y_Σ and we find that the correct relic density is achieved for $y_\Sigma = 0.854 \times 10^{-9}$. As the total decay width $\Gamma^{\rm Total}_{\phi^0}$ of ϕ^0 is proportional to y_Σ^2, the smaller y_Σ results in a late decay of ϕ^0 to ψ_1^0. Hence, the increase of $Y_{\psi_1^0}$ due to the non-thermal decay of $\phi^0 \to \psi_1^0 + \nu$ also occurs much later for smaller value of y_Σ. This effect can be understood by comparing the magenta dashed curve and blue dashed-dotted curve in figure 4.5(d), where magenta and blue lines are for $y_\Sigma = 0.171 \times 10^{-8}$ and 0.854×10^{-10} respectively. Further, we have seen an anomalous behaviour in the effect of Yukawa coupling y_Σ on $Y_{\psi_1^0}$. Generally for the non-thermal DM (FIMP), the relic abundance increases as we increase the coupling between mother particle and DM. As a result, more DM particles are produced from the decay of mother particle which is assumed to be in thermal equilibrium and the equilibrium abundance of mother particle does not depend on its decay width to FIMP DM. However, in the present case the mother particle ϕ^0 becomes out of thermal equilibrium at the time of non-thermal production of ψ_1^0. Now, from the Boltzmann equation of ψ_1^0 (equation (4.17)), one can easily see that the rate of increase of $Y_{\psi_1^0}$ due to the decay to ϕ^0 is proportional to Y_{ϕ^0} and $\Gamma_{\phi^0 \to \psi_1^0}$. The comoving number density Y_{ϕ^0} can be obtained by solving the Boltzmann equation for ϕ^0 (equation (4.18)), where the last term proportional to the total decay width of ϕ^0 ($\Gamma^{\rm Total}_{\phi^0}$) further decreases Y_{ϕ^0} from its freeze-out abundance. Now, if we increase the Yukawa coupling y_Σ, the total decay width $\Gamma^{\rm Total}_{\phi^0}$ which is proportional to y_Σ^2, also increases. This in turn decreases Y_{ϕ^0}. On the other hand, any increase of y_Σ is also accompanied by an enhancement of the decay width $\Gamma_{\phi^0 \to \psi_1^0}$. Therefore, in the Boltzmann equation of ψ_1^0, there is a competition between the two quantities Y_{ϕ^0} and $\Gamma_{\phi^0 \to \psi_1^0}$, which are behaving oppositely with respect to the variation of y_Σ. The final abundance of ψ_1^0 will follow the behaviour of that quantity which depends more strongly on y_Σ. From figure 4.5(d), we find that the final abundance of ψ_1^0 actually decreases as we increase the Yukawa coupling y_Σ from 0.171×10^{-10} to 0.854×10^{-8}. This makes the present scenario different from the usual FIMP scenario [11, 108, 393, 414], where the final abundance of DM always increases with associated couplings.

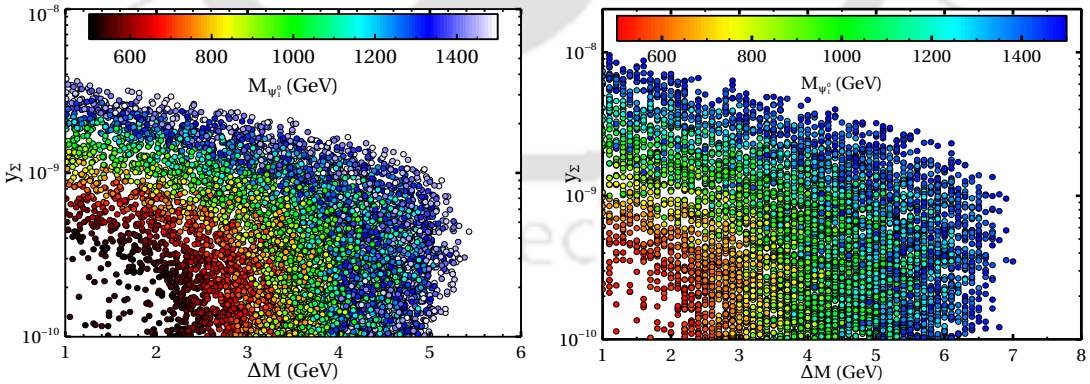

Figure 4.6: Allowed parameter space in $y_\Sigma - \Delta M$ for $y_s = 1.5$ (left panel) and $0.1 \leq y_s \leq 2.0$ (right panel). In both plots mass of ϕ^0 has been varied between 1 TeV to 5 TeV and M_s is kept fixed at 200 GeV.

In figure 4.6, we show our allowed parameter space in $y_\Sigma - \Delta M$ plane which reproduces the correct DM relic density. The colour code is indicating the mass of our DM ψ_1^0 which we

have varied between 500 GeV to 1500 GeV while the corresponding mass of ϕ^0 is scanned over the following range: $2\,M_{\psi_1^0} \leq M_{\phi^0} \leq 2\,M_{\psi_1^0} + 2000$ GeV. The plot in left panel is for a fixed value of other Yukawa coupling y_s which we have kept fixed at 1.5 while for the plot in the right panel, we have varied the Yukawa coupling y_s between 0.1 to 2. From the plot in the left panel, one can see that to produce the DM relic density in the right ballpark, we need $10^{-10} \leq y_\Sigma \leq 4 \times 10^{-9}$ depending upon the mass splitting ΔM between the inert scalars, which is also tightly constrained to be less than 5.5 GeV. However, from the right panel it is also noticeable that these ranges of Yukawa coupling y_Σ and mass splitting ΔM are slightly larger when we have also varied the singlet Yukawa coupling $0.1 \leq y_s \leq 2$. This is because the thermal contribution to relic density becomes fixed for a particular set of values of $M_{\psi_1^0}$, M_{ϕ^0}, M_s, ΔM and y_s. In this case, the amount of deficit in relic density which is compensated by the non-thermal production is also a definite number as the total relic density should lie with the observed band $0.1166 \leq \Omega_{\rm DM}h^2 \leq 0.1206$ in 68% C.L. However, if we vary the singlet Yukawa y_s while keeping others fixed at their respective values (ΔM, M_ϕ, $M_{\psi_1^0}$ and M_s) then the thermal contribution to $\Omega_{\psi_1^0}h^2$ also varies and hence we require different non-thermal contributions to achieve correct DM relic density and consequently more parameter space in $y_\Sigma - \Delta M$ plane become allowed. Later when we will discuss the constrains coming from the indirect detection we will see that for the considered mass range of $M_{\psi_1^0}$ we need $y_s \gtrsim 1$ (see figure 4.10). Moreover, from both these plots it is clearly evident the for heavier DM mass we need larger values of y_Σ and ΔM to achieve $\Omega_{\psi_1^0}h^2$ in the correct ballpark.

4.2.5 LHC constraints on $\psi_1^\pm$

In this section, we briefly discuss the testability of our model at the LHC experiment. There have been several dedicated searches for possible DM signatures at colliders, a recent summary of which can be found in [144, 415]. Instead of usual missing transverse energy associated with DM production at colliders, in our model there exists a different (rather unique to a limited class of scenarios) signature that is within the reach of LHC. This is basically the collider production of different components of the fermion triplet Σ_{1R} through gauge interactions and subsequent decay of the heavier components into the lighter one. Since DM candidate ψ_1^0 is the lightest component, the heavier component $\psi_1^\pm$ must decay into ψ_1^0 and other SM particles. This decay is actually interesting due to small mass splitting $\Delta M_{\rm triplet} \simeq 166$ MeV between $M_{\psi_1^\pm}$ and $M_{\psi_1^0}$ for $M_\Sigma \gtrsim 1$ TeV. For such a small mass difference, the dominant decay mode is $\psi_1^\pm \to \psi_1^0\,\pi^\pm$, the corresponding decay width of which is given by equation (4.20). Such tiny decay width keeps the lifetime of $\psi_1^\pm$ considerably long enough that it can reach the detector before decaying. In fact, the ATLAS experiment at the LHC has already searched for such long-lived charged particles with lifetime ranging from 10 ps to 10 ns, with maximum sensitivity around 1 ns [331]. In the decay $\psi_1^\pm \to \psi_1^0\,\pi^\pm$, the final state pion typically has very low momentum and it is not reconstructed in the detector. On the other hand the DM particle in the final state ψ_1^0 is perfectly stable and leaves the detector without interacting. Therefore, it gives rise to a signature where a charged particle leaves a track in the inner parts of the detector and then disappears leaving no tracks in the portions of the detector at higher radii. The ATLAS constraints on such disappearing charged track signatures for a long lived chargino decaying into a pion and wino DM is

shown as the solid green line in figure 4.7. Since our DM multiplet is similar to the multiplet containing chargino, wino with similar production cross section at LHC as shown in Table 4.1 for fermion triplets and in [416, 417] for gauginos, we compare our model predictions against this constraint from ATLAS. The lifetime predictions for $\psi_1^{\pm}$ as a function of DM mass is shown as the solid red line in figure 4.7. It can be seen that the existing LHC constraint can already rule out DM masses below 500 GeV from its searches for disappearing charged tracks, keeping the DM parameter space considered in this study within near future sensitivity.

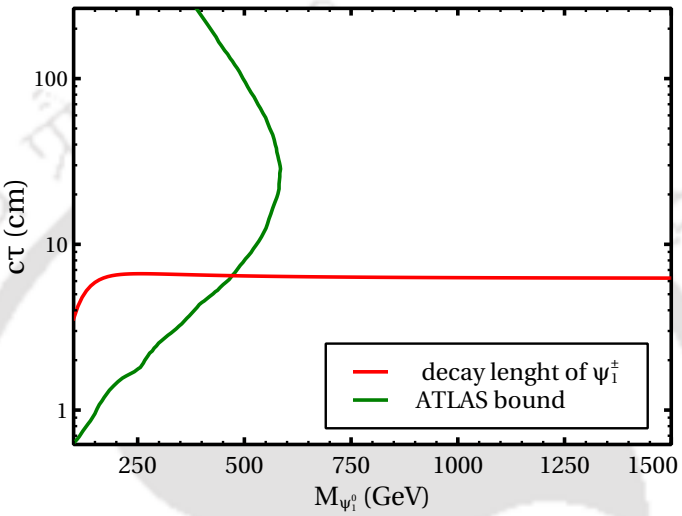

Figure 4.7: Lifetime of $\psi_1^{\pm}$ versus DM mass compared with the ATLAS bound on disappearing charge track searches.

$M_{\psi_1^0}$ (TeV)	$\sigma_{pp\to\psi_1^+\psi_1^-}$ (pb)	$\sigma_{pp\to\psi_1^{\pm}\psi_1^0}$ (pb)
0.5	1.493×10^{-2}	4.394×10^{-2}
0.6	6.338×10^{-3}	1.92×10^{-2}
0.7	2.938×10^{-3}	9.1×10^{-3}
0.8	1.464×10^{-3}	4.6×10^{-3}
0.9	7.588×10^{-4}	2.43×10^{-3}
1.0	4.103×10^{-4}	1.33×10^{-3}
1.1	2.305×10^{-4}	7.468×10^{-4}
1.2	1.305×10^{-4}	4.308×10^{-4}
1.3	7.600×10^{-5}	2.508×10^{-4}
1.4	4.490×10^{-5}	1.494×10^{-4}
1.5	2.687×10^{-5}	8.978×10^{-5}

Table 4.1: Production cross sections of $\psi_1^+\psi_1^-$ and $\psi_1^{\pm}\psi_1^0$ from pp collisions at $\sqrt{s} = 14$ TeV LHC.

4.2.6 Direct Detection

The most convincing way to probe a particle DM candidate is the direct detection experiments. There have been serious efforts in this direction for last few decades where ground based detectors made up of different heavy nuclei have been used to probe processes where a DM particle passing through the detector can interact with a nuclei giving rise to some recoil. Such experiments have significantly improved their sensitivities over the years, with their present exclusion limits on spin independent DM-nucleon scattering cross section lying very close to the coherent neutrino-nucleon scattering rate [6, 53, 55–57]. Interestingly, our present model has good prospects for direct detection frontiers which is usually not there for purely freeze-in type DM candidates. Being part of an electroweak multiplet, the DM can interact with SM through gauge interactions and also through scalar interactions present due to the singlet scalar field S'. Due to the absence of neutral current interactions of our DM candidate at tree level, the gauge boson mediated DM-nucleon scattering can arise only at radiative level. However, due to the existence of singlet scalar mixing with the SM like Higgs, such scalar mediated DM-nucleon scattering can occur at tree level as well. The Feynman diagrams corresponding to these processes are shown in figure 4.8 all of which can lead to spin independent (SI) direct detection (DD) scattering processes. For pure triplet fermion case we have to exclude the last one as there exists no singlet scalar in that scenario. The DM candidate ψ_1^0 has two different one loop DD scattering: a Higgs penguin with $W^\pm$ loop and the box diagram in figure 4.8. The low energy effective Lagrangian for the ψ_1^0-quark one loop interaction have already been discussed in [418]. So the effective Lagrangian for the loop diagrams can be written as

$$\mathcal{L}_{\psi_1^0 q} = \sum_i \lambda_q^i \bar{\psi_1^0} \psi_1^0 \bar{q} q \tag{4.22}$$

$$\begin{aligned} \lambda_q^i \;=\; & -\alpha_2^2 \frac{m_{q_i}}{m_{\psi_1^0} m_h^2} \frac{1 - 4\eta_W + 3\eta_W^2 + (2 - 4\eta_W)\log\eta_W}{(1-\eta_W)^3} \\ & + \alpha_2^2 \frac{m_{q_i}}{m_{\psi_1^0} m_W^2} \frac{2 - 3\eta_W + 6\eta_W^2 - 5\eta_W^3 + 3\eta_W(1+\eta_W^2)\log\eta_W}{6(1-\eta_W)^4} \end{aligned} \tag{4.23}$$

where $\eta_W \equiv \frac{m_W^2}{m_{\psi_1^0}^2}$ and $\alpha_2 = \frac{g^2}{4\pi}$. In equation (4.23), the first term is the effective coupling for the Higgs penguin diagram and the second term is the same for the box diagram. We have shown the corresponding spin-independent direct detection cross-section as a function of DM mass in the left panel of figure 4.9, which is about two orders of magnitude below the current XENON1T bound [55]. In spite of electroweak gauge interactions being involved in the scattering, this is in a way expected due to loop suppressions involved.

The other possible diagram coming from the introduction of the singlet scalar can, on the other hand, give rise to larger DD cross-section if the singlet scalar S' has sizeable mixing with the SM like Higgs. The relevant cross section can be written as

$$\sigma_{\rm SI} = \frac{y_s^2 \; \mu_{\psi_1^0 n}^2 \; m_n^2}{\pi \; m_s^4 \; v^2} f_p^2 \xi^2 \tag{4.24}$$

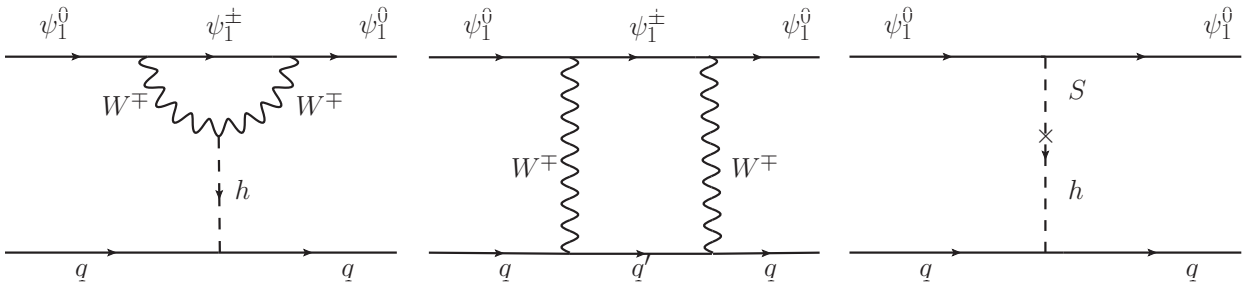

Figure 4.8: Spin-independent DD scattering processes in the model. The first two processes are for pure triplet fermion DM model while the last one arises additionally in the present model due to the introduction of the singlet scalar S'.

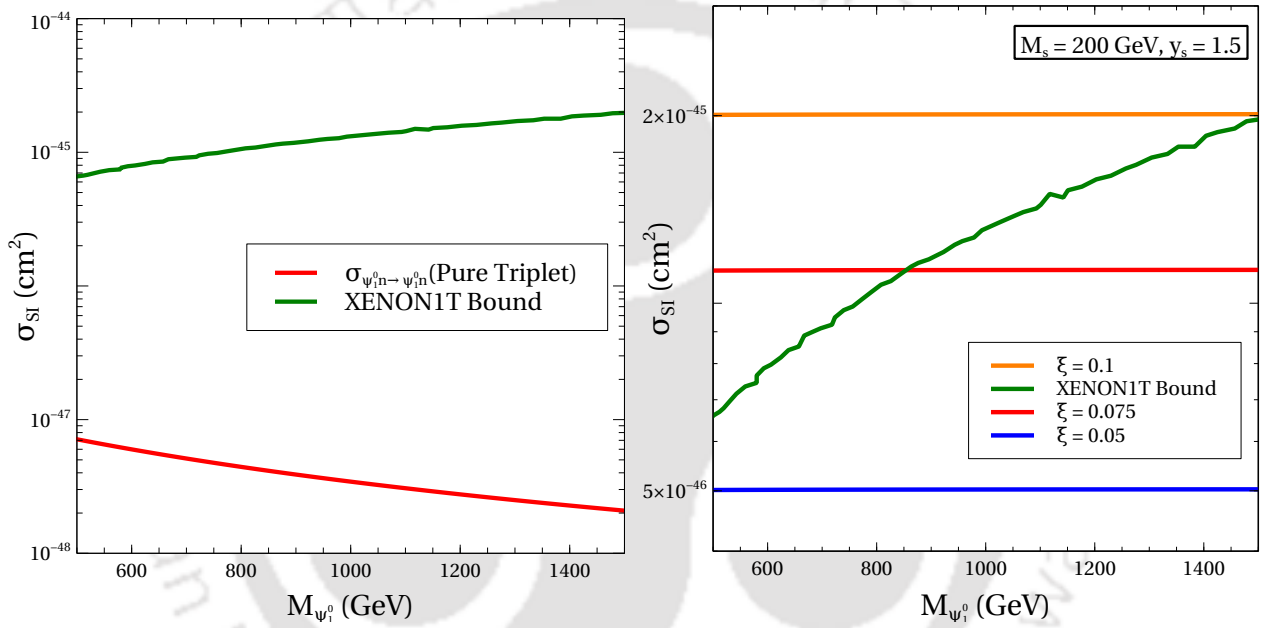

Figure 4.9: Left panel: DD cross-section for pure triplet fermion as a functions of DM mass. Right panel: DD cross-section for singlet scalar mediated diagram as a function of DM mass for different benchmark values of ξ with fixed M_s =200 GeV and y_s = 1.5.

where y_s, f_p, ξ and m_n are the new Yukawa coupling, form factor, S'-Higgs mixing parameter (defined in equation (4.12)), and nucleon mass respectively. We have also fixed the singlet mass (M_s) at 200 GeV, like in the calculation for relic abundance. As the DM-nucleon reduced mass $\mu_{\psi_1^0 n}$ is nearly close to the mass of the nucleon for the chosen range of DM masses, this scattering cross section is almost independent of the DM mass. This in fact serves as another motivation of introducing the singlet scalar S' apart from being responsible for generating DM mass dynamically. This singlet scalar allows the model to be testable at ongoing and upcoming direct detection experiments for a wide range of DM masses. We show the contribution of this scalar mediated diagram to DD scattering in the right panel of figure 4.9 for three different mixing parameter ξ values (ξ = 0.1, 0.075, 0.05). From the figure 4.9 it is clear that the $\sigma_{\rm SI}$ lies above the XENON1T bound for ξ = 0.1, whereas for

$\xi = 0.075$ it is partially allowed and for $\xi = 0.05$ it is just below the present bound for the chosen mass range of DM.

4.2.7 Indirect Detection

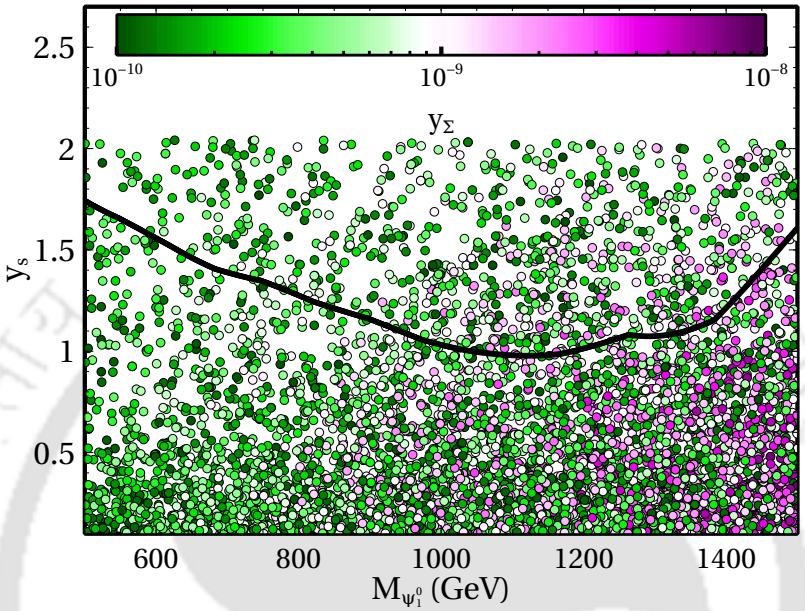

Figure 4.10: Parameter space of Yukawa coupling y_s and $M_{\psi_1^0}$ that satisfy the relic density constraint. The color-bar indicates the variation of the another Yukawa y_Σ. The Black line corresponds to the Fermi-LAT bound, the points above that line are allowed. To generate this plot we have fixed the singlet mass (M_s) at 200 GeV.

Apart from direct detection experiments, DM parameter space in our model can also be probed at different indirect detection experiments (space as well as ground based) that are looking for SM particles produced either through DM annihilations or via DM decay in the local Universe. Among these final states, photon and neutrinos, being neutral and stable can reach the indirect detection experiments without getting affected much by intermediate regions. If the DM is of the type we have in our model, having TeV scale masses and sizeable interaction with the SM particles, these photons lie in the gamma ray regime that can be measured at space based telescopes like the Fermi-LAT or ground based telescopes like MAGIC. Here we constrain the DM parameter space from the indirect detection bounds arising from the global analysis of the Fermi-LAT and MAGIC observations of dSphs [8].

Since the heavier components of the fermion triplet are not there in the present Universe, we need to consider the DM self annihilations into the charged particles of the SM. The only possible process of this type is the DM annihilation into a pair of W bosons which is indeed constrained tightly from gamma ray observations [8]. Such bounds on $\langle\sigma v\rangle_{\rm DMDM\to W^+W^-}$ are derived assuming 100% annihilation of DM into these final states. Since we have another DM annihilation in this model namely, the one with a pair of singlet scalars S' in the final states which do not contribute to gamma rays due to neutral final states, we take into

account the relative factor between these two annihilation rates while applying the indirect detection bound on $\langle\sigma v\rangle_{\rm DMDM\to W^+W^-}$. Due to sizeable DM annihilation rates into neutral singlet scalars in our model, the gamma ray constraints on DM annihilations into W boson pairs get weaker in our model, saving the parameter space under study. It should be noted that in the pure FTDM model, gamma ray bound will completely rule out low mass region of DM mass we are studying [390] as the annihilation rate for $\langle\sigma v\rangle_{\rm DMDM\to W^+W^-}$ is 100% in that model. Therefore, weakening the indirect detection bound arise as another motivation for the singlet scalar S' apart from generating DM mass dynamically and giving rise to tree level direct detection rates as discussed before. In figure 4.10 we have shown allowed parameter space in the y_s versus $M_{\psi_1^0}$ plane where we have also varied Yukawa of the inert doublet y_Σ while fixing the singlet scalar mass at 200 GeV. All the points shown there are satisfying the relic density constraint and the black solid line corresponds to the present Fermi-LAT plus MAGIC bound on DM annihilation to $W^\pm$. The points below the black line are ruled out from these bounds which shows that we need large y_s to satisfy the present bound. As the x-axis goes all the way upto DM mass of 1.5 TeV where non-perturbative effects (Sommerfeld enhancement) on DM annihilations can be sizeable, we use the results of [390] to derive the exclusion line shown in figure 4.10. As we go into higher mass values, the Sommerfeld enhancement becomes more and more efficient which can be seen by the sharp rise in the black solid line towards the right end of the plot, requiring stronger Yukawa coupling y_s to keep the DM self annihilations to neutral particles more dominant over $\langle\sigma v\rangle_{\rm DMDM\to W^+W^-}$. Future data from gamma ray telescopes should be able to probe more parts of this region of DM masses as well as Yukawa coupling y_s, keeping the indirect detection prospects of the model very promising.

4.3 A_4 Model for Dirac neutrinos and FIMP dark matter

We first consider a minimal model based on A_4 flavour symmetry that can give rise to tiny Dirac neutrino masses and mixing at dimension six level. A brief details of A_4 group is given in Appendix C.2. The fermion sector of the SM is extended by three copies of gauge singlet right handed neutrinos (ν_R) and an additional gauge singlet fermion (ψ) which plays the role of FIMP DM. These right handed neutrinos transform in the same way just like the SM lepton doublets (L) do under A_4, a typical feature of most of the A_4 flavour symmetric realisations of neutrino mass. We also introduce four different flavon fields for the desired phenomenology of neutrino mass and dark matter. The A_4 flavour symmetry is augmented by additional discrete symmetries $Z_4 \times Z_4'$ and a global unbroken lepton number symmetry $U(1)_L$ in order to forbid the unwanted terms. Transformations of the fields under the complete flavour symmetry of the model $A_4 \times Z_4 \times Z_4' \times U(1)_L$ are given in Table 4.2. The construction here includes two A_4 triplet flavons, ϕ_T and ϕ_S, which play a crucial role in generating masses and mixing for charged leptons and Dirac neutrinos respectively. Now, for charged lepton sector, the relevant Yukawa Lagrangian can be written as

$$\mathcal{L}_l = \frac{y_e}{\Lambda}(\bar{L}\phi_T)He_R + \frac{y_\mu}{\Lambda}(\bar{L}\phi_T)_{1'}H\mu_R + \frac{y_\tau}{\Lambda}(\bar{L}\phi_T)_{1''}H\tau_R \tag{4.25}$$

Fields	L	e_R, μ_R, τ_R	H	ν_R	ψ	ϕ_S	ϕ_T	ζ	η
A_4	3	1,1″,1′	1	3	1	3	3	1	1
Z_4	-i	-i	1	i	i	i	1	i	1
Z_4'	1	1	1	1	i	1	1	i	-1
$U(1)_L$	1	1	0	1	0	0	0	0	0

Table 4.2: Field content and transformation properties under $A_4 \times Z_4 \times Z_4' \times U(1)_L$ symmetry of the model.

where Λ is the cut-off scale of the theory. Here and subsequently all the y's stand for the respective coupling constants, unless otherwise mentioned. The leading contributions to the charged lepton mass via $\bar{L}H\ell_i$ (where ℓ_i are the RH charged leptons) are not allowed due to the specific A_4 symmetry. When the triplet flavon ϕ_T is present in the model it leads to an A_4 invariant dimension five operator as given in equation (4.25) which subsequently generates the relevant masses after flavons and the SM Higgs field acquire non-zero vacuum expectation value (vev)'s. Using the A_4 product rules given in Appendix C.2 and taking generic triplet flavon vev alignment $\langle \phi_T \rangle = (v_T, v_T, v_T)$, we can write down the charged lepton mass matrix as

$$m_l = \frac{v v_T}{\Lambda} \begin{pmatrix} y_e & y_\mu & y_\tau \\ y_e & \omega y_\mu & \omega^2 y_\tau \\ y_e & \omega^2 y_\mu & \omega y_\tau \end{pmatrix}. \tag{4.26}$$

Here v denotes the vev of the SM Higgs doublet H and $\omega = e^{i2\pi/3}$ is the cube root of unity. This mass matrix can be diagonalised by using the magic matrix U_ω, given by

$$U_\omega = \frac{1}{\sqrt{3}} \begin{pmatrix} 1 & 1 & 1 \\ 1 & \omega & \omega^2 \\ 1 & \omega^2 & \omega \end{pmatrix}. \tag{4.27}$$

Now, as indicated earlier, the complete $A_4 \times Z_4 \times Z_4'$ discrete symmetry plays an instrumental role in generating tiny Dirac neutrino mass and mixing at dimension six level. Any contribution to the neutrino mass (through $\bar{L}\tilde{H}\nu_R$) is forbidden up to dimension five level in the present set-up. Since charged lepton masses are generated at dimension five level, it naturally explains the observed hierarchy between charged and neutral lepton masses. Presence of the A_4 triplet flavon ϕ_S generates the required dimension six operator for neutrino mass and mixing. The relevant Yukawa Lagrangian for neutrino sector is given by

$$\mathcal{L}_\nu = \bar{L}\tilde{H}\nu_R \frac{(\phi_S)^2}{\Lambda^2} + \text{h.c.} \tag{4.28}$$

$$\begin{aligned} &= \frac{y_s}{\Lambda^2}(\bar{L}\tilde{H}\nu_R)_S(\phi_S\phi_S)_S + \frac{y_{s'}}{\Lambda^2}(\bar{L}\tilde{H}\nu_R)_S(\phi_S\phi_S)_A + \frac{y_a}{\Lambda^2}(\bar{L}\tilde{H}\nu_R)_A(\phi_S\phi_S)_S \\ &+ \frac{y_{a'}}{\Lambda^2}(\bar{L}\tilde{H}\nu_R)_A(\phi_S\phi_S)_A + \frac{y_{x_1}}{\Lambda^2}(\bar{L}\tilde{H}\nu_R)_1(\phi_S\phi_S)_1 + \frac{y_{x_2}}{\Lambda^2}(\bar{L}\tilde{H}\nu_R)_{1'}(\phi_S\phi_S)_{1''} \\ &+ \frac{y_{x_3}}{\Lambda^2}(\bar{L}\tilde{H}\nu_R)_{1''}(\phi_S\phi_S)_{1'} + \text{h.c.}. \end{aligned} \tag{4.29}$$

Here the subscripts S and A stands for symmetric and anti-symmetric parts of A_4 triplets products (see Appendix C.2 for details) in the S diagonal basis adopted in the analysis

and $1, 1'$ and $1''$ stand for three singlets of A_4. For the most general vev alignment $\langle\phi_S\rangle = (v_{S_1}, v_{S_2}, v_{S_3})$, the effective mass matrix for neutrinos can be written as

$$m_\nu = \begin{pmatrix} x_{11} & s_{21}+a_{21} & s_{31}+a_{31} \\ s_{21}-a_{21} & x_{22} & s_{32}+a_{32} \\ s_{31}-a_{31} & s_{32}-a_{32} & x_{33} \end{pmatrix} \tag{4.30}$$

where the diagonal elements are given by

$$x_{11} = \left[y_{x_1}(v_{S_1}^2+v_{S_2}^2+v_{S_3}^2) + y_{x_2}(v_{S_1}^2+\omega^2 v_{S_2}^2+\omega v_{S_3}^2) + y_{x_3}(v_{S_1}^2+\omega v_{S_2}^2+\omega^2 v_{S_3}^2)\right] v/\Lambda^2, \tag{4.31}$$

$$x_{22} = \left[y_{x_1}(v_{S_1}^2+v_{S_2}^2+v_{S_3}^2) + y_{x_2}\omega(v_{S_1}^2+\omega^2 v_{S_2}^2+\omega v_{S_3}^2) + y_{x_3}\omega^2(v_{S_1}^2+\omega v_{S_2}^2+\omega^2 v_{S_3}^2)\right] v/\Lambda^2, \tag{4.32}$$

$$x_{33} = \left[y_{x_1}(v_{S_1}^2+v_{S_2}^2+v_{S_3}^2) + y_{x_2}\omega^2(v_{S_1}^2+\omega^2 v_{S_2}^2+\omega v_{S_3}^2) + y_{x_3}\omega(v_{S_1}^2+\omega v_{S_2}^2+\omega^2 v_{S_3}^2)\right] v/\Lambda^2. \tag{4.33}$$

Now, the symmetric part originated from A_4 triplet products are given by

$$s_{32} = y_s v(v_{S_2}v_{S_3}+v_{S_3}v_{S_2})/\Lambda^2 + y_s' v(v_{S_2}v_{S_3}-v_{S_3}v_{S_2})/\Lambda^2, \tag{4.34}$$

$$s_{31} = y_s v(v_{S_3}v_{S_1}+v_{S_1}v_{S_3})/\Lambda^2 + y_s' v(v_{S_3}v_{S_1}-v_{S_1}v_{S_3})/\Lambda^2, \tag{4.35}$$

$$s_{21} = y_s v(v_{S_1}v_{S_2}+v_{S_2}v_{S_1})/\Lambda^2 + y_s' v(v_{S_1}v_{S_2}-v_{S_2}v_{S_1})/\Lambda^2. \tag{4.36}$$

As seen above, when neutrinos are Dirac fermions instead of Majorana, then there is an additional anti-symmetric contribution in the neutrino mass matrix which remains absent in the Majorana case due to symmetric property of the Majorana mass term. This additional contribution can in fact explain nonzero θ_{13} in a more economical setup [234, 235, 419] compared to the one for Majorana neutrinos [420]. In the mass matrix given by equation (4.30) these anti-symmetric contributions are given by

$$a_{32} = y_a v(v_{S_2}v_{S_3}+v_{S_3}v_{S_2})/\Lambda^2 + y_a' v(v_{S_2}v_{S_3}-v_{S_3}v_{S_2})/\Lambda^2, \tag{4.37}$$

$$a_{31} = y_a v(v_{S_3}v_{S_1}+v_{S_1}v_{S_3})/\Lambda^2 + y_a' v(v_{S_3}v_{S_1}-v_{S_1}v_{S_3})/\Lambda^2, \tag{4.38}$$

$$a_{21} = y_s v(v_{S_1}v_{S_2}+v_{S_2}v_{S_1})/\Lambda^2 + y_a' v(v_{S_1}v_{S_2}-v_{S_2}v_{S_1})/\Lambda^2. \tag{4.39}$$

The most general mass matrix for Dirac neutrinos given in equation (4.30) can be further simplified depending upon the specific and simpler vev alignments of the triplet flavon ϕ_S. Here we briefly discuss a few such possible alignments analytically and then restrict ourselves to one such scenario for numerical analysis which can explain neutrino masses and mixing in a minimal way. Note that such vev alignments demand a complete analysis of the scalar sector of the model and can be obtained in principle, from the minimisation of the scalar potential [421–425]. For simplicity, when we consider the vev alignment of ϕ_S to be $\langle\phi_S\rangle = (v_S, v_S, v_S)$ from equation (4.31)-(4.37), we obtain $s_{32} = s_{31} = s_{21} = 2y_s v v_S^2/\Lambda^2 = s$ (say) and $a_{32} = a_{31} = a_{21} = 2y_a v v_S^2/\Lambda^2 = a$ (say). Hence the neutrino mass matrix takes the form

$$m_\nu = \begin{pmatrix} x & s+a & s+a \\ s-a & x & s+a \\ s-a & s-a & x \end{pmatrix}, \tag{4.40}$$

where $x_{11} = x_{22} = x_{33} = 3y_{x_1} v v_S^2/\Lambda^2 = x$ (say). For even more simplified[7] scenarios of vev alignments $\langle\phi_S\rangle = (v_S, v_S, 0)$ and $\langle\phi_S\rangle = (0, v_S, v_S)$ the neutrino mass matrices are given by

$$m_\nu = \begin{pmatrix} x_{11} & s+a & 0 \\ s-a & x_{22} & 0 \\ 0 & 0 & x_{33} \end{pmatrix}; \quad m_\nu = \begin{pmatrix} x_{11} & 0 & 0 \\ 0 & x_{22} & s+a \\ 0 & s-a & x_{33} \end{pmatrix}, \tag{4.41}$$

[7] Vev alignments like $\langle\phi_S\rangle = (0,0,v_S), (0,v_S,0)$ and $(v_S,0,0)$ are not allowed in the present construction of Dirac neutrino mass.

respectively, where the elements are defined as $s_{21} = 2y_s vv_S^2/\Lambda^2 = s$ (say), $a_{21} = 2y_a vv_S^2/\Lambda^2 = a$ (say), $x_{11} = (2y_{x_1} - y_{x_2}\omega - y_{x_3}\omega^2)vv_S^2/\Lambda^2$, $x_{22} = (2y_{x_1} - y_{x_2}\omega^2 - y_{x_3}\omega)vv_S^2/\Lambda^2$, $x_{33} = (2y_{x_1} - y_{x_2} - y_{x_3})vv_S^2/\Lambda^2$ and $s_{32} = 2y_s vv_S^2/\Lambda^2 = s$ (say), $a_{32} = 2y_a vv_S^2/\Lambda^2 = a$ (say), $x_{11} = (2y_{x_1} - y_{x_2} - y_{x_3})vv_S^2/\Lambda^2$, $x_{22} = (2y_{x_1} - y_{x_2}\omega - y_{x_3}\omega^2)vv_S^2/\Lambda^2$, $x_{33} = (2y_{x_1} - y_{x_2}\omega^2 - y_{x_3}\omega)vv_S^2/\Lambda^2$ respectively. As evident from these two neutrino mass matrices given by equation (4.41), a Hermitian matrix $(m_\nu m_\nu^\dagger)$ obtained from these demands a rotation in the 12 and 23 planes respectively. This, however, is not sufficient to to explain observed neutrino mixing along with the contribution (U_ω) from the charged lepton sector given in equation (4.27). Now, a third possibility with vev alignment $\langle \phi_S \rangle = (v_S, 0, v_S)$, yields a compatible neutrino mass matrix, given by,

$$m_\nu = \begin{pmatrix} x_{11} & 0 & s+a \\ 0 & x_{22} & 0 \\ s-a & 0 & x_{33} \end{pmatrix}, \tag{4.42}$$

where $s_{31} = 2y_s vv_S^2/\Lambda^2 = s$ (say), $a_{31} = 2y_a vv_S^2/\Lambda^2 = a$ (say), $x_{11} = (2y_{x_1} - y_{x_2}\omega^2 - y_{x_3}\omega)vv_S^2/\Lambda^2$, $x_{22} = (2y_{x_1} - y_{x_2} - y_{x_3})vv_S^2/\Lambda^2$ and $x_{33} = (2y_{x_1} - y_{x_2}\omega - y_{x_3}\omega^2)vv_S^2/\Lambda^2$. Although parameters present here are in general complex, for the diagonal elements we consider them to be equal that is, $x_{11} = x_{22} = x_{33} = x$ and real without loss of any generality. Now, to diagonalise this mass matrix, let us first define a Hermitian matrix as

$$\begin{aligned} \mathcal{M} &= m_\nu m_\nu^\dagger \\ &= \begin{pmatrix} x^2 + |s+a|^2 & 0 & x(s-a)^* + x(s+a) \\ o & x^2 & 0 \\ x(s-a) + x(s+a)^* & 0 & x^2 + |s-a|^2 \end{pmatrix}. \end{aligned} \tag{4.43}$$

Here the complex terms corresponding to the symmetric and anti-symmetric parts of A_4 products can be written as $s = |s|^{i\phi_s}$ and $a = |a|^{i\phi_a}$. These complex phases essentially dictates the CP violation of the theory. Clearly, the structure of $\mathcal{M}$ given in equation (4.43) indicates rotation in the 13 plane through the relation $U_{13}^\dagger \mathcal{M} U_{13} = \text{diag}(m_1^2, m_2^2, m_3^2)$ is sufficient to diagonalise this matrix, where the U_{13} is given by

$$U_{13} = \begin{pmatrix} \cos\theta & 0 & \sin\theta e^{-i\psi} \\ 0 & 1 & 0 \\ -\sin\theta e^{i\psi} & 0 & \cos\theta \end{pmatrix}, \tag{4.44}$$

and the mass eigenvalues are found to be

$$m_1^2 = x^2 + A - B, \tag{4.45}$$
$$m_2^2 = x^2, \tag{4.46}$$
$$m_3^2 = x^2 + A + B, \tag{4.47}$$

where $A = |s|^2 + |a|^2$ and $B = \sqrt{(2|s||a|\cos(\phi_s - \phi_a))^2 + 4x^2(|s|^2\cos^2\phi_s + |a|^2\sin^2\phi_a)}$. One important inference of such ordering is that inverted hierarchy of neutrino mass is not feasible in this setup as $\Delta m_{23}^2 + \Delta m_{21}^2 = -2(|s|^2 + |a|^2) < 0$, implying $m_3 > m_2$. Also, the two parameters θ and ψ appearing in U_{13} can be expressed as

$$\tan 2\theta = \frac{x(|a|\sin\phi_a \sin\psi - |s|\cos\phi_s\cos\psi)}{|s||a|\cos(\phi_s - \phi_a)} \quad \text{and} \quad \tan\psi = -\frac{|a|\sin\phi_a}{|s|\cos\phi_s}, \tag{4.48}$$

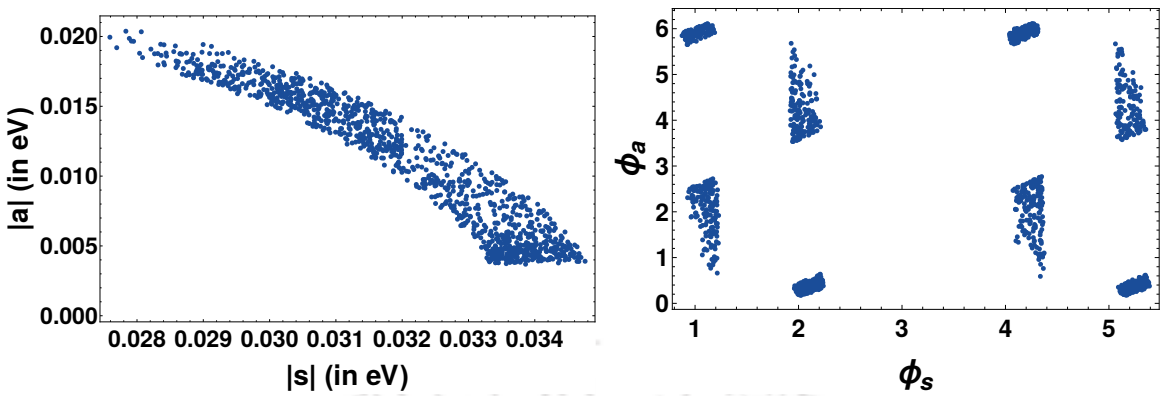

Figure 4.11: Correlations between different model parameters for 3σ allowed ranges of θ_{13}, θ_{12}, θ_{23}, mass squared differences [13] and $\sum m_i \leq 0.17$ eV. Left panel: the allowed points in $|s| - |a|$ (symmetric and anti-symmetric parts of the neutrino mass matrix respectively) plane. Right panel: the allowed points in the $\phi_s - \phi_a$ (phases associated with symmetric nd anti-symmetric parts respectively) plane.

in terms of the parameters appearing in the mass matrix. Hence the final lepton mixing matrix is given by

$$U \;=\; U_{\omega}^{\dagger} U_{13}. \tag{4.49}$$

Comparing this with the Pontecorvo Maki Nakagawa Sakata (PMNS) mixing matrix parametrised as

$$U_{\rm PMNS} = \begin{pmatrix} c_{12}c_{13} & s_{12}c_{13} & s_{13}e^{-i\delta} \\ -s_{12}c_{23} - c_{12}s_{23}s_{13}e^{i\delta} & c_{12}c_{23} - s_{12}s_{23}s_{13}e^{i\delta} & s_{23}c_{13} \\ s_{12}s_{23} - c_{12}c_{23}s_{13}e^{i\delta} & -c_{12}s_{23} - s_{12}c_{23}s_{13}e^{i\delta} & c_{23}c_{13} \end{pmatrix}, \tag{4.50}$$

one can obtain correlations between neutrino mixing angles $\theta_{13}, \theta_{12}, \theta_{23}$, Dirac CP phase δ and parameters appearing in equation (4.49) very easily [234, 235, 426–429]. Hence, from equations (4.48-4.50) it is evident that the mixing angles $(\theta_{13}, \theta_{12}, \theta_{23})$ and Dirac CP phase (δ) involved in the lepton mixing matrix $U_{\rm PMNS}$ are functions of x, $|s|$, $|a|$, ϕ_s and ϕ_a. Neutrino mass eigenvalues are also function of these parameters as obtained in equations (4.45-4.47). These parameters can be constrained using the current data on neutrino mixing angles and mass squared differences [13, 430]. Here in our analysis we adopt the 3σ variation of neutrino oscillation data obtained from the global fit [13] to do so. In figure 4.11 we have plotted the allowed parameter values in $|s| - |a|$ plane (left panel) and $\phi_s - \phi_a$ plane (right panel) respectively satisfying 3σ range of neutrino mixing data as mentioned earlier.

After constraining the model parameters, the predictions for absolute neutrino mass (m_1 in case of normal hierarchy) is plotted in the left panel of figure 4.12. In this figure, the lightest neutrino mass (m_1) is shown as a function of the diagonal element of neutrino mass matrix x. Whereas in the right panel of figure 4.12 we present the correlation between Dirac CP phase δ and $\sin^2\theta_{23}$. Interestingly the model predicts δ in the range $-\pi/2 \lesssim \delta \lesssim -\pi/5$ and $\pi/5 \lesssim \delta \lesssim \pi/2$ whereas $\sin^2\theta_{23}$ lies in the lower octant. Here it is worth mentioning

that, the presently preferred value $\delta \sim \pm\pi/2$ as indicated in global fit analysis [13], predicts the atmospheric mixing angle θ_{23} to be in the lower octant within our framework, as seen from the right panel of figure 4.12.

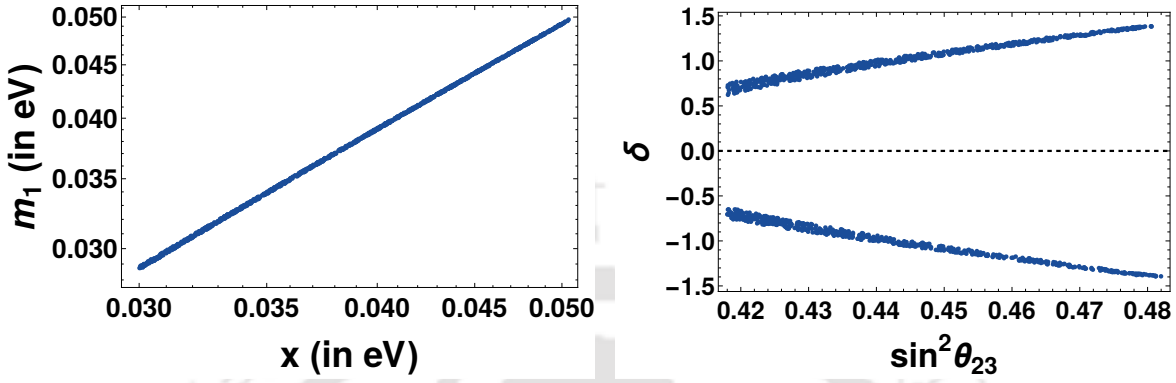

Figure 4.12: Correlations between different light neutrino as well as model parameters for 3σ allowed ranges of θ_{13}, θ_{12}, θ_{23}, mass squared differences [13] and $\sum m_i \leq 0.17$ eV. Left panel: the lightest neutrino mass is shown as a function of model parameter x. Right panel: the predicted correlation between Dirac CP phase δ and atmospheric mixing angle θ_{23}.

FIMP interactions: After studying the neutrino sector, we briefly comment upon the Yukawa Lagrangian involving the FIMP DM candidate ψ upto dimension six level. From the field content shown in Table 4.2, it is obvious that a bare mass term for ψ is not allowed. However, we can generate its mass at dimension five level (same as that of charged leptons). The corresponding Yukawa Lagrangian is

$$\mathcal{L}_{\psi\zeta} = \frac{1}{2} Y_{\psi\zeta} \frac{\zeta^2}{\Lambda} \psi\psi. \tag{4.51}$$

Once ζ acquires a non-zero vev, we can generate a mass $M_\psi = Y_{\psi\zeta} \frac{\langle\zeta\rangle^2}{\Lambda}$. Another important Yukawa interaction of ψ is with the singlet flavon η that arises at dimension six level, given by

$$\begin{aligned}
\mathcal{L}_{\psi\eta} &= \frac{(\phi_S)^2}{\Lambda^2} \eta\psi\psi && (4.52)\\
&= \frac{v_{S_1}^2 + v_{S_2}^2 + v_{S_3}^2}{\Lambda^2} \eta\psi\psi \quad \text{for} \quad \langle\phi_S\rangle = (v_{S_1}, v_{S_2}, v_{S_3}) && (4.53)\\
&= \frac{3v_S^2}{\Lambda^2} \eta\psi\psi \quad \text{for} \quad \langle\phi_S\rangle = (v_S, v_S, v_S) && (4.54)\\
&= \frac{2v_S^2}{\Lambda^2} \eta\psi\psi \quad \text{for} \quad \langle\phi_S\rangle = (v_S, v_S, 0), (v_S, 0, v_S), \text{ or } (0, v_S, v_S) && (4.55)
\end{aligned}$$

It is interesting to note that the same flavon field ϕ_S and the ratio $\frac{\langle\phi_S\rangle^2}{\Lambda^2}$ generates the effective coupling of $\eta - \psi - \psi$ as well as $H - \nu_L - \nu_R$ as discussed earlier in equation (4.28). We will use these interactions while discussing the DM phenomenology in the next section.

4.3.1 Freeze-in Dark Matter

In this section, we discuss the details of calculation related to the relic abundance of FIMP DM candidate ψ. As per requirement for such DM [11], the interactions of DM particle with the visible sector ones are so feeble that it never attains thermal equilibrium in the early Universe. In the simplest possible scenario of this type, the DM candidate has negligible initial thermal abundance and gets populated later due to the decay of a mother particle. Such non-thermal DM scenario which gets populated in the Universe through freeze-in (rather than freeze-out of WIMP type scenarios) should have typical coupling of the order 10^{-12} with the decaying mother particle. Unless such decays of mother particles into DM are kinematically forbidden, the contributions of scattering to freeze-in of DM remains typically suppressed compared to the former.

In our model, the fermion ψ naturally satisfies the criteria for being a FIMP DM candidate without requiring highly fine-tuned couplings mentioned above. This is due to the fact that this fermion is a gauge singlet and its leading order interaction to the mother particle η arises only at dimension six level. As discussed in the previous section, the effective Yukawa coupling for $\eta\psi\psi$ interaction is dynamically generated by flavon vev's $Y \sim \frac{v_S^2}{\Lambda^2}$. Now, the decay width of η into two DM particles (ψ) can be written as

$$\Gamma_{\eta\to\psi\psi} = \frac{Y^2\left(m_\eta^2 - 4m_\psi^2\right)\sqrt{1-\frac{4m_\psi^2}{m_\eta^2}}}{8\pi m_\eta} \tag{4.56}$$

where Y is the effective Yukawa coupling, m_η and m_ψ are the masses of the mother particle and ψ respectively. From the transformation of the singlet scalar η under the symmetry group of the model, it is clear that it does not have any linear term in the scalar sector and hence does not have any other decay modes apart from the one into two DM particles. Since this decay is governed by a tiny effective Yukawa coupling, this makes the singlet scalar long lived. However, this singlet scalar can have sizeable quartic interactions with other scalars like the SM Higgs doublet and hence can be thermally produced in the early Universe. Now, considering the mother particle η to be in thermal equilibrium in the early Universe which also decays into the DM particle ψ, we can write down the relevant Boltzmann equations for co-moving number densities of η, ψ as

$$\begin{aligned}\frac{dY_\eta}{dx} &= -\frac{4\pi^2}{45}\frac{M_{\rm Pl}M_{\rm sc}}{1.66}\frac{\sqrt{g_\star(x)}}{x^2}\left[\sum_{p=\text{SM particles}}\langle\sigma{\rm v}\rangle_{\eta\eta\to p\bar{p}}\left(Y_\eta^2-(Y_\eta^{\rm eq})^2\right)\right] \\ &\quad -\frac{M_{\rm Pl}}{1.66}\frac{x\sqrt{g_\star(x)}}{M_{\rm sc}^2\ g_s(x)}\Gamma_{\eta\to\bar{\psi}\psi}\ Y_\eta,\end{aligned} \tag{4.57}$$

$$\frac{dY_\psi}{dx} = \frac{2M_{\rm Pl}}{1.66}\frac{x\sqrt{g_\star(x)}}{M_{\rm sc}^2\ g_s(x)}\Gamma_{\eta\to\bar{\psi}\psi}\ Y_\eta \tag{4.58}$$

where $x = \dfrac{M_{\rm sc}}{T}$, is a dimensionless variable while $M_{\rm sc}$ is some arbitrary mass scale which we choose equal to the mass of η and $M_{\rm Pl}$ is the Planck mass. Moreover, $g_s(x)$ is the number

of effective degrees of freedom associated to the entropy density of the Universe and the quantity $g_\star(x)$ is defined as

$$\sqrt{g_\star(x)} = \frac{g_s(x)}{\sqrt{g_\rho(x)}} \left(1 - \frac{1}{3}\frac{\mathrm{d}\ln g_s(x)}{\mathrm{d}\ln x}\right) . \tag{4.59}$$

Here, $g_\rho(x)$ denotes the effective number of degrees of freedom related to the energy density of the Universe at $x = \dfrac{M_{\rm sc}}{T}$. The first term on the right hand side of the Boltzmann equation (4.57) corresponds to the self annihilation of η into SM particles and vice versa which play the role in its freeze-out. The second term on the right hand side of this equation corresponds to the dilution of η due to its decay into DM ψ. Let us denote the freeze-out temperature of η as T_F and its decay temperature as T_D. If we assume that the mother particle freezes out first followed by its decay into DM particles, we can consider $T_F > T_D$. In such a case, we can first solve the Boltzmann equation for η considering only the self-annihilation part to calculate its freeze-out abundance.

$$\frac{dY_\eta}{dx} = -\frac{4\pi^2}{45}\frac{M_{\rm Pl}M_{\rm sc}}{1.66}\frac{\sqrt{g_\star(x)}}{x^2}\left[\sum_{p={\rm SM\ particles}} \langle\sigma {\rm v}\rangle_{\eta\eta\to p\bar{p}} \left(Y_\eta^2 - (Y_\eta^{\rm eq})^2\right)\right] \tag{4.60}$$

Then we solve the following two equations for temperature $T < T_F$

$$\frac{dY_\eta}{dx} = -\frac{M_{\rm Pl}}{1.66}\frac{x\sqrt{g_\star(x)}}{M_{\rm sc}^2\ g_s(x)}\Gamma_{\eta\to\bar{\psi}\psi}\ Y_\eta, \tag{4.61}$$

$$\frac{dY_\psi}{dx} = \frac{2M_{\rm Pl}}{1.66}\frac{x\sqrt{g_\star(x)}}{M_{\rm sc}^2\ g_s(x)}\Gamma_{\eta\to\bar{\psi}\psi}\ Y_\eta. \tag{4.62}$$

We stick to this simplified assumption $T_F > T_D$ in this work and postpone a more general analysis without any assumption to an upcoming work. The assumption $T_F > T_D$ allows us to solve the Boltzmann equation (4.60) for η first, calculate its freeze-out abundance and then solve the corresponding equations (4.61), (4.62) for η, ψ using the freeze-out abundance of η as initial condition[8]. In such a scenario, we can solve the Boltzmann equations (4.61), (4.62) for different benchmark choices of $Y, m_\eta, m_{\rm DM} \equiv M_\psi$ and estimate the freeze-out abundance of η that can generate $\Omega h^2 = 0.12$, the *canonical* value of the DM (ψ) relic abundance in the present Universe. This required freeze-out abundance of η then restricts the parameters involved in its coupling to the SM particles. It turns out that a scalar singlet like η interacts with the SM particles only through the Higgs portal and hence depends upon the $\eta - H$ coupling, denoted by $\lambda_{H\eta}$. In figure 4.13, we show different benchmark scenarios that give rise to the correct relic abundance of DM. In the left panel of figure 4.13, we show the abundance of both η (after its thermal freeze-out) and ψ for benchmark values of their masses ($m_\eta = 200$ GeV, $m_{\rm DM} = 1$ GeV) as a function of temperature for three different values of Yukawa coupling $Y = 10^{-13}, 10^{-12}, 10^{-11}$. It can be clearly seen that while the

[8]Recently another scenario was proposed where the DM freezes out first with underproduced freeze-out abundance followed by the decay of a long lived particle into DM, filling the deficit [389].

freeze-out abundance of η drops due to its decay into ψ, the abundance of the latter grows. The value of $\eta - H$ coupling is chosen to be $\lambda_{H\eta} = 0.004$ in order to generate the correct freeze-out abundance of η which can later give rise to the required DM abundance through its decay. It can be seen that, once we fix the ψ and η masses, the final abundance of ψ does not depend upon the specific Yukawa coupling Y as η dominantly decays into ψ only. However, different values of Y can lead to different temperatures at which the freeze-in of ψ occurs, as seen from the left panel of figure 4.13. The right panel of figure 4.13 shows the relic abundance of DM for a fixed value of Yukawa coupling $Y = 10^{-12}$ but three different benchmark choices of $m_\eta, m_{\rm DM}$ where the $\lambda_{H\eta}$ parameter is chosen appropriately in each case so as to generate the correct freeze-out abundance of η.

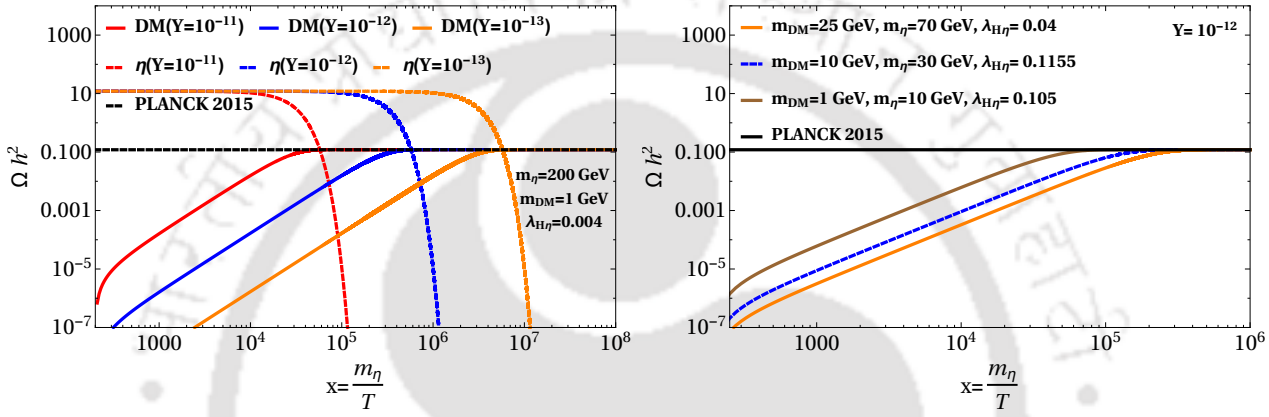

Figure 4.13: Left panel: Relic abundance of η and DM (ψ) as a function of temperature for different benchmark values of Yukawa coupling Y. Right panel: Relic abundance of DM (ψ) as a function of temperature for different benchmark values of ψ and η masses and fixed Yukawa $Y = 10^{-12}$.

The freeze-out abundance of η can be calculated similar to the way the relic abundance of scalar singlet DM is calculated. For the details of scalar singlet DM, one may refer to the recent article [431] and references therein for earlier works. In figure 4.14, we show the parameter space of scalar singlet η in terms of $\lambda_{H\eta}, m_\eta$ that can give rise to the required freeze-out abundance in order to generate the correct FIMP abundance through $\eta \to \psi\psi$ decay. In this plot, the resonance region is clearly visible at $m_\eta = m_h/2$ where $m_h \approx 125$ GeV is the SM like Higgs boson. The parameter space corresponding to DM mass of 50 GeV is seen only at the extreme right end of the plot in figure 4.14 due to the requirement of $m_\eta \geq 2m_{\rm DM}$ to enable the decay of ψ into two DM candidates. Since η is long lived and it decays only into DM at leading order, any production of η at experiments like the LHC could be probed through invisible decay of SM like Higgs. However, this constraint is applicable only for DM mass $m_\eta < m_h/2$. The invisible decay width is given by

$$\Gamma(h \to \text{Invisible}) = \frac{\lambda_{H\eta}^2 v^2}{64\pi m_h}\sqrt{1 - 4\,m_\eta^2/m_h^2} \tag{4.63}$$

The latest constraint on invisible Higgs decay from the ATLAS experiment at the LHC

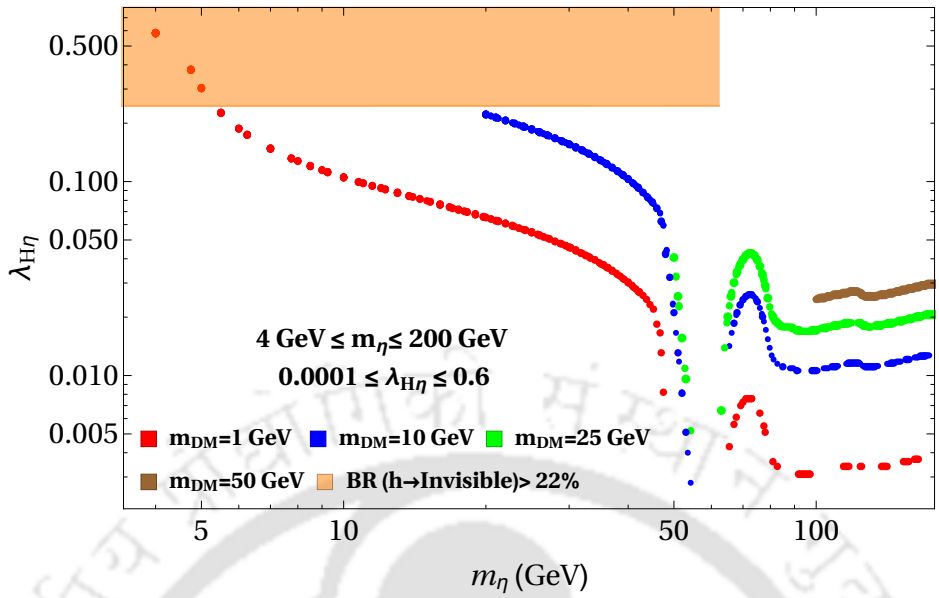

Figure 4.14: The allowed parameter space in $\lambda_{H\eta}$-m$_\eta$ plane for different DM masses which gives rise to the required freeze-out abundance of η followed by the correct DM abundance from η decay.

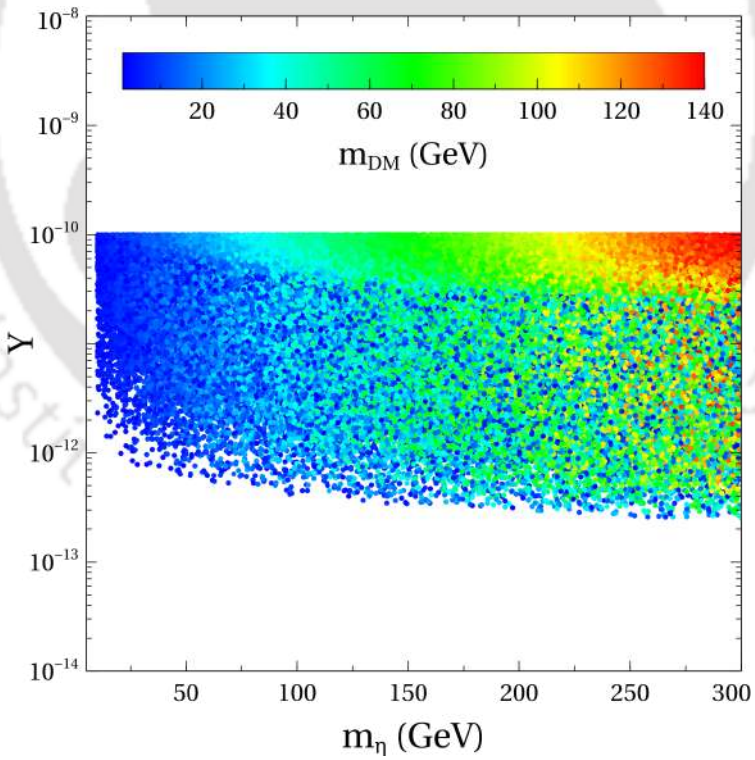

Figure 4.15: Parameter space for Yukawa coupling and η-DM masses that satisfy the upper and lower bounds on lifetime of $\eta : T_{\rm BBN} < T_D < T_F$.

is [292]

$$\mathrm{BR}(h \to \text{Invisible}) = \frac{\Gamma(h \to \text{Invisible})}{\Gamma(h \to \text{Invisible}) + \Gamma(h \to \text{SM})} < 22\%.$$

We incorporate this in figure 4.14 and find that some part of parameter space in $\lambda_{H\eta}$-m$_\eta$ plane can be excluded for low DM masses $m_{\mathrm{DM}} < 10$ GeV by LHC constraints.

Although we are considering a simplified case where the decay of mother particle occurs after the mother particle freezes out $T_F > T_D$, we note that this decay can not be delayed indefinitely. Considering the successful predictions of big bang nucleosynthesis (BBN) which occurs around typical time scale $t \sim 1$ s, we constrain the lifetime of η to be less than this BBN epoch so as not to alter the cosmology post-BBN era. The upper and lower bound on η lifetime therefore, constrains the corresponding Yukawa which we show as a scan plot in figure 4.15 for different values of η and DM masses. DM masses are also varied in such a way that $m_\eta \geq 2m_{\mathrm{DM}}$ is satisfied. We have not incorporated the constraints on DM relic abundance in figure 4.15, as we still have freedom in choosing $\lambda_{H\eta}$ that can decide the freeze-out abundance of η required for producing correct DM abundance through freeze-in. We leave a more general scan of such parameter space to an upcoming work.

It should be noted that we did not consider the production of DM from the decay of the flavon ζ responsible for its mass, as shown in equation (4.51). Since we intended to explain FIMP coupling and Dirac neutrino mass through same dimension six couplings, we did not take this dimension five term into account. This can be justified if we consider the masses of such flavons to be larger than the reheat temperature of the Universe, so that any contribution to FIMP production from ζ decay is Boltzmann suppressed. For example, the authors of [432] considered such heavy mediators having mass greater than the reheat temperature, in a different DM scenario. We also note that there was no contribution to FIMP production through annihilations in our scenario through processes like SM, SM $\to \psi\psi$ with η being the mediator. This is justified due to the specific flavour transformations of η and the fact that η does not acquire any vev.

CHAPTER 5

Summary

In this thesis, a few particle physics models have been discussed to address the puzzles of DM and neutrino mass. We have investigated both thermal as well as non-thermal DM scenarios. In chapter 2, we have discussed three different WIMP DM scenarios within gauged $B-L$ extension of the SM. In section 2.3, we have proposed a framework for the common origin of neutrino mass and DM within a $U(1)_{B-L}$ gauge extension of the SM so that the fermion fields responsible for radiative neutrino mass and DM phenomenology can also keep the $U(1)_{B-L}$ model anomaly free. DM is stabilized by a remnant symmetry after the spontaneous breaking of the $U(1)_{B-L}$ gauge symmetry, without requiring any ad-hoc symmetry to guarantee stability. We discuss both scalar and fermion DM in two different versions of the model and show that the model, apart from predicting a vanishing lightest neutrino mass scenario, can have signatures at a cosmic, intensity as well as energy frontier experiments. Ongoing and near-future experiments in all these three frontiers will probe a significant region of parameter space of the proposed model.

In section 2.4 of this chapter, we have proposed a gauged $U(1)_{B-L}$ version of the type III seesaw model, which naturally predicts a two-component Dirac fermion DM scenario due to the requirements of anomaly cancellation. Unlike type I seesaw scenario in $U(1)_{B-L}$ model where three right-handed singlet neutrinos with $B-L$ charge -1 each leads to cancellation of all anomalies without any need of additional chiral fermions, type III seesaw implementation leads to additional anomalies due to the non-trivial $SU(2)_L$ structure of triplet fermions. We show that a gauged $U(1)_{B-L}$ model with three fermion triplets required for type III seesaw can be anomaly free due to the presence of two neutral Dirac fermions having fractional $B-L$ charges. Both of these fermions are naturally stable due to a remnant $\mathbb{Z}_2 \times \mathbb{Z}_2'$ symmetry. We study the DM phenomenology of the two-component DM scenario in the model after incorporating all relevant theoretical and experimental bounds. Among the theoretical bounds, the bounded from below criteria of the scalar potential plays a crucial role in restricting the parameter space. The relic abundance of the DM candidates is primarily dictated by their annihilations into SM particles mediated by Z_{BL} as well as additional singlet scalars. We find the parameter space allowed from total relic abundance criteria and then apply the bounds from direct detection experiments on individual DM candidates. We find that all these constraints tightly constrain the parameter space which we scan through in our study, leaving a small region that can be probed at experiments operational at different frontiers. Finally, we comment upon one interesting prospect of probing this model through

the production of charged components of fermion triplets at colliders. The presence of additional neutral gauge boson Z_{BL} can significantly enhance the production cross-section of charged triplets at LHC or 100 TeV future proton-proton collider compared to the usual type III seesaw extension of SM. The charged components can then decay into the neutral ones and a pion with a long decay lifetime, leaving a disappearing charged track signature. Comparing with the ATLAS bounds on such signatures, we find that such triplets with masses up to 500 GeV or so can already be ruled out. While the charged components of fermion triplets can be probed via such disappearing charged track signatures, the neutral components, if long-lived enough, could be probed at proposed future experiments like MATHUSLA [433]. These triplets, however, do not affect the DM phenomenology much apart from opening another DM annihilation channel to triplet fermions whenever allowed kinematically.

Finally, in the last section 2.5, we have proposed a gauged $B-L$ model where light Dirac neutrinos and two-component fermion DM can be realized without invoking the presence of additional discrete symmetries. The novel feature of this model is the possibility of sub-eV Dirac neutrino mass at tree level and the existence of two stable fermion DM candidates within a minimal gauged $B-L$ symmetric framework. The right-handed part of light Dirac neutrino and the two Dirac fermion DM candidates have appropriate $B-L$ charges to make the model anomaly free. The chosen $B-L$ charge of right-handed part of light Dirac neutrino not only dictates the origin of Dirac neutrino mass from a neutrinophillic Higgs doublet with appropriate $B-L$ charge but also gives rise to the possibility of two stable fermion DM whose $B-L$ charges are related to that of right-handed neutrinos via anomaly cancellation conditions. The scalar sector of the model is chosen in such a way that it not only gives rise to the desired particle masses but also leaves a remnant $\mathbb{Z}_2 \times Z_2'$ symmetry after spontaneous symmetry breaking to stabilize the two DM candidates. We constrain the model parameters from different available constraints, both theoretical as well as experimental. After showing the behaviour of DM relic density for different choices of benchmark parameters, we perform a numerical scan to show the available parameter space in terms of DM masses and the parameters of the $B-L$ gauge sector, namely, $g_{BL}, M_{Z_{BL}}$. Apart from the usual bounds from LEP, LHC, DM direct detection, DM relic density constraints, the strongest bound for $M_{Z_{BL}} > 3$ TeV comes from BBN, CMB limits on the effective number of relativistic degrees of freedom. This interesting situation arises due to the Dirac nature of light neutrinos, which introduces additional relativistic species (right-handed part of light Dirac neutrinos) that can be thermalised in the early Universe due to their sizeable $B-L$ gauge interactions. Thus, the model not only allows the possibility of sub-eV Dirac neutrino mass with two-component fermion DM from the requirement of canceling triangle anomalies but also leads to new contributions to $\Delta N_{\rm eff}$ that can be probed by future CMB experiments. The model also remains within reach of ongoing as well as near-future direct detection experiments. Thus the model not only offers a unified picture of light Dirac neutrino and multi-component DM but also allows the tantalising possibility of probing it at experiments operating at different frontiers.

In chapter 3, we have studied the minimal left-right symmetric model with Higgs doublets, known as doublet left-right model, where the left-right symmetry is broken spontaneously by Higgs doublet instead of Higgs triplets in LRSM with type I plus type II seesaw for light neutrino masses. In the minimal DLRM, light neutrino mass can be realised only through the Higgs bidoublet with tiny coupling to neutrinos leading to sub-eV Dirac neutrino mass.

Due to $SU(2)_R \times U(1)_{B-L}$ gauge interactions, the right-handed neutrinos can thermalise in the early Universe, thereby contributing to the effective relativistic degrees of freedom $N_{\rm eff}$ which is tightly constrained by CMB measurements. We constrain the scale of left-right symmetry from the requirement of satisfying Planck 2018 bound on $\Delta N_{\rm eff}$ not only for pure left-right symmetric limit $g_R = g_L$ but also for other values of g_R. While g_R, g_{BL} can not be chosen arbitrarily in LRSM due to their relation with $U(1)_Y$ coupling of SM, the parameter space gets tightly constrained. For $g_R = g_L$, Planck 2018 bound at 2σ CL can rule out W_R mass all the way up to 4.06 TeV, which is as competitive as the existing collider bounds on W_R from dijet resonance searches. For example, ATLAS dijet resonance search rules out such additional charged vector boson mass up to 4 TeV [355] while similar analysis by CMS rules out up to 3.6 TeV for SM like gauge couplings [356]. Our conclusions also agree with the recent model-independent calculations [434] where, considering four fermion interactions of right-handed neutrinos and their contribution to $N_{\rm eff}$, the authors constrained the interaction strength to be $10^{-5} - 10^{-3}$ times the usual Fermi coupling constant. This bound we derive here that is, $M_{W_R} > 4.06$ TeV can be made weaker for smaller values of g_R. For example, in case of $g_R = 0.5$, we get $M_{W_R} > 3.17$ TeV and $g_R = 0.4$ leads to $M_{W_R} > 2.77$ TeV. We also make a comparison with similar constraints derived in $U(1)_{B-L}$ gauge model with light Dirac neutrinos where due to the freedom in choosing the gauge coupling arbitrarily, one can have a much lighter $B - L$ gauge boson as well. However, the choices of g_R as well as g_{BL} are not arbitrary in DLRM due to their non-trivial connection to g_Y of SM. While we perform our analysis without explicitly solving the Boltzmann equations, the conclusions do not change much as long as the decoupling temperature of right-handed neutrinos remains much higher than that of active neutrinos. This was also noted by the authors of [434], and our parameter space is precisely confined to this regime.

We also show the impact of $\Delta N_{\rm eff}$ constraints on DM parameter space in DLRM. While DLRM does not have a DM candidate on its own, we incorporate the presence of an additional fermion quintuplet DM in the minimal DM spirit. Since such a real fermion quintuplet does not have any renormalisable coupling with other fermions or scalars of DLRM, the relic abundance of DM, the neutral component of right-handed fermion quintuplet, depends crucially on its annihilation and coannihilation mediated by W_R, Z_R gauge bosons. We constrain the parameter space satisfying correct DM relic by using the respective $\Delta N_{\rm eff}$ bounds for different g_R. We find available parameter space satisfying correct DM relic even after applying Planck 2018 bound on $\Delta N_{\rm eff}$ at 2σ CL.

We also compare our results in view of more stringent Planck 2018 1σ bound $N_{\rm eff} = 2.99 \pm 0.17$, which rules out all the parameter space if we assume only SM plus three right-handed neutrinos to be contributing to the relativistic degrees of freedom (DOF) below the scale of left-right symmetry breaking. However, if there are more relativistic degrees of freedom due to the presence of light physical fields resulting from the scalar and fermion multiplets, one can satisfy the Planck 2018 1σ bound as well. In figure 3.8, we have shown the required additional DOF in the early universe as a function of temperature. Additionally, possible UV completion of this minimal model in order to explain the tiny origin of Dirac neutrino mass naturally [210, 226–228, 230, 231, 358, 359] may involve additional interaction portals of right-handed neutrinos to thermalise with the standard bath. While the strength of these portals can be tuned with more freedom compared to the gauge portals discussed in this work and hence are unlikely to put stronger constraints than what we obtain here,

it will be interesting to study the details of such scenarios, especially in the context of DM and collider phenomenology.

In the last chapter 4, we have discussed two different scenarios. In section 4.2, we have studied a minimal model for DM and radiative neutrino mass where DM relic abundance is generated from a hybrid setup consisting of both freeze-out and freeze-in scenarios. Considering a radiative type III seesaw scenario with the lightest fermion triplet being the DM candidate stabilised by an in built $\mathbb{Z}_2$ symmetry, we first show how the neutral component of this fermion triplet having mass around 1 TeV remains under-abundant from thermal freeze-out mechanism. We then consider a non-thermal (freeze-in) contribution from the late decay of $\mathbb{Z}_2$-odd scalar doublet to fill the deficit created during thermal freeze-out. We solve the coupled Boltzmann equations involving the mother particles and the DM candidate and find the parameter space that can lead to the correct relic abundance of DM. Due to the coupled nature of these equations, we can simultaneously constrain both DM as well as mother particle parameter space. The mother particle, being heavy, freezes out first, followed by the freeze-out of DM and then the late decay of the mother particle into the DM particles. Such a hybrid setup has some interesting differences from the usual freeze-in DM scenarios. One notable difference we found was the dependence of non-thermal contribution on the corresponding Yukawa coupling between mother particle and DM. In the usual FIMP scenario, the non-thermal contribution always increases with such Yukawa, while in the present case, it is not necessarily so. This is due to the role of the same Yukawa coupling in deciding the freeze-out abundance of the mother particle, which later gets converted into a non-thermal part of DM through late decay.

Apart from satisfying the correct relic abundance of DM within this hybrid setup having distinguishable features from pure WIMP and pure FIMP scenarios, the model also has promising detection prospects at collider, direct and indirect detection experiments. The presence of a scalar singlet that generates the DM mass dynamically in this model plays a non-trivial role in keeping the model parameter space not only allowed from current experimental constraints but also very close to present as well as upcoming experimental sensitivity leaving a very promising scope for verifiability. This is in contrast to the typical freeze-in DM models, which have very limited detection prospects due to tiny couplings. In principle, any mass of DM in the thermally under-abundant regime ($M_{\psi_1^0} \leq 2.2$ TeV) can be revived by adding a non-thermal contribution. However, due to tight constraints from LHC (evident from figure 4.7), we get a lower bound of around 500 GeV. Also, as we go above 1 TeV mass, the indirect detection constraints become severe (evident from figure 4.10), requiring large couplings of DM with the singlet scalar. Such large couplings will get large corrections under renormalisation group evolutions, making the model non-perturbative at a low scale. Therefore we stick to a mass window near the 1 TeV.

In the neutrino sector also this model remains predictive as the lightest neutrino mass is vanishingly small due to tiny Yukawa couplings of the lightest fermion triplet, required for its non-thermal production at late epochs. Such vanishing lightest neutrino mass can have interesting consequences at experiments sensitive to the absolute neutrino mass scale. However, the model suffers from the fine-tuning issue related to the above mentioned Yukawa coupling of the lightest fermion triplet to the leptons. Such tiny couplings can be generated within the framework of more general scenarios, some of which also provide a UV completion [239, 393, 435].

In section 4.3, we have proposed a scenario that can simultaneously explain the tiny Yukawa coupling required for Dirac neutrino masses from the SM Higgs field and the coupling of non-thermal DM populating the Universe through the freeze-in mechanism. The proposed scenario is based on the dynamical origin of such tiny couplings from a flavour symmetric scenario based on discrete non-abelian group A_4 that allows such couplings at dimension six level only, thereby explaining their smallness naturally. The A_4 flavour symmetry is augmented by additional discrete symmetries like Z_N and a global lepton number symmetry to forbid the unwanted terms from the Lagrangian. The charged lepton and DM masses are generated at dimension five level while the sub-eV Dirac neutrino masses arise only at dimension six level. The correct leptonic mixing can be produced depending on the alignment of flavon vev's. One such alignment which we analyse numerically predicts a normal hierarchical pattern of light neutrino masses and interesting correlations between neutrino oscillation parameters. The atmospheric mixing angle is preferred to be in the lower octant for maximal Dirac CP phase in this scenario.

In the DM sector, the effective coupling of non-thermal DM (ψ, a singlet fermion) with its mother particle (η, a singlet scalar) arises at dimension six level through the same flavons responsible for neutrino mass. The mother particle, though restricted to decay only to the DM particles at cosmological scales, can have sizeable interactions with the SM sector through Higgs portal couplings. Adopting a simplified scenario where the mother particle freezes out first and then decays into the DM particles, we first calculate the freeze-out abundance of η and then calculate the DM abundance from η decay. Although such non-thermal or freeze-in massive particle DM remains difficult to be probed due to tiny couplings, its mother particle can be produced at ongoing experiments like the LHC. We, in fact, show that some part of the mother particle's parameter space can be constrained from the LHC limits on the invisible decay rate of the SM like Higgs boson, and hence can be probed in near future data. Since η is long-lived, its decay into DM particles on cosmological scales can be constrained if we demand such a decay to occur before the BBN epoch. We find the lower bound on Yukawa coupling Y governing the decay of η into DM and show it to be larger than around 10^{-13}.

Until now, we have discussed a few particle physics models to find the origin of cold dark matter and its connection to neutrino mass. We have confronted the validity of those models in the light of observational and experimental data. However, the models with lighter dark matter particles has not been discussed in this thesis. However, such scenarios are motivated from different astrophysical and cosmological anomalies and can have interesting consequences in different ongoing experiments looking for sub-GeV scale dark matter particles. For example, one of the most prominent issues in cosmology is the so-called "Hubble Tension". It represents an unsolved issue in cosmology: measurement of the Hubble constant H_0, which tells us how fast the universe is expanding, does not agree with each other. I want to explore such scenarios in my future whether the DM has any connection to this anomaly. In addition to the study of sub-GeV dark matter scenarios, it will also be interesting to study the possible ways of distinguishing Dirac vs Majorana light neutrinos in the light of cosmology, the magnetic moment of neutrino, neutrinoless double/quadrupole beta decay, cosmic neutrino background, etc.

APPENDIX A

Here we have shown some detail calculations regarding the works discussed in chapter 2.

A.1 Important vertices

Here we list the relevant vertices of different interactions, derived from the Lagrangian in 2.3. They are used in calculation of different cross sections and decay widths. Some notations are defined in the table A.2 followed by the interaction vertices in table A.1.

Table A.1: All new possible vertices

Interactions	Vertices	Interactions	Vertices
$\eta^{0r}\ \eta^{0r}\ h$	$\lambda_L v$	$\eta^{0r}\ \eta^{0r}\ \phi_1$	$\lambda_{\eta\phi_1} u_1$
$\eta^{+}\ \eta^{-}\ h$	$\lambda_L v - (M^2_{\eta^{0r}} + M^2_{\eta^{0i}} - 2M^2_{\eta^{+}})/v$	$\eta^{+}\ \eta^{-}\ \phi_1$	$\lambda_{\eta\phi_1} u_1$
$\eta^{0i}\ \eta^{0i}\ h$	$\lambda_L v = (\lambda_{H\eta} + \lambda'_{H\eta})v$	$\eta^{0i}\ \eta^{0i}\ \phi_1$	$\lambda_{\eta\phi_1} u_1$
$\eta^{0i}\ \eta^{0i}\ h\ h$	$2\lambda_L$	$\eta^{0r}\ \eta^{0r}\ Z\ Z$	$(ig^2/2\cos^2\theta_w)g_{\mu\nu}$
$\eta^{+}\ \eta^{-}\ h\ h$	$\lambda_L - (M^2_{\eta^{0r}} + M^2_{\eta^{0i}} - 2M^2_{\eta^{+}})/v^2$	$\eta^{+}\ \eta^{-}\ \gamma$	$-ie$
$\eta^{0r}\ \eta^{0r}\ h\ h$	$2\lambda_L$	$\eta^{0I}\ \eta^{-}\ W^{+}$	$g/2$
$\phi_1\ h\ h$	$i(\lambda_{H\phi_1}\ u_1/2)$	$\eta^{+}\ \eta^{-}\ W^{+}\ W^{-}$	$(ig^2/2)g_{\mu\nu}$
$\eta^{0r}\ \eta^{-}\ W^{+}$	$g/2$	$\eta^{0R}\ \eta^{0I}\ Z_{BL}$	$i\ n_\eta\ g_{BL}$
$\eta^{+}\ \eta^{-}\ Z\ Z$	$(ig^2(1-2\sin^2\theta_w)^2/2\cos^2\theta_w)g_{\mu\nu}$	$\phi_1\ f\ f$	$(i\ \xi\ m_f/v)$
$\eta^{+}\ \eta^{-}\ Z$	$(-ig(1-2\sin^2\theta_w)/2\cos\theta_w)$	$\phi_1\ W^{+}\ W^{-}$	$ig\ m_W\ g_{\mu\nu}$
$\eta^{0I}\ \eta^{0I}\ Z\ Z$	$(ig^2/2\cos^2\theta_w)g_{\mu\nu}$	$\phi_1\ Z\ Z$	$(ig\ m_Z/\cos\theta_w)\ g_{\mu\nu}$
$\eta^{0r}\ \eta^{0i}\ Z$	$(g/2\cos\theta_w)$	$f\ f\ Z_{BL}$	$-i\ n_f\ g_{BL}\ \gamma^\mu$
$\eta^{0r}\ \eta^{0r}\ W^{+}\ W^{-}$	$(ig^2/2)g_{\mu\nu}$	$\chi\ \chi\ \phi_1$	$-f/2$
$\eta^{0I}\ \eta^{0I}\ W^{+}\ W^{-}$	$(ig^2/2)g_{\mu\nu}$	$\chi\ \chi\ Z_{BL}$	$i\ n_\chi\ g_{BL}\ \gamma^\mu\ R$
$\eta^{+}\ \eta^{-}\ \gamma\ \gamma$	$2ie^2 g_{\mu\nu}$		

Table A.2: Relevant Parameters for Interaction Vertices

$\lambda_L = (\lambda_{H\eta} + \lambda'_{H\eta})$
$n_f = U(1)_{B-L}$ charge of SM fermions
$n_\eta = U(1)_{B-L}$ charge of η
$n_\chi = U(1)_{B-L}$ charge of χ
$\lambda_{H\phi_1} = \frac{m^2_{\phi_1} - m^2_h}{2vu_1}\xi$
$f = \frac{m_\chi}{u_1}$

A.2 Diagonalisation of mass matrix of real scalars

In this section, we have shown some calculation for the diagonalisation of the scalar mass matrix given in section 2.4. We have listed all the elements of the diagonalising matrix $\mathcal{O}$ of $\mathcal{M}_{rs}$ in terms of mixing angles under the assumption that all the mixing angles among the singlet scalars are identical and equal to θ_{24}:

$$
\begin{aligned}
\mathcal{O}_{11} &= c_{12}\, c_{13}\, c_{14}, \\
\mathcal{O}_{12} &= c_{13}\, c_{14}\, s_{12}, \\
\mathcal{O}_{13} &= c_{14}\, s_{13}, \\
\mathcal{O}_{14} &= s_{14}, \\
\mathcal{O}_{21} &= -c_{12}\, c_{13}\, s_{14}\, s_{24} - c_{12}\, c_{24}\, s_{13}\, s_{24} - c^2_{24}\, s_{12}, \\
\mathcal{O}_{22} &= c_{12}\, c^2_{24} - c_{13}\, s_{12}\, s_{14}\, s_{24} - c_{24}\, s_{12}\, s_{13}\, s_{24}, \\
\mathcal{O}_{23} &= c_{13}\, c_{24}\, s_{24} - \ s_{13}\, s_{14}\, s_{24}, \\
\mathcal{O}_{24} &= c_{14}\, s_{24}, \\
\mathcal{O}_{31} &= -c_{12}\, c_{13}\, c_{24}\, s_{14}\, s_{24} - c_{12}\, c^2_{24}\, s_{13} + c_{12}\, s_{13}\, s^3_{24} + c_{24}\, s_{12}\, s^2_{24} + c_{24}\, s_{12}\, s_{24}, \\
\mathcal{O}_{32} &= -c_{24}\ \left(c_{12}\, s^2_{24} + c_{24}\, s_{12}\, s_{13}\right) - c_{12}\, c_{24}\, s_{24} + s_{12}\, s_{24}\left(s_{13}\, s^2_{24} - c_{13}\, c_{24}\, s_{14}\right), \\
\mathcal{O}_{33} &= c_{13}\, c^2_{24} - c_{13}\, s^3_{24} - c_{24}\, s_{13}\, s_{14}\, s_{24}, \\
\mathcal{O}_{34} &= c_{14}\, c_{24}\, s_{24}, \\
\mathcal{O}_{41} &= s_{12}\, (c^2_{24}\, s_{24} - s^2_{24}) + c_{12}\, (-c_{13}\, c^2_{24}\, s_{14} + s_{13}\, (c_{24}\, s_{24} + c_{24}\, s^2_{24})), \\
\mathcal{O}_{42} &= -c_{13}\, c^2_{24}\, s_{12}\, s_{14} + c_{12}\, (-c^2_{24}\, s_{24} + s^2_{24}) + s_{12}\, s_{13}(c_{24}\, s_{24} + c_{24}\, s^2_{24}), \\
\mathcal{O}_{43} &= -c^2_{24}\, s_{13}\, s_{14} - c_{13}(c_{24}\, s_{24} + c_{24}\, s^2_{24}), \\
\mathcal{O}_{44} &= c_{14}\, c^2_{24}\,.
\end{aligned}
$$

Here, we have denoted $c_{ij} \equiv \cos\theta_{ij}$ and $s_{ij} \equiv \sin\theta_{ij}$ respectively. Now, using the elements of the diagonalising matrix, the physical scalar fields can be expressed as a linear combinations of unphysical states as

$$h = \mathcal{O}_{11}h' + \mathcal{O}_{21}s'_1 + \mathcal{O}_{31}s'_2 + \mathcal{O}_{41}s'_3\,, \tag{A.1}$$
$$s_1 = \mathcal{O}_{12}h' + \mathcal{O}_{22}s'_1 + \mathcal{O}_{32}s'_2 + \mathcal{O}_{42}s'_3\,, \tag{A.2}$$
$$s_2 = \mathcal{O}_{13}h' + \mathcal{O}_{23}s'_1 + \mathcal{O}_{33}s'_2 + \mathcal{O}_{43}s'_3\,, \tag{A.3}$$
$$s_3 = \mathcal{O}_{14}h' + \mathcal{O}_{24}s'_1 + \mathcal{O}_{34}s'_2 + \mathcal{O}_{44}s'_3\,. \tag{A.4}$$

A.3 Diagonalisation of mass matrix of pseudo scalars

The pseudo scalar mass matrix discussed in equation (2.57) with respect to the basis state $\frac{1}{\sqrt{2}}\left(A_1'\ A_2'\ A_3'\right)^T$ is given by

$$\mathcal{M}_{ps} = \begin{pmatrix} -2u\left(u\,\beta+\sqrt{2}\,\delta\right) & u^2\,\beta & u\left(-u\,\beta+\sqrt{2}\,\delta\right) \\ u^2\,\beta & -\frac{u}{2}\left(u\,\beta+\sqrt{2}\,\zeta\right) & \frac{u}{2}\left(u\,\beta+2\sqrt{2}\,\zeta\right) \\ u\left(-u\,\beta+\sqrt{2}\,\delta\right) & \frac{u}{2}\left(u\,\beta+2\sqrt{2}\,\zeta\right) & -\frac{u}{2}\left(u\,\beta+\sqrt{2}(\delta+4\,\zeta)\right) \end{pmatrix}.$$

As expected, the pseudo scalar mass matrix is also real symmetric. Therefore, the matrix $\mathcal{M}_{ps}$ can be diagonalised by a 3×3 orthogonal matrix and the corresponding eigenvalues are given below,

$$\begin{aligned} m^2_{A_1} &= 0\,, \\ m^2_{A_2} &= \frac{-6\beta u^4 - 5\sqrt{2}u^3(\delta+\zeta) + \sqrt{2}\sqrt{u^6\left(25\delta^2 - 34\,\delta\zeta + 25\zeta^2 + 18\beta^2u^2 - 12\sqrt{2}\beta u(\delta+\zeta)\right)}}{4u^2}\,, \\ m^2_{A_3} &= -\frac{6\beta u^4 + 5\sqrt{2}u^3(\delta+\zeta) + \sqrt{2}\sqrt{u^6\left(25\delta^2 - 34\,\delta\zeta + 25\zeta^2 + 18\beta^2u^2 - 12\sqrt{2}\beta u(\delta+\zeta)\right)}}{4u^2}\,. \end{aligned} \tag{A.5}$$

A.4 Collision term of the Boltzmann equation for DM conversion process $\xi_2\bar{\xi}_2 \to \xi_1\bar{\xi}_1$

In this section, we have derived the Boltzmann equation for an interaction which converts one type of DM into another i.e. $\xi_2\bar{\xi}_2 \to \xi_1\bar{\xi}_1$, as discussed in section 2.4.3. In this process, both initial and final states particles are DM candidates which are not in thermal equilibrium during and after their freeze-out. The situation is completely different when each type of DM annihilates into the SM particles in thermal equilibrium. The collision term of the Boltzmann equations depends strongly on whether the final state particles in a scattering process are in thermal contact with thermal bath of the Universe or not. This actually modifies the form of the collision term which reduces to the known form when outgoing particles are in thermal equilibrium. The contribution of the process $\xi_2\bar{\xi}_2 \to \xi_1\bar{\xi}_1$ to the collision term of ξ_2 is given by

$$-\frac{g_{\xi_2}}{(2\pi)^3}\int \frac{\mathcal{C}[f_{\xi_2}]}{E_{\xi_2}}\,d^3\vec{p}_{\xi_2}\,, \tag{A.6}$$

$$\begin{aligned} = &-\int d\Pi_{\xi_2} d\Pi_{\bar{\xi}_2} d\Pi_{\xi_1} d\Pi_{\bar{\xi}_1} (2\pi)^4\,\delta^4(p_{\xi_2} + p_{\bar{\xi}_2} - p_{\xi_1} - p_{\bar{\xi}_1})\left|\mathcal{M}_{\xi_2\bar{\xi}_2\to\xi_1\bar{\xi}_1}\right|^2 \times \\ &\left(f_{\xi_2}(|\vec{p}_{\xi_2}|,T)\,f_{\bar{\xi}_2}(|\vec{p}_{\bar{\xi}_2}|,T) - f_{\xi_1}(|\vec{p}_{\xi_1}|,T)\,f_{\bar{\xi}_1}(|\vec{p}_{\bar{\xi}_1}|,T)\right), \end{aligned} \tag{A.7}$$

where, p_i is the four momentum of species i while the corresponding three momentum and energy are denoted by $\vec{p}_i$ and E_i respectively. The phase space factor $d\Pi_i \equiv \frac{g_i\,d^3\vec{p}_i}{(2\,\pi)^3 E_i}$ with g_i

is the internal degrees of freedom of species i having distribution function $f_i(|\vec{p}_i|, T)$. Here we have neglected the factors related to Pauli blocking for fermions (DM candidates) as those are not significant enough for the present context. Furthermore, $|\mathcal{M}_{\xi_2\bar{\xi}_2\to\xi_1\bar{\xi}_1}|^2$ is the Feynman amplitude square of the concerned process $\xi_2\bar{\xi}_2 \to \xi_1\bar{\xi}_1$ and it is spin-averaged over both initial and final states particles. The above collision term can also be as

$$-\int d\Pi_{\xi_2} d\Pi_{\bar{\xi}_2} \int d\Pi_{\xi_1} d\Pi_{\bar{\xi}_1} (2\pi)^4 \, \delta^4(p_{\xi_2} + p_{\bar{\xi}_2} - p_{\xi_1} - p_{\bar{\xi}_1}) \, |\mathcal{M}_{\xi_2\bar{\xi}_2\to\xi_1\bar{\xi}_1}|^2 \exp\left(-\frac{E_{\xi_2} + E_{\bar{\xi}_2}}{T}\right) \times \left(\frac{f_{\xi_2}(|\vec{p}_{\xi_2}|, T)}{\exp\left(-\frac{E_{\xi_2}}{T}\right)} \frac{f_{\bar{\xi}_2}(|\vec{p}_{\bar{\xi}_2}|, T)}{\exp\left(-\frac{E_{\bar{\xi}_2}}{T}\right)} - \frac{f_{\xi_1}(|\vec{p}_{\xi_1}|, T)}{\exp\left(-\frac{E_{\xi_1}}{T}\right)} \frac{f_{\bar{\xi}_1}(|\vec{p}_{\bar{\xi}_1}|, T)}{\exp\left(-\frac{E_{\bar{\xi}_1}}{T}\right)}\right). \tag{A.8}$$

In the denominator of the last term, we have used the energy conservation condition i.e. $E_{\xi_2} + E_{\bar{\xi}_2} = E_{\xi_1} + E_{\bar{\xi}_1}$. The distribution function of a DM species ξ_i which not in equilibrium (both thermally as well as chemically) can be written as $f_{\xi_i} = \exp\left(\frac{\mu_{\xi_i} - E_{\xi_i}}{T}\right)$ with chemical potential $\mu_{\xi_i} \neq 0$ and $\mu_{\xi_i} = 0$ represents the equilibrium distribution function of ξ_i which is just $f^{\rm eq}_{\xi_i} = \exp\left(-\frac{E_{\xi_i}}{T}\right)$. Therefore, one can easily show that $\frac{f_{\xi_i}}{f^{\rm eq}_{\xi_i}} = \frac{n_{\xi_i}}{n^{\rm eq}_{\xi_i}}$, where the number density $n^{(\rm eq)}_{\xi_i}$ is defined as

$$n^{(\rm eq)}_{\xi_i} = \frac{g_{\xi_i}}{(2\pi)^3} \int f^{(\rm eq)}_{\xi_i} \, d^3\vec{p}_{\xi_i}. \tag{A.9}$$

Using this, the terms within the brackets in equation (A.8) can be replaced by number densities of ξ_1 and ξ_2 as

$$-\int d\Pi_{\xi_2} d\Pi_{\bar{\xi}_2} \left\{\int d\Pi_{\xi_1} d\Pi_{\bar{\xi}_1} (2\pi)^4 \, \delta^4(p_{\xi_2} + p_{\bar{\xi}_2} - p_{\xi_1} - p_{\bar{\xi}_1}) \, |\mathcal{M}_{\xi_2\bar{\xi}_2\to\xi_1\bar{\xi}_1}|^2\right\} \times \exp\left(-\frac{E_{\xi_2} + E_{\bar{\xi}_2}}{T}\right) \left(\frac{n_{\xi_2}}{n^{\rm eq}_{\xi_2}} \frac{n_{\bar{\xi}_2}}{n^{\rm eq}_{\bar{\xi}_2}} - \frac{n_{\xi_1}}{n^{\rm eq}_{\xi_1}} \frac{n_{\bar{\xi}_1}}{n^{\rm eq}_{\bar{\xi}_1}}\right). \tag{A.10}$$

Now, the quantity within the curly brackets is equal to $4\,\sigma {\rm v}\, E_{\xi_2} E_{\bar{\xi}_2}$ with σ being the annihilation cross section of $\xi_2\bar{\xi}_2 \to \xi_1\bar{\xi}_1$. Substituting this in the above we get

$$-\left\{\frac{1}{n^{\rm eq}_{\xi_2} n^{\rm eq}_{\bar{\xi}_2}} \int \frac{d^3\vec{p}_{\xi_2}}{(2\pi)^3} \frac{d^3\vec{p}_{\bar{\xi}_2}}{(2\pi)^3} (\sigma {\rm v})_{\xi_2\bar{\xi}_2\to\xi_1\bar{\xi}_1} \exp\left(-\frac{E_{\xi_2} + E_{\bar{\xi}_2}}{T}\right)\right\} \times \left(n_{\xi_2} \, n_{\bar{\xi}_2} - \frac{n^{\rm eq}_{\xi_2}}{n^{\rm eq}_{\xi_1}} \frac{n^{\rm eq}_{\bar{\xi}_2}}{n^{\rm eq}_{\bar{\xi}_1}} n_{\xi_1} \, n_{\bar{\xi}_1}\right), \tag{A.11}$$

where, the quantity within curly brackets is the thermal averaged cross section $\langle \sigma {\rm v}_{\xi_2\bar{\xi}_2\to\xi_1\bar{\xi}_1}\rangle$. Therefore, in terms of the thermal averaged cross section, the collision term of ξ_2 due to DM conversion process is given by

$$-\langle \sigma {\rm v}_{\xi_2\bar{\xi}_2\to\xi_1\bar{\xi}_1}\rangle \left(n_{\xi_2} \, n_{\bar{\xi}_2} - \frac{n^{\rm eq}_{\xi_2}}{n^{\rm eq}_{\xi_1}} \frac{n^{\rm eq}_{\bar{\xi}_2}}{n^{\rm eq}_{\bar{\xi}_1}} n_{\xi_1} \, n_{\bar{\xi}_1}\right). \tag{A.12}$$

In this work, we have assumed that there is no asymmetry between the number densities of DM candidate ξ_i and its antiparticle $\bar{\xi}_i$ and therefore, $n_{\xi_i}^{(\rm eq)} = n_{\bar{\xi}_i}^{(\rm eq)}$. Hence, the contribution of $\xi_2\bar{\xi}_2 \to \xi_1\bar{\xi}_1$ to the collision term of ξ_2 is given by

$$-\langle\sigma \mathrm{v}_{\xi_2\bar{\xi}_2\to\xi_1\bar{\xi}_1}\rangle\left\{n_{\xi_2}^2 - \left(\frac{n_{\xi_2}^{\rm eq}}{n_{\xi_1}^{\rm eq}}\right)^2 n_{\xi_1}^2\right\}, \tag{A.13}$$

while the collision term of ξ_1 also has an additional contribution which is exactly identical to the above except the overall $-$ve sign will be replaced by a $+$ve sign as the DM conversion process $\xi_2\bar{\xi}_2 \to \xi_1\bar{\xi}_1$ increases the number densities of both ξ_1 and $\bar{\xi}_1$.

A.5 The 4×4 rotation matrices for diagonalization of the real scalar mass matrix

Here we have shown the 4×4 rotational matrices, used in the diagonalization of the mass matrices discussed in section 2.5

$$\mathcal{O}_{\mathcal{S}} = \mathcal{O}_{S_{12}}\mathcal{O}_{S_{13}}\mathcal{O}_{S_{14}}\mathcal{O}_{S_{24}}\mathcal{O}_{S_{23}}\mathcal{O}_{S_{34}} \tag{A.14}$$

where $\mathcal{O}_{S_{ij}}$ represents the rotation in i-j plane.

$$\mathcal{O}_{\rm S_{12}} = \begin{pmatrix} \cos\theta_{12} & \sin\theta_{12} & 0 & 0 \\ -\sin\theta_{12} & \cos\theta_{12} & 0 & 0 \\ 0 & 0 & 1 & 0 \\ 0 & 0 & 0 & 1 \end{pmatrix}, \mathcal{O}_{\rm S_{13}} = \begin{pmatrix} \cos\theta_{13} & 0 & \sin\theta_{13} & 0 \\ 0 & 1 & 0 & 0 \\ -\sin\theta_{13} & 0 & \cos\theta_{13} & 0 \\ 0 & 0 & 0 & 1 \end{pmatrix} \tag{A.15}$$

$$\mathcal{O}_{\rm S_{14}} = \begin{pmatrix} \cos\theta_{14} & 0 & 0 & \sin\theta_{14} \\ 0 & 1 & 0 & 0 \\ 0 & 0 & 1 & 0 \\ -\sin\theta_{14} & 0 & 0 & \cos\theta_{14} \end{pmatrix}, \mathcal{O}_{\rm S_{24}} = \begin{pmatrix} 1 & 0 & 0 & 0 \\ 0 & \cos\theta_{24} & 0 & \sin\theta_{24} \\ 0 & 0 & 1 & 0 \\ 0 & -\sin\theta_{24} & 0 & \cos\theta_{24} \end{pmatrix} \tag{A.16}$$

$$\mathcal{O}_{\rm S_{23}} = \begin{pmatrix} 1 & 0 & 0 & 0 \\ 0 & \cos\theta_{23} & \sin\theta_{23} & 0 \\ 0 & -\sin\theta_{23} & \cos\theta_{23} & 0 \\ 0 & 0 & 0 & 1 \end{pmatrix}, \mathcal{O}_{\rm S_{34}} = \begin{pmatrix} 1 & 0 & 0 & 0 \\ 0 & 1 & 0 & 0 \\ 0 & 0 & \cos\theta_{34} & \sin\theta_{34} \\ 0 & 0 & -\sin\theta_{34} & \cos\theta_{34} \end{pmatrix} \tag{A.17}$$

A.6 The 3×3 rotation matrices required to diagonalize the pseudo scalar mass matrix

Here we have shown the 3×3 rotational matrices, used in the diagonalization of the mass matrices discussed in section 2.5

$$\mathcal{O}_{\mathcal{P}} = \begin{pmatrix} \cos\alpha_{12}\cos\alpha_{13} & \sin\alpha_{12}\cos\alpha_{13} & \sin\alpha_{13} \\ -\sin\alpha_{12}\cos\alpha_{23} - \cos\alpha_{12}\sin\alpha_{23}\sin\alpha_{13} & \cos\alpha_{12}\cos\alpha_{23} - \sin\alpha_{12}\sin\alpha_{23}sin\alpha_{13} & \sin\alpha_{23}\cos\alpha_{13} \\ \sin\alpha_{12}\sin\alpha_{23} - \cos\alpha_{12}\cos\alpha_{23}\sin\alpha_{13} & -\cos\alpha_{12}\sin\alpha_{23} - \sin\alpha_{12}\cos\alpha_{23}\sin\alpha_{13} & \cos\alpha_{23}\cos\alpha_{13} \end{pmatrix}$$

APPENDIX B

Here some detail calculations have been shown related to the work discussed in chapter 3.

B.1 Physical Masses of Gauge Bosons

Covariant derivatives of the scalar fields in DLRM can be written as

$$\begin{aligned} D_\mu\Phi &= \partial_\mu\Phi - i\frac{g_L}{2}(\sigma.W_{L\mu})\Phi + i\frac{g_R}{2}\Phi(\sigma.W_{R\mu}) \\ D_\mu\chi_L &= \partial_\mu\chi_L - i\frac{g_L}{2}(\sigma.W_{L\mu})\chi_L - i\ g_{BL}\,Q_{BL}B'_\mu\chi_L \\ D_\mu\chi_R &= \partial_\mu\chi_R - i\frac{g_R}{2}(\sigma.W_{R\mu})\chi_R - i\ g_{BL}\,Q_{BL}B'_\mu\chi_R \end{aligned} \tag{B.1}$$

where

$$\sigma.W_{L/R\mu} = \begin{pmatrix} W^3_{L/R\mu} & \sqrt{2}W^+_{L/R\mu} \\ \sqrt{2}W^-_{L/R\mu} & -W^3_{L/R\mu} \end{pmatrix}. \tag{B.2}$$

The corresponding kinetic Lagrangian of scalar fields are

$$\mathcal{L}_{scalar} = Tr\big[(D_\mu\Phi)^\dagger(D_\mu\Phi)\big] + (D_\mu\chi_L)^\dagger(D_\mu\chi_L) + (D_\mu\chi_R)^\dagger(D_\mu\chi_R). \tag{B.3}$$

Considering the scalar vevs as,

$$\langle\Phi\rangle = \begin{pmatrix} \frac{k_1}{\sqrt{2}} & 0 \\ 0 & \frac{k_2}{\sqrt{2}} \end{pmatrix},\ \langle\chi_L\rangle = \begin{pmatrix} 0 \\ \frac{v_L}{\sqrt{2}} \end{pmatrix},\ \langle\chi_R\rangle = \begin{pmatrix} 0 \\ \frac{v_R}{\sqrt{2}} \end{pmatrix}$$

The charged vector boson mass matrix can be written as

$$M^2_{V^\pm} = \begin{pmatrix} \frac{1}{4}v_L^2g_L^2 + \frac{1}{4}\left(k_1^2+k_2^2\right)g_L^2 & -\frac{1}{2}g_Lg_Rk_1k_2 \\ -\frac{1}{2}g_Lg_Rk_1k_2 & \frac{1}{4}v_R^2g_R^2 + \frac{1}{4}\left(k_1^2+k_2^2\right)g_R^2 \end{pmatrix} \tag{B.4}$$

whereas the neutral vector boson mass matrix is

$$M^2_{V^0} = \begin{pmatrix} \frac{1}{8}g_L^2\left(k_1^2+k_2^2+v_L^2\right) & -\frac{1}{4}g_Lg_R\left(k_1^2+k_2^2\right) & -\frac{1}{4}g_{\rm BL}g_Lv_L^2 \\ -\frac{1}{4}g_Lg_R\left(k_1^2+k_2^2\right) & \frac{1}{8}g_L^2\left(k_1^2+k_2^2+v_R^2\right) & -\frac{1}{4}g_{\rm BL}g_Rv_R^2 \\ -\frac{1}{4}g_{\rm BL}g_Lv_L^2 & -\frac{1}{4}g_{\rm BL}g_Rv_R^2 & \frac{1}{8}g_{\rm BL}^2\left(v_L^2+v_R^2\right) \end{pmatrix} \tag{B.5}$$

As expected, the neutral gauge boson mass matrix has one vanishing eigenvalue, corresponding to massless photon. After diagonalisation of the mass matrices we can represent the gauge fields in terms of physical gauge boson states as

$$\begin{aligned} W^3_{L_\mu} &= \frac{e}{g_Y} Z_{L\mu} + \frac{e}{g_L} A_\mu + 0\ Z_{R\mu} \\ W^3_{R_\mu} &= -\frac{e g_Y}{g_L g_R} Z_{L\mu} + \frac{e}{g_R} A_\mu + \frac{g_Y}{g_{BL}}\ Z_{R\mu} \\ B'_\mu &= -\frac{e g_Y}{g_L g_{BL}} Z_{L\mu} + \frac{e}{g_{BL}} A_\mu - \frac{g_Y}{g_R}\ Z_{R\mu} \end{aligned} \tag{B.6}$$

Also, we can express these couplings as, $\sin\theta_W = \frac{e}{g_L}$ and $\cos\theta_W = \frac{e}{g_Y}$ with θ_W being the Weinberg angle. In DLRM, $Z_{L\mu}$ and $Z_{R\mu}$ will also mix as the bi-doublet Φ transform non-trivially under both $SU(2)_L$ and $SU(2)_R$ gauge groups. The mixing can be represented as

$$\begin{aligned} Z_{L\mu} &= \cos\delta\ Z_\mu - \sin\delta\ Z'_\mu \\ Z_{R\mu} &= \sin\delta\ Z_\mu + \cos\delta\ Z'_\mu \end{aligned} \tag{B.7}$$

where the mixing angle can be written as

$$\tan 2\delta = \frac{2(M^0_{L,R})^2}{(M^0_L)^2 - (M^0_R)^2} \tag{B.8}$$

with

$$(M^0_L)^2 = \frac{e^2(g_L^2+g_Y^2)^2(k_1^2+k_2^2+v_L^2)}{8 g_L^2 g_Y^2} \tag{B.9}$$

$$(M^0_{L,R})^2 = \frac{e(g_L^2+g_Y^2)(g_R^2(k_1^2+k_2^2) - g_{BL}^2 v_L^2)}{4 g_{BL} g_L g_R} \tag{B.10}$$

$$(M^0_R)^2 = \frac{g_Y^2(2 g_{BL}^2 g_R^2 v_R^2 + g_R^4(k_1^2+k_2^2+v_R^2) + g_{BL}^4(v_L^2+v_R^2))}{8 g_{BL}^2 g_R^2} \tag{B.11}$$

The charged vector boson states are

$$\begin{aligned} W^\pm_{L\mu} &= \cos\zeta\ W^\pm_{1\mu} - \sin\zeta\ W^\pm_{2\mu} \\ W^\pm_{R\mu} &= \sin\zeta\ W^\pm_{1\mu} + \cos\zeta\ W^\pm_{2\mu} \end{aligned} \tag{B.12}$$

with

$$\tan 2\zeta = \frac{2M^2_{LR}}{M^2_L - M^2_R} \tag{B.13}$$

where,

$$M^2_L = \frac{1}{4} g_L^2 (k_1^2+k_2^2+v_L^2) \tag{B.14}$$

$$M^2_R = \frac{1}{4} g_R^2 (k_1^2+k_2^2+v_R^2) \tag{B.15}$$

$$M^2_{LR} = -\frac{1}{2} g_L g_R k_1 k_2 \tag{B.16}$$

After diagonalisation of $\{W_L^{\pm}, W_R^{\pm}\}$ to $\{W_1^{\pm}, W_2^{\pm}\}$, we can have the corresponding mass-squared terms for the charged physical gauge bosons as,

$$M_1^2 = \frac{1}{4}\left(g_L^2(k_1^2+k_2^2+v_L^2)\cos^2\zeta - 2g_Lg_Rk_1k_2\sin 2\zeta + g_R^2(k_1^2+k_2^2+v_R^2)\sin^2\zeta\right) \quad \text{(B.17)}$$

$$M_2^2 = \frac{1}{4}\left(g_R^2(k_1^2+k_2^2+v_R^2)\cos^2\zeta + 2g_Lg_Rk_1k_2\sin 2\zeta + g_L^2(k_1^2+k_2^2+v_L^2)\sin^2\zeta\right) \quad \text{(B.18)}$$

Note that we have taken $k_2 = 0$ which is equivalent to vanishing tree level mixing angle ζ. One can however generate radiative mixing between charged vector bosons, but that is typically very small $< 10^{-7}$ [231]. Note that although we write W_1, W_2, Z, Z' as physical massive gauge boson states here to show the details, in the main text we continue to use W_L, W_R, Z_L, Z_R for better clarity.

B.2 Fermion-gauge boson interactions in DLRM

In this section, we note down the fermion interactions with massive vector bosons. The kinetic term of leptons in DLRM is given by

$$\mathcal{L}_\ell = i\overline{\ell_L}\not{D}^L\ell_L + i\overline{\ell_R}\not{D}^R\ell_R \quad \text{(B.19)}$$

where,

$$D_\mu^L\ell_L = \partial_\mu\,\ell_L - i\frac{g_L}{2}(\sigma.W_{L\mu})\ell_L + i\,\frac{g_{BL}}{2}\,B_\mu\ell_L \quad \text{(B.20)}$$

$$D_\mu^R\ell_R = \partial_\mu\,\ell_R - i\frac{g_R}{2}(\sigma.W_{R\mu})\ell_R + i\,\frac{g_{BL}}{2}\,B_\mu\ell_R \quad \text{(B.21)}$$

The same kinetic Lagrangian is, in fact, applicable to quarks too if we include gluons in the covariant derivative. We show the interactions with neutral massive vector bosons in table B.1, B.2 respectively.

Fermions	Z' in LRSM
$\overline{\mathrm{e_L}}\gamma_\mu \mathrm{e_L}$	$i\left(\frac{g_{BL}g_L\tan\theta_W\cos\delta}{2g_R}+\frac{g_L\cos2\theta_W\sin\delta}{\cos\theta_W}\right)$
$\overline{\mathrm{e_R}}\gamma_\mu \mathrm{e_R}$	$i\left(\frac{1}{2}g_L\tan\theta_W\left(\left(\frac{g_{BL}}{g_R}-\frac{g_R}{g_{BL}}\right)\cos\delta-2\sin\theta_W\sin\delta\right)\right)$
$\overline{\nu_\mathrm{L}}\gamma_\mu \nu_\mathrm{L}$	$i\left(\frac{g_{BL}g_L\tan\theta_W\cos\delta}{2g_R}-\frac{g_L(1-2\sin^2\theta_W\cos^2\theta_W)\sin\delta}{2\cos^2\theta_W\sin\theta_W}\right)$
$\overline{\nu_\mathrm{R}}\gamma_\mu \nu_\mathrm{R}$	$i\left(\frac{(g_{BL}^2+g_R^2)g_L\tan\theta_W\cos\delta}{2g_{BL}g_R}\right)$
$\overline{\mathrm{u_L}}\gamma_\mu \mathrm{u_L}$	$i\left(-\frac{g_{BL}g_L\tan\theta_W\cos\delta}{6g_R}+g_L\sin\theta_W\left(-\frac{\cot\theta_W}{2}+\frac{\tan\theta_W}{6}\right)\sin\delta\right)$
$\overline{\mathrm{u_R}}\gamma_\mu \mathrm{u_R}$	$i\left(\frac{1}{6}g_L\tan\theta_W\left(-\frac{g_{BL}}{g_R}+\frac{3g_R}{g_{BL}}\right)\cos\delta+4\sin\theta_W\sin\delta\right)$
$\overline{\mathrm{d_L}}\gamma_\mu \mathrm{d_L}$	$i\left(-\frac{g_{BL}g_L\tan\theta_W\cos\delta}{6g_R}+g_L\sin\theta_W\left(\frac{\cot\theta_W}{2}+\frac{\tan\theta_W}{6}\right)\sin\delta\right)$
$\overline{\mathrm{d_R}}\gamma_\mu \mathrm{d_R}$	$i\left(-g_L\tan\theta_W\left(\frac{(g_{BL}^2+3g_R^2)\cos\delta}{6g_{BL}g_R}+\frac{\sin\theta_W\sin\delta}{3}\right)\right)$

Table B.2: Fermion interaction with Z' boson.

Fermions	Z Bosons	
	Z in SM	Z in DLRM
$\overline{\mathrm{e_L}}\gamma_\mu \mathrm{e_L}$	$-i\frac{g_L}{2\cos\theta_W}\cos2\theta_W$	$i\left(-\frac{g_L\cos2\theta_W}{2\cos\theta_W}\cos\delta+\frac{g_{BL}g_L\tan\theta_W\sin\delta}{2g_R}\right)$
$\overline{\mathrm{e_R}}\gamma_\mu \mathrm{e_R}$	$i\frac{g_L}{\cos\theta_W}\sin^2\theta_W$	$i\left(\frac{g_L\sin^2\theta_W\cos\delta}{\cos\theta_W}+\frac{1}{2}\left(\frac{g_{BL}}{g_R}-\frac{g_R}{g_{BL}}\right)g_L\tan\theta_W\sin\delta\right)$
$\overline{\nu_\mathrm{L}}\gamma_\mu \nu_\mathrm{L}$	$i\frac{g_L}{2\cos\theta_W}$	$i\left(\frac{g_L(1-2\sin^2\theta_W\cos^2\theta_W)\cos\delta}{2\cos^2\theta_W\sin\theta_W}+\frac{g_{BL}g_L\tan\theta_W\sin\delta}{2g_R}\right)$
$\overline{\mathrm{u_L}}\gamma_\mu \mathrm{u_L}$	$-i\frac{g_L}{2\cos\theta_W}\left(\cos^2\theta_W-\frac{\sin^2\theta_W}{3}\right)$	$i\left(-g_L\sin\theta_W\left(\frac{\cot\theta_W}{2}-\frac{\tan\theta_W}{6}\right)\cos\delta+\frac{g_{BL}g_L\tan\theta_W\sin\delta}{6g_R}\right)$
$\overline{\mathrm{u_R}}\gamma_\mu \mathrm{u_R}$	$-i\frac{2}{3}g_L\frac{\sin^2\theta_W}{\cos\theta_W}$	$i\left(\frac{1}{6}g_L\tan\theta_W\left(-4\sin\theta_W\cos\delta+\left(-\frac{g_{BL}}{g_R}+\frac{3g_R}{g_{BL}}\right)\sin\delta\right)\right)$
$\overline{\mathrm{d_L}}\gamma_\mu \mathrm{d_L}$	$-i\frac{g_L}{2\cos\theta_W}$	$i\left(-\left(\frac{g_L\cos\theta_W}{2}+\frac{g_L\sin^2\theta_W}{6\cos\theta_W}\right)\cos\delta-\frac{g_{BL}g_L\tan\theta_W\sin\delta}{6g_R}\right)$
$\overline{\mathrm{d_R}}\gamma_\mu \mathrm{d_R}$	$i\frac{1}{3}g_L\frac{\sin^2\theta_W}{\cos\theta_W}$	$i\left(\frac{1}{6}g_L\tan\theta_W\left(2\sin\theta_W\cos\delta+\left(-\frac{g_{BL}}{g_R}-\frac{3g_R}{g_{BL}}\right)\sin\delta\right)\right)$
$\overline{\nu_\mathrm{R}}\gamma_\mu \nu_\mathrm{R}$	0	$i\left(\frac{(g_{BL}^2+g_R^2)g_L\tan\theta_W\sin\delta}{2g_{BL}g_R}\right)$

Table B.1: Fermion interactions with Z boson.

The interaction of neutrino ν, charged leptons ℓ with W_2 (or W_R) is similar to the ones with W_L except that g_L is replaced by g_R:

$$-\frac{ig_R}{\sqrt{2}}\gamma_\mu P_R$$

where we have ignored the details of right handed lepton mixing matrix, taking it to be a unit matrix.

B.3 Annihilation cross-sections of right handed neutrinos

The annihilation cross sections of ν_R mediated by right sector gauge bosons are

$$\sigma_{\nu_R\overline{\nu_R}\to q\bar{q}} = \frac{(a^2+b^2)\sqrt{1-\frac{4m_q^2}{s}}\left(c^2\left(2m_q^2+s\right)+d^2\left(s-4m_q^2\right)\right)}{192\pi M_{Z_R}^4} \tag{B.22}$$

$$\begin{aligned}\sigma_{\nu_R\overline{\nu_R}\to\ell_R\overline{\ell_R}} = \frac{\sqrt{1-\frac{4m_\ell^2}{s}}}{192\pi M_{W_R}^4 M_{Z_R}^4}\Big(&2m_\ell^2\big(M_{W_R}^4\left(a^2+b^2\right)\left(c^2-2d^2\right)-M_{W_R}^2M_{Z_R}^2(a+b)(c-2d)-\\ &M_{Z_R}^4(a+b)\big)+s\big(M_{W_R}^4\left(a^2+b^2\right)\left(c^2+d^2\right)\\ &-M_{W_R}^2M_{Z_R}^2(a+b)(c+d)+2M_{Z_R}^4(a+b)\big)\Big)\end{aligned} \tag{B.23}$$

where

$$a = b = \frac{g_L\,\tan\theta_W}{2}\frac{g_{BL}^2+g_R^2}{2g_{BL}\,g_R} \tag{B.24}$$

$$c = \begin{cases} \frac{g_L\,\tan\theta_W}{2}\frac{2g_{BL}^2-g_R^2}{2g_{BL}g_R} & \text{(for charged leptons)}\\ \frac{g_L\,\tan\theta_W}{2}\frac{3g_R^2-2g_{BL}^2}{6g_{BL}g_R} & \text{(for up type quark)}\\ -\frac{g_L\,\tan\theta_W}{2}\frac{2g_{BL}^2+g_R^2}{2g_{BL}g_R} & \text{(for down type quark)}\end{cases} \tag{B.25}$$

$$d = \begin{cases} -\frac{g_L\,\tan\theta_W}{4g_{BL}}g_R & \text{(for charged leptons)}\\ \frac{g_L\,\tan\theta_W}{4g_{BL}}g_R & \text{(for up type quark)}\\ -\frac{g_L\,\tan\theta_W}{4g_{BL}}g_R & \text{(for down type quarks)}\end{cases} \tag{B.26}$$

We consider the mixing between left and right sector gauge bosons to be negligible and hence do not take it into account in our analysis.

APPENDIX C

Here some detail calculations have been shown related to the works discussed in chapter 4.

C.1 Full calculation of the Lagrangian of fermionic triplet Σ

In this section, the full calculation of the Lagrangian in section 4.2.1 have been discussed.First, we have constructed a fermionic triplet Σ using Σ_R and its CP conjugate ${\Sigma_R}^c = C\,\overline{\Sigma_R}^T$ as $\Sigma = \Sigma_R + {\Sigma_R}^c$. The Lagrangian of Σ can be written as

$$\mathcal{L}_{triplet} = \frac{i}{2}\mathrm{Tr}[\overline{\Sigma}\not{D}\Sigma] - \frac{1}{2}\mathrm{Tr}[\overline{\Sigma}\,M_\Sigma\,\Sigma]\,, \tag{C.1}$$

$$= \frac{i}{2}\mathrm{Tr}[\overline{\Sigma_R}\not{D}\,\Sigma_R] + \frac{i}{2}\mathrm{Tr}[\overline{{\Sigma_R}^c}\not{D}\,{\Sigma_R}^c] - \left(\frac{1}{2}\,\mathrm{Tr}[\overline{{\Sigma_R}^c}\,M_\Sigma\,\Sigma_R] + h.c.\right)\,. \tag{C.2}$$

The covariant derivative of Σ_R is defined as

$$D_\mu\Sigma_R = \partial_\mu\Sigma_R + i\,g\left[\sum_{a=1}^{3}\frac{\sigma^a}{2}\,W_\mu^a, \Sigma_R\right]\,, \tag{C.3}$$

where, g is the $\mathrm{SU(2)_L}$ gauge coupling and W_μ^a ($a = 1$ to 3) are three corresponding gauge bosons. Now, using the expression of Σ_R given in equation (4.1), the covariant derivative of Σ_R can be further expressed in terms of the components of Σ_R as

$$D_\mu\Sigma_R = \partial_\mu\Sigma_R + \frac{i\,g}{2}\begin{pmatrix} \sqrt{2}(W_\mu^+\,\Sigma_R^- - W_\mu^-\,\Sigma_R^+) & 2\,(W_\mu^3\,\Sigma_R^+ - W_\mu^+\,\Sigma_R^0) \\ 2\,(W_\mu^-\,\Sigma_R^0 - W_\mu^3\,\Sigma_R^-) & \sqrt{2}(W_\mu^-\,\Sigma_R^+ - W_\mu^+\,\Sigma_R^-) \end{pmatrix}\,. \tag{C.4}$$

Moreover, using equation (4.1) and the definition of Σ_R^c, the CP conjugate of Σ_R can also be expressed in a 2×2 matrix notation as

$$\Sigma_R^c = \begin{pmatrix} {\Sigma_R^0}^c/\sqrt{2} & \Sigma_R^{-c} \\ \Sigma_R^{+c} & -{\Sigma_R^0}^c/\sqrt{2} \end{pmatrix}\,, \tag{C.5}$$

Similarly, using equation (C.3) and equation (C.5), the covariant derivative of Σ_R^c is given by

$$D_\mu \Sigma_R^c = \partial_\mu \Sigma_R^c + \frac{i\,g}{2}\begin{pmatrix} \sqrt{2}(W_\mu^+ \Sigma_R^{+c} - W_\mu^- \Sigma_R^{-c}) & 2\,(W_\mu^3 \Sigma_R^{-c} - W_\mu^+ \Sigma_R^{0\,c}) \\ 2\,(W_\mu^- \Sigma_R^{0\,c} - W_\mu^3 \Sigma_R^{+c}) & \sqrt{2}(W_\mu^- \Sigma_R^{-c} - W_\mu^+ \Sigma_R^{+c}) \end{pmatrix} . \quad \text{(C.6)}$$

Now, using equation (C.4), let us simplify the first term of equation (C.2):

$$\begin{aligned} &\frac{i}{2}\mathrm{Tr}[\overline{\Sigma_R}\,\not{D}\,\Sigma_R] \\ =\ &\frac{i}{2}\left(\overline{\Sigma_R^0}\,\not{\partial}\Sigma_R^0 + \overline{\Sigma_R^-}\,\not{\partial}\Sigma_R^- + \overline{\Sigma_R^+}\,\not{\partial}\Sigma_R^+\right) - \frac{g}{4}\Big(2\,\overline{\Sigma_R^0}\gamma^\mu\Sigma_R^- W_\mu^+ - 2\,\overline{\Sigma_R^0}\gamma^\mu\Sigma_R^+ W_\mu^- \\ &+2\,\overline{\Sigma_R^-}\gamma^\mu\Sigma_R^0 W_\mu^- - 2\,\overline{\Sigma_R^+}\gamma^\mu\Sigma_R^0 W_\mu^+ + 2\,\overline{\Sigma_R^+}\gamma^\mu\Sigma_R^+ W_\mu^3 - 2\,\overline{\Sigma_R^-}\gamma^\mu\Sigma_R^- W_\mu^3\Big) . \end{aligned} \quad \text{(C.7)}$$

Moreover, using the relations $\Sigma_R^{+c} = C\,\overline{\Sigma_R^+}^T$ and $\Sigma_R^{0\,c} = C\,\overline{\Sigma_R^0}^T$, one can further rewrite the above equation in terms of Σ_R^{+c} instead of Σ_R^+ as

$$\begin{aligned} &\frac{i}{2}\mathrm{Tr}[\overline{\Sigma_R}\,\not{D}\,\Sigma_R] \\ =\ &\frac{i}{2}\left(\overline{\Sigma_R^0}\,\not{\partial}\Sigma_R^0 + \overline{\Sigma_R^-}\,\not{\partial}\Sigma_R^- + \overline{\Sigma_R^{+c}}\,\not{\partial}\Sigma_R^{+c}\right) - \frac{g}{4}\Big(2\,\overline{\Sigma_R^0}\gamma_\mu\Sigma_R^- W_\mu^+ + 2\,\overline{\Sigma_R^{+c}}\gamma^\mu\Sigma_R^{0\,c} W_\mu^- \\ &+2\,\overline{\Sigma_R^-}\gamma^\mu\Sigma_R^0 W_\mu^- + 2\,\overline{\Sigma_R^{0\,c}}\gamma^\mu\Sigma_R^{+c} W_\mu^+ - 2\,\overline{\Sigma_R^{+c}}\gamma^\mu\Sigma_R^{+c} W_\mu^3 - 2\,\overline{\Sigma_R^-}\gamma^\mu\Sigma_R^- W_\mu^3\Big) . \end{aligned} \quad \text{(C.8)}$$

In the above equation, we have used the following properties of charge conjugation operator:

$$\begin{aligned} C^{-1}\,\gamma_\mu\,C &= -\gamma_\mu^T\ , \\ C^{-1}\,\gamma_5\,C &= \gamma_5^T\ , \\ C^T &= -C\ , \\ C^\dagger &= C^{-1} . \end{aligned} \quad \text{(C.9)}$$

Similarly, let us simplify the second term of equation (C.2) using equation (C.6):

$$\begin{aligned} &\frac{i}{2}\mathrm{Tr}[\overline{\Sigma_R{}^c}\,\not{D}\,\Sigma_R{}^c] \\ =\ &\frac{i}{2}\left(\overline{\Sigma_R^{0\,c}}\,\not{\partial}\Sigma_R^{0\,c} + \overline{\Sigma_R^{-c}}\,\not{\partial}\Sigma_R^{-c} + \overline{\Sigma_R^{+c}}\,\not{\partial}\Sigma_R^{+c}\right) - \frac{g}{4}\Big(2\,\overline{\Sigma_R^{0\,c}}\gamma^\mu\Sigma_R^{+c} W_\mu^+ - 2\,\overline{\Sigma_R^{0\,c}}\gamma^\mu\Sigma_R^{-c} W_\mu^- \\ &+2\,\overline{\Sigma_R^{+c}}\gamma^\mu\Sigma_R^{0\,c} W_\mu^- - 2\,\overline{\Sigma_R^{-c}}\gamma^\mu\Sigma_R^{0\,c} W_\mu^+ + 2\,\overline{\Sigma_R^{-c}}\gamma^\mu\Sigma_R^{-c} W_\mu^3 - 2\,\overline{\Sigma_R^{+c}}\gamma^\mu\Sigma_R^{+c} W_\mu^3\Big) . \end{aligned} \quad \text{(C.10)}$$

One can change the field Σ_R^{-c} by Σ_R^- in the above equation using the relation $\Sigma_R^{-c} = C\,\overline{\Sigma_R^-}^T$ and the properties of C operator mentioned in equation (C.9) as

$$\begin{aligned} &\frac{i}{2}\mathrm{Tr}[\overline{\Sigma_R{}^c}\,\not{D}\,\Sigma_R{}^c] \\ =\ &\frac{i}{2}\left(\overline{\Sigma_R^{0\,c}}\,\not{\partial}\Sigma_R^{0\,c} + \overline{\Sigma_R^-}\,\not{\partial}\Sigma_R^- + \overline{\Sigma_R^{+c}}\,\not{\partial}\Sigma_R^{+c}\right) - \frac{g}{4}\Big(2\,\overline{\Sigma_R^{0\,c}}\gamma^\mu\Sigma_R^{+c} W_\mu^+ + 2\,\overline{\Sigma_R^-}\gamma^\mu\Sigma_R^0 W_\mu^- \\ &+2\,\overline{\Sigma_R^{+c}}\gamma^\mu\Sigma_R^{0\,c} W_\mu^- + 2\,\overline{\Sigma_R^0}\gamma^\mu\Sigma_R^- W_\mu^+ - 2\,\overline{\Sigma_R^-}\gamma^\mu\Sigma_R^- W_\mu^3 - 2\,\overline{\Sigma_R^{+c}}\gamma^\mu\Sigma_R^{+c} W_\mu^3\Big) . \end{aligned} \quad \text{(C.11)}$$

Now, adding equation (C.8) and equation (C.11), we get

$$\begin{aligned}
&\frac{i}{2}\mathrm{Tr}[\overline{\Sigma_R}\,\not{D}\,\Sigma_R] + \frac{i}{2}\mathrm{Tr}[\overline{\Sigma_R{}^c}\,\not{D}\,\Sigma_R{}^c]\,, \\
= \;& \frac{i}{2}\left(\overline{\Sigma_R^0}\not{\partial}\Sigma_R^0 + \overline{\Sigma_R^{0\,c}}\not{\partial}\Sigma_R^{0\,c}\right) + i\left(\overline{\Sigma_R^-}\not{\partial}\Sigma_R^- + \overline{\Sigma_R^{+c}}\not{\partial}\Sigma_R^{+c}\right) - g\left(\overline{\Sigma_R^-}\gamma^\mu\Sigma_R^0\,W_\mu^- + \overline{\Sigma_R^{+c}}\gamma^\mu\Sigma_R^{0\,c}\,W_\mu^-\right. \\
& \left. + \overline{\Sigma_R^0}\gamma^\mu\Sigma_R^-\,W_\mu^+ + \overline{\Sigma_R^{0\,c}}\gamma^\mu\Sigma_R^{+c}\,W_\mu^+ - \overline{\Sigma_R^{+c}}\gamma^\mu\Sigma_R^{+c}\,W_\mu^3 - \overline{\Sigma_R^-}\gamma^\mu\Sigma_R^-\,W_\mu^3\right)\,. \qquad \text{(C.12)}
\end{aligned}$$

Let us define two fermionic state as

$$\psi^0 = \Sigma_R^0 + \Sigma_R^{0\,c}\,, \qquad \text{(C.13)}$$

$$\psi^- = \Sigma_R^- + \Sigma_R^{+c}\,. \qquad \text{(C.14)}$$

Finally, we can write the equation (C.12) in terms of ψ^0 and ψ^- as

$$\begin{aligned}
&\frac{i}{2}\mathrm{Tr}[\overline{\Sigma_R}\,\not{D}\,\Sigma_R] + \frac{i}{2}\mathrm{Tr}[\overline{\Sigma_R{}^c}\,\not{D}\,\Sigma_R{}^c]\,, \\
= \;& \frac{i}{2}\,\overline{\psi^0}\not{\partial}\psi^0 + i\,\overline{\psi^-}\not{\partial}\psi^- - g\,\left(\overline{\psi^-}\gamma^\mu\psi^0\,W^- + h.c.\right) + g\,\overline{\psi^-}\gamma^\mu\psi^-W_\mu^3\,. \qquad \text{(C.15)}
\end{aligned}$$

Furthermore, we can also simplify the mass terms in equation (C.2) as well using the expressions of Σ_R and $\Sigma_R{}^c$ (equations (4.1 and C.5)) and considering M_Σ real, i.e.

$$\begin{aligned}
&-\frac{1}{2}\,\mathrm{Tr}[\overline{\Sigma_R{}^c}\,M_\Sigma\,\Sigma_R] - \frac{1}{2}\,\mathrm{Tr}[\overline{\Sigma_R}\,M_\Sigma\,\Sigma_R{}^c] \\
= \;& -\frac{M_\Sigma}{2}\left(\overline{\Sigma_R^0}\Sigma_R^{0\,c} + \overline{\Sigma_R^-}\Sigma_R^{+c} + \overline{\Sigma_R^+}\Sigma_R^{-c}\right) - \frac{M_\Sigma}{2}\left(\overline{\Sigma_R^{0\,c}}\Sigma_R^0 + \overline{\Sigma_R^{-c}}\Sigma_R^+ + \overline{\Sigma_R^{+c}}\Sigma_R^-\right)\,, \qquad \text{(C.16)}
\end{aligned}$$

Now, using the relation $\Sigma_R^\pm = C\,\overline{\Sigma_R^\pm}^T$, one can have the following identities

$$\begin{aligned}
\overline{\Sigma_R^+}\Sigma_R^{-c} &= \overline{\Sigma_R^-}\Sigma_R^{+c}\,, \\
\overline{\Sigma_R^{-c}}\Sigma_R^+ &= \overline{\Sigma_R^{+c}}\Sigma_R^-\,. \qquad \text{(C.17)}
\end{aligned}$$

Therefore, using equation (C.17), we can further simplify the mass terms of triplet Σ as

$$\begin{aligned}
&-\frac{1}{2}\,\mathrm{Tr}[\overline{\Sigma_R{}^c}\,M_\Sigma\,\Sigma_R] - \frac{1}{2}\,\mathrm{Tr}[\overline{\Sigma_R}\,M_\Sigma\,\Sigma_R{}^c] \\
= \;& -\frac{M_\Sigma}{2}\left(\overline{\Sigma_R^0}\Sigma_R^{0\,c} + \overline{\Sigma_R^{0\,c}}\Sigma_R^0\right) - M_\Sigma\left(\overline{\Sigma_R^-}\Sigma_R^{+c} + \overline{\Sigma_R^{+c}}\Sigma_R^-\right)\,, \\
= \;& -\frac{M_\Sigma}{2}\overline{\psi^0}\psi^0 - M_\Sigma\overline{\psi^-}\psi^-\,, \qquad \text{(C.18)}
\end{aligned}$$

while deriving in the last line we have used the definitions of ψ^0 and ψ^- fields given in equation (C.13) and equation (C.14). Finally, using equation (C.15) and equation (C.18), we can write the Lagrangian of the triplet field Σ in terms of newly defined two fields ψ^0

and ψ^- as

$$\mathcal{L}_{triplet} = \frac{i}{2}\mathrm{Tr}[\overline{\Sigma}\,\not{D}\Sigma] - \frac{1}{2}\mathrm{Tr}[\overline{\Sigma}\,M_\Sigma\,\Sigma]\,, \tag{C.19}$$

$$= \frac{i}{2}\mathrm{Tr}[\overline{\Sigma_R}\,\not{D}\,\Sigma_R] + \frac{i}{2}\mathrm{Tr}[\overline{\Sigma_R{}^c}\,\not{D}\,\Sigma_R{}^c] - \left(\frac{1}{2}\,\mathrm{Tr}[\overline{\Sigma_R{}^c}\,M_\Sigma\,\Sigma_R] + h.c.\right),$$

$$= \frac{i}{2}\,\overline{\psi^0}\,\not{\partial}\psi^0 + i\,\overline{\psi^-}\,\not{\partial}\psi^- - \frac{M_\Sigma}{2}\overline{\psi^0}\psi^0 - M_\Sigma\overline{\psi^-}\psi^-$$

$$-g\,\left(\overline{\psi^-}\gamma^\mu\psi^0\,W^- + h.c.\right) + g\,\overline{\psi^-}\gamma^\mu\psi^- W^3_\mu\,. \tag{C.20}$$

C.2 A_4 Multiplication Rules

Here we have shown the multiplication rules of A_4 group discussed in section 4.3. A_4, the symmetry group of a tetrahedron, is a discrete non-abelian group of even permutations of four objects. It has four irreducible representations: three one-dimensional and one three dimensional which are denoted by $\mathbf{1}, \mathbf{1'}, \mathbf{1''}$ and $\mathbf{3}$ respectively, being consistent with the sum of square of the dimensions $\sum_i n_i^2 = 12$. We denote a generic permutation $(1,2,3,4) \to (n_1, n_2, n_3, n_4)$ simply by $(n_1 n_2 n_3 n_4)$. The group A_4 can be generated by two basic permutations S and T given by $S = (4321), T = (2314)$. This satisfies

$$S^2 = T^3 = (ST)^3 = 1$$

which is called a presentation of the group. Their product rules of the irreducible representations are given as

$$\mathbf{1} \otimes \mathbf{1} = \mathbf{1}$$

$$\mathbf{1'} \otimes \mathbf{1'} = \mathbf{1''}$$

$$\mathbf{1'} \otimes \mathbf{1''} = \mathbf{1}$$

$$\mathbf{1''} \otimes \mathbf{1''} = \mathbf{1'}$$

$$\mathbf{3} \otimes \mathbf{3} = \mathbf{1} \otimes \mathbf{1'} \otimes \mathbf{1''} \otimes \mathbf{3_a} \otimes \mathbf{3_s}$$

where a and s in the subscript corresponds to anti-symmetric and symmetric parts respectively. Denoting two triplets as (a_1, b_1, c_1) and (a_2, b_2, c_2) respectively, their direct product can be decomposed into the direct sum mentioned above. In the S diagonal basis, the products are given as

$$\mathbf{1} \backsim \mathbf{a_1 a_2} + \mathbf{b_1 b_2} + \mathbf{c_1 c_2}$$

$$\mathbf{1'} \backsim \mathbf{a_1 a_2} + \omega^\mathbf{2}\mathbf{b_1 b_2} + \omega\mathbf{c_1 c_2}$$

$$\mathbf{1''} \backsim \mathbf{a_1 a_2} + \omega\mathbf{b_1 b_2} + \omega^\mathbf{2}\mathbf{c_1 c_2}$$

$$\mathbf{3_s} \backsim (\mathbf{b_1 c_2} + \mathbf{c_1 b_2}, \mathbf{c_1 a_2} + \mathbf{a_1 c_2}, \mathbf{a_1 b_2} + \mathbf{b_1 a_2})$$

$$\mathbf{3_a} \backsim (\mathbf{b_1 c_2} - \mathbf{c_1 b_2}, \mathbf{c_1 a_2} - \mathbf{a_1 c_2}, \mathbf{a_1 b_2} - \mathbf{b_1 a_2})$$

In the T diagonal basis on the other hand, they can be written as

$$\mathbf{1} \backsim \mathbf{a_1 a_2} + \mathbf{b_1 c_2} + \mathbf{c_1 b_2}$$

$$1' \backsim c_1c_2 + a_1b_2 + b_1a_2$$

$$1'' \backsim b_1b_2 + c_1a_2 + a_1c_2$$

$$3_s \backsim \frac{1}{3}(2a_1a_2 - b_1c_2 - c_1b_2, 2c_1c_2 - a_1b_2 - b_1a_2, 2b_1b_2 - a_1c_2 - c_1a_2)$$

$$3_a \backsim \frac{1}{2}(b_1c_2 - c_1b_2, a_1b_2 - b_1a_2, c_1a_2 - a_1c_2)$$

Bibliography

[1] V.C. Rubin, N. Thonnard, and Jr. Ford, W.K. Rotational properties of 21 SC galaxies with a large range of luminosities and radii, from NGC 4605 /R = 4kpc/ to UGC 2885 /R = 122 kpc/. *Astrophys. J.*, 238:471, 1980.

[2] Douglas Clowe, Marusa Bradac, Anthony H. Gonzalez, Maxim Markevitch, Scott W. Randall, Christine Jones, and Dennis Zaritsky. A direct empirical proof of the existence of dark matter. *Astrophys. J. Lett.*, 648:L109–L113, 2006.

[3] L. Kantha. A Time-Dependent and Cosmological Model Consistent with Cosmological Constraints. *Adv. Astron.*, 2016:9743970, 2016.

[4] P Tanedo. Defense Against the Dark Arts. 2011.

[5] Edward W. Kolb and Michael S. Turner. *The Early Universe*, volume 69. 1990.

[6] E. Aprile et al. Dark Matter Search Results from a One Ton-Year Exposure of XENON1T. *Phys. Rev. Lett.*, 121(11):111302, 2018.

[7] E. Aprile et al. Constraining the spin-dependent WIMP-nucleon cross sections with XENON1T. *Phys. Rev. Lett.*, 122(14):141301, 2019.

[8] M.L. Ahnen et al. Limits to Dark Matter Annihilation Cross-Section from a Combined Analysis of MAGIC and Fermi-LAT Observations of Dwarf Satellite Galaxies. *JCAP*, 02:039, 2016.

[9] Oliver Buchmueller, Caterina Doglioni, and Lian Tao Wang. Search for dark matter at colliders. *Nature Phys.*, 13(3):217–223, 2017.

[10] Nicolás Bernal, Matti Heikinheimo, Tommi Tenkanen, Kimmo Tuominen, and Ville Vaskonen. The Dawn of FIMP Dark Matter: A Review of Models and Constraints. *Int. J. Mod. Phys. A*, 32(27):1730023, 2017.

[11] Lawrence J. Hall, Karsten Jedamzik, John March-Russell, and Stephen M. West. Freeze-In Production of FIMP Dark Matter. *JHEP*, 03:080, 2010.

[12] Ernest Ma. Verifiable radiative seesaw mechanism of neutrino mass and dark matter. *Phys. Rev. D*, 73:077301, 2006.

[13] Ivan Esteban, M.C. Gonzalez-Garcia, Michele Maltoni, Ivan Martinez-Soler, and Thomas Schwetz. Updated fit to three neutrino mixing: exploring the accelerator-reactor complementarity. *JHEP*, 01:087, 2017.

[14] Ivan Esteban, M.C. Gonzalez-Garcia, Michele Maltoni, Thomas Schwetz, and Albert Zhou. The fate of hints: updated global analysis of three-flavor neutrino oscillations. *JHEP*, 09:178, 2020.

[15] G. Hinshaw et al. Nine-Year Wilkinson Microwave Anisotropy Probe (WMAP) Observations: Cosmological Parameter Results. *Astrophys. J. Suppl.*, 208:19, 2013.

[16] Y. Akrami et al. Planck 2018 results. X. Constraints on inflation. *Astron. Astrophys.*, 641:A10, 2020.

[17] F. Zwicky. Die Rotverschiebung von extragalaktischen Nebeln. *Helv. Phys. Acta*, 6:110–127, 1933.

[18] F. Zwicky. On the Masses of Nebulae and of Clusters of Nebulae. *Astrophys. J.*, 86:217–246, 1937.

[19] A. Bosma. 21-cm line studies of spiral galaxies. 2. The distribution and kinematics of neutral hydrogen in spiral galaxies of various morphological types. *Astron. J.*, 86:1825, 1981.

[20] Massimo Persic, Paolo Salucci, and Fulvio Stel. The Universal rotation curve of spiral galaxies: 1. The Dark matter connection. *Mon. Not. Roy. Astron. Soc.*, 281:27, 1996.

[21] Yoshiaki Sofue and Vera Rubin. Rotation curves of spiral galaxies. *Ann. Rev. Astron. Astrophys.*, 39:137–174, 2001.

[22] Markus Weber and Wim de Boer. Determination of the Local Dark Matter Density in our Galaxy. *Astron. Astrophys.*, 509:A25, 2010.

[23] Yoshiaki Sofue. A Grand Rotation Curve and Dark Matter Halo in the Milky Way Galaxy. *Publ. Astron. Soc. Jap.*, 64:75, 2012.

[24] Maxim Markevitch, A.H. Gonzalez, D. Clowe, A. Vikhlinin, L. David, W. Forman, C. Jones, S. Murray, and W. Tucker. Direct constraints on the dark matter self-interaction cross-section from the merging galaxy cluster 1E0657-56. *Astrophys. J.*, 606:819–824, 2004.

[25] Douglas Clowe, Anthony Gonzalez, and Maxim Markevitch. Weak lensing mass reconstruction of the interacting cluster 1E0657-558: Direct evidence for the existence of dark matter. *Astrophys. J.*, 604:596–603, 2004.

[26] Marusa Bradac, Steven W. Allen, Tommaso Treu, Harald Ebeling, Richard Massey, R.Glenn Morris, Anja von der Linden, and Douglas Applegate. Revealing the properties of dark matter in the merging cluster MACSJ0025.4-1222. *Astrophys. J.*, 687:959, 2008.

[27] Liliya L.R. Williams and Prasenjit Saha. Light/Mass Offsets in the Lensing Cluster Abell 3827: Evidence for Collisional Dark Matter? *Mon. Not. Roy. Astron. Soc.*, 415:448, 2011.

[28] A.K. Drukier, Katherine Freese, and D.N. Spergel. Detecting Cold Dark Matter Candidates. *Phys. Rev. D*, 33:3495–3508, 1986.

[29] Katherine Freese, Joshua A. Frieman, and Andrew Gould. Signal Modulation in Cold Dark Matter Detection. *Phys. Rev. D*, 37:3388–3405, 1988.

[30] J. Diemand, M. Kuhlen, P. Madau, M. Zemp, B. Moore, D. Potter, and J. Stadel. Clumps and streams in the local dark matter distribution. *Nature*, 454:735–738, 2008.

[31] Joachim Stadel, Doug Potter, Ben Moore, Jurg Diemand, Piero Madau, Marcel Zemp, Michael Kuhlen, and Vicent Quilis. Quantifying the heart of darkness with GHALO - a multi-billion particle simulation of our galactic halo. *Mon. Not. Roy. Astron. Soc.*, 398:L21–L25, 2009.

[32] Volker Springel, Jie Wang, Mark Vogelsberger, Aaron Ludlow, Adrian Jenkins, Amina Helmi, Julio F. Navarro, Carlos S. Frenk, and Simon D.M. White. The Aquarius Project: the subhalos of galactic halos. *Mon. Not. Roy. Astron. Soc.*, 391:1685–1711, 2008.

[33] Mark Vogelsberger, A. Helmi, Volker Springel, Simon D.M. White, Jie Wang, Carlos S. Frenk, Adrian Jenkins, A.D. Ludlow, and Julio F. Navarro. Phase-space structure in the local dark matter distribution and its signature in direct detection experiments. *Mon. Not. Roy. Astron. Soc.*, 395:797–811, 2009.

[34] F.S. Ling, E. Nezri, E. Athanassoula, and R. Teyssier. Dark Matter Direct Detection Signals inferred from a Cosmological N-body Simulation with Baryons. *JCAP*, 02:012, 2010.

[35] Michael Kuhlen, Neal Weiner, Jurg Diemand, Piero Madau, Ben Moore, Doug Potter, Joachim Stadel, and Marcel Zemp. Dark Matter Direct Detection with Non-Maxwellian Velocity Structure. *JCAP*, 02:030, 2010.

[36] Mariangela Lisanti, Louis E. Strigari, Jay G. Wacker, and Risa H. Wechsler. The Dark Matter at the End of the Galaxy. *Phys. Rev. D*, 83:023519, 2011.

[37] Julio F. Navarro, Carlos S. Frenk, and Simon D.M. White. The Structure of cold dark matter halos. *Astrophys. J.*, 462:563–575, 1996.

[38] Julio F. Navarro, Carlos S. Frenk, and Simon D.M. White. A Universal density profile from hierarchical clustering. *Astrophys. J.*, 490:493–508, 1997.

[39] John N. Bahcall and R.M. Soneira. The Universe at faint magnetidues. 2. Models for the predicted star counts. *Astrophys. J. Suppl.*, 44:73–110, 1980.

[40] Jurg Diemand, Ben Moore, and Joachim Stadel. Convergence and scatter of cluster density profiles. *Mon. Not. Roy. Astron. Soc.*, 353:624, 2004.

[41] Andrey V. Kravtsov, Anatoly A. Klypin, James S. Bullock, and Joel R. Primack. The Cores of dark matter dominated galaxies: Theory versus observations. *Astrophys. J.*, 502:48, 1998.

[42] A. Burkert. The Structure of dark matter halos in dwarf galaxies. *IAU Symp.*, 171:175, 1996.

[43] Alister W. Graham, David Merritt, Ben Moore, Juerg Diemand, and Balsa Terzic. Empirical models for Dark Matter Halos. I. Nonparametric Construction of Density Profiles and Comparison with Parametric Models. *Astron. J.*, 132:2685–2700, 2006.

[44] Julio F. Navarro, Aaron Ludlow, Volker Springel, Jie Wang, Mark Vogelsberger, Simon D.M. White, Adrian Jenkins, Carlos S. Frenk, and Amina Helmi. The Diversity and Similarity of Cold Dark Matter Halos. *Mon. Not. Roy. Astron. Soc.*, 402:21, 2010.

[45] W.J.G. de Blok. The Core-Cusp Problem. *Adv. Astron.*, 2010:789293, 2010.

[46] Ya. B. Zel'dovich. Magnetic Model of the Universe. *Soviet Journal of Experimental and Theoretical Physics*, 21:656, September 1965.

[47] Hong-Yee Chiu. Symmetry between particle and anti-particle populations in the universe. *Phys. Rev. Lett.*, 17:712, 1966.

[48] Benjamin W. Lee and Steven Weinberg. Cosmological Lower Bound on Heavy Neutrino Masses. *Phys. Rev. Lett.*, 39:165–168, 1977.

[49] Paolo Gondolo and Graciela Gelmini. Cosmic abundances of stable particles: Improved analysis. *Nucl. Phys. B*, 360:145–179, 1991.

[50] N. Aghanim et al. Planck 2018 results. VI. Cosmological parameters. *Astron. Astrophys.*, 641:A6, 2020.

[51] Mark W. Goodman and Edward Witten. Detectability of Certain Dark Matter Candidates. *Phys. Rev. D*, 31:3059, 1985.

[52] Stefano Profumo. *An Introduction to Particle Dark Matter*. World Scientific, 2017.

[53] D.S. Akerib et al. Results from a search for dark matter in the complete LUX exposure. *Phys. Rev. Lett.*, 118(2):021303, 2017.

[54] E. Aprile et al. Dark Matter Results from 225 Live Days of XENON100 Data. *Phys. Rev. Lett.*, 109:181301, 2012.

[55] E. Aprile et al. First Dark Matter Search Results from the XENON1T Experiment. *Phys. Rev. Lett.*, 119(18):181301, 2017.

[56] Andi Tan et al. Dark Matter Results from First 98.7 Days of Data from the PandaX-II Experiment. *Phys. Rev. Lett.*, 117(12):121303, 2016.

[57] Xiangyi Cui et al. Dark Matter Results From 54-Ton-Day Exposure of PandaX-II Experiment. *Phys. Rev. Lett.*, 119(18):181302, 2017.

[58] Rouven Essig, Jeremy Mardon, and Tomer Volansky. Direct Detection of Sub-GeV Dark Matter. *Phys. Rev. D*, 85:076007, 2012.

[59] E. Aprile et al. Light Dark Matter Search with Ionization Signals in XENON1T. *Phys. Rev. Lett.*, 123(25):251801, 2019.

[60] Itay M. Bloch, Andrea Caputo, Rouven Essig, Diego Redigolo, Mukul Sholapurkar, and Tomer Volansky. Exploring New Physics with O(keV) Electron Recoils in Direct Detection Experiments. 6 2020.

[61] Chen Cheng et al. Search for Light Dark Matter-Electron Scatterings in the PandaX-II Experiment. 1 2021.

[62] Oscar Adriani et al. An anomalous positron abundance in cosmic rays with energies 1.5-100 GeV. *Nature*, 458:607–609, 2009.

[63] R. Cowsik, B. Burch, and T. Madziwa-Nussinov. The origin of the spectral intensities of cosmic-ray positrons. *Astrophys. J.*, 786:124, 2014.

[64] R. Abbasi et al. Limits on a muon flux from neutralino annihilations in the Sun with the IceCube 22-string detector. *Phys. Rev. Lett.*, 102:201302, 2009.

[65] M. Ageron et al. ANTARES: the first undersea neutrino telescope. *Nucl. Instrum. Meth. A*, 656:11–38, 2011.

[66] F. Aharonian et al. The h.e.s.s. survey of the inner galaxy in very high-energy gamma-rays. *Astrophys. J.*, 636:777–797, 2006.

[67] T.C. Weekes et al. VERITAS: The Very energetic radiation imaging telescope array system. *Astropart. Phys.*, 17:221–243, 2002.

[68] Fermi Large Area Telescope Second Source Catalog. *Astrophys. J. Suppl.*, 199:31, 2012.

[69] Mariangela Lisanti. Lectures on Dark Matter Physics. In *Theoretical Advanced Study Institute in Elementary Particle Physics: New Frontiers in Fields and Strings*, pages 399–446, 2017.

[70] Martin J.L. Turner et al. The European Photon Imaging Camera on XMM-Newton: The MOS cameras. *Astron. Astrophys.*, 365:L27–35, 2001.

[71] Joseph P. Conlon, Francesca Day, Nicholas Jennings, Sven Krippendorf, and Markus Rummel. Consistency of Hitomi, XMM-Newton, and Chandra 3.5 keV data from Perseus. *Phys. Rev. D*, 96(12):123009, 2017.

[72] Alexey Boyarsky, Oleg Ruchayskiy, Dmytro Iakubovskyi, and Jeroen Franse. Unidentified Line in X-Ray Spectra of the Andromeda Galaxy and Perseus Galaxy Cluster. *Phys. Rev. Lett.*, 113:251301, 2014.

[73] Esra Bulbul, Maxim Markevitch, Adam Foster, Randall K. Smith, Michael Loewenstein, and Scott W. Randall. Detection of An Unidentified Emission Line in the Stacked X-ray spectrum of Galaxy Clusters. *Astrophys. J.*, 789:13, 2014.

[74] Oleg Ruchayskiy, Alexey Boyarsky, Dmytro Iakubovskyi, Esra Bulbul, Dominique Eckert, Jeroen Franse, Denys Malyshev, Maxim Markevitch, and Andrii Neronov. Searching for decaying dark matter in deep XMM–Newton observation of the Draco dwarf spheroidal. *Mon. Not. Roy. Astron. Soc.*, 460(2):1390–1398, 2016.

[75] Esra Bulbul, Maxim Markevitch, Adam R. Foster, Randall K. Smith, Michael Loewenstein, and Scott W. Randall. Comment on "Dark matter searches going bananas: the contribution of Potassium (and Chlorine) to the 3.5 keV line". 9 2014.

[76] Jeroen Franse et al. Radial Profile of the 3.55 keV line out to R_{200} in the Perseus Cluster. *Astrophys. J.*, 829(2):124, 2016.

[77] Esra Bulbul, Maxim Markevitch, Adam Foster, Eric Miller, Mark Bautz, Mike Loewenstein, Scott W. Randall, and Randall K. Smith. Searching for the 3.5 keV Line in the Stacked Suzaku Observations of Galaxy Clusters. *Astrophys. J.*, 831(1):55, 2016.

[78] Chintan Shah, Stepan Dobrodey, Sven Bernitt, René Steinbrügge, José R. Crespo López-Urrutia, Liyi Gu, and Jelle Kaastra. Laboratory measurements compellingly support charge-exchange mechanism for the 'dark matter' ∼3.5 keV X-ray line. *Astrophys. J.*, 833(1):52, 2016.

[79] Jurgen Knodlseder et al. Early SPI / INTEGRAL contraints on the morphology of the 511 keV line emission in the 4th galactic quadrant. *Astron. Astrophys.*, 411:L457–L460, 2003.

[80] Thomas Siegert, Roland Diehl, Aaron C. Vincent, Fabrizia Guglielmetti, Martin G. H. Krause, and Celine Boehm. Search for 511 keV Emission in Satellite Galaxies of the Milky Way with INTEGRAL/SPI. *Astron. Astrophys.*, 595:A25, 2016.

[81] Thomas Siegert et al. Gamma-Ray Observations of Nova Sgr 2015 No. 2 with INTEGRAL. *Astron. Astrophys.*, 615:A107, 2018.

[82] Thomas Siegert, Roland Diehl, Gerasim Khachatryan, Martin G.H. Krause, Fabrizia Guglielmetti, Jochen Greiner, Andrew W. Strong, and Xiaoling Zhang. Gamma-ray spectroscopy of Positron Annihilation in the Milky Way. *Astron. Astrophys.*, 586:A84, 2016.

[83] Tansu Daylan, Douglas P. Finkbeiner, Dan Hooper, Tim Linden, Stephen K. N. Portillo, Nicholas L. Rodd, and Tracy R. Slatyer. The characterization of the gamma-ray signal from the central Milky Way: A case for annihilating dark matter. *Phys. Dark Univ.*, 12:1–23, 2016.

[84] Lisa Goodenough and Dan Hooper. Possible Evidence For Dark Matter Annihilation In The Inner Milky Way From The Fermi Gamma Ray Space Telescope. 10 2009.

[85] Dan Hooper and Lisa Goodenough. Dark Matter Annihilation in The Galactic Center As Seen by the Fermi Gamma Ray Space Telescope. *Phys. Lett. B*, 697:412–428, 2011.

[86] Alexey Boyarsky, Denys Malyshev, and Oleg Ruchayskiy. A comment on the emission from the Galactic Center as seen by the Fermi telescope. *Phys. Lett. B*, 705:165–169, 2011.

[87] Dan Hooper and Tim Linden. On The Origin Of The Gamma Rays From The Galactic Center. *Phys. Rev. D*, 84:123005, 2011.

[88] Kevork N. Abazajian and Manoj Kaplinghat. Detection of a Gamma-Ray Source in the Galactic Center Consistent with Extended Emission from Dark Matter Annihilation and Concentrated Astrophysical Emission. *Phys. Rev. D*, 86:083511, 2012. [Erratum: Phys.Rev.D 87, 129902 (2013)].

[89] Dan Hooper and Tracy R. Slatyer. Two Emission Mechanisms in the Fermi Bubbles: A Possible Signal of Annihilating Dark Matter. *Phys. Dark Univ.*, 2:118–138, 2013.

[90] Kevork N. Abazajian, Nicolas Canac, Shunsaku Horiuchi, and Manoj Kaplinghat. Astrophysical and Dark Matter Interpretations of Extended Gamma-Ray Emission from the Galactic Center. *Phys. Rev. D*, 90(2):023526, 2014.

[91] David Green, Tsutomu Nagayoshi, and Francesco dePalma. Gamma-ray Spectral and Morphological study of HESS J1912+101 observed by MAGIC and Fermi-LAT. *PoS*, ICRC2019:564, 2020.

[92] W.B. Atwood et al. The Large Area Telescope on the Fermi Gamma-ray Space Telescope Mission. *Astrophys. J.*, 697:1071–1102, 2009.

[93] Christoph Weniger. A Tentative Gamma-Ray Line from Dark Matter Annihilation at the Fermi Large Area Telescope. *JCAP*, 08:007, 2012.

[94] Dong-Ze He, Xiao-Jun Bi, Su-Jie Lin, Peng-Fei Yin, and Xin Zhang. Prospect for dark matter annihilation signatures from gamma-ray observation of dwarf galaxies by LHAASO. *Phys. Rev. D*, 100(8):083003, 2019.

[95] Elmo Tempel, Andi Hektor, and Martti Raidal. Fermi 130 GeV gamma-ray excess and dark matter annihilation in sub-haloes and in the Galactic centre. *JCAP*, 09:032, 2012. [Addendum: JCAP 11, A01 (2012)].

[96] Meng Su and Douglas P. Finkbeiner. Strong Evidence for Gamma-ray Line Emission from the Inner Galaxy. 6 2012.

[97] Tesla E. Jeltema and Stefano Profumo. Discovery of a 3.5 keV line in the Galactic Centre and a critical look at the origin of the line across astronomical targets. *Mon. Not. Roy. Astron. Soc.*, 450(2):2143–2152, 2015.

[98] Eric Carlson, Tesla Jeltema, and Stefano Profumo. Where do the 3.5 keV photons come from? A morphological study of the Galactic Center and of Perseus. *JCAP*, 02:009, 2015.

[99] Kevork N. Abazajian. The Consistency of Fermi-LAT Observations of the Galactic Center with a Millisecond Pulsar Population in the Central Stellar Cluster. *JCAP*, 03:010, 2011.

[100] Chris Gordon and Oscar Macias. Dark Matter and Pulsar Model Constraints from Galactic Center Fermi-LAT Gamma Ray Observations. *Phys. Rev. D*, 88(8):083521, 2013. [Erratum: Phys.Rev.D 89, 049901 (2014)].

[101] Qiang Yuan and Bing Zhang. Millisecond pulsar interpretation of the Galactic center gamma-ray excess. *JHEAp*, 3-4:1–8, 2014.

[102] Ryan M. O'Leary, Matthew D. Kistler, Matthew Kerr, and Jason Dexter. Young Pulsars and the Galactic Center GeV Gamma-ray Excess. 4 2015.

[103] J. Knodlseder et al. The All-sky distribution of 511 keV electron-positron annihilation emission. *Astron. Astrophys.*, 441:513–532, 2005.

[104] Dan Hooper, Francesc Ferrer, Celine Boehm, Joseph Silk, Jacques Paul, N.Wyn Evans, and Michel Casse. Possible evidence for MeV dark matter in dwarf spheroidals. *Phys. Rev. Lett.*, 93:161302, 2004.

[105] Douglas P. Finkbeiner and Neal Weiner. Exciting Dark Matter and the INTEGRAL/SPI 511 keV signal. *Phys. Rev. D*, 76:083519, 2007.

[106] Steven Weinberg. A No-Truncation Approach to Cosmic Microwave Background Anisotropies. *Phys. Rev. D*, 74:063517, 2006.

[107] K.S. Babu and Rabindra N. Mohapatra. 7 keV Scalar Dark Matter and the Anomalous Galactic X-ray Spectrum. *Phys. Rev. D*, 89:115011, 2014.

[108] Anirban Biswas, Debasish Majumdar, and Probir Roy. Nonthermal two component dark matter model for Fermi-LAT γ-ray excess and 3.55 keV X-ray line. *JHEP*, 04:065, 2015.

[109] Debasish Borah, Arnab Dasgupta, and Rathin Adhikari. Common origin of the 3.55 keV x-ray line and the Galactic Center gamma-ray excess in a radiative neutrino mass model. *Phys. Rev. D*, 92(7):075005, 2015.

[110] Debasish Borah, Arnab Dasgupta, and Sudhanwa Patra. Common origin of 3.55 keV x-ray line and gauge coupling unification with left-right dark matter. *Phys. Rev. D*, 96(11):115019, 2017.

[111] F. Hofmann and C. Wegg. 7.1 keV sterile neutrino dark matter constraints from a deep Chandra X-ray observation of the Galactic bulge Limiting Window. *Astron. Astrophys.*, 625:L7, 2019.

[112] Anirban Biswas, Sandhya Choubey, Laura Covi, and Sarif Khan. Explaining the 3.5 keV X-ray Line in a $L_\mu - L_\tau$ Extension of the Inert Doublet Model. *JCAP*, 02:002, 2018.

[113] Pei-Hong Gu. Quasi-degenerate dark matter for DAMPE excess and 3.5 keV line. *Sci. China Phys. Mech. Astron.*, 61(10):101005, 2018.

[114] Dmytro Iakubovskyi. Observation of the new emission line at ˜3.5 keV in X-ray spectra of galaxies and galaxy clusters. *Adv. Astron. Space Phys.*, 6(1):3–15, 2016.

[115] Ryan J. Wilkinson, Aaron C. Vincent, Céline Bœhm, and Christopher McCabe. Ruling out the light weakly interacting massive particle explanation of the Galactic 511 keV line. *Phys. Rev. D*, 94(10):103525, 2016.

[116] Yasaman Farzan and M. Rajaee. Pico-charged particles explaining 511 keV line and XENON1T signal. *Phys. Rev. D*, 102(10):103532, 2020.

[117] Rong-Gen Cai, Yu-Chen Ding, Xing-Yu Yang, and Yu-Feng Zhou. Constraints on a mixed model of dark matter particles and primordial black holes from the Galactic 511 keV line. 7 2020.

[118] George M. Fuller, Alexander Kusenko, David Radice, and Volodymyr Takhistov. Positrons and 511 keV Radiation as Tracers of Recent Binary Neutron Star Mergers. *Phys. Rev. Lett.*, 122(12):121101, 2019.

[119] Richard Bartels, Francesca Calore, Emma Storm, and Christoph Weniger. Galactic binaries can explain the Fermi Galactic centre excess and 511 keV emission. *Mon. Not. Roy. Astron. Soc.*, 480(3):3826–3841, 2018.

[120] M. Aguilar et al. Antiproton Flux, Antiproton-to-Proton Flux Ratio, and Properties of Elementary Particle Fluxes in Primary Cosmic Rays Measured with the Alpha Magnetic Spectrometer on the International Space Station. *Phys. Rev. Lett.*, 117(9):091103, 2016.

[121] M. Aguilar et al. The Alpha Magnetic Spectrometer (AMS) on the international space station: Part II — Results from the first seven years. *Phys. Rept.*, 894:1–116, 2021.

[122] M. Ackermann et al. Measurement of separate cosmic-ray electron and positron spectra with the Fermi Large Area Telescope. *Phys. Rev. Lett.*, 108:011103, 2012.

[123] S. Abdollahi et al. Search for Cosmic-Ray Electron and Positron Anisotropies with Seven Years of Fermi Large Area Telescope Data. *Phys. Rev. Lett.*, 118(9):091103, 2017.

[124] S. Abdollahi et al. Cosmic-ray electron-positron spectrum from 7 GeV to 2 TeV with the Fermi Large Area Telescope. *Phys. Rev. D*, 95(8):082007, 2017.

[125] M. N. Mazziotta. Search for features in the cosmic-ray electron and positron spectrum measured by the Fermi Large Area Telescope. *J. Phys. Conf. Ser.*, 1390(1):012062, 2019.

[126] Gaëlle Giesen, Mathieu Boudaud, Yoann Génolini, Vivian Poulin, Marco Cirelli, Pierre Salati, and Pasquale D. Serpico. AMS-02 antiprotons, at last! Secondary astrophysical component and immediate implications for Dark Matter. *JCAP*, 09:023, 2015.

[127] M. Di Mauro, F. Donato, N. Fornengo, R. Lineros, and A. Vittino. Interpretation of AMS-02 electrons and positrons data. *JCAP*, 04:006, 2014.

[128] Stefano Gabici, Carmelo Evoli, Daniele Gaggero, Paolo Lipari, Philipp Mertsch, Elena Orlando, Andrew Strong, and Andrea Vittino. The origin of Galactic cosmic rays: challenges to the standard paradigm. *Int. J. Mod. Phys. D*, 28(15):1930022, 2019.

[129] Mattia Di Mauro, Fiorenza Donato, and Silvia Manconi. On the interpretation of the latest AMS-02 cosmic ray electron spectrum. 10 2020.

[130] Mattia Di Mauro and Martin Wolfgang Winkler. Multimessenger constraints on the dark matter interpretation of the Fermi-LAT Galactic center excess. 1 2021.

[131] Pei-pei Zhang, Bing-qiang Qiao, Wei Liu, Shu-wang Cui, Qiang Yuan, and Yi-qing Guo. Possible bump structure of cosmic ray electrons unveiled by AMS-02 data. 1 2021.

[132] Ming-Yang Cui, Qiang Yuan, Yue-Lin Sming Tsai, and Yi-Zhong Fan. Possible dark matter annihilation signal in the AMS-02 antiproton data. *Phys. Rev. Lett.*, 118(19):191101, 2017.

[133] Alessandro Cuoco, Jan Heisig, Lukas Klamt, Michael Korsmeier, and Michael Krämer. Scrutinizing the evidence for dark matter in cosmic-ray antiprotons. *Phys. Rev. D*, 99(10):103014, 2019.

[134] Dan Hooper, Rebecca K. Leane, Yu-Dai Tsai, Shalma Wegsman, and Samuel J. Witte. A systematic study of hidden sector dark matter:application to the gamma-ray and antiproton excesses. *JHEP*, 07(07):163, 2020.

[135] Sun Xu-Dong and Dai Ben-Zhong. Dark matter annihilation into leptons through gravity portals. 8 2020.

[136] Johan Alwall, Philip Schuster, and Natalia Toro. Simplified Models for a First Characterization of New Physics at the LHC. *Phys. Rev. D*, 79:075020, 2009.

[137] Daniele Alves. Simplified Models for LHC New Physics Searches. *J. Phys. G*, 39:105005, 2012.

[138] Daniel Abercrombie et al. Dark Matter Benchmark Models for Early LHC Run-2 Searches: Report of the ATLAS/CMS Dark Matter Forum. *Phys. Dark Univ.*, 27:100371, 2020.

[139] Dilia María Portillo Quintero. *Search for Dark Matter Produced in Association with a Higgs Boson Decaying to a pair of bottom quarks with the ATLAS Detector*. PhD thesis, Paris U., VI-VII, 2018.

[140] Anthony Paul Di Franzo. *Simplified Models for Dark Matter Model Building*. PhD thesis, UC, Irvine, 2016.

[141] Andrea De Simone and Thomas Jacques. Simplified models vs. effective field theory approaches in dark matter searches. *Eur. Phys. J. C*, 76(7):367, 2016.

[142] M. Tanabashi et al. Review of Particle Physics. *Phys. Rev. D*, 98(3):030001, 2018.

[143] Jessica Goodman, Masahiro Ibe, Arvind Rajaraman, William Shepherd, Tim M.P. Tait, and Hai-Bo Yu. Constraints on Dark Matter from Colliders. *Phys. Rev. D*, 82:116010, 2010.

[144] Björn Penning. The pursuit of dark matter at colliders—an overview. *J. Phys. G*, 45(6):063001, 2018.

[145] F. Pobbe, A. Wulzer, and M. Zanetti. Setting limits on Effective Field Theories: the case of Dark Matter. *JHEP*, 08:074, 2017.

[146] Ben Geytenbeek and Ben Gripaios. Effective field theory analysis of composite higgsino-like and wino-like thermal relic dark matter. 11 2020.

[147] Moritz Habermehl, Mikael Berggren, and Jenny List. WIMP Dark Matter at the International Linear Collider. *Phys. Rev. D*, 101(7):075053, 2020.

[148] Yang Bai, Patrick J. Fox, and Roni Harnik. The Tevatron at the Frontier of Dark Matter Direct Detection. *JHEP*, 12:048, 2010.

[149] Andreas Birkedal, Konstantin Matchev, and Maxim Perelstein. Dark matter at colliders: A Model independent approach. *Phys. Rev. D*, 70:077701, 2004.

[150] Frank J. Petriello, Seth Quackenbush, and Kathryn M. Zurek. The Invisible Z' at the CERN LHC. *Phys. Rev. D*, 77:115020, 2008.

[151] Yuri Gershtein, Frank Petriello, Seth Quackenbush, and Kathryn M. Zurek. Discovering hidden sectors with mono-photon Z'o searches. *Phys. Rev. D*, 78:095002, 2008.

[152] Qing-Hong Cao, Chuan-Ren Chen, Chong Sheng Li, and Hao Zhang. Effective Dark Matter Model: Relic density, CDMS II, Fermi LAT and LHC. *JHEP*, 08:018, 2011.

[153] Maria Beltran, Dan Hooper, Edward W. Kolb, Zosia A.C. Krusberg, and Tim M.P. Tait. Maverick dark matter at colliders. *JHEP*, 09:037, 2010.

[154] Patrick J. Fox, Roni Harnik, Joachim Kopp, and Yuhsin Tsai. Missing Energy Signatures of Dark Matter at the LHC. *Phys. Rev. D*, 85:056011, 2012.

[155] T. Aaltonen et al. Search for large extra dimensions in final states containing one photon or jet and large missing transverse energy produced in $p\bar{p}$ collisions at $\sqrt{s} =$ 1.96-TeV. *Phys. Rev. Lett.*, 101:181602, 2008.

[156] Anirban Biswas and Aritra Gupta. Calculation of Momentum Distribution Function of a Non-thermal Fermionic Dark Matter. *JCAP*, 03:033, 2017. [Addendum: JCAP 05, A02 (2017)].

[157] Bibhushan Shakya. Sterile Neutrino Dark Matter from Freeze-In. *Mod. Phys. Lett. A*, 31(06):1630005, 2016.

[158] John McDonald. Thermally generated gauge singlet scalars as selfinteracting dark matter. *Phys. Rev. Lett.*, 88:091304, 2002.

[159] Carlos E. Yaguna. The Singlet Scalar as FIMP Dark Matter. *JHEP*, 08:060, 2011.

[160] Seth Koren and Robert McGehee. Freezing-in twin dark matter. *Phys. Rev. D*, 101(5):055024, 2020.

[161] Basabendu Barman, Subhaditya Bhattacharya, and Mohammadreza Zakeri. Non-Abelian Vector Boson as FIMP Dark Matter. *JCAP*, 02:029, 2020.

[162] Oleg Lebedev and Takashi Toma. Relativistic Freeze-in. *Phys. Lett. B*, 798:134961, 2019.

[163] P.S. Bhupal Dev, Anupam Mazumdar, and Saleh Qutub. Constraining Non-thermal and Thermal properties of Dark Matter. *Front. in Phys.*, 2:26, 2014.

[164] Fatemeh Elahi, Christopher Kolda, and James Unwin. UltraViolet Freeze-in. *JHEP*, 03:048, 2015.

[165] Samuel B. Roland, Bibhushan Shakya, and James D. Wells. Neutrino Masses and Sterile Neutrino Dark Matter from the PeV Scale. *Phys. Rev. D*, 92(11):113009, 2015.

[166] Basabendu Barman, Debasish Borah, and Rishav Roshan. Effective Theory of Freeze-in Dark Matter. *JCAP*, 11:021, 2020.

[167] Nicolás Bernal, Javier Rubio, and Hardi Veermäe. UV Freeze-in in Starobinsky Inflation. *JCAP*, 10:021, 2020.

[168] Nicolás Bernal, Javier Rubio, and Hardi Veermäe. Boosting Ultraviolet Freeze-in in NO Models. *JCAP*, 06:047, 2020.

[169] Thomas Hambye, Michel H. G. Tytgat, Jérôme Vandecasteele, and Laurent Vanderheyden. Dark matter direct detection is testing freeze-in. *Phys. Rev. D*, 98(7):075017, 2018.

[170] Raymond T. Co, Francesco D'Eramo, Lawrence J. Hall, and Duccio Pappadopulo. Freeze-In Dark Matter with Displaced Signatures at Colliders. *JCAP*, 12:024, 2015.

[171] Amin Aboubrahim, Wan-Zhe Feng, and Pran Nath. A long-lived stop with freeze-in and freeze-out dark matter in the hidden sector. *JHEP*, 02:118, 2020.

[172] K.S. Hirata et al. Observation of a small atmospheric muon-neutrino / electron-neutrino ratio in Kamiokande. *Phys. Lett. B*, 280:146–152, 1992.

[173] B.T. Cleveland, Timothy Daily, Jr. Davis, Raymond, James R. Distel, Kenneth Lande, C.K. Lee, Paul S. Wildenhain, and Jack Ullman. Measurement of the solar electron neutrino flux with the Homestake chlorine detector. *Astrophys. J.*, 496:505–526, 1998.

[174] W. Hampel et al. GALLEX solar neutrino observations: Results for GALLEX IV. *Phys. Lett. B*, 447:127–133, 1999.

[175] J.N. Abdurashitov et al. Measurement of the solar neutrino capture rate with gallium metal. *Phys. Rev. C*, 60:055801, 1999.

[176] Y. Fukuda et al. Evidence for oscillation of atmospheric neutrinos. *Phys. Rev. Lett.*, 81:1562–1567, 1998.

[177] S. Fukuda et al. Solar B-8 and hep neutrino measurements from 1258 days of Super-Kamiokande data. *Phys. Rev. Lett.*, 86:5651–5655, 2001.

[178] Q.R. Ahmad et al. Direct evidence for neutrino flavor transformation from neutral current interactions in the Sudbury Neutrino Observatory. *Phys. Rev. Lett.*, 89:011301, 2002.

[179] M. Altmann et al. Complete results for five years of GNO solar neutrino observations. *Phys. Lett. B*, 616:174–190, 2005.

[180] M.H. Ahn et al. Measurement of Neutrino Oscillation by the K2K Experiment. *Phys. Rev. D*, 74:072003, 2006.

[181] D.G. Michael et al. Observation of muon neutrino disappearance with the MINOS detectors and the NuMI neutrino beam. *Phys. Rev. Lett.*, 97:191801, 2006.

[182] S. Abe et al. Precision Measurement of Neutrino Oscillation Parameters with KamLAND. *Phys. Rev. Lett.*, 100:221803, 2008.

[183] K. Abe et al. Indication of Electron Neutrino Appearance from an Accelerator-produced Off-axis Muon Neutrino Beam. *Phys. Rev. Lett.*, 107:041801, 2011.

[184] Y. Abe et al. Indication of Reactor $\bar{\nu}_e$ Disappearance in the Double Chooz Experiment. *Phys. Rev. Lett.*, 108:131801, 2012.

[185] F.P. An et al. Observation of electron-antineutrino disappearance at Daya Bay. *Phys. Rev. Lett.*, 108:171803, 2012.

[186] J.K. Ahn et al. Observation of Reactor Electron Antineutrino Disappearance in the RENO Experiment. *Phys. Rev. Lett.*, 108:191802, 2012.

[187] K. Abe et al. Precise Measurement of the Neutrino Mixing Parameter θ_{23} from Muon Neutrino Disappearance in an Off-Axis Beam. *Phys. Rev. Lett.*, 112(18):181801, 2014.

[188] B. Pontecorvo. Inverse beta processes and nonconservation of lepton charge. *Sov. Phys. JETP*, 7:172–173, 1958.

[189] Ziro Maki, Masami Nakagawa, and Shoichi Sakata. Remarks on the unified model of elementary particles. *Prog. Theor. Phys.*, 28:870–880, 1962.

[190] S.P. Mikheev and A.Yu. Smirnov. Resonant amplification of neutrino oscillations in matter and solar neutrino spectroscopy. *Nuovo Cim. C*, 9:17–26, 1986.

[191] L. Wolfenstein. Neutrino Oscillations in Matter. *Phys. Rev. D*, 17:2369–2374, 1978.

[192] Ch. Kraus et al. Final results from phase II of the Mainz neutrino mass search in tritium beta decay. *Eur. Phys. J. C*, 40:447–468, 2005.

[193] V.N. Aseev et al. An upper limit on electron antineutrino mass from Troitsk experiment. *Phys. Rev. D*, 84:112003, 2011.

[194] V.M. Lobashev. The search for the neutrino mass by direct method in the tritium beta-decay and perspectives of study it in the project KATRIN. *Nucl. Phys. A*, 719:153–160, 2003.

[195] A. Osipowicz et al. KATRIN: A Next generation tritium beta decay experiment with sub-eV sensitivity for the electron neutrino mass. Letter of intent. 9 2001.

[196] M. Aker et al. Improved Upper Limit on the Neutrino Mass from a Direct Kinematic Method by KATRIN. *Phys. Rev. Lett.*, 123(22):221802, 2019.

[197] Werner Rodejohann. Neutrino-less Double Beta Decay and Particle Physics. *Int. J. Mod. Phys. E*, 20:1833–1930, 2011.

[198] J. Schechter and J. W. F. Valle. Neutrinoless Double beta Decay in SU(2) x U(1) Theories. *Phys. Rev. D*, 25:2951, 1982.

[199] Steven Weinberg. Baryon and Lepton Nonconserving Processes. *Phys. Rev. Lett.*, 43:1566–1570, 1979.

[200] Peter Minkowski. $\mu \to e\gamma$ at a Rate of One Out of 10^9 Muon Decays? *Phys. Lett. B*, 67:421–428, 1977.

[201] Murray Gell-Mann, Pierre Ramond, and Richard Slansky. Complex Spinors and Unified Theories. *Conf. Proc. C*, 790927:315–321, 1979.

[202] Rabindra N. Mohapatra and Goran Senjanovic. Neutrino Mass and Spontaneous Parity Nonconservation. *Phys. Rev. Lett.*, 44:912, 1980.

[203] J. Schechter and J.W.F. Valle. Neutrino Masses in SU(2) x U(1) Theories. *Phys. Rev. D*, 22:2227, 1980.

[204] Rabindra N. Mohapatra and Goran Senjanovic. Neutrino Masses and Mixings in Gauge Models with Spontaneous Parity Violation. *Phys. Rev. D*, 23:165, 1981.

[205] George Lazarides, Q. Shafi, and C. Wetterich. Proton Lifetime and Fermion Masses in an SO(10) Model. *Nucl. Phys. B*, 181:287–300, 1981.

[206] C. Wetterich. Neutrino Masses and the Scale of B-L Violation. *Nucl. Phys. B*, 187:343–375, 1981.

[207] J. Schechter and J.W.F. Valle. Neutrino Decay and Spontaneous Violation of Lepton Number. *Phys. Rev. D*, 25:774, 1982.

[208] B. Brahmachari and R.N. Mohapatra. Unified explanation of the solar and atmospheric neutrino puzzles in a minimal supersymmetric SO(10) model. *Phys. Rev. D*, 58:015001, 1998.

[209] Robert Foot, H. Lew, X.G. He, and Girish C. Joshi. Seesaw Neutrino Masses Induced by a Triplet of Leptons. *Z. Phys. C*, 44:441, 1989.

[210] K.S. Babu and X.G. He. DIRAC NEUTRINO MASSES AS TWO LOOP RADIATIVE CORRECTIONS. *Mod. Phys. Lett. A*, 4:61, 1989.

[211] J.T. Peltoniemi, D. Tommasini, and J.W.F. Valle. Reconciling dark matter and solar neutrinos. *Phys. Lett. B*, 298:383–390, 1993.

[212] Salvador Centelles Chuliá, Ernest Ma, Rahul Srivastava, and José W. F. Valle. Dirac Neutrinos and Dark Matter Stability from Lepton Quarticity. *Phys. Lett. B*, 767:209–213, 2017.

[213] Alfredo Aranda, Cesar Bonilla, S. Morisi, E. Peinado, and J.W.F. Valle. Dirac neutrinos from flavor symmetry. *Phys. Rev. D*, 89(3):033001, 2014.

[214] Peng Chen, Gui-Jun Ding, Alma. D. Rojas, C.A. Vaquera-Araujo, and J.W.F. Valle. Warped flavor symmetry predictions for neutrino physics. *JHEP*, 01:007, 2016.

[215] Ernest Ma, Nicholas Pollard, Rahul Srivastava, and Mohammadreza Zakeri. Gauge $B-L$ Model with Residual Z_3 Symmetry. *Phys. Lett. B*, 750:135–138, 2015.

[216] Mario Reig, Jose W. F. Valle, and C.A. Vaquera-Araujo. Realistic $\mathrm{SU(3)_c \otimes SU(3)_L \otimes U(1)_X}$ model with a type II Dirac neutrino seesaw mechanism. *Phys. Rev. D*, 94(3):033012, 2016.

[217] Weijian Wang and Zhi-Long Han. Naturally Small Dirac Neutrino Mass with Intermediate $SU(2)_L$ Multiplet Fields. *JHEP*, 04:166, 2017.

[218] Weijian Wang, Ronghui Wang, Zhi-Long Han, and Jin-Zhong Han. The $B-L$ Scotogenic Models for Dirac Neutrino Masses. *Eur. Phys. J. C*, 77(12):889, 2017.

[219] Fei Wang, Wenyu Wang, and Jin Min Yang. Split two-Higgs-doublet model and neutrino condensation. *Europhys. Lett.*, 76:388–394, 2006.

[220] S. Gabriel and S. Nandi. A New two Higgs doublet model. *Phys. Lett. B*, 655:141–147, 2007.

[221] Shainen M. Davidson and Heather E. Logan. Dirac neutrinos from a second Higgs doublet. *Phys. Rev. D*, 80:095008, 2009.

[222] Shainen M. Davidson and Heather E. Logan. LHC phenomenology of a two-Higgs-doublet neutrino mass model. *Phys. Rev. D*, 82:115031, 2010.

[223] Cesar Bonilla and Jose W. F. Valle. Naturally light neutrinos in *Diracon* model. *Phys. Lett. B*, 762:162–165, 2016.

[224] Yasaman Farzan and Ernest Ma. Dirac neutrino mass generation from dark matter. *Phys. Rev. D*, 86:033007, 2012.

[225] Cesar Bonilla, Ernest Ma, Eduardo Peinado, and Jose W. F. Valle. Two-loop Dirac neutrino mass and WIMP dark matter. *Phys. Lett. B*, 762:214–218, 2016.

[226] Ernest Ma and Oleg Popov. Pathways to Naturally Small Dirac Neutrino Masses. *Phys. Lett. B*, 764:142–144, 2017.

[227] Ernest Ma and Utpal Sarkar. Radiative Left-Right Dirac Neutrino Mass. *Phys. Lett. B*, 776:54–57, 2018.

[228] Debasish Borah. Light sterile neutrino and dark matter in left-right symmetric models without a Higgs bidoublet. *Phys. Rev. D*, 94(7):075024, 2016.

[229] Debasish Borah and Arnab Dasgupta. Common Origin of Neutrino Mass, Dark Matter and Dirac Leptogenesis. *JCAP*, 12:034, 2016.

[230] Debasish Borah and Arnab Dasgupta. Observable Lepton Number Violation with Predominantly Dirac Nature of Active Neutrinos. *JHEP*, 01:072, 2017.

[231] Debasish Borah and Arnab Dasgupta. Naturally Light Dirac Neutrino in Left-Right Symmetric Model. *JCAP*, 06:003, 2017.

[232] Salvador Centelles Chuliá, Rahul Srivastava, and José W. F. Valle. Generalized Bottom-Tau unification, neutrino oscillations and dark matter: predictions from a lepton quarticity flavor approach. *Phys. Lett. B*, 773:26–33, 2017.

[233] Cesar Bonilla, J. M. Lamprea, Eduardo Peinado, and Jose W. F. Valle. Flavour-symmetric type-II Dirac neutrino seesaw mechanism. *Phys. Lett. B*, 779:257–261, 2018.

[234] Nina Memenga, Werner Rodejohann, and He Zhang. A_4 flavor symmetry model for Dirac neutrinos and sizable U_{e3}. *Phys. Rev. D*, 87(5):053021, 2013.

[235] Debasish Borah and Biswajit Karmakar. A_4 flavour model for Dirac neutrinos: Type I and inverse seesaw. *Phys. Lett. B*, 780:461–470, 2018.

[236] Salvador Centelles Chuliá, Rahul Srivastava, and José W. F. Valle. Seesaw roadmap to neutrino mass and dark matter. *Phys. Lett. B*, 781:122–128, 2018.

[237] Salvador Centelles Chuliá, Rahul Srivastava, and José W. F. Valle. Seesaw Dirac neutrino mass through dimension-six operators. *Phys. Rev. D*, 98(3):035009, 2018.

[238] Zhi-Long Han and Weijian Wang. Z' Portal Dark Matter in $B - L$ Scotogenic Dirac Model. *Eur. Phys. J. C*, 78(10):839, 2018.

[239] Debasish Borah, Biswajit Karmakar, and Dibyendu Nanda. Common Origin of Dirac Neutrino Mass and Freeze-in Massive Particle Dark Matter. *JCAP*, 07:039, 2018.

[240] Debasish Borah and Biswajit Karmakar. Linear seesaw for Dirac neutrinos with A_4 flavour symmetry. *Phys. Lett. B*, 789:59–70, 2019.

[241] Salvador Centelles Chuliá, Ricardo Cepedello, Eduardo Peinado, and Rahul Srivastava. Systematic classification of two loop $d = 4$ Dirac neutrino mass models and the Diracness-dark matter stability connection. *JHEP*, 10:093, 2019.

[242] Sudip Jana, P. K. Vishnu, and Shaikh Saad. Minimal realizations of Dirac neutrino mass from generic one-loop and two-loop topologies at $d = 5$. *JCAP*, 04:018, 2020.

[243] Arnab Dasgupta, Sin Kyu Kang, and Oleg Popov. Radiative Dirac neutrino mass, neutrinoless quadruple beta decay, and dark matter in B-L extension of the standard model. *Phys. Rev. D*, 100(7):075030, 2019.

[244] S. S. Correia, R. G. Felipe, and F. R. Joaquim. Dirac neutrinos in the 2HDM with restrictive Abelian symmetries. *Phys. Rev. D*, 100(11):115008, 2019.

[245] Seungwon Baek. Dirac neutrino from the breaking of Peccei-Quinn symmetry. *Phys. Lett. B*, 805:135415, 2020.

[246] Rabindra N. Mohapatra and R.E. Marshak. Local B-L Symmetry of Electroweak Interactions, Majorana Neutrinos and Neutron Oscillations. *Phys. Rev. Lett.*, 44:1316–1319, 1980. [Erratum: Phys.Rev.Lett. 44, 1643 (1980)].

[247] R.E. Marshak and Rabindra N. Mohapatra. Quark - Lepton Symmetry and B-L as the U(1) Generator of the Electroweak Symmetry Group. *Phys. Lett. B*, 91:222–224, 1980.

[248] A. Masiero, J.F. Nieves, and T. Yanagida. B^{-}l Violating Proton Decay and Late Cosmological Baryon Production. *Phys. Lett. B*, 116:11–15, 1982.

[249] Rabindra N. Mohapatra and Goran Senjanovic. Spontaneous Breaking of Global B^{-}l Symmetry and Matter - Antimatter Oscillations in Grand Unified Theories. *Phys. Rev. D*, 27:254, 1983.

[250] W. Buchmuller, C. Greub, and P. Minkowski. Neutrino masses, neutral vector bosons and the scale of B-L breaking. *Phys. Lett. B*, 267:395–399, 1991.

[251] Werner Rodejohann and Carlos E. Yaguna. Scalar dark matter in the B−L model. *JCAP*, 12:032, 2015.

[252] Nobuchika Okada and Osamu Seto. Higgs portal dark matter in the minimal gauged $U(1)_{B-L}$ model. *Phys. Rev. D*, 82:023507, 2010.

[253] Arnab Dasgupta and Debasish Borah. Scalar Dark Matter with Type II Seesaw. *Nucl. Phys. B*, 889:637–649, 2014.

[254] Nobuchika Okada and Satomi Okada. Z'-portal right-handed neutrino dark matter in the minimal $\mathrm{U}(1)_X$ extended Standard Model. *Phys. Rev. D*, 95(3):035025, 2017.

[255] Michael Klasen, Florian Lyonnet, and Farinaldo S. Queiroz. NLO+NLL collider bounds, Dirac fermion and scalar dark matter in the B–L model. *Eur. Phys. J. C*, 77(5):348, 2017.

[256] Nobuchika Okada and Yuta Orikasa. Dark matter in the classically conformal B-L model. *Phys. Rev. D*, 85:115006, 2012.

[257] Jun Guo, Zhaofeng Kang, P. Ko, and Yuta Orikasa. Accidental dark matter: Case in the scale invariant local B-L model. *Phys. Rev. D*, 91(11):115017, 2015.

[258] Tanushree Basak and Tanmoy Mondal. Constraining Minimal $U(1)_{B-L}$ model from Dark Matter Observations. *Phys. Rev. D*, 89:063527, 2014.

[259] Nobuchika Okada and Satomi Okada. Z'_{BL} portal dark matter and LHC Run-2 results. *Phys. Rev. D*, 93(7):075003, 2016.

[260] Marcela Carena, Alejandro Daleo, Bogdan A. Dobrescu, and Timothy M.P. Tait. Z' gauge bosons at the Tevatron. *Phys. Rev. D*, 70:093009, 2004.

[261] G. Cacciapaglia, C. Csaki, G. Marandella, and A. Strumia. The Minimal Set of Electroweak Precision Parameters. *Phys. Rev. D*, 74:033011, 2006.

[262] Nicolás Bernal, Diego Restrepo, Carlos Yaguna, and Óscar Zapata. Two-component dark matter and a massless neutrino in a new $B-L$ model. *Phys. Rev. D*, 99(1):015038, 2019.

[263] John Ellis, Malcolm Fairbairn, and Patrick Tunney. Anomaly-Free Dark Matter Models are not so Simple. *JHEP*, 08:053, 2017.

[264] Pavel Fileviez Pérez, Elliot Golias, Rui-Hao Li, Clara Murgui, and Alexis D. Plascencia. Anomaly-free dark matter models. *Phys. Rev. D*, 100(1):015017, 2019.

[265] Stephen F. King. Littlest Seesaw. *JHEP*, 02:085, 2016.

[266] Aharon Davidson. $B - L$ as the fourth color within an $\mathrm{SU}(2)_L \times \mathrm{U}(1)_R \times \mathrm{U}(1)$ model. *Phys. Rev. D*, 20:776, 1979.

[267] J.C. Montero and V. Pleitez. Gauging U(1) symmetries and the number of right-handed neutrinos. *Phys. Lett. B*, 675:64–68, 2009.

[268] Ernest Ma and Rahul Srivastava. Dirac or inverse seesaw neutrino masses with $B-L$ gauge symmetry and S_3 flavor symmetry. *Phys. Lett. B*, 741:217–222, 2015.

[269] B.L. Sánchez-Vega, J.C. Montero, and E.R. Schmitz. Complex Scalar DM in a B-L Model. *Phys. Rev. D*, 90(5):055022, 2014.

[270] B.L. Sánchez-Vega and E.R. Schmitz. Fermionic dark matter and neutrino masses in a B-L model. *Phys. Rev. D*, 92:053007, 2015.

[271] Shivaramakrishna Singirala, Rukmani Mohanta, and Sudhanwa Patra. Singlet scalar Dark matter in $U(1)_{B-L}$ models without right-handed neutrinos. *Eur. Phys. J. Plus*, 133(11):477, 2018.

[272] Takaaki Nomura and Hiroshi Okada. Radiative neutrino mass in an alternative $U(1)_{B-L}$ gauge symmetry. *Nucl. Phys. B*, 941:586–599, 2019.

[273] Nobuchika Okada, Satomi Okada, and Digesh Raut. Natural Z' -portal Majorana dark matter in alternative U(1) extended standard model. *Phys. Rev. D*, 100(3):035022, 2019.

[274] Weijian Wang and Zhi-Long Han. Radiative linear seesaw model, dark matter, and $U(1)_{B-L}$. *Phys. Rev. D*, 92:095001, 2015.

[275] Sudhanwa Patra, Werner Rodejohann, and Carlos E. Yaguna. A new B − L model without right-handed neutrinos. *JHEP*, 09:076, 2016.

[276] Dibyendu Nanda and Debasish Borah. Common origin of neutrino mass and dark matter from anomaly cancellation requirements of a $U(1)_{B-L}$ model. *Phys. Rev. D*, 96(11):115014, 2017.

[277] Anirban Biswas, Debasish Borah, and Dibyendu Nanda. Type III seesaw for neutrino masses in $U(1)_{B-L}$ model with multi-component dark matter. *JHEP*, 12:109, 2019.

[278] Dibyendu Nanda and Debasish Borah. Connecting Light Dirac Neutrinos to a Multi-component Dark Matter Scenario in Gauged $B-L$ Model. *Eur. Phys. J. C*, 80(6):557, 2020.

[279] Grace Dupuis. Collider Constraints and Prospects of a Scalar Singlet Extension to Higgs Portal Dark Matter. *JHEP*, 07:008, 2016.

[280] Robert J. Scherrer and Michael S. Turner. On the Relic, Cosmic Abundance of Stable Weakly Interacting Massive Particles. *Phys. Rev. D*, 33:1585, 1986. [Erratum: Phys.Rev.D 34, 3263 (1986)].

[281] Gerard Jungman, Marc Kamionkowski, and Kim Griest. Supersymmetric dark matter. *Phys. Rept.*, 267:195–373, 1996.

[282] Kim Griest and David Seckel. Three exceptions in the calculation of relic abundances. *Phys. Rev. D*, 43:3191–3203, 1991.

[283] Joakim Edsjo and Paolo Gondolo. Neutralino relic density including coannihilations. *Phys. Rev. D*, 56:1879–1894, 1997.

[284] Nicole F. Bell, Yi Cai, and Anibal D. Medina. Co-annihilating Dark Matter: Effective Operator Analysis and Collider Phenomenology. *Phys. Rev. D*, 89(11):115001, 2014.

[285] C. Patrignani et al. Review of Particle Physics. *Chin. Phys. C*, 40(10):100001, 2016.

[286] Erik Lundstrom, Michael Gustafsson, and Joakim Edsjo. The Inert Doublet Model and LEP II Limits. *Phys. Rev. D*, 79:035013, 2009.

[287] Aaron Pierce and Jesse Thaler. Natural Dark Matter from an Unnatural Higgs Boson and New Colored Particles at the TeV Scale. *JHEP*, 08:026, 2007.

[288] Genevieve Belanger, Beranger Dumont, Andreas Goudelis, Bjorn Herrmann, Sabine Kraml, and Dipan Sengupta. Dilepton constraints in the Inert Doublet Model from Run 1 of the LHC. *Phys. Rev. D*, 91(11):115011, 2015.

[289] Riccardo Barbieri, Lawrence J. Hall, and Vyacheslav S. Rychkov. Improved naturalness with a heavy Higgs: An Alternative road to LHC physics. *Phys. Rev. D*, 74:015007, 2006.

[290] Laura Lopez Honorez and Carlos E. Yaguna. A new viable region of the inert doublet model. *JCAP*, 01:002, 2011.

[291] Michael E. Peskin and Tatsu Takeuchi. Estimation of oblique electroweak corrections. *Phys. Rev. D*, 46:381–409, 1992.

[292] Georges Aad et al. Constraints on new phenomena via Higgs boson couplings and invisible decays with the ATLAS detector. *JHEP*, 11:206, 2015.

[293] Asher Berlin, Dan Hooper, and Samuel D. McDermott. Simplified Dark Matter Models for the Galactic Center Gamma-Ray Excess. *Phys. Rev. D*, 89(11):115022, 2014.

[294] Parikshit Junnarkar and Andre Walker-Loud. Scalar strange content of the nucleon from lattice QCD. *Phys. Rev. D*, 87:114510, 2013.

[295] Morad Aaboud et al. Search for new high-mass phenomena in the dilepton final state using 36 fb^{-1} of proton-proton collision data at $\sqrt{s} = 13$ TeV with the ATLAS detector. *JHEP*, 10:182, 2017.

[296] Joel Giedt, Anthony W. Thomas, and Ross D. Young. Dark matter, the CMSSM and lattice QCD. *Phys. Rev. Lett.*, 103:201802, 2009.

[297] Y. Mambrini. Higgs searches and singlet scalar dark matter: Combined constraints from XENON 100 and the LHC. *Phys. Rev. D*, 84:115017, 2011.

[298] A. Abramowski et al. Constraints on an Annihilation Signal from a Core of Constant Dark Matter Density around the Milky Way Center with H.E.S.S. *Phys. Rev. Lett.*, 114(8):081301, 2015.

[299] H. Abdallah et al. Search for dark matter annihilations towards the inner Galactic halo from 10 years of observations with H.E.S.S. *Phys. Rev. Lett.*, 117(11):111301, 2016.

[300] A.M. Baldini et al. Search for the lepton flavour violating decay $\mu^+ \to e^+\gamma$ with the full dataset of the MEG experiment. *Eur. Phys. J. C*, 76(8):434, 2016.

[301] L. Lavoura. General formulae for f(1) —> f(2) gamma. *Eur. Phys. J. C*, 29:191–195, 2003.

[302] Takashi Toma and Avelino Vicente. Lepton Flavor Violation in the Scotogenic Model. *JHEP*, 01:160, 2014.

[303] U. Bellgardt et al. Search for the Decay mu+ —> e+ e+ e-. *Nucl. Phys. B*, 299:1–6, 1988.

[304] Wilhelm H. Bertl et al. A Search for muon to electron conversion in muonic gold. *Eur. Phys. J. C*, 47:337–346, 2006.

[305] A. Gando et al. Search for Majorana Neutrinos near the Inverted Mass Hierarchy Region with KamLAND-Zen. *Phys. Rev. Lett.*, 117(8):082503, 2016. [Addendum: Phys.Rev.Lett. 117, 109903 (2016)].

[306] Lorenzo Basso, Alexander Belyaev, Stefano Moretti, and Claire H. Shepherd-Themistocleous. Phenomenology of the minimal B-L extension of the Standard model: Z' and neutrinos. *Phys. Rev. D*, 80:055030, 2009.

[307] Vardan Khachatryan et al. Search for heavy resonances decaying to tau lepton pairs in proton-proton collisions at $\sqrt{s} = 13$ TeV. *JHEP*, 02:048, 2017.

[308] Anirban Biswas, Debasish Borah, and Dibyendu Nanda. When Freeze-out Precedes Freeze-in: Sub-TeV Fermion Triplet Dark Matter with Radiative Neutrino Mass. *JCAP*, 09:014, 2018.

[309] Georges Aad et al. Search for high-mass dilepton resonances using 139 fb^{-1} of pp collision data collected at $\sqrt{s}$ =13 TeV with the ATLAS detector. *Phys. Lett. B*, 796:68–87, 2019.

[310] Albert M Sirunyan et al. Search for high-mass resonances in dilepton final states in proton-proton collisions at $\sqrt{s} = 13$ TeV. *JHEP*, 06:120, 2018.

[311] Basabendu Barman, Debasish Borah, Purusottam Ghosh, and Abhijit Kumar Saha. Flavoured gauge extension of singlet-doublet fermionic dark matter: neutrino mass, high scale validity and collider signatures. *JHEP*, 10:275, 2019.

[312] Tania Robens and Tim Stefaniak. Status of the Higgs Singlet Extension of the Standard Model after LHC Run 1. *Eur. Phys. J. C*, 75:104, 2015.

[313] Guillaume Chalons, David Lopez-Val, Tania Robens, and Tim Stefaniak. The Higgs singlet extension at LHC Run 2. *PoS*, ICHEP2016:1180, 2016.

[314] D. López-Val and T. Robens. Δr and the W-boson mass in the singlet extension of the standard model. *Phys. Rev. D*, 90:114018, 2014.

[315] Vardan Khachatryan et al. Search for a Higgs boson in the mass range from 145 to 1000 GeV decaying to a pair of W or Z bosons. *JHEP*, 10:144, 2015.

[316] Matthew J. Strassler and Kathryn M. Zurek. Discovering the Higgs through highly-displaced vertices. *Phys. Lett. B*, 661:263–267, 2008.

[317] Genevieve Belanger and Jong-Chul Park. Assisted freeze-out. *JCAP*, 03:038, 2012.

[318] Anirban Biswas, Debasish Majumdar, Arunansu Sil, and Pijushpani Bhattacharjee. Two Component Dark Matter : A Possible Explanation of 130 GeV $\gamma-$ Ray Line from the Galactic Centre. *JCAP*, 12:049, 2013.

[319] Anirban Biswas. Explaining Low Energy γ-ray Excess from the Galactic Centre using a Two Component Dark Matter Model. *J. Phys. G*, 43(5):055201, 2016.

[320] G. Bélanger, F. Boudjema, A. Pukhov, and A. Semenov. micrOMEGAs4.1: two dark matter candidates. *Comput. Phys. Commun.*, 192:322–329, 2015.

[321] Adam Alloul, Neil D. Christensen, Céline Degrande, Claude Duhr, and Benjamin Fuks. FeynRules 2.0 - A complete toolbox for tree-level phenomenology. *Comput. Phys. Commun.*, 185:2250–2300, 2014.

[322] Alexander Belyaev, Neil D. Christensen, and Alexander Pukhov. CalcHEP 3.4 for collider physics within and beyond the Standard Model. *Comput. Phys. Commun.*, 184:1729–1769, 2013.

[323] D.S. Akerib et al. LUX-ZEPLIN (LZ) Conceptual Design Report. 9 2015.

[324] E. Aprile et al. Physics reach of the XENON1T dark matter experiment. *JCAP*, 04:027, 2016.

[325] J. Aalbers et al. DARWIN: towards the ultimate dark matter detector. *JCAP*, 11:017, 2016.

[326] Krzysztof Rolbiecki and Kazuki Sakurai. Long-lived bino and wino in supersymmetry with heavy scalars and higgsinos. *JHEP*, 11:091, 2015.

[327] Kenji Kadota and Andrew Spray. Electroweak Multiplet Dark Matter at Future Lepton Colliders. *JHEP*, 02:017, 2019.

[328] Sudip Jana, Nobuchika Okada, and Digesh Raut. Displaced Vertex and Disappearing Track Signatures in type-III Seesaw. 11 2019.

[329] Marco Cirelli, Nicolao Fornengo, and Alessandro Strumia. Minimal dark matter. *Nucl. Phys. B*, 753:178–194, 2006.

[330] Ernest Ma and Daijiro Suematsu. Fermion Triplet Dark Matter and Radiative Neutrino Mass. *Mod. Phys. Lett. A*, 24:583–589, 2009.

[331] Morad Aaboud et al. Search for long-lived charginos based on a disappearing-track signature in pp collisions at $\sqrt{s} = 13$ TeV with the ATLAS detector. *JHEP*, 06:022, 2018.

[332] Elena Accomando, Diego Becciolini, Alexander Belyaev, Stefano Moretti, and Claire Shepherd-Themistocleous. Z' at the LHC: Interference and Finite Width Effects in Drell-Yan. *JHEP*, 10:153, 2013.

[333] E. Accomando, F. Coradeschi, T. Cridge, J. Fiaschi, F. Hautmann, S. Moretti, C. Shepherd-Themistocleous, and C. Voisey. Production of Z'-boson resonances with large width at the LHC. *Phys. Lett. B*, 803:135293, 2020.

[334] Yann Mambrini. The ZZ' kinetic mixing in the light of the recent direct and indirect dark matter searches. *JCAP*, 07:009, 2011.

[335] Kevork N. Abazajian and Julian Heeck. Observing Dirac neutrinos in the cosmic microwave background. *Phys. Rev. D*, 100:075027, 2019.

[336] Pavel Fileviez Pérez, Clara Murgui, and Alexis D. Plascencia. Neutrino-Dark Matter Connections in Gauge Theories. *Phys. Rev. D*, 100(3):035041, 2019.

[337] Pablo F. de Salas and Sergio Pastor. Relic neutrino decoupling with flavour oscillations revisited. *JCAP*, 07:051, 2016.

[338] J. Billard, L. Strigari, and E. Figueroa-Feliciano. Implication of neutrino backgrounds on the reach of next generation dark matter direct detection experiments. *Phys. Rev. D*, 89(2):023524, 2014.

[339] Jogesh C. Pati and Abdus Salam. Lepton Number as the Fourth Color. *Phys. Rev. D*, 10:275–289, 1974. [Erratum: Phys.Rev.D 11, 703–703 (1975)].

[340] Rabindra N. Mohapatra and Jogesh C. Pati. Left-Right Gauge Symmetry and an Isoconjugate Model of CP Violation. *Phys. Rev. D*, 11:566–571, 1975.

[341] R.N. Mohapatra and Jogesh C. Pati. A Natural Left-Right Symmetry. *Phys. Rev. D*, 11:2558, 1975.

[342] G. Senjanovic and Rabindra N. Mohapatra. Exact Left-Right Symmetry and Spontaneous Violation of Parity. *Phys. Rev. D*, 12:1502, 1975.

[343] Goran Senjanovic. Spontaneous Breakdown of Parity in a Class of Gauge Theories. *Nucl. Phys. B*, 153:334–364, 1979.

[344] Rabindra N. Mohapatra, Frank E. Paige, and D.P. Sidhu. Symmetry Breaking and Naturalness of Parity Conservation in Weak Neutral Currents in Left-Right Symmetric Gauge Theories. *Phys. Rev. D*, 17:2462, 1978.

[345] C.S. Lim and T. Inami. Lepton Flavor Nonconservation and the Mass Generation Mechanism for Neutrinos. *Prog. Theor. Phys.*, 67:1569, 1982.

[346] J.F. Gunion, J. Grifols, A. Mendez, Boris Kayser, and Fredrick I. Olness. Higgs Bosons in Left-Right Symmetric Models. *Phys. Rev. D*, 40:1546, 1989.

[347] N.G. Deshpande, J.F. Gunion, Boris Kayser, and Fredrick I. Olness. Left-right symmetric electroweak models with triplet Higgs. *Phys. Rev. D*, 44:837–858, 1991.

[348] Pavel Fileviez Perez. Type III Seesaw and Left-Right Symmetry. *JHEP*, 03:142, 2009.

[349] R.N. Mohapatra et al. Theory of neutrinos: A White paper. *Rept. Prog. Phys.*, 70:1757–1867, 2007.

[350] Morad Aaboud et al. Search for a new heavy gauge boson resonance decaying into a lepton and missing transverse momentum in 36 fb^{-1} of pp collisions at $\sqrt{s} = 13$ TeV with the ATLAS experiment. *Eur. Phys. J. C*, 78(5):401, 2018.

[351] Morad Aaboud et al. Search for new phenomena in dijet events using 37 fb^{-1} of pp collision data collected at $\sqrt{s}$ =13 TeV with the ATLAS detector. *Phys. Rev. D*, 96(5):052004, 2017.

[352] Albert M Sirunyan et al. Search for dijet resonances in proton–proton collisions at $\sqrt{s}$ = 13 TeV and constraints on dark matter and other models. *Phys. Lett. B*, 769:520–542, 2017. [Erratum: Phys.Lett.B 772, 882–883 (2017)].

[353] Vardan Khachatryan et al. Search for heavy gauge W' boson in events with an energetic lepton and large missing transverse momentum at $\sqrt{s} = 13$ TeV. *Phys. Lett. B*, 770:278–301, 2017.

[354] Albert M Sirunyan et al. Search for high-mass resonances in final states with a lepton and missing transverse momentum at $\sqrt{s} = 13$ TeV. *JHEP*, 06:128, 2018.

[355] Georges Aad et al. Search for new resonances in mass distributions of jet pairs using 139 fb^{-1} of pp collisions at $\sqrt{s} = 13$ TeV with the ATLAS detector. *JHEP*, 03:145, 2020.

[356] Albert M Sirunyan et al. Search for high mass dijet resonances with a new background prediction method in proton-proton collisions at $\sqrt{s} = 13$ TeV. *JHEP*, 05:033, 2020.

[357] Véronique Bernard, Sébastien Descotes-Genon, and Luiz Vale Silva. Constraining the gauge and scalar sectors of the doublet left-right symmetric model. *JHEP*, 09:088, 2020.

[358] Ernest Ma. Radiative Quark and Lepton Masses in a Left-right Gauge Model. *Phys. Rev. Lett.*, 63:1042, 1989.

[359] Henry Diaz, V. Pleitez, and O. Pereyra Ravinez. Dirac neutrinos in an SU(2) left-right symmetric model. *Phys. Rev. D*, 102(7):075006, 2020.

[360] Gianpiero Mangano, Gennaro Miele, Sergio Pastor, Teguayco Pinto, Ofelia Pisanti, and Pasquale D. Serpico. Relic neutrino decoupling including flavor oscillations. *Nucl. Phys. B*, 729:221–234, 2005.

[361] E. Grohs, G. M. Fuller, C. T. Kishimoto, M. W. Paris, and A. Vlasenko. Neutrino energy transport in weak decoupling and big bang nucleosynthesis. *Phys. Rev. D*, 93(8):083522, 2016.

[362] Kevork Abazajian et al. CMB-S4 Science Case, Reference Design, and Project Plan. 7 2019.

[363] Yue Zhang, Haipeng An, Xiangdong Ji, and Rabindra N. Mohapatra. General CP Violation in Minimal Left-Right Symmetric Model and Constraints on the Right-Handed Scale. *Nucl. Phys. B*, 802:247–279, 2008.

[364] Chengcheng Han, M.L. López-Ibáñez, Bo Peng, and Jin Min Yang. Dirac dark matter in $U(1)_{B-L}$ with the Stueckelberg mechanism. *Nucl. Phys. B*, 959:115154, 2020.

[365] Vera C. Rubin and Jr. Ford, W.Kent. Rotation of the Andromeda Nebula from a Spectroscopic Survey of Emission Regions. *Astrophys. J.*, 159:379–403, 1970.

[366] Camilo Garcia-Cely, Alejandro Ibarra, Anna S. Lamperstorfer, and Michel H. G. Tytgat. Gamma-rays from Heavy Minimal Dark Matter. *JCAP*, 10:058, 2015.

[367] Marco Cirelli, Thomas Hambye, Paolo Panci, Filippo Sala, and Marco Taoso. Gamma ray tests of Minimal Dark Matter. *JCAP*, 10:026, 2015.

[368] Julian Heeck and Sudhanwa Patra. Minimal Left-Right Symmetric Dark Matter. *Phys. Rev. Lett.*, 115(12):121804, 2015.

[369] Camilo Garcia-Cely and Julian Heeck. Phenomenology of left-right symmetric dark matter. *JCAP*, 03:021, 2016.

[370] Asher Berlin, Patrick J. Fox, Dan Hooper, and Gopolang Mohlabeng. Mixed Dark Matter in Left-Right Symmetric Models. *JCAP*, 06:016, 2016.

[371] Debasish Borah, Arnab Dasgupta, Ujjal Kumar Dey, Sudhanwa Patra, and Gaurav Tomar. Multi-component Fermionic Dark Matter and IceCube PeV scale Neutrinos in Left-Right Model with Gauge Unification. *JHEP*, 09:005, 2017.

[372] P. S. Bhupal Dev, D. Kazanas, R.N. Mohapatra, V.L. Teplitz, and Yongchao Zhang. Heavy right-handed neutrino dark matter and PeV neutrinos at IceCube. *JCAP*, 08:034, 2016.

[373] P.S. Bhupal Dev, Rabindra N. Mohapatra, and Yongchao Zhang. Naturally stable right-handed neutrino dark matter. *JHEP*, 11:077, 2016.

[374] P. S. Bhupal Dev, Rabindra N. Mohapatra, and Yongchao Zhang. Heavy right-handed neutrino dark matter in left-right models. *Mod. Phys. Lett. A*, 32:1740007, 2017.

[375] Debasish Borah and Arnab Dasgupta. Left–right symmetric models with a mixture of keV–TeV dark matter. *J. Phys. G*, 46(10):105004, 2019.

[376] P. Ko and Takaaki Nomura. $SU(2)_L \times SU(2)_R$ minimal dark matter with 2 TeV W'. *Phys. Lett. B*, 753:612–618, 2016.

[377] D. Chang, R.N. Mohapatra, and M.K. Parida. Decoupling Parity and SU(2)-R Breaking Scales: A New Approach to Left-Right Symmetric Models. *Phys. Rev. Lett.*, 52:1072, 1984.

[378] D. Chang, R.N. Mohapatra, and M.K. Parida. A New Approach to Left-Right Symmetry Breaking in Unified Gauge Theories. *Phys. Rev. D*, 30:1052, 1984.

[379] D. Chang, R.N. Mohapatra, J. Gipson, R.E. Marshak, and M.K. Parida. Experimental Tests of New SO(10) Grand Unification. *Phys. Rev. D*, 31:1718, 1985.

[380] Maximilian H. Abitbol et al. The Simons Observatory: Astro2020 Decadal Project Whitepaper. *Bull. Am. Astron. Soc.*, 51:147, 2019.

[381] B.A. Benson et al. SPT-3G: A Next-Generation Cosmic Microwave Background Polarization Experiment on the South Pole Telescope. *Proc. SPIE Int. Soc. Opt. Eng.*, 9153:91531P, 2014.

[382] Garv Chauhan, P.S. Bhupal Dev, Rabindra N. Mohapatra, and Yongchao Zhang. Perturbativity constraints on $U(1)_{B-L}$ and left-right models and implications for heavy gauge boson searches. *JHEP*, 01:208, 2019.

[383] Florian Staub. SARAH 4 : A tool for (not only SUSY) model builders. *Comput. Phys. Commun.*, 185:1773–1790, 2014.

[384] G. Belanger, F. Boudjema, A. Pukhov, and A. Semenov. micrOMEGAs_3: A program for calculating dark matter observables. *Comput. Phys. Commun.*, 185:960–985, 2014.

[385] Malcolm Fairbairn and Jure Zupan. Dark matter with a late decaying dark partner. *JCAP*, 07:001, 2009.

[386] Clifford Cheung, Gilly Elor, Lawrence J. Hall, and Piyush Kumar. Origins of Hidden Sector Dark Matter I: Cosmology. *JHEP*, 03:042, 2011.

[387] Anibal D. Medina. Higgsino-like Dark Matter From Sneutrino Late Decays. *Phys. Lett. B*, 770:161–165, 2017.

[388] Tony Gherghetta, Benedict von Harling, Anibal D. Medina, Michael A. Schmidt, and Timothy Trott. SUSY implications from WIMP annihilation into scalars at the Galactic Center. *Phys. Rev. D*, 91:105004, 2015.

[389] Debasish Borah and Aritra Gupta. New viable region of an inert Higgs doublet dark matter model with scotogenic extension. *Phys. Rev. D*, 96(11):115012, 2017.

[390] Junji Hisano, Shigeki. Matsumoto, Mihoko M. Nojiri, and Osamu Saito. Non-perturbative effect on dark matter annihilation and gamma ray signature from galactic center. *Phys. Rev. D*, 71:063528, 2005.

[391] Junji Hisano, Shigeki Matsumoto, Minoru Nagai, Osamu Saito, and Masato Senami. Non-perturbative effect on thermal relic abundance of dark matter. *Phys. Lett. B*, 646:34–38, 2007.

[392] John McDonald. Warm Dark Matter via Ultra-Violet Freeze-In: Reheating Temperature and Non-Thermal Distribution for Fermionic Higgs Portal Dark Matter. *JCAP*, 08:035, 2016.

[393] Anirban Biswas, Debasish Borah, and Arnab Dasgupta. UV complete framework of freeze-in massive particle dark matter. *Phys. Rev. D*, 99(1):015033, 2019.

[394] Shrihari Gopalakrishna, Andre de Gouvea, and Werner Porod. Right-handed sneutrinos as nonthermal dark matter. *JCAP*, 05:005, 2006.

[395] Andre de Gouvea, Shrihari Gopalakrishna, and Werner Porod. Stop Decay into Right-handed Sneutrino LSP at Hadron Colliders. *JHEP*, 11:050, 2006.

[396] Veronique Page. Non-thermal right-handed sneutrino dark matter and the Omega(DM)/Omega(b) problem. *JHEP*, 04:021, 2007.

[397] Takehiko Asaka, Koji Ishiwata, and Takeo Moroi. Right-handed sneutrino as cold dark matter of the universe. *Phys. Rev. D*, 75:065001, 2007.

[398] Takehiko Asaka, Koji Ishiwata, and Takeo Moroi. Right-handed sneutrino as cold dark matter. *Phys. Rev. D*, 73:051301, 2006.

[399] Jonathan L. Feng, Arvind Rajaraman, and Fumihiro Takayama. SuperWIMP dark matter signals from the early universe. *Phys. Rev. D*, 68:063504, 2003.

[400] P.A.R. Ade et al. Planck 2015 results. XIII. Cosmological parameters. *Astron. Astrophys.*, 594:A13, 2016.

[401] Sandhya Choubey, Sarif Khan, Manimala Mitra, and Subhadeep Mondal. Singlet-Triplet Fermionic Dark Matter and LHC Phenomenology. *Eur. Phys. J. C*, 78(4):302, 2018.

[402] P. Chardonnet, P. Salati, and Pierre Fayet. Heavy triplet neutrinos as a new dark matter option. *Nucl. Phys. B*, 394:35–72, 1993.

[403] Ernest Ma. Pathways to naturally small neutrino masses. *Phys. Rev. Lett.*, 81:1171–1174, 1998.

[404] Ernest Ma and D.P. Roy. Heavy triplet leptons and new gauge boson. *Nucl. Phys. B*, 644:290–302, 2002.

[405] Wei Chao. Dark matter, LFV and neutrino magnetic moment in the radiative seesaw model with fermion triplet. *Int. J. Mod. Phys. A*, 30(01):1550007, 2015.

[406] Federico von der Pahlen, Guillermo Palacio, Diego Restrepo, and Oscar Zapata. Radiative Type III Seesaw Model and its collider phenomenology. *Phys. Rev. D*, 94(3):033005, 2016.

[407] Georges Aad et al. Observation of a new particle in the search for the Standard Model Higgs boson with the ATLAS detector at the LHC. *Phys. Lett. B*, 716:1–29, 2012.

[408] Serguei Chatrchyan et al. Observation of a New Boson at a Mass of 125 GeV with the CMS Experiment at the LHC. *Phys. Lett. B*, 716:30–61, 2012.

[409] Laura Lopez Honorez, Emmanuel Nezri, Josep F. Oliver, and Michel H.G. Tytgat. The Inert Doublet Model: An Archetype for Dark Matter. *JCAP*, 02:028, 2007.

[410] Laura Lopez Honorez and Carlos E. Yaguna. The inert doublet model of dark matter revisited. *JHEP*, 09:046, 2010.

[411] Abdesslam Arhrib, Yue-Lin Sming Tsai, Qiang Yuan, and Tzu-Chiang Yuan. An Updated Analysis of Inert Higgs Doublet Model in light of the Recent Results from LUX, PLANCK, AMS-02 and LHC. *JCAP*, 06:030, 2014.

[412] Alexander Belyaev, Giacomo Cacciapaglia, Igor P. Ivanov, Felipe Rojas-Abatte, and Marc Thomas. Anatomy of the Inert Two Higgs Doublet Model in the light of the LHC and non-LHC Dark Matter Searches. *Phys. Rev. D*, 97(3):035011, 2018.

[413] Debasish Borah, Soumya Sadhukhan, and Shibananda Sahoo. Lepton Portal Limit of Inert Higgs Doublet Dark Matter with Radiative Neutrino Mass. *Phys. Lett. B*, 771:624–632, 2017.

[414] Anirban Biswas, Sandhya Choubey, and Sarif Khan. FIMP and Muon $(g-2)$ in a $U(1)_{L_\mu - L_\tau}$ Model. *JHEP*, 02:123, 2017.

[415] Felix Kahlhoefer. Review of LHC Dark Matter Searches. *Int. J. Mod. Phys. A*, 32(13):1730006, 2017.

[416] Benjamin Fuks, Michael Klasen, David R. Lamprea, and Marcel Rothering. Gaugino production in proton-proton collisions at a center-of-mass energy of 8 TeV. *JHEP*, 10:081, 2012.

[417] Benjamin Fuks, Michael Klasen, David R. Lamprea, and Marcel Rothering. Precision predictions for electroweak superpartner production at hadron colliders with Resummino. *Eur. Phys. J. C*, 73:2480, 2013.

[418] Yi Cai and Andrew Paul Spray. Fermionic Semi-Annihilating Dark Matter. *JHEP*, 01:087, 2016.

[419] Debasish Borah, Mrinal Kumar Das, and Ananya Mukherjee. Common origin of nonzero θ_{13} and baryon asymmetry of the Universe in a TeV scale seesaw model with A_4 flavor symmetry. *Phys. Rev. D*, 97(11):115009, 2018.

[420] Biswajit Karmakar and Arunansu Sil. Nonzero $-_{13}$ and leptogenesis in a type-I seesaw model with A_4 symmetry. *Phys. Rev. D*, 91:013004, 2015.

[421] Xiao-Gang He, Yong-Yeon Keum, and Raymond R. Volkas. A(4) flavor symmetry breaking scheme for understanding quark and neutrino mixing angles. *JHEP*, 04:039, 2006.

[422] G.C. Branco, R. Gonzalez Felipe, M.N. Rebelo, and H. Serodio. Resonant leptogenesis and tribimaximal leptonic mixing with A(4) symmetry. *Phys. Rev. D*, 79:093008, 2009.

[423] Yin Lin. A Predictive A(4) model, Charged Lepton Hierarchy and Tri-bimaximal Sum Rule. *Nucl. Phys. B*, 813:91–105, 2009.

[424] L. Dorame, S. Morisi, E. Peinado, J.W.F. Valle, and Alma D. Rojas. A new neutrino mass sum rule from inverse seesaw. *Phys. Rev. D*, 86:056001, 2012.

[425] Werner Rodejohann and Xun-Jie Xu. A left–right symmetric flavor symmetry model. *Eur. Phys. J. C*, 76(3):138, 2016.

[426] W. Grimus and L. Lavoura. A Model for trimaximal lepton mixing. *JHEP*, 09:106, 2008.

[427] Carl H. Albright and Werner Rodejohann. Comparing Trimaximal Mixing and Its Variants with Deviations from Tri-bimaximal Mixing. *Eur. Phys. J. C*, 62:599–608, 2009.

[428] Carl H. Albright, Alexander Dueck, and Werner Rodejohann. Possible Alternatives to Tri-bimaximal Mixing. *Eur. Phys. J. C*, 70:1099–1110, 2010.

[429] Xiao-Gang He and A. Zee. Minimal Modification to Tri-bimaximal Mixing. *Phys. Rev. D*, 84:053004, 2011.

[430] P.F. de Salas, D.V. Forero, C.A. Ternes, M. Tortola, and J.W.F. Valle. Status of neutrino oscillations 2018: 3σ hint for normal mass ordering and improved CP sensitivity. *Phys. Lett. B*, 782:633–640, 2018.

[431] Peter Athron et al. Status of the scalar singlet dark matter model. *Eur. Phys. J. C*, 77(8):568, 2017.

[432] Yann Mambrini, Keith A. Olive, Jeremie Quevillon, and Bryan Zaldivar. Gauge Coupling Unification and Nonequilibrium Thermal Dark Matter. *Phys. Rev. Lett.*, 110(24):241306, 2013.

[433] David Curtin et al. Long-Lived Particles at the Energy Frontier: The MATHUSLA Physics Case. *Rept. Prog. Phys.*, 82(11):116201, 2019.

[434] Xuheng Luo, Werner Rodejohann, and Xun-Jie Xu. Dirac neutrinos and $N_{\rm eff}$. *JCAP*, 06:058, 2020.

[435] Gautam Bhattacharyya, Maíra Dutra, Yann Mambrini, and Mathias Pierre. Freezing-in dark matter through a heavy invisible Z'. *Phys. Rev. D*, 98(3):035038, 2018.